TU Delft

TUD Civil Engineering
Concrete structures

FBG optical fibers in proof loading of concrete slab bridges

Master Thesis

FBG optical fibers in proof loading of concrete slab bridges

Master Thesis
July, 2021

By
Luuk Faassen

Supervisor:	Dr. ir. Y. Yang	TU Delft
Thesis committee:	Dr. E. Noordermeer	Fugro
	Dr.ir. E.O.L. Lantsoght	TU Delft & USFQ
	Dr. A. Cicirello	TU Delft

Cover photo: Luuk Faassen, 2020
Published by: Technische Universiteit Delft, Concrete structures, Delft, Building 23, 2628 CN, Stevinweg 1 The Netherlands
www.tudelft.nl/en/ceg/about-faculty/departments/engineering-structures/sections-labs/concrete-structures/

Preface

This Master's thesis has been written to conclude my study at Delft University of Technology. This thesis is a partial fulfilment of the requirements for the degree of Master of Science in Structural Engineering, with a specialization in Concrete Structures. This thesis has been completed under the strangest of circumstances, which no one could have imagined. Its completion would not have been possible without the support and assistance of a number of people.

First, I would like to thank my committee, your guidance throughout this process has been invaluable. Yuguang Yang, you have helped me shape this project from the very beginning, and has always made time for me when I needed your opinion on a specific topic. I really appreciate all your effort. Eva Lantsoght, thank you for all the feedback moments. It has lifted this final product to anther level. Alice Cicirello, your fresh view on the topic has kept me sharp to perform on the committee meetings and I really enjoyed your enthusiasm on the project. Edo Noordermeer, our meetings have really been a joyful moment every week. Your academic attitude, and knowledge on project management and personality provided me with the best company mentor I could wish for.

Secondly, I would like to express my sincere gratitude to Gabriela Zárate Garnica, for letting me install one of her specimen with fiber optical sensors. I really enjoyed our meetings, and it has been really helpful receiving feedback on the technical part, but also to be able to discuss the project management part. You, Eva and Yuguang did everything possible to keep to the planning as much as possible, in difficult times, which enabled me to run an experiment in the lab. This is something for which I am eternally grateful.

Also, I would like to thank the people at Fugro, for enabling me to write my thesis at their company. Vincent, your practical knowledge on how to get things done, has come in handy quite a few times. Nicolas, thank you for introducing me to fiber optics and answering every single question I've had.

About five years ago, I was doubting if I should start working, or if I should proceed studying to obtain the master's degree, in addition to my bachelors. It is due to the people I discussed this with, mainly at the company of ABT, and with the encouragement from my parents , that I made the choice to go for it.

Four years ago, when I started my masters, I could have never imagined how much I would learn. I really enjoyed learning from all the professors at the university. Much more I enjoyed how it all seemed like rocket science at first, but by working together with my fellow students from the HAN, we were able to figure it out together. It would not have been so enjoyable without you guys !

Jane, thank you for saving my thesis from many typos and writing mistakes. I really appreciate that you took time to go through the whole thesis. Bas, who I could always bother with all my questions. I always found our technical discussions enjoyable. Above all, I really enjoyed your presence as a friend in Delft. I am thankful for all the relaxing moments you provided.

Mara, thank you for your love and support. While being with you, I was really able to forget about all the work and enjoy some time together.

completion of this study would not have been possible without the unconditional support and love from my family and friends, Thank you.

Luuk Faassen
Groesbeek, July 2021

Abstract

As the average age of bridges in the Netherlands is increasing and loads are rising, more research on the capacity of these bridges is required. One of the methods to determine if a bridge still has sufficient safety is proof load testing. This method has been extensively researched over the past decade and has led to the development of stop criteria. Stop criteria are values of structural responses at which further loading may course irreversibly damage to the structure. Stop criteria, based on beam experiments, are available for flexural failure but not yet for shear failure as these proposals are not yet verified and shear failure is a brittle failure mode. Additionally, the advantage of the redistribution of the forces as a result of the additional dimensions of a plate bridge are not accounted for during the development of stop criteria. Measuring all currently proposed stop criteria requires a lot of single sensors, and it is holding back the application of the method in practice. No standard approach on where the sensors must be placed is available. A method to improve the applicability of proof load testing in practice is to simplify the sensor setup by using multifunctional, multiplexable sensors which can capture the global and local behavior of the slab simultaneously. It is found that such a sensor system can be designed by fiber optical sensors.

In this research, a fiber optical measurement system is developed to measure stop criteria for proof load testing. For application of the system to the slab a stiff glued anchorage system is designed, which is able to transfer the concrete strains to the reusable, long gauge fiber optic sensor system. The performance of this anchorage system is checked by preliminary experiments that include the comparison of various glues and investigates time-dependent effects. An installation method for these anchors is developed to improve practical applicability.

Based on the proposed measurement system for a slab bridge, adjustments are made to the stop criteria from the literature to be able to analyze them with the fiber optical measurement system. Additionally, new stop criteria for fiber optical measurements are proposed based based on strain measurements on the bottom side of a slab bridge. These stop criteria are based on the critical shear crack theory for one way, and two-way shear.

The proposed measurement system was installed to a slab, part of an ongoing experimental program, to investigate stop criteria on reinforced concrete slab bridges. The performance of the designed fiber optical measurement system has been analyzed based on a 1:2 scale proof load test. The results from the optical fiber sensors measure the global behavior of the slab bridge such as cracking and deflection well.

In addition to the external sensor system which can be applied during proof load tests, internal optical fiber sensors were included within the reinforcement. These sensors provide information on the strains up until the yielding point of the reinforcement bars. The inclusion of these sensors in the experimental program gave the opportunity to compare external results with the internal strains and get more insight in the behavior of the slab itself. The performance of the theoretical assumptions to develop the stop criteria could be confirmed with these measurements.

Finally, the results from these tests were used to analyze the performance of the proposed stop criteria measured by optical fibers. The optical fiber measurement system was able to measure the stop criteria. However, due to the crack spacing and the applied gauge length, the crack width of single cracks was not measured accurately on critical locations of the slab. The flexural strain stop criterion straight underneath the load was reached at 78% of the failure load. The conversion from the external strain to the reinforcement strain to determine the stop criterion was not very accurate as the set limit on the reinforcement

strain was reached at 55% of the failure load. This is a difference of 23% It was found that this method achieves higher accuracy (with a difference around 10%) when measured further away from the point load. The best performing one-dimensional shear stop criteria were the stop criterion on crack width based on loss of aggregate interlock which were reached at an average of 55% of the failure load. And the newly derived strain stop criterion based on the critical shear crack theory which was reached at an average of 74% of the failure load. The stop criterion on flexure induced punching shear was reached at 86% of the failure load.

In conclusion, the fiber optical measurement system does provide insight on global and local behavior of the slab, and is able to monitor stop criteria. More importantly, the critical location cannot be missed with this sensor setup, as well as that more simplifications in the measurement setup are possible. It is therefore recommended to apply this measurement technique in future applications of proof load testing.

Contents

Notation

Abbreviations

ACI	American Concrete Institute
AEs	Accoustic emmision sensor
BOFDA	Brilouin optical frequency domain analyzer
BOTDA	Brillouin Optical Time Domain Reflectometry
BOTDR	Brilouin optical time domain analyzer
CSCT	Criterial shear crack theory
CSDT	Critical shear displacement theory
DIC	Digital image correlation
FBG	Fiber bragg grating
FO	Fiber optic
Fos	Fiber optic sensor
LVDT	Lineair variable differential transformer
OBR	Optical backscatter reflectometry
OF	Optical fiber
OFDR	Optical Frequency Domain Reflectometry
RBK	Richtlijn beoordeling kunstwerken
SLS	Serviceability limit state

Roman Upper Case

A	FBG temperature strain coefficient
A_c	Sectional area of the concrete
$A_{s,bot}$	Sectional area of the bottom reinforcement
A_s	Sectional area of the reinforcement
B	FBG strain strain coefficient
E	Young's modulus
E_c	Concrete young's modulus
E_{cm}	Mean Concrete Young's modulus
E_s	Steel young's modulus
$EI_{loading}$	Stiffness of the loading branch
$F_{applied}$	Applied Force
F_y	Force at yielding
L_m	Mean crack spacing
M	Moment
M_{cr}	Cracking moment
M_r	Moment of rupture
M_u	Ultimate moment
M_y	Yielding moment
R_{ai}	Correction factor for high strength concrete
V	Shear force
V_{ai}	Shear force carried by aggregate interlock
V_c	Shear force component carried in the uncracked concrete compression zone
V_{CSDT}	Shear force determined by the critical shear displacement theory
V_d	Shear force component carried by the dowel action
V_r	Shear force resistance
V_{R0}	Punching shear level in which the critical direction reaches maximum transferred force
V_{Rx}	Punching shear strength corresponding to b_x
V_{Ry}	Punching shear strength corresponding to b_y

Roman lower case

a	Distance between support and load
a_m	Distance between the bottom fiber of the concrete and the sensor
a_p	Dimension of the glueing plate
b	Width
b_0	Length of control perimeter
b_{eff}	Effective width
b_{load}	Width of the loading plate
b_{sup}	width of the support
c	Height of the concrete compressive zone
d	Effective depth
d_c	Bottom cover measured from center of lowest bar
$d_{g,0}$	Reference aggregate size of 16mm
d_g	Aggregate size
d_l	Longditudinal effective depth
d_t	Transversal effective depth
$f_{c,m}$	Avarage concrete compressive strength
$f_{c,th}$	Stress in the concrete using Thorenfeldt's stress-strain diagram at yielding of the steel
f_c	Concrete compressive strength
f_{cd}	Design concrete compressive strength
$f_{cm,cube}$	Avarage concrete cube compressive strength
f_{cm}	Mean concrete compressive strength
$f_{ctm,fl}$	Mean concrete flexural tensile strength
f_{ctm}	Mean concrete tensile strength
f_s	Steel stress calculated by elastic crack section theory
f_{yd}	Design value of yielding stress
f_{ym}	Mean steel yield strength
h	Height of the concrete specimen
k	Size effect factor
k_c	Inclination of the stress line
k_{sec}	Sectional stiffness
k_{slab}	Correction factor for shear stresses in slabs
l	Length
$l_{cr,m}$	Mean major crack spacing
l_{gauge}	Gauge length
l_{load}	length of the loading plate
l_{st}	transfer length of the steel reinforcement
n_e	Elastic stiffness ratio between E_s and E_c
n_{eff}	Refractive index
n_{th}	Material parameter of concrete
s	Distance between reinforcement bars
s_{cr}	Major crack height
v_{min}	Minimum shear stress
$v_{R,c}$	Shear stress
v_{RBK}	Design shear stress by RBK
$w_{max,DAfstB}$	Maximum crack width stop criterion
$w_{max,vos}$	Maximum crack width stop criterion
$w_{res,DAfstB}$	Maximum residual crack width stop criterion
$w_{res,vos}$	Maximum residual crack width stop criterion

w	Crack width
w_{ai}	Crack width at which aggregate interlock is lost
w_b	Crack opening at the level of the tensile reinforcement in the longitudinal direction
w_c	Crack width
$w_{cr,m}$	Mean crack width
w_{cr}	Crack width
w_{fict}	Ficticious crack width
w_{m0}	Initial crack width
w_{max}	Maximum crack width
w_{mv}	Mean crack width
w_{stop}	Crack width stop criterion
x_u	Ultimate compressive zone height of the concrete
y_{top}	Neutral axis from the top
z	Length of the internal level arm between the loading point of the equivalent compressive force and the centroid of the tension force in tensile reinforcement
z_c	The height of the uncracked compressive zone at tip of the major crack

Greek upper case

Δ	Difference
ΔL	Elongation
ΔT	Difference in temperature
Δw	Difference in crack width
Δ_{λ}	Difference in wavelenngth
Δ_{vos}	Stop criterion for displacement
Δ_{ε}	Difference in strain
Δ_{cr}	Critical shear displacement
Λ	Grating constant

Greek lower case

α	Material parameter of concrete
α_e	Elastic stiffness ratio between E_s and E_c
β_{fr}	Strain gradient
δ_{vos}	Deflection stop criterion
ε	Strain
ε_λ	Amount of strain possible by bandwidth of the FBG
$\varepsilon_{c,bot}$	Strain at the bottom of the concrete
ε_{CSDT}	Strain stop criterion based on CSDT
ε_{sensor}	Measured strain in the sensor
ε_t	Amount of strain possible by maximum tensile force of the optical fiber
ε_y	Yielding strain of the reinforcement
ε_0	Material parameter of concrete
$\varepsilon_{c,comp}$	Concrete strain of top fiber
$\varepsilon_{c,lim}$	Concrete strain stop criterion
ε_c	Concrete strain
ε_{c0}	Initial strain
ε_{cr}	Cracking strain of concrete
ε_{csct}	Strain calculated by the CSCT
ε_{DAfstB}	Strain stop criterion
$\varepsilon_{DAfstB}\mu\varepsilon$	Strain stop criterion
$\varepsilon_{lim,CSDT}\mu\varepsilon$	Strain stop criterion
$\varepsilon_{mean,concrete,gauge}$	Mean strain over gauge length
ε_s	Strain in the reinforcement steel
ε_{s0}	initial steel strain
ε_{stop}	Strain stop criterion
ε_{sw}	Strain in the bottom fiber of the concrete due to self weight
κ	Curvature
κ_{cr}	Curvature at cracking moment
κ_{ult}	Curvature at ultimate moment
κ_y	Curvature at yielding moment
λ	Wavelength
λ_b	Center wavelength
$\mu\varepsilon_{external}$	Strain measured by external sensors
νmin	Minimum shear stress
ρ_l	Londitudinal reinforcement percentage
ρ_s	Reinforcement ratio, ratio of reinforcing bar area over effective area of the beam cross-section $\rho_s = A_s/bd$
ρ_t	Transversal reinforcement percentage
ρ_x	Reinforcement percentage in x direction
ρ_y	Reinforcement percentage in y direction
σ_{cr}	Cracking stress
$\sigma_{s,cr}$	Steel stress after cracking
σ_s	Steel stress

ϕ	Rotation
ϕ_i	Rotation of one section
ϕ_{max}	Maximum rotation
$\phi_{support}$	Rotation at the support
ψ	Slab rotation
ψ_{CSCT}	rotation regarding the CSCT
ψ_x	Rotation in x direction
ψ_y	Rotation in y direction

1 Introduction

The added value of fiber optical measurements in proof load testing is investigated in this thesis. This chapter provides insight in how the research is drafted, and what the motivation behind this study is. The scope of the study is set, and the research questions are presented.

1.1 Background

Many bridges were built after the Second World War in the Netherlands as there were more resources available, and there was more need for infrastructure. These bridges are now approaching the end of their theoretical lifetime. Over the years, information about these bridges has gone missing and assessment is required to guarantee safe usage of the bridges. There are various reasons to doubt the structural performance of a bridge such as changing loads, standards and deterioration of the structure. The existing structures are often not initially designed for these changes. However, in many cases the structure is able to withstand these changes. It is up to engineers to investigate these capacities [1].

These capacities can be studied by various methods. From a simple calculation, to a non linear finite element model. The increase in complexity of the calculation and therefore also the required time increases the accuracy on the approximation of the capacity of the slab bridge. This is illustrated in Figure 1.1. These methods however, do rely on often conservative assumptions of material properties.

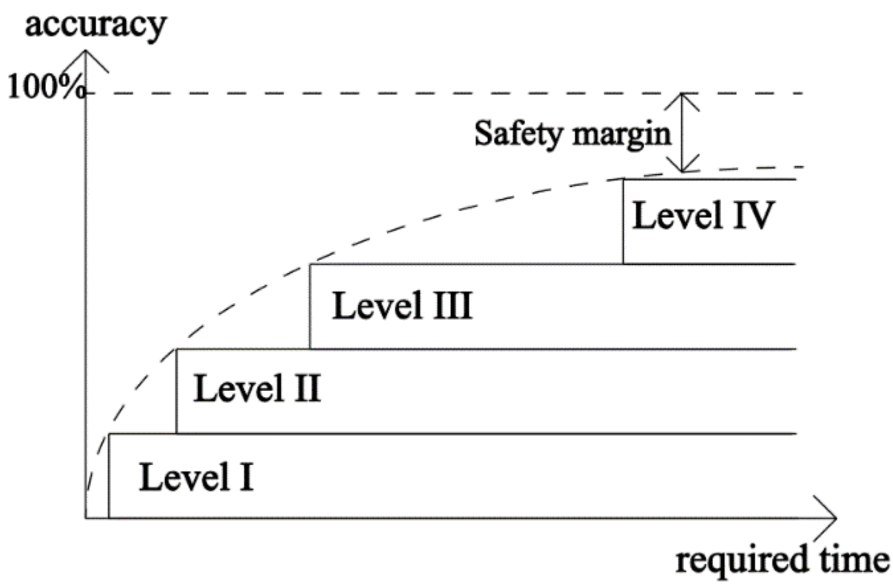

Figure 1.1: Levels of approximation fib Model Code [2]

An evaluation method which does take into account the exact properties of the slab bridge is proof load testing. “In a proof load test, a load that corresponds to the factored live load is applied to the bridge structure, to directly demonstrate that a bridge fulfils the code requirements” [2].To prevent collapse of the structure, the structural responses are monitored. The proof load test should be aborted when a certain threshold in the structural response is reached, such a threshold is called stop criterion.

The current proposal for stop criteria provides verified limits for flexural failure. For shear failure also limits are proposed. However, these are not verified yet and are not optimized for slabs. When concentrated loading near the support is applied, the load spreads over a limited length of the support, the effective width. When calculating slabs for shear loading near supports this effective width has a great influence on the total capacity. One of the models to determine this effective width is the French method, which can be seen in Figure 1.2. The load is spread under 45 degrees from the far end of the loading plate to the edge of the support.

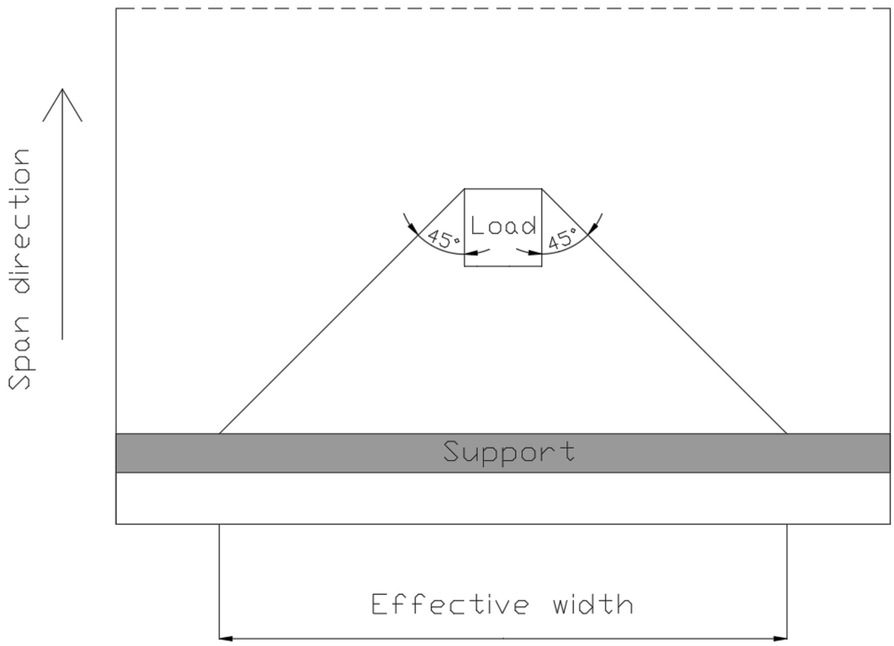

Figure 1.2: Effective width concept on a concrete slab bridge with a concentrated load near the support

Previous studies mainly used local measurements such as strain, crack width and displacement to measure these structural responses, but analyses of the obtained results indicate that improvements could be made by applying distributed measurements [3]. Distributed results could improve assessment of the results by showing the global behaviour of the structure. In addition, when measuring the full length, it is not possible to miss the critical location.

A distributed measurement solution which has evolved to a precise and accurate measurement technique is optical fiber sensing. Over the past decade, the concepts of distributed optical fibers have become more commercialized, and the robustness of sensors has increased so that the application of optical fibers in the field has become more practical. In specific places where many sensors are used, long gauge optical fibers turn out to be a competitive sensing solution in comparison to conventional sensors [4]. This is mainly because conventional sensors need to be connected to an interrogation unit for each individual sensor, while for optical fibers, there can be multiple sensors along the length of one fiber which makes it easier to install and organise.

Therefore, this could be the ideal solution for proof load testing and an improvement in assessing bridges with this method.

1.2 Scope

This study focuses on the optical fibers which can be applied to proof load testing of concrete slab bridges without shear reinforcement. Therefore, the procedure of a proof load test and the expected structural responses are investigated in a literature review. These characteristics can then determine which optical fiber sensing system should be used. Optical fiber technologies which are still in the experimental stage are excluded from this study as they are not readily available on the market. When one measurement system is chosen based on the literature study, the rest of the thesis focuses on this specific optical fiber measurement system only and does not analyse alternative optical fiber methods.

The combination of an optical fiber measurement setup and cyclic loading conditions up until failure are not found in literature. Therefore, no comparison can be made to other studies. This implies that this will be an orientational study. Not all details can be covered in this research. Only if the solution works, it would be justified to invest more money to optimise the solution for practical applications. Therefore, optimisation is not included in the scope of this research. The main goal is to elaborate on how such a measuring system can be designed, to see if the solutions works, and to identify key issues which can be solved in a follow-up study.

As described above, the application of fiber optics on stop criteria for concrete slab bridges are investigated in this study. The concrete slab bridge for which the stop criteria are determined is assumed to be without prestressing, without external reinforcement and straight. The considered failure modes are flexural, shear and flexure induced punching shear failure.

1.3 Research question

This research contributes to the ongoing research on concrete slab bridges and proof load testing. The applicability of fiber optical strain sensors to proof load testing of concrete slab bridges is investigated, and a proposal for measuring continuously along the length of a bridge is evaluated. The main question therefore is:

How can strain fiber optic measurements be used to monitor structural responses of reinforced concrete slab bridges during proof load testing and which stop criteria should be used for these sensors?

This main question is divided into the following sub-questions:

- Which failure modes are governing for a RC slab bridge?
- What deformations/signs are expected to be present before failure?
- In what projects are fiber optics applied in concrete structures?
- How should cracks be measured related to specific actions by optical fiber sensors?
- What is the accuracy of measurements?
- How can the relation between strains on the outside of the concrete, and strains of the internal steel reinforcement be described?
- Which stop criteria can be measured by the fiber optical measurement design?
- How should the optical fiber measurements be verified?
- How should the sensor be applied to the concrete?
- What should be the layout of sensors to detect the critical failure mode?

1.4 Research methodology

To answer the research question, this study is divided into three main approaches. Each approach answers sub-questions. These approaches are combined to provide the answer to the main question. Each of the approaches and corresponding questions is described below. An overview of these approaches is presented in Figure 1.3.

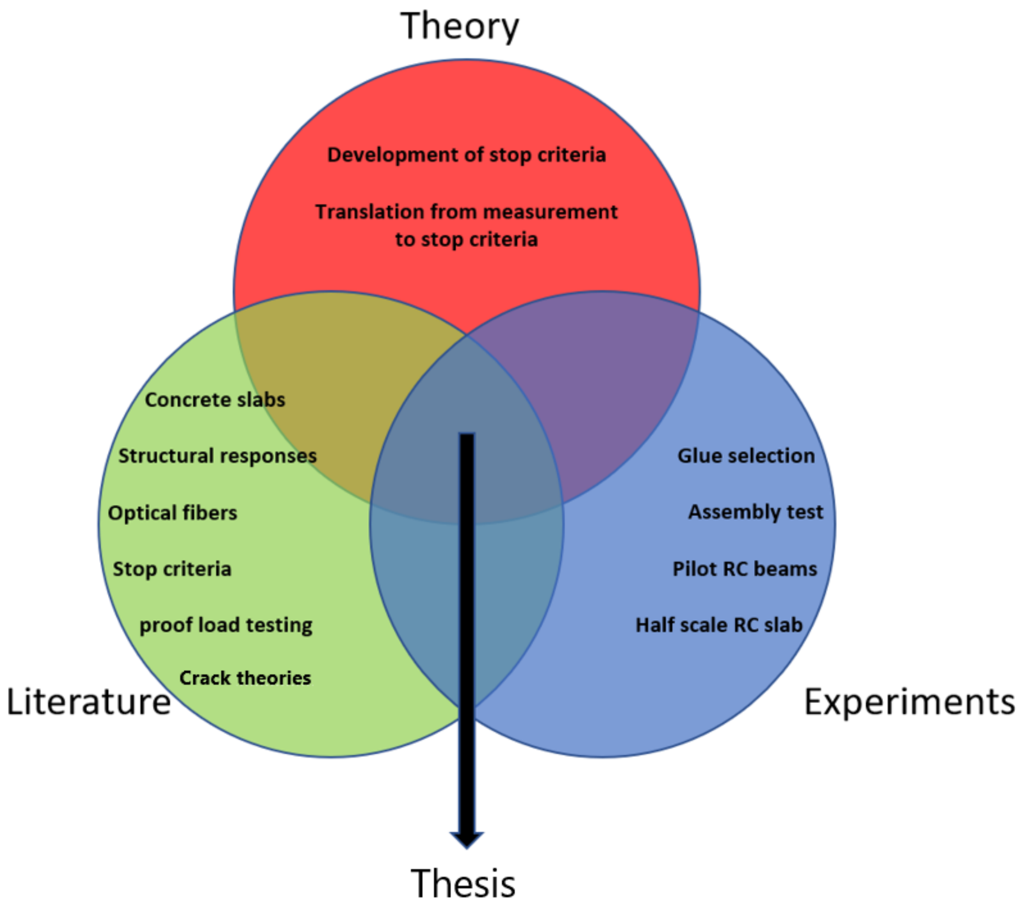

Figure 1.3: Approaches of the main question

Literature

This approach leads to understanding of the relevant concrete concepts and the sensing method. It is investigated how concrete slabs behave under certain loads. Information on theories and mechanisms are gathered within the literature study. It is investigated what the state of the art on stop criteria is, and which of them can be measured with optical fibers. This part leads to contributions on answers to the following sub-questions:

- Which failure modes are governing for a RC slab bridge?
- What deformations/signs are expected to be present before failure?
- In which projects are fiber optics applied in concrete structures?

Theory

The theory is used to link measurements to structural responses and to provide guidance on how to interpret the structural responses in terms of stop criteria. Theoretical backgrounds are used to analyze the results. It becomes clear how the strain results from the optical fiber measurements should be converted to physical quantities, which can be interpreted as stop criteria. Additionally, new stop criteria can be derived using the advantage of a distributed measurement technique. This part mainly contributes to answers on the following sub-questions:

- How should cracks be measured related to specific actions by optical fiber sensors?
- What is the accuracy of measurements?
- How can the relation between strains on the outside of the concrete, and strains of the internal steel reinforcement be described?
- Which stop criteria can be measured by the fiber optical measurement design?

Experiments
This approach leads to a test and measuring plan. The specimen properties and sensor layout are elaborated on. It becomes clear which data is acquired, and what the expected behavior is. The accuracy, spacing and layout is based on the expected behavior of the concrete. This part contributes to answers on the following sub-questions:

- How should cracks be measured related to specific actions by optical fiber sensors?
- What is the accuracy of measurements?
- How can the relation between strains on the outside of the concrete, and strains of the internal steel reinforcement be described?
- Which stop criteria can be measured by the fiber optical measurement design?
- How should the optical fiber measurements be verified?
- How should the sensor be applied to the concrete?
- What should be the layout of sensors to detect the critical failure mode?

1.5 Outline

This thesis includes a total of 9 chapters. As a guide for readers, a brief introduction of each chapter is provided here. First, a brief introduction on the current experimental program at Delft University of Technology is given in Chapter 2. Then, Chapter 3 includes the literature review on concrete slab bridges and the developed stop criteria. In the first part, the behaviour of concrete slabs is elaborated on. Current calculation methods and theories are described. Secondly, the current approach of stop criteria for proof load testing are discussed. Theories are described and important aspects of the theoretical backgrounds on stop criteria are elaborated on. This chapter results in the gap in the literature. In Chapter 4, a review of multiple optical fiber systems is given. This chapter results in a choice for FBG technology and the limits on the application of fiber optic sensors. Chapter 5 provides more insights in how the strain results can be interpreted based on theoretical backgrounds. Current stop criteria are modified to fit in the newly developed measurement system and new stop criteria are proposed. Chapter 6 shows how the measurement system for measuring strains of reinforced concrete bridges with fiber optic sensors is developed and how it can be applied to a concrete bridge. This method is then used in Chapter 7 to determine a measurement setup for the specimen used in the current experimental program at Delft University of Technology. A theoretical interpretation of the gathered data is given and the developed stop criteria are applied. The obtained stop criteria results are analyzed. All methods and improvements are discussed in Chapter 8. Chapter 9 consist of the conclusions and recommendations for further research on this matter.

2 Experimental program at Delft university of technology

For the past decade, Delft University of Technology has been investigating proof load testing as an assessment method for concrete structures. Based on theoretical derivations, researchers proposed stop criteria for concrete beams in flexural failure as well as in shear failure. This chapter gives a brief overview on the ongoing experimental program on stop criteria at Delft University of Technology. A detailed description of the current test setup is given as these experiments were used to test the developed method for measuring structural responses with fiber optical sensors during proof load tests.

2.1 Previous experiments at Delft university of technology

The current proposal of flexural stop criteria is verified by several beam experiments in the Stevin laboratory. Failure tests gave insight in the level of safety on the stop criteria. These tests consisted of 2 beams designed and cast in the laboratory (P-series) [5] and 3 beams sawn from the Ruytenschild bridge (RSB-series) [5]. In additions to these failure tests, several pilot-proof load tests were executed on the following bridges: Vlijmen Oost [6] , Halvemaans [7], Zijlweg [8] and de Beek [9]. On these pilot proof load tests, practical experience was gathered as well as a verification of the stop criteria. However, the level of safety was not determined since these bridges were not loaded until failure.

The shear stop criteria are not yet verified by a significant amount of failure tests. Only three beam tests qualified as shear critical. The inconsistency in the results shows that more investigation on the shear critical sections is necessary. As an intermediate result, the flexural failure stop criteria can be used when a bridge may be considered not shear-critical [10].

2.2 Safety philosophy on stop criteria

One of the latest innovations within this research topic is the development of a stop light method for proof loading, which indicates the level of approximation on the capacity [11]. These are presented in Table 2.1.

Table 2.1: Proposed levels of approximation for stop criteria [11]

Level	Meaning	Risk	Action	Measuring
1	Reach the target load with a conservative margin of safety (e.g., internal cracking)	No risk	No repair	AEs
2	Provide warning of irreversible damage (eg., cracking or yielding of reinfocement)	Moderate	Some repair (e.g, injection of cracks with epoxy	AEs+ LVDTs/FOs+ DIC
3	No further loading is permitted and the test must be terminated (e.g., large opening of a flexural shear crack)	High		AEs+ LVDTs/FOs+ DIC

2.3 Proposed layout of the experiment

In the Stevin laboratory, a half-scale reinforced concrete slab bridge is subjected to a proof load testing load protocol. The dimensions of the concrete slab are 5 m x 2.5 m with a thickness of 0.3 m and the span is 3.6 m. A sketch of the set up is shown in Figure 2.1.

With this setup, two support conditions are tested. The first support is a simple support, and the second support is considered a continuous support. Prestressing bars anchored in the specimen and in the laboratory floor are used to prevent rotation of the slab at the continuous support side. The goal of the experiment is to verify proposed stop criteria for flexural and shear failure, for slabs [11].

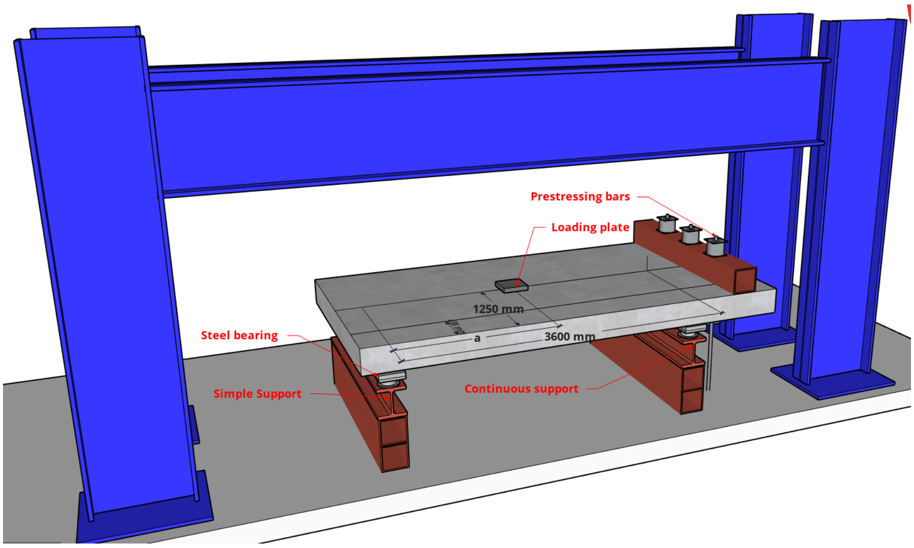

Figure 2.1: Sketch of the proposed experiment [11]

2.4 Design specimen properties

The specimen dimensions are chosen as such that it represents a typical half-scale model of a continuous solid slab bridge like described in Zarate [11]. As the design of the sensor setup is based on the design properties of the specimen, these properties are presented in Table 2.2. These values are based on the Eurocode NEN-EN 1992-1-1 properties of the applied materials.

Table 2.2: Design material properties [11]

Variable		Value
Mean concrete compressive strength	f_{cm} [N/mm^2]	43
Mean concrete tensile strength	f_{ctm} [N/mm^2]	3.21
Mean concrete flexural tensile strength	$f_{ctm,fl}$ [N/mm^2]	4.17
Concrete Young's modulus	E_{cm} [N/mm^2]	34962
Mean steel yield strength	f_{ym} [N/mm^2]	510
Bottom reinforcement	$A_{s,bot}$ [mm^2/m]	6597
Reinforcement ratio	ρ_l [%]	0.996
Effective depth	$d[mm]$	265
Steel Young's modulus	E_s [N/mm^2]	200000

The applied concrete class is C35/45. This concrete class has a mean compressive strength of 43 N/mm^2, and a maximum aggregate size of 16 mm. This is a representative value for existing slab bridges in the Netherlands with continuous hydration [11]. The applied steel is ribbed steel with a characteristic yielding point of 500 N/mm^2. This is one of the two most used steel types in existing slab bridges in the Netherlands [11].

The reinforcement layout is presented in Figure 2.2 and consists out of 21 ø20 mm rebars in longitudinal direction, and 41 ø10 mm rebars in transverse direction. The concrete cover is set to be 25 mm, which results in effective heights of d_l = 265 mm and d_t = 250 mm. The corresponding reinforcement ratios are, ρ_l = 0.996% and ρ_t = 0.258%. In comparison to the mean concrete slab bridge, it can be noticed that the reinforcement diameters are not scaled 1:2. This is a conscious decision since scaling the diameter would imply changes in dowel action, rebar spacing and crack widths, which are complicated to compensate for in post-processing. Zarate used several calculations to show that the reinforcement bars should not be scaled [11].

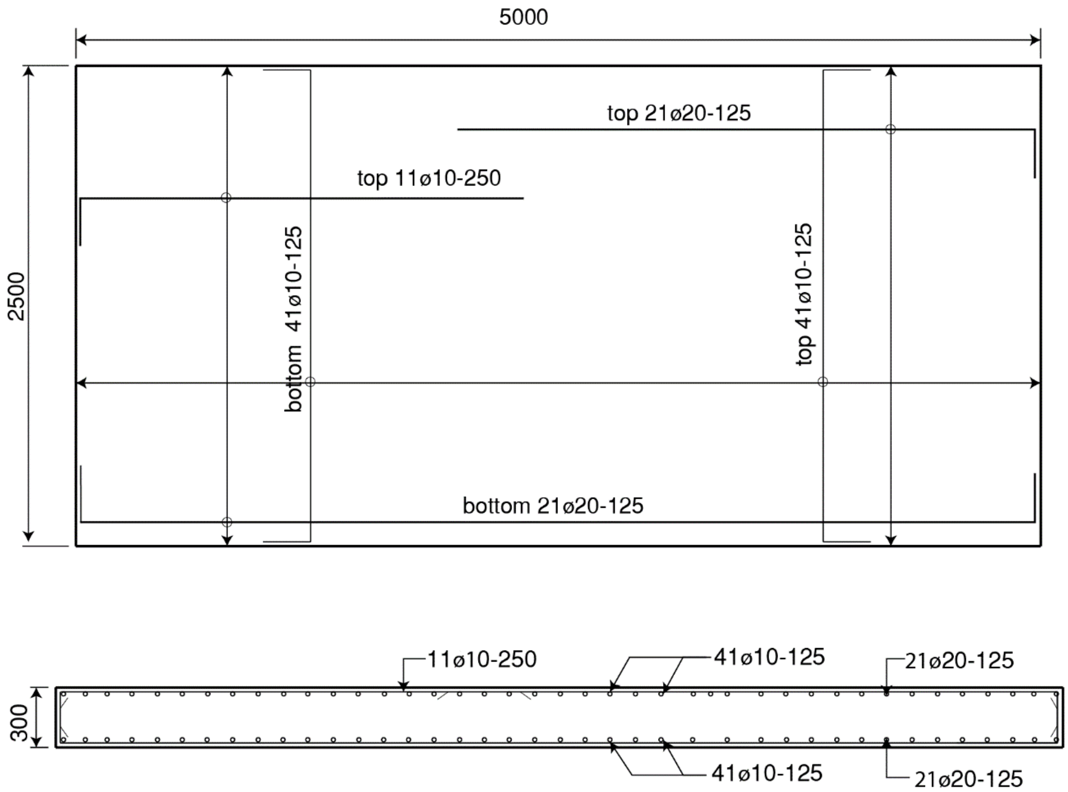

Figure 2.2: Reinforcement layout of the specimen [11]

2.5 Loading positions

The load to the slab is applied with a 200 mm x 200 mm loading plate. The loading position varies between tests. First, the slab is loaded in the middle of the span. This loading position is flexural critical. According to design calculation, loading positions SR1E1 and SR1E3 are expected to fail in flexure. However, there is an increased chance of these experiments te fail in shear, as the load is closer to the calculated shear critical zone. Experiment SR1E2 and SR1E4, are expected to fail in shear [11]. The loading positions are shown in Figure 2.3.

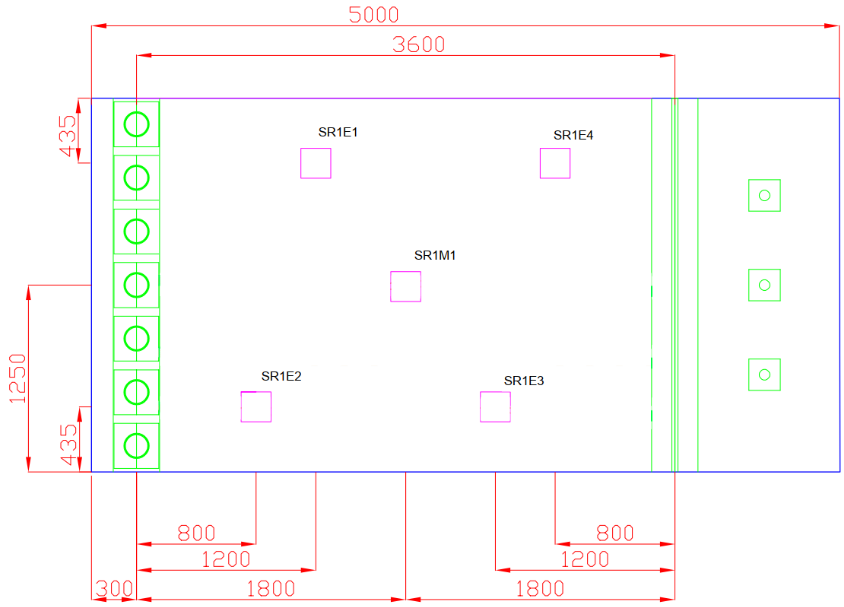

Figure 2.3: Final loading positions

2.6 Loading protocol

The loading protocol is shown in Figure 2.4. Each load level is repeated three times to check if any non-linearity arises. The load levels are determined based on the expected behavior of the slab. First, a relatively low load is applied to check if all measurement systems are functioning as expected. Second, the load is increased up until the SLS level. Then, a intermediate load level between the SLS load level and the ULS load level is applied to the slab. Subsequent load levels are set at the ULS load level, 1.25 times the ULS load level and 1.5 times the ULS load level. In between these load steps, the SLS load level is repeated to check for differences in behavior of the slab. Finally, the slab is loaded up until failure.

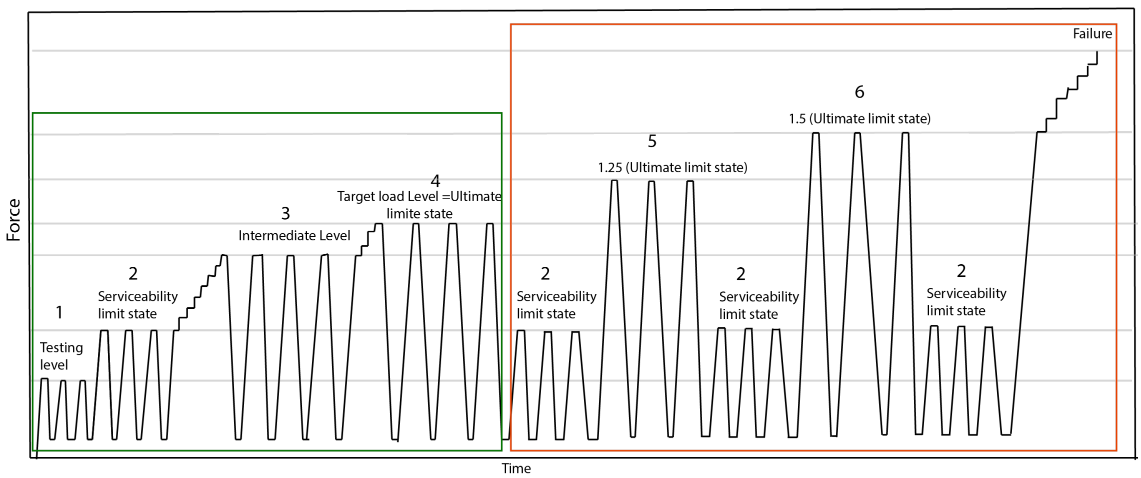

Figure 2.4: Loading protocol [11]

2.7 Measurements

The following measurement techniques are used to monitor the overall behavior of the slab and to gather measurements which can be checked with earlier proposed stop criteria.

- Force and displacement of the loading jack
- Load cells under all supports and prestressing bars
- Vertical displacements on several locations with lasers and LVDTs on the top side and the bottom side of the slab
- Various LVDT strain measurements
- Digital Image Correlation to monitor cracks at the bottom side and side face of the slab
- Acoustic Emission sensors along the possible shear crack path on the top side and bottom side of the slab
- 2 BDI transducers for strain measurement at the bottom side of the concrete

A typical overview of the sensor layout is provided in Figure 2.5. The sensor layout of the subsequent tests slightly differs. Several sensors are relocated closer to the loading position.

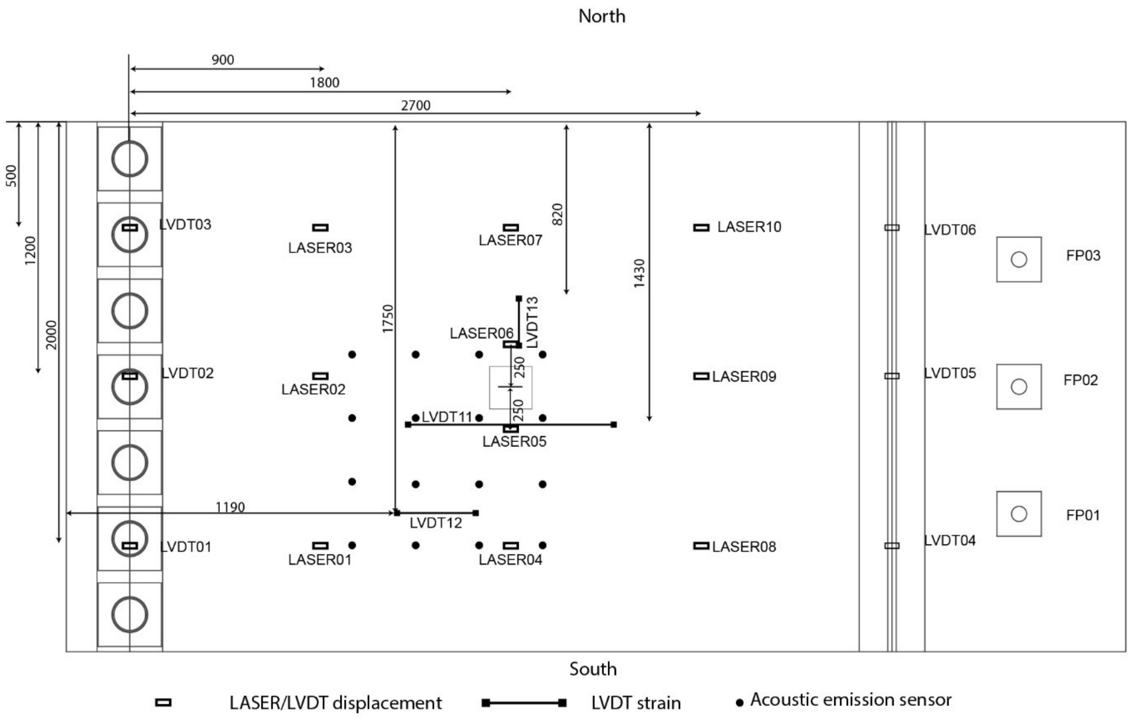

(a) Top view

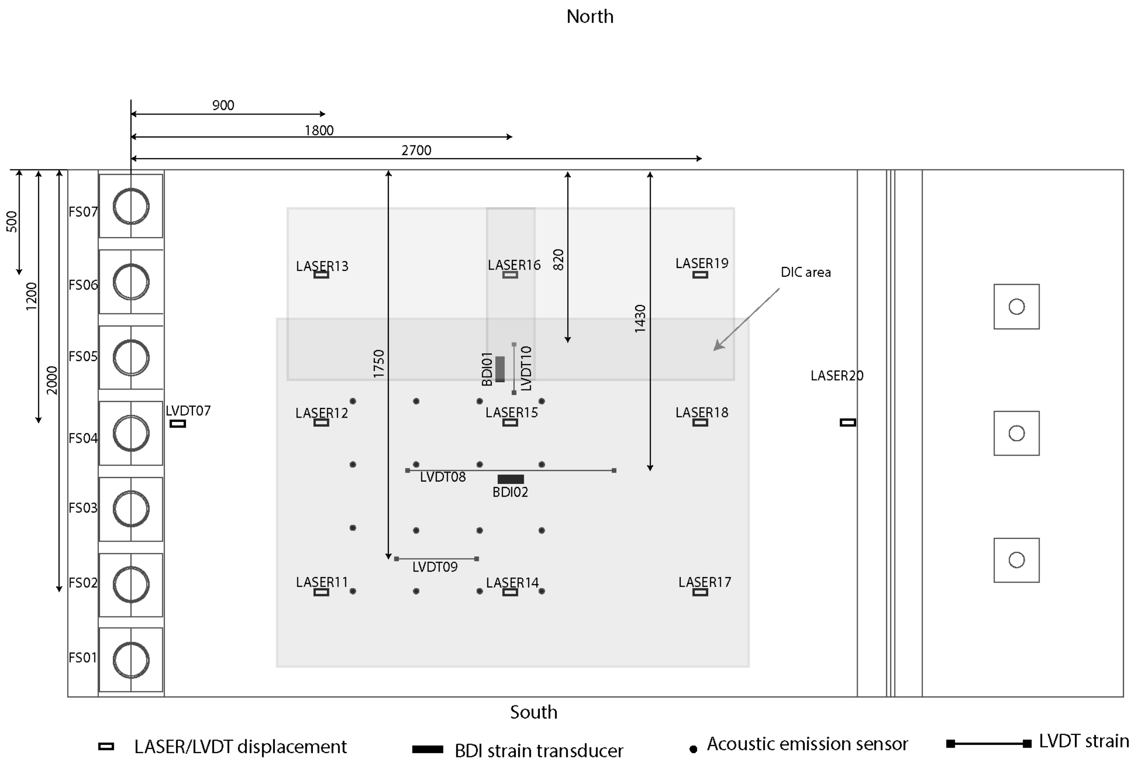

(b) Bottom view

Figure 2.5: Sensor layout flexural test [11]

2.8 Ultimate forces

To design the sensor layout, the moment capacity and the shear capacity can be calculated. Cracking moment, yielding moment and ultimate moment are calculated in Appendix A and the results of this analysis are summarized in Table 2.3. The longitudinal bending results can, in combination with the corresponding curvatures, be plotted as a moment-curvature diagram, which is shown in Figure 2.6.

Table 2.3: Design calculations

Variable		Value
Cracking moment	M_{cr} [kNm/m]	68
Curvature at cracking moment	κ_{cr} [1/mm]	$0.8 * 10^{-6}$
Yielding moment	M_y [kNm/m]	318
Curvature at yielding moment	κ_y [1/mm]	$13.5 * 10^{-6}$
Ultimate moment	M_u[kNm/m]	360
Curvature at ultimate moment	κ_{ult} [1/mm]	$61.2 * 10^{-6}$

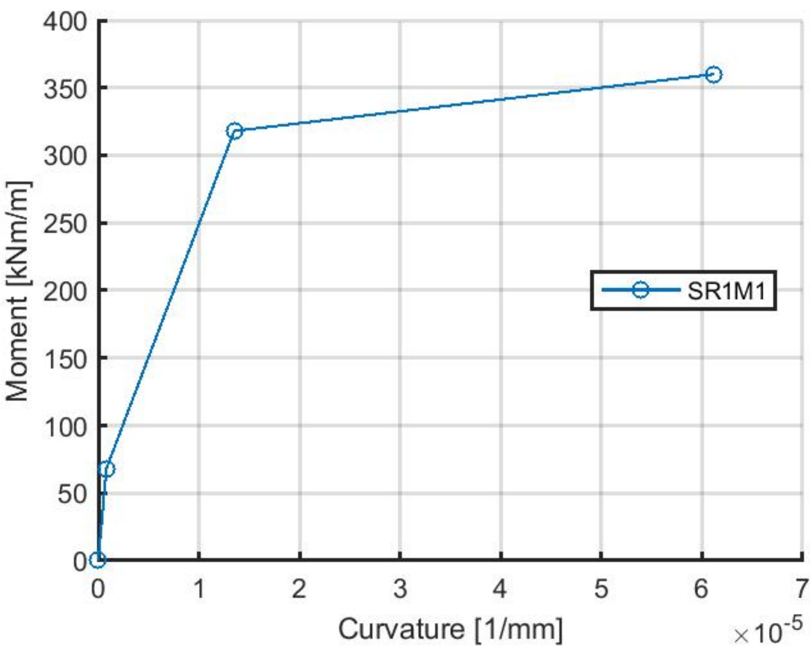

Figure 2.6: Moment-curvature diagram concrete slab [11]

To determine the maximum shear capacity, the effective width needs to be determined. If the French method is used, the effective width is dependent on the distance between the load and the support, the dimensions of the loading plate and the dimensions of the support. The effective width can be determined with Equation (2.1) [11].

$$b_{eff} = min\left(2 * \left[a - \frac{b_{sup}}{2} + \frac{l_{load}}{2}\right] + b_{load}, b\right) \tag{2.1}$$

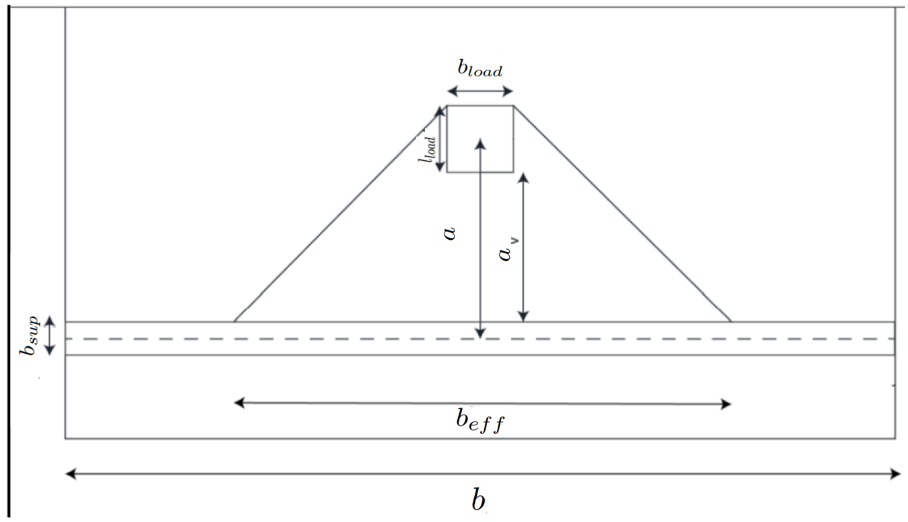

Figure 2.7: Effective width with the French method [11]

Based on the load spreading and the loading positions, the effective width (b_{eff}) can be determined. the maximum shear load can be determined by Eurocode expressions shown in Appendix A. The results of this calculation can be found in Table 2.4. For each experiment, the distance (a) between load and support, effective width and the maximum shear force($V_{max,EC}$) are presented.

Table 2.4: Effective width according to French method [11]

	SR1E1 [mm]	SR1E2 [mm]	SR1E3 [mm]	SR1E4 [mm]
a [mm]	1200	800	1200	800
b_{eff} [mm]	1785	1385	1785	1385
$V_{max,EC}$ [kN]	465	361	465	361

3 Review of proof load testing for concrete slab bridges

In this chapter, an elaboration is given on the proof load testing of reinforced concrete slab bridges. First, some calculation methods for reinforced concrete slab bridges are discussed. These calculation methods focus on the link between theories and measurements. Then, the stop criteria from literature are elaborated on. These stop criteria can be subdivided into flexural and shear stop criteria.

3.1 Concrete slab bridges

A concrete solid slab bridge, is defined as a short span bridge (7 - 14 m), consisting out a reinforced concrete slab, which has equal height over the width, and has the reinforcement evenly distributed over the width. A typical slab bridge in the Netherlands has a thickness of 600 mm, a width of 10.25 m and often contains multiple spans [11]. An example of a slab bridge is presented in Figure 3.1.

Figure 3.1: Typical slab bridge [12]

3.1.1 Modeling of a concrete slab bridge and its loads

Modeling of structural behavior is one of the core activities in engineering. Modeling is based on making assumptions, by which proper approximations can be calculated. Assessing a concrete bridge implies the use of at least one model: the loading model. This model describes which traffic loads a bridge must withstand without failure. For the Netherlands, this is described in the Eurocode NEN:EN 1991-2-2003 [13]. Typical loads on a slab bridge are permanent loads, live loads, and environmental loads. Considering all live load models, the Eurocode load model 1, is typically the most severe loading to a concrete slab bridges [11]. When all the properties of the concrete slab are known the force distribution can be calculated. This can then be compared with the resistance models.

Load model 1

Load model 1 divides the width of the bridge in notional lanes, with a width of 3 m. Load model 1 combines distributed lane loads with tandem loads. These are shown in Figure 3.2.

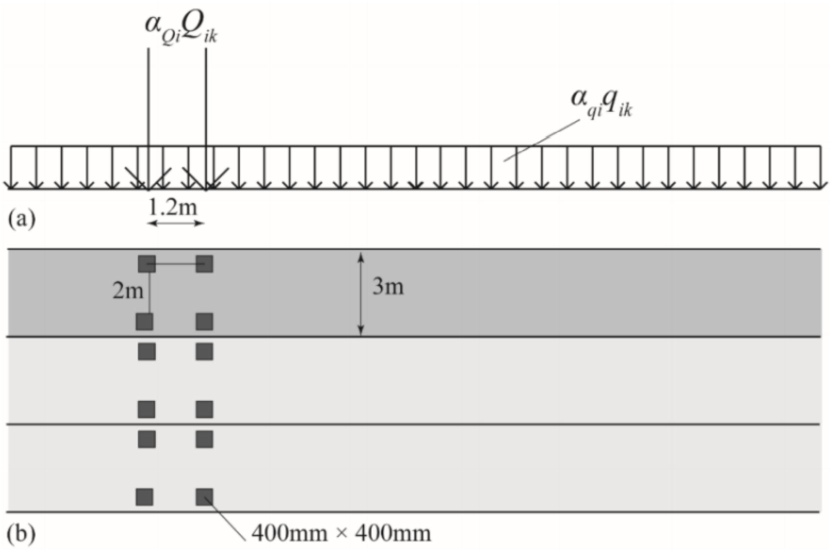

Figure 3.2: Load model 1 [13]

The tandem loads vary for each individual lane. In the first lane, the axle load is αQ1 x 300 kN, in the second lane, the axle load is α_{Q1} x 200 kN and in the third lane the axle load is α_{Q1} x 100 kN. The wheel print is 400x400mm, with a distance between the wheels of 1.2 m. The transverse spacing of the wheels is 2 m. A uniformly distributed load of α_{q1} x 9kN/m^2 is present in the first lane. The remaining lanes are loaded by 2.5kN/m^2. The critical loading position of the tandem systems vary between the failure modes in flexure and in shear. This is indicated in Figure 3.3 [11] [14].

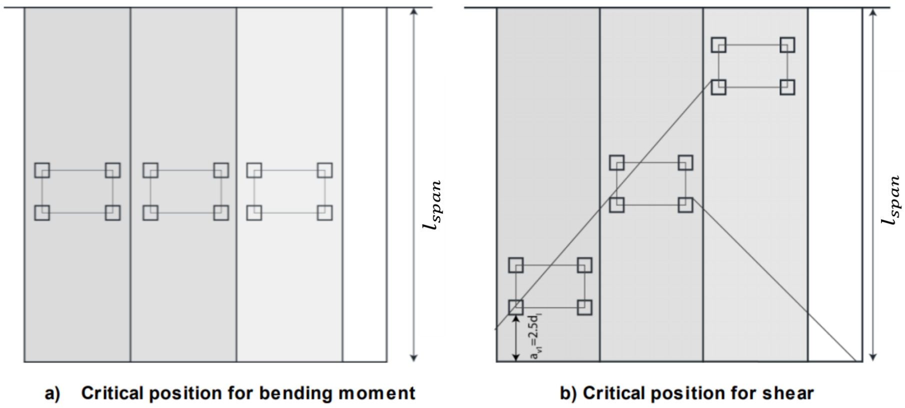

Figure 3.3: Critical position load model 1 [11]

One-dimensional models

A slab bridge can be designed with a beam model. A critical strip, with the maximum load on it, can be designed to withstand these forces. When a slab is modeled as a critical strip, the section forces can be determined by basic mechanics. The reinforcement layout is determined based on these sectional forces. The required reinforcing steel is applied over the full width of the slab. To calculate the sectional forces, line models are used, with Euler-Bernoulli elements.

Two-dimensional models

Two dimensional models take distribution of forces in the width direction into account. When the second dimension is used, plate theories are often used. Several plate theories are available in literature, but two of them are mostly implemented in engineering: the Mindlin-Reissner theory for thick plates, and the thin plate theory of Kirchhoff. A two-dimensional model can give insight in critical locations in the slab. It provides force trajectories and more realistic deflections.

3.1.2 Flexural cracking of a concrete slab bridge

To gain better understanding on the development of cracking stop criteria and how sensors should be placed to monitor crack widths well, cracking of a concrete slab bridge is studied. Most analytical models are one dimensional. Hence, cracking of beams and beam models are shown first. Later in this section cracking of concrete plates is discussed.

Cracking of a concrete beam

When a concrete beam is loaded in pure bending, this causes a linear and symmetric stress distribution in the cross section. The tensile stress at the bottom, is approximately equal to the compressive stress at the top. The loading on the beam can be increased until the tensile strength of the concrete is reached. This causes cracking of the concrete on the bottom side of the beam. This is called cracking moment (M_{cr}) or moment of rupture (M_r). The tensile stresses in the concrete at the location of the crack are released. The major part of the tensile forces is taken by the reinforcement located at the bottom side of the concrete [15]. As the load increases further, more cracking occurs over the length of the beam, as more sections reach the maximum tensile strength of concrete. This is called the crack development stage. When the load on the beam is increased even further, the force in the reinforcement starts to increase without formation of new cracks, this is called stabilized cracking stage. This leads to higher stresses and strains in the steel which leads to an increase of the crack width and crack height. When the steel reaches yielding strain, the force in the steel remains constant, while the crack height and width is still increasing. This can increase until a minimum height of the concrete compressive zone is reached and the concrete crushes. During this process, the deformation increases, while the force in the reinforcing steel in the critical section remains constant [15]. The described path can be depicted by a moment-curvature diagram and can be seen in Figure 3.4. This can be considered a ductile failure. The structure will show high strains and deformations, before failure.

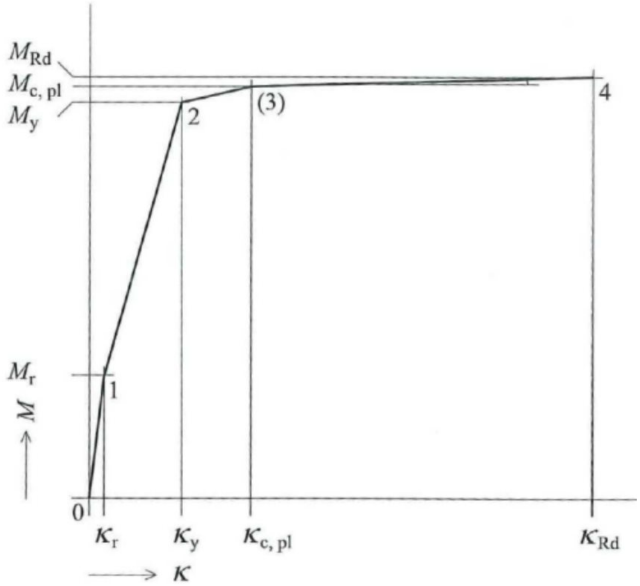

Figure 3.4: M-kappa diagram [16]

Tensile tie model
A method to gain a better understanding of cracking of a concrete beam, is by the use of the tension tie model shown in Figure 3.5. This assumes a zone on the bottom side of the beam, which is axially loaded. The distance between the cracks is in that case fully dependent on the anchorage length and the bond force of the steel rebar. This makes the calculation of the distance between the cracks and the crack width more clear.

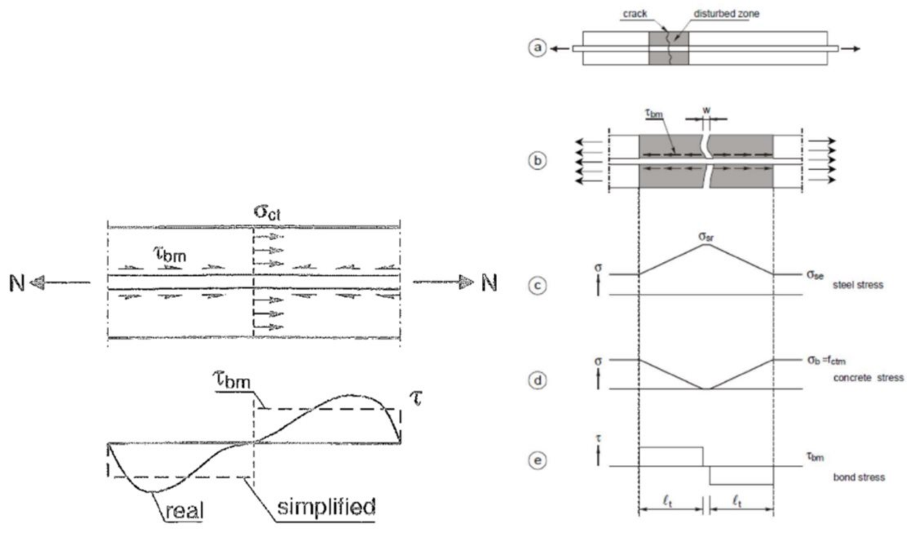

Figure 3.5: Bond model for anchorage of reinforcement in concrete of a tensile tie model [15]

The tension tie model assumes a constant bond stress(τ_{bm}) along the anchorage length of the reinforcement bar. Based on this assumption, the (maximum) crack width can be calculated with can be calculated with Equation (3.1). Within this formulation, a strong relationship between steel stress and crack width can be observed.

$$w_{max} = \frac{1}{2}\frac{f_{ctm}}{\tau_{bm}}\frac{\Phi}{\rho_{eff}}\frac{1}{E_s}(\sigma_s - \alpha\sigma_{sr}) \quad (3.1)$$

However, as can also be seen from Figure 3.5, the assumption of the constant bond stresses along the rebar is not very accurate. This indicates that the calculation of concrete stresses in between cracks are not very accurate with this method.

Major cracks
Due to the stability condition of the whole system, not all cracks reach the same height [17, 18]. The cracks that reach the maximum crack height (s_{cr}) are called major cracks. The formation of major cracks is shown in Figure 3.6. This is one of the things the tensile tie model does not account for. The flexure-critical location in a beam is always located at one of the major cracks. Hence, the distance between the major cracks is critical in measuring critical locations. The distance between the major cracks can be determined by Equations (3.2) and (3.3). The spacing between the cracks is dependent on the major crack height (s_{cr}) and the inclination of the stress line (k_c). The major crack height can be determined based on the ratio between elasticity modulus (n_e), the reinforcement ratio (ρ_l) and the effective depth (d) [19].

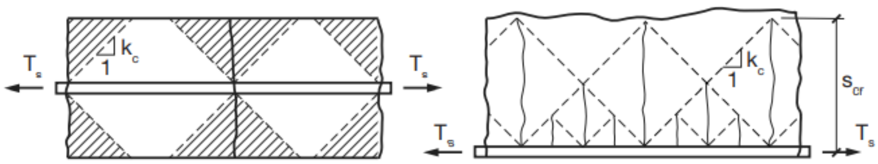

Figure 3.6: Equilibrium condition for a cracked structure [19]

$$s_{cr} = (1 - 1.05(\rho_l n_e)^{0.45})d \quad (3.2)$$

$$l_{cr,m} = \frac{s_{cr}}{k_c}. \quad (3.3)$$

Cracking formula for slab bridges
Concrete slab bridges usually have a high cover in comparison to other horizontal load bearing concrete structures like indoor floors because of the harsh environmental conditions the bridge is in. The cover has influence on the cracking behavior of a beam or slab. The above standing formulations are developed for concrete specimens with relatively low cover. The calculation method developed by Frosch [20] is based on specimen with a higher cover. Equations (3.4) and (3.5) are the Frosch formulations by Lantsoght [21] in which β_{fr} is the strain gradient. This strain gradient may also be approximated with Equation (3.6)

$$w_c = 2\frac{f_s}{E_s}\beta_{fr}\sqrt{d_c^2 + (\frac{s}{2})^2} \quad (3.4)$$

$$\beta_{fr} = \frac{h - c}{d - c} \quad (3.5)$$

$$\beta_{fr} = 1 + 3.15 * 10^{-3} d_c \quad (3.6)$$

3.1.3 Shear in concrete slabs under concentrated loading

Shear failure is one of the critical failure modes for concrete specimens. Calculation of shear strength of structures without shear reinforcement does not rely on a theoretical derivation of the shear problem. At this moment, there is not yet consensus between researchers when it comes to a theoretical derivation of the shear problem in reinforced concrete structures without reinforcement for shear. Consequently, the design and assessment of these structures is based on empirical formulas [19]. Shear failure is a relatively brittle failure mode. The structural responses of concrete slabs without shear reinforcement which fail in shear are less ductile and therefore less noticeable [22]. From theory, the following mechanisms are identified to transfer shear force [23]:

- Shear stress in the uncracked concrete compression zone (V_c).
- Aggregate interlock caused by displacement in the tangential direction of the crack face (V_{ai}).
- Residual tensile stresses at locations where the crack width is limited.
- Dowel action of the longitudinal bars (V_d).
- Arch action caused by direct load transfer between the load and the support.

Three of these mechanisms can be explained by drawing a free body diagram alongside a flexural crack. This can be seen in Figure 3.7.

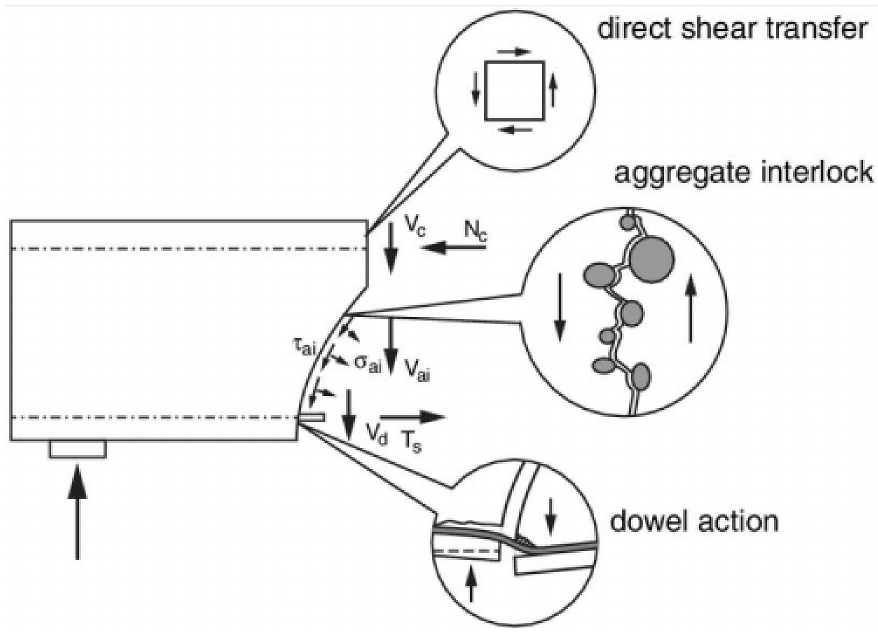

Figure 3.7: Free body diagram of a flexural shear crack [23]

Critical shear crack theory for beams

One of the methods to determine shear capacity is the Critical Shear Crack Theory (CSCT) developed by Muttoni [24] [25]. This theory uses a failure criterion, which allows for less shear force to be transferred, when the crack width of the critical shear crack increases. This can be observed in the CSCT expression in Equation (3.7).

$$\frac{V_r}{bd\sqrt{f_c}} = \frac{1}{6}\frac{2}{1+120\frac{\varepsilon d}{16+d_g}} \tag{3.7}$$

For application of this theory, it is assumed that the width of the critical shear crack can be represented by the strain at 0.6d from the top compression fiber. The strain at this point (ε_{csct}) can be analytically derived with Equation (3.8).

$$\varepsilon_{csct} = \frac{M}{bd\rho E_s(d-c/3)}\frac{0.6d-c}{d-c} \tag{3.8}$$

Transition between one-way and two-way shear

To apply shear theories to a concrete slab bridge, it should be determined if one-way or two-way shear theories are applicable to the specific slab and loading position. And if one-way shear is applicable, it should be determined over which width the load spreads. When the stress trajectories around a concentrated load are studied, it can be observed that both one way and two way stress distributions are present (see Figure 3.8).

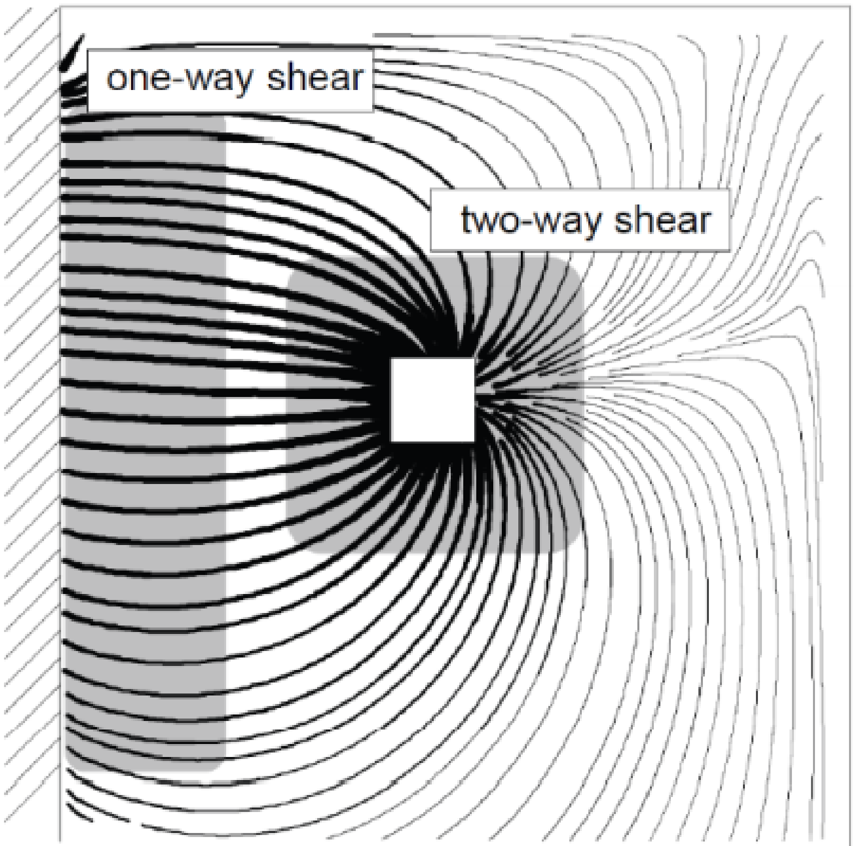

Figure 3.8: One-way and two-way shear stress trajectories [26]

Since both stress distributions are present, the slab bridge can also fail because of multiple failure mechanisms. Three main failure mechanisms for slabs with concentrated loads near supports are shown in Figure 3.9 [27]. Categories in which research on shear can be categorized are one-dimensional and two-dimensional theories. Where one-dimensional theories focus on shear failure in beams and two-dimensional theories mainly focus on punching shear failure in plates. Previous research at the TU Delft has shown that a third failure mechanism is of most importance for concrete slab bridges under concentrated loading. This failure mode is a combination of one-dimensional and two-dimensional shear [27].

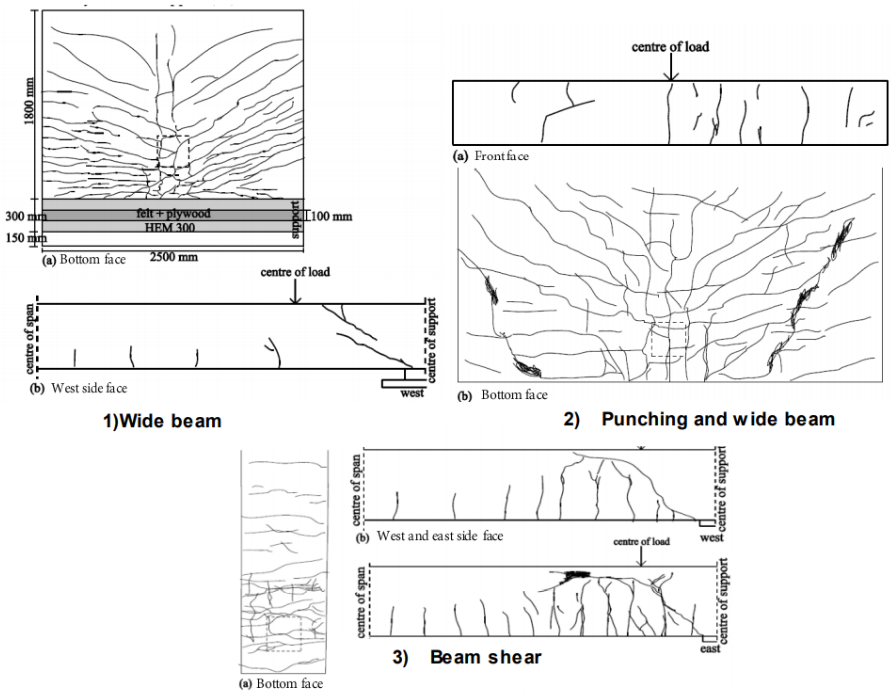

Figure 3.9: Forms of shear failure for concrete slabs [27]

Previous research at Delft University of Technology has shown that the bearing capacity of concrete slabs is greater than currently accounted for. The current capacity calculation method uses the RBK [28] formulation for shear. These formulations are shown in Equations (3.9) to (3.11). This method is combined with the effective width concept to find the maximum capacity.

$$\nu_{R,c} = 0.15 k_{slab} k (100 \rho_l f_{cm})^{\frac{1}{3}} \geq \nu_{min} \tag{3.9}$$

$$k = 1 + \sqrt{\frac{200mm}{d_l}} \leq 2.0 \tag{3.10}$$

$$\nu_{min} = 1.13 k_{slab} k^{3/2} \sqrt{\frac{f_{cm}}{f_{ym}}} \tag{3.11}$$

Critical shear crack theory for punching
As discussed above, The CSCT was first derived for beams [24]. Later, it was optimized for punching failure [29]. The adjusted formulation for punching failure is shown in Equation (3.12). The theory is still based on the critical shear crack. However, the rotation of the crack is measured instead of the strain at $0.6d$. For measuring this rotation (ψ), a conical type of deformation, with all rotation concentrated in the critical shear crack is assumed.

$$\frac{V_R}{b_0 d\,(f_c)^{1/2}} = \frac{3/4}{1 + 15\,[\psi d/(d_{g,0} + d_g)]} \tag{3.12}$$

This extension is derived based on axis symmetric conditions. It assumes a critical perimeter $0.5d$ from the load, with rounded corners, as displayed in Figure 3.10.

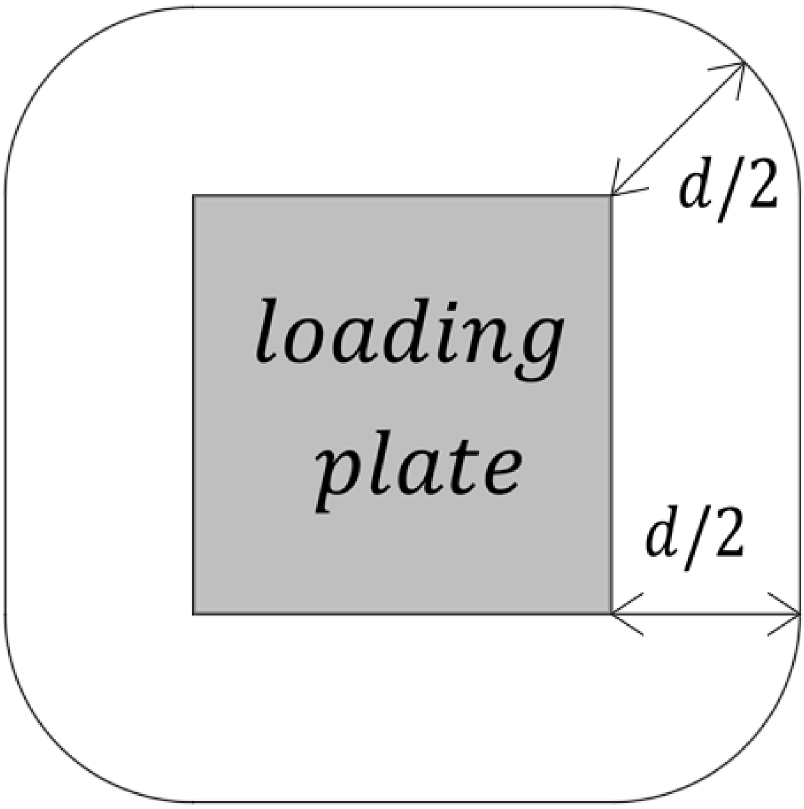

Figure 3.10: Critical perimeter with rounded corners [30]

Sagasta [30] extended the CSCT for punching for non-axis-symmetrical conditions. To account for these non-axis-symmetry conditions and slab behavior, the control perimeter is subdivided into the x and y direction (see Figure 3.11), which can be examined separately. The summation of these components is then the maximum punching resistance.

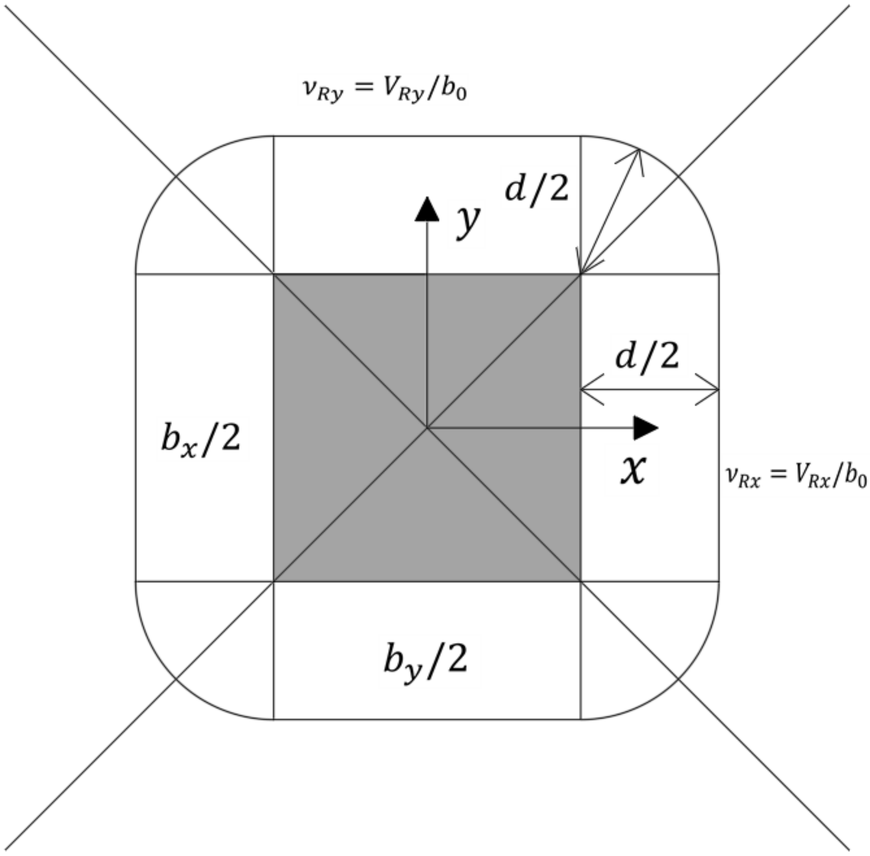

Figure 3.11: Subdivision of the critical perimeter into x and y direction [30]

It has to be noted that the above approach not necessarily is applicable to concrete slab bridges. The experimental program of Sagasta did not include a combination of a one way span, with a non-axis symmetrical reinforcement. This is generally present in a concrete slab bridge. Sagasta's results show that for a slab spanning in one direction, with equal reinforcement in both directions, the slab rotation in span direction is way higher compared to the slab rotation in the transversal direction. From this it can be concluded that the span direction reaches the maximum capacity first. However, this does not account for the difference in reinforcement ratio in both directions. For plates with different reinforcement ratios in x and y direction, Sagasta found 2 different results. At high reinforcement ratios (ρ_x = 1.46%, ρ_y = 0.75% & ρ_x=1.64%, ρ_y = 0.84%) he found that the force rotation graph showed similar results in both directions. At lower reinforcement ratios(ρ_x = 0.76%, ρ_y = 0.32% & ρ_x=0.85%, ρ_y = 0.36%) he found that the y direction provided significantly higher rotations compared to the x direction. However, these tests were performed on a slab spanning in x and y direction [30].

The CSCT($\psi_x - \psi_y$) method is developed to evaluate the x and y direction separately. By doing this, first the critical direction reaches the general (Equation (3.12)) CSCT limit. Then, a softening occurs along the failure slope of the CSCT limit (point O to B), while the other orientation can still carry more load (point O* to B*). The increasing amount of load, the non-critical orientation carries, is bigger than the softening curve of the critical orientation. This causes the critical orientation to exceed the CSCT limit. This process is shown in Figure 3.12, in which point O is the predicted strength from CSCT, point B shows the V_r component after shear redistribution and point C is the predicted strength and maximum rotation according to the CSCT$(\psi_x - \psi_y)$, which is obtained after the x direction reaches the failure criterion.

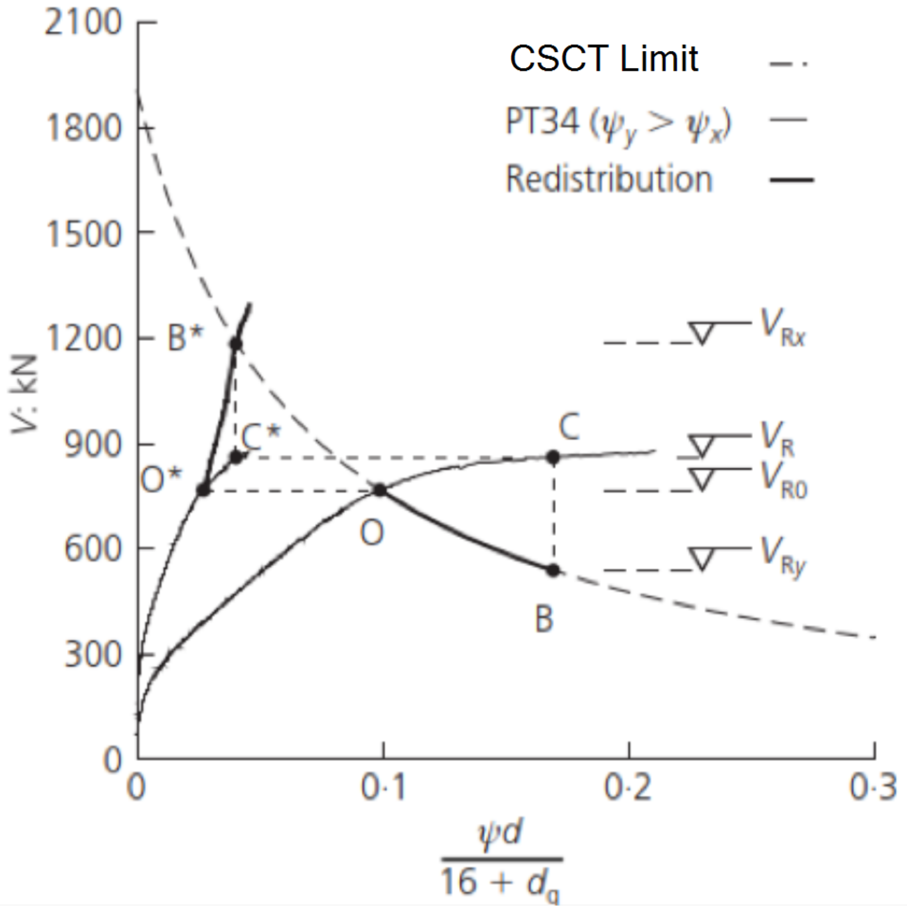

Figure 3.12: Redistribution of the shear force from the critical direction to the non-critical direction [30]

3.2 Stop criteria

When a structure is evaluated by proof load testing, the aim is to directly demonstrate that a given bridge can carry the required loads [31]. This is done by gradually increasing the load on the structure and to measure the responses of the bridge. To prevent structures from failing or getting uneconomically damaged, a number of stop criteria have been developed. When one of these values are reached, the proof load test should be stopped immediately. The other situation of stopping the proof load test is when the target load is reached. If the target load is reached it means that the assessed bridge complies with the regulations and is safe to use [32]. The determination of a appropriate target load is still under debate.

Stop criteria are based on strains in the steel, strains in the concrete, deflections, concrete crack width and stiffness of the structure. Stop criteria can be subdivided into stop criteria to prevent flexural failure and stop criteria to prevent shear failure. A selection of proposed stop criteria is presented in this section. For each type of stop criteria the proposals for a certain value or formula are discussed briefly. The required parameters are discussed, and the preferred method of calculation is given.

3.2.1 National guidelines

Several national guidelines provide guidance on load testing. There is one major division to be made in these provisions based on the purpose and the level of loading. A diagnostic load test, as typically performed before opening of a bridge in countries as Italy, France and Switzerland makes use of a relatively small load to the structure. The structural responses are later analyzed to update the calculation models on the bridge. A proof load test uses high load levels above the SLS level of the bridge and has as goal to prove sufficient capacity. National guidelines for proof load testing are available in North America by ACI [33] and the Manual for Bridge Rating through Load Testing [34], France, Great Britain, Ireland and Germany. Only the latter one is providing quantitative stop criteria past which irreversible damage is caused in the structure. This is not acceptable for non-destructive load testing [12, 32, 1].

3.2.2 Flexural failure

Flexural failure occurs when yielding of the reinforcing steel leads to ductile failure behavior. Hence, the structural responses observed before flexural failure are clearly noticeable. The various proposed stop criteria for flexural failure are described below.

Concrete strain

Concrete strain should be assessed over the whole structure. Locations of high strain can be estimated on beforehand by engineering judgement. Previous research indicated that it is interesting to measure over the full length of the slab with optical fibers [3]. The basic formula for limiting concrete strain is given by the German guideline [35]:

$$\varepsilon_c < \varepsilon_{c,lim} - \varepsilon_{c0} \tag{3.13}$$

Within the German guideline the limit is set to 800 $\mu\varepsilon$ for flexural as well as shear failure.

A second approach was proposed by Lantsoght. A theoretical determination of the strain limit ($\varepsilon_{c,lim}$) [21]. This approach is based on equilibrium between internal forces. The compressive zone (c) is determined by Thorenfelds parabola (see Equations (3.15) to (3.21)). To include a sufficient margin of safety the strain in the steel is limited to 65% of the main yield stress. The calculation of the stop criterion is given in Equation (3.14).

$$\varepsilon_{c,lim} = \frac{h-c}{d-c}\frac{0.65 f_{ym}}{E_s} \tag{3.14}$$

The compressive parabola is shown in Figure 3.13.

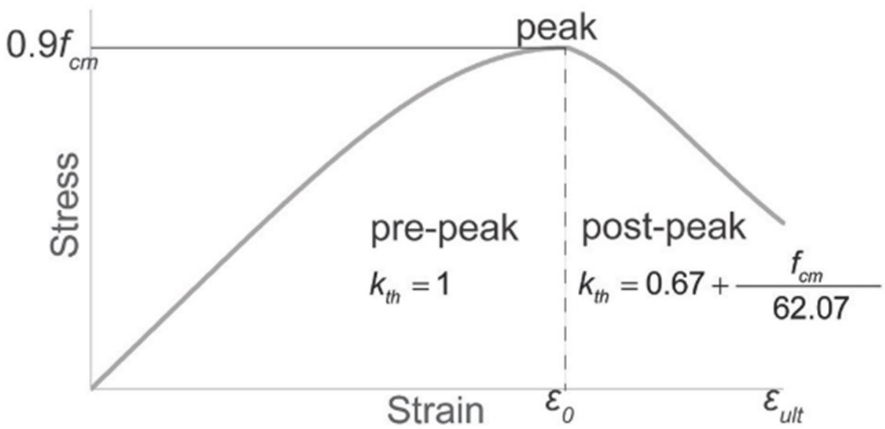

Figure 3.13: Stress-strain parabola of concrete with f_{ctm} in MPa [21]

The relation between steel strain and concrete strain is:

$$\varepsilon_{c,comp} = \frac{c}{d-c} * \varepsilon_s \tag{3.15}$$

The following material parameters of concrete need to be determined for defining the parabola:

$$n_{th} = 0.8 + \frac{f_{cm}}{17.24} \tag{3.16}$$

$$\varepsilon_0 = \frac{f_{cm}}{E_c} * (\frac{n_{th}}{n_{th}-1}) \tag{3.17}$$

The pre- and post-peak behavior can be described with factor k_{th}. The relations between the stresses and strains can then be described with:

$$\begin{cases} 1 \text{ if } \frac{\varepsilon_{c,comp}}{\varepsilon_0} \leq 1 \\ 0.67 + \frac{f_{ctm}}{62.07} \text{ if } \frac{\varepsilon_{c,comp}}{\varepsilon_0} > 1 \end{cases} \tag{3.18}$$

The specific shape at certain steel stresses can then be calculated by horizontal equilibrium between the compressive force (C) and the tensile force (T):

$$C = \beta_{th} * f_{c,th} * b * c \tag{3.19}$$

$$T = A_s * f_{ym} \tag{3.20}$$

In which factor β_{th} is introduced to go from a maximum stress to an average stress. This factor can be calculated with:

$$\beta_{th} = \frac{ln(1 + (\frac{\varepsilon_{c,comp}}{\varepsilon_0})^2)}{\frac{\varepsilon_{c,comp}}{\varepsilon_0}} \tag{3.21}$$

For sections at failure, the Eurocode expression for the ultimate compressive zone height (x_u) can be used, which can be described by Equation (3.22).

$$x_u = \frac{f_{yd} * A_s}{\alpha * b * f_{cd}} \tag{3.22}$$

Reinforcing steel strains

For using this stop criterion, the strain of the reinforcement should be measured on the critical locations. The German guideline provides a maximum measured strain which can be seen in Equation (3.23). The calculated maximum reinforcement strain is reduced by the strain in the steel cause by permanent loads (ε_{s0}).

$$\varepsilon_s < 1.0\frac{f_{ym}}{E_s} - \varepsilon_{s0} \tag{3.23}$$

The principle of this stop criterion is to stop loading at the onset of yielding of the reinforcement. The method however is hard to monitor since the sensors should measure the actual reinforcement strain.

Crack width
Cracking of concrete is probably one of the most visual responses to proof load testing. It is therefore that a lot of stop criteria are proposed based on the behavior of cracks in concrete. The German guideline [35] provides values for maximum crack width during proof load testing, and maximum residual crack width, when the load is removed. This maximum residual crack width is a percentage of the maximum occurring crack width during loading. The values are shown in Table 3.1.

Table 3.1: Stop criteria for crack width [35]

	During proof loading	After proof loading
New cracks	$w \leq 0.5mm$	$\leq 0.3w$
Existing cracks	$\Delta w \leq 0.3mm$	$\leq 0.2\Delta w$

Other limits on maximum crack width are based on a theoretical derivation [21], they depend on the following variables to be known:

- Mean yielding point of the reinforcement.
- Amount of reinforcement in the cross section.
- Dimensions of the concrete.
- Properties of the concrete.

The theoretical derivations hold up till yielding of the reinforcing steel, and depend heavily on the assumed maximum stress in the reinforcement. Limiting the strain in the reinforcement, ensures a certain margin of safety. The limit value for the strain in the reinforcing steel should be reduced by the strains in the reinforcement, induced by the permanent loads. The stop criterion is shown in Equation (3.24). Lantsoght et al. use the model developed by Frosch [20]. The allowable strain in the reinforcement is set to 65%

$$w_{stop} = 2\frac{0.65 f_{ym} - f_{perm}}{E_s}\beta_{fr}\sqrt{d_c^2 + (\frac{s}{2})^2} \tag{3.24}$$

.

Vos proposed to calculate the maximum allowable crack width based on van Leeuwen's [36] approach to cracking of concrete structures [22]. Vos limits the allowable strain in the reinforcement to 90%.

Vos also proposed a residual crack width criterion based on van Leeuwen's approach. The stress in the steel is in that case limited to the stress that could be caused by the permanent load, neglecting aggregate interlock [22].

Stiffness
The stiffness of a structure is deflection divided by the amount of load on the structure. One of the challenges is that this stiffness is dependent on previous loads on the structure, and also heavily depends on time and loading speed. The deflection can, with the use of some integrations, be related to the curvature of a beam. This is the basis of a stop criteria proposed by Vos. Vos uses the moment-curvature diagram by Monnier [37] to estimate the stiffness in certain branches of the loading of a structure. The stiffness of the unloading branch at the onset of yielding is used to estimate the upper limit of deflection. Vos uses a maximum of 90% of the calculated deflection as stop criterion [22].

Another method to use the deflection as a stiffness indicator is described in [5]. Lantsoght proposes a criterion based on decrease in stiffness between the loading and unloading branch of 25%.

Deformation profiles
Lantsoght et al. proposes to use the deformation profiles as a stop criteria. For every load step the deformation profiles can be plotted. The load step in which discrepancies start to occur, in comparison to previous load steps, the onset of plasticity is recognized and the proof load test is stopped [5].

Evaluation of the stop criteria
Zarate compared the proposed stop criteria described above, as load at reaching stop criterion divided by bearing capacity [10]. An overview of these results is shown in Table 3.2. A total of 8 beams were used to compare the stop criteria for flexural failure. Four of these beams were casted and tested in the laboratory. The other four beams were sawn from a slab bridge in the Netherlands which needed to be replaced. The set up and results of the beam tests can be found in [5]. The results lead to the conclusion that cracks with a width below 0.05 mm should be neglected.

Table 3.2: Results of comparison flexural stop criteria [10]

	ε_{DAfstB}	ε_{stop}	$\omega_{max,DAfstB}$	$\omega_{max,\nu_{os}}$	ω_{stop}	$\omega_{res,DAfstB}$	$\omega_{res,\nu_{os}}$	$\Delta_{\nu_{os}}$	Stiffness reduction	DPH	DPV
P502A1	64%	71%	96%	70%	70%	-	-	96%	-	-	-
P502A2*	62%	81%	100%	56%	52%	-	-	99%	100%	84%	84%
P502B	63%	67%	93%	51%	50%	67%	42%	78%	67%	-	-
P804A1	44%	52%	87%	58%	56%	68%	36%	68%	58%	58%	77%
RSB01F	54%	53%	99%	72%	53%	54%	45%	91%	28%-99%	54%	54%
RSB02A	53%	62%	-	69%	64%	-	15%	69%	-	42%	42%
RSB02B	53%	71%	100%	62%	53%	61%	47%	70%	47%-100%	61%	61%
RSB03F	54%	62%	100%	80%	64%	100%	49%	80%	100%	58%	58%

*previously cracked in bending

From the strain stop criteria results, it can be concluded that the German guideline provided a safety margin of 36% till 56% when compared to the bearing capacity of the beam. The method proposed by Lantsoght et al. [21], provided a safety margin of 19% till 48%. Hence, it can be concluded that the German approach is probably more conservative. Additionally, the German approach does not account for sectional properties. Therefore, the method proposed by Lantsoght et al. is the preferred approach, when the parameters are known [10]. When the parameters are not known, the German guideline provides a limit, but this limit should be investigated for more different cases.

The results on the crack width indicate that the method from the German guideline is unsafe since more than half of the tests failed before reaching the stop criterion. The methods proposed by Lantsoght and Vos perform better, in which Lantsoght's proposal shows slightly less scatter [10].

The residual crack width proposal of Vos was too conservative because the limit was reached in the first load cycle in several cases, and the lowest margin between reaching stop criterion and capacity is over 50% and yields up to 85%. Therefore, this criterion seems uneconomical. The proposal from the German guideline as presented in Table 3.1 were never reached in 2 of the 6 considered cases and is therefore considered unsafe. The remaining four tests show safety margins of approximately 38% [10].

Several proposed stop criteria for flexural failure based on crack width are considered unsafe because the capacity is reached prior to reaching the stop criterion. The two most promising proposals came from Vos and Lantsoght and are based on maximum crack width. This however has a drawback since several variables on the structure need to be known and all cracks need to be monitored.

For the stiffness criterion indicated by δ_{vos} , Zarate's comparison shows that Vos's criterion gives consistent results with a small, and sometimes almost too small, margin of safety. This could be a good stop criterion if the amount of safety is increased. However, the integration to solve the differential equation for different boundary conditions is complex. This makes using this stop criterion unpractical to use in more complicated systems [10]. The criterion formulated by Lantsoght is exceeded for more then 50% of the cases. Therefore, this criterion seems not feasible.

The deformation profiles seem a promising stop criterion, however, it is not quantified. This makes it a stop criterion which requires a lot of understanding of the tested structure.

As can be noticed from Table 3.2, the stop criterion for maximum steel strain is not included in the table. This is due to the complicated applicability in the field. When other stop criteria are available, bridge owners try to avoid removing the cover and damaging the structure as this is costly and can lead to durability issues [21].

3.2.3 Shear failure

Shear failure is a brittle failure mode compared to flexural failure. The structure loses capacity with only slight warnings. It is common to locate possible shear cracks locations, and to access these locations with stop criteria for flexural failure, flexural shear failure, and shear failure. In this paragraph the specific stop criteria for shear failure are discussed. These are often stricter than the limits for flexural failure. This is mainly because a higher margin of safety is required for brittle failure mechanisms.

Concrete strain

The concrete strain can be measured in shear-critical zones. The stop criterion for the strain can be found by either using the German guideline which is based on a fixed value, or a method proposed by Benitez which is based on a theoretical derivation of the maximum strain [38]. This approach uses the critical shear displacement method proposed by Yang [19], to find the critical shear force. The force is then placed at the critical shear location with a mechanical model. The occurring bending moment due to this force is calculated. This moment is expected before yielding of the reinforcement. With the moment curvature diagram the corresponding curvature is calculated, from which the corresponding strain can be calculated using Thorenfeldt's parabola. The following equations apply:

$$V_{CSDT} = V_c + V_d + V_{ai} \tag{3.25}$$

$$V_c = \frac{2}{3}\frac{z_c}{z}V = \frac{d - s_{cr}}{d + 0.5s_{cr}}V \tag{3.26}$$

$$s_{cr} = \left[1 + \rho_s n_e - \sqrt{2p_s n_e + (\rho_s n_e)^2}\right] d \tag{3.27}$$

$$V_d = 1.64 b_n \phi^3 \sqrt{f_c} \tag{3.28}$$

$$w_{ai} = f_c^{0.56} s_{cr} b \frac{0.003}{w_b - 0.01}\left(-978\Delta^2 + 85\Delta - 0.27\right) \tag{3.29}$$

$$\Delta_{cr} = \frac{25d}{30610\phi} + 0.0022 \leq 0.025mm \tag{3.30}$$

$$w_b = \frac{M}{zA_sE_s} l_{cr,m} \tag{3.31}$$

$$l_{cr,m} = \frac{s_{cr}}{k_c} \tag{3.32}$$

The calculated strain at shear failure is reduced with 35% to prevent brittle failure. Additionally, the strains before measurements started are subtracted from the allowable strain, to find the maximum value of the strain measurement.

Crack width

The German guideline provides maximum crack widths as a static value. Lantsoght proposed a stop criterion based on aggregate interlock. This criterion uses the formula for aggregate interlock, developed by Walraven [39] and simplified by Yang [19], which can be rewritten to a maximum crack width on the bottom side of the structure. The distance between cracks is taken as the distance between the major cracks as in Equation (3.32). The maximum allowable shear stress is taken from the RBK [40]. The calculation of the maximum crack width is shown in Equation (3.33).

$$w_{ai} = \frac{0.03 f_c^{0.56} \frac{s_{cr}}{d}\left(978\Delta_{cr}^2 + 85\Delta_{cr} - 0.27\right) R_{ai}}{v_{RBK}} + 0.01mm \tag{3.33}$$

The resulting maximum crack width is reduced by 25% for beams cracked in bending, and 60% for beams not cracked in bending. The underlying reason for this is because cracks that are already present, increase gradually in crack width, while uncracked beams can fail in a brittle manner.

Table 3.3: Results of comparison shear stop criteria [10]

Beam	ε_{DAfstB}	$\varepsilon_{lim,CSDT}$	$w_{max,DAfstB}$	$w_{ai,CSDT}$	Stiffness reduction	DPH	PHV
P804A2*	47%	50%	69%	65%	-	86%	-
P804B	57%	57%	-	88%	56%	56%	56%
RSB03A	85%	82%	-	81%	57%	-	57%

*previously cracked in bending

Stiffness and deformation profiles
The same stiffness reduction method developed by Lantsoght et al. [5] as described in Section 3.2.2, is applied to shear failure. The deformation profiles are applied as in Section 3.2.2 to shear.

Test results
In Table 3.3 all above stop criteria are compared for three beam experiments. The percentages are obtained by comparing the load at which the stop criterion is reached with the load at which the beam failed in shear. Beam P804A2 and beam P804B were previously cracked in bending before the shear load was applied. Beam RSB03A was uncracked before loading it in shear.

It can be concluded form Zarate's comparison that the stop criterion on crack width from the German guideline is unsafe, since it was not reached in 2 of the 3 cases [10]. Beam P804A2, for which the stop criterion did work, was previously cracked in bending. The stop criterion on aggregate interlock, however, provides quite consistent results.

The results regarding the maximum allowable strain are quite similar for the German method and the CSDT method. More variables should be researched to find out if these stop criteria still hold under other conditions. It should also be mentioned that the amount of safety which is applied to the stop criteria on shear failure for Lantsoghts approach is based on the presented beam results. The current method therefore still needs to be verified.

The data on the stiffness reduction show good results on the two uncracked beams. However, the limit is not reached for the beam which was already cracked in bending. More tests are necessary to determine if this can be a good stop criterion.

The horizontal and vertical deformation profiles provide a good stop criterion in 4 of the 6 cases. More results are necessary to determine the accuracy of this stop criterion. It should be noted that this is a qualitative stop criterion, which requires experience to interpret.

3.3 Conclusion

From this chapter it can be concluded that not all stop criteria are equally consistent, and that not all stop criteria for a specific failure mechanism are reached before failure. For flexural failure, the most consistent results are obtained with ε_{stop} and w_{stop}. For the evaluated structures these stop criteria were always exceeded before failure. Other stop criteria which were not exceeded in some cases but still provided good results on other specimen are the stiffness reduction and the deformation profiles. Therefore, the stop criteria should be used as a set of multiple stop criteria. Whenever one of the stop criteria is reached, the loading should be stopped.

This approach causes a very extensive and complex sensor layout, as multiple parameters need to be monitored at several locations. Additionally, if sensors with a limited length are used, the critical location can be outside of the measured length of the sensor. To reduce the risk of missing the critical location, even more sensors can be applied. As this complexity withholds proof load testing from being used in field applications, a method to reduce the level of complexity is required [32]. One of the possibilities to do this is by measuring continuously over the full length of the slab. In that case local and global behaviour of the slab can be monitored.

As no continuous longitudinal sensing system has been used during proof load tests, the applicability of the current set of stop criteria should be evaluated. The applied safety to the current stop criteria might be reconsidered based on the accuracy of the continuous measurement system. Furthermore, the continuous sensing system will be able to describe local and global behaviour. This can lead to new stop criteria.

A continuous measurement can be especially interesting for shear-critical proof load testing as the critical location is less obvious as for flexure critical proof load testing. The critical shear crack can reach the bottom face at any location between the load and the support.

As the current stop criteria are based on beam experiments, redistribution of forces is not taken into account. Concrete slab bridges have a lot of extra capacity because of redistribution. This is still missing in the literature.

4 Review of optical fiber measurement systems

Various continuous fiber optic measurement techniques are available to apply to proof load testing. This chapter elaborates on the differences between the available techniques, and which limits each of the techniques has. Based on the requirements for proof load testing, the best fiber optic measurement technique is selected.

4.1 Fundametals

In general, an optical fiber consists of a core, a cladding and a coating layer. The core is typically 4 to 600 µm in diameter [41]. The core has the function to transmit the light inside the optical fiber. These fibers are often made from silica glass. The cladding acts as a mirror, to keep the light inside the core. This effect of a mirror is created by having 2 mediums, the core and the cladding, with a difference in refractive index. If the incident ray is in a medium of a higher refractive index, the reflected ray bends toward the boundary. If the light approaches the edge of the core in an angle higher than the critical angle, no transmission of the light occurs, and the cladding acts as if it were a perfect mirror [42]. This is shown in Figure 4.1. The coating functions as a protective layer for the fragile fiber. It can be made from various materials like plastic or metal [43]. The optical fibers can be used to transmit light with loss rates as low as 3.6% over 1 km [42].

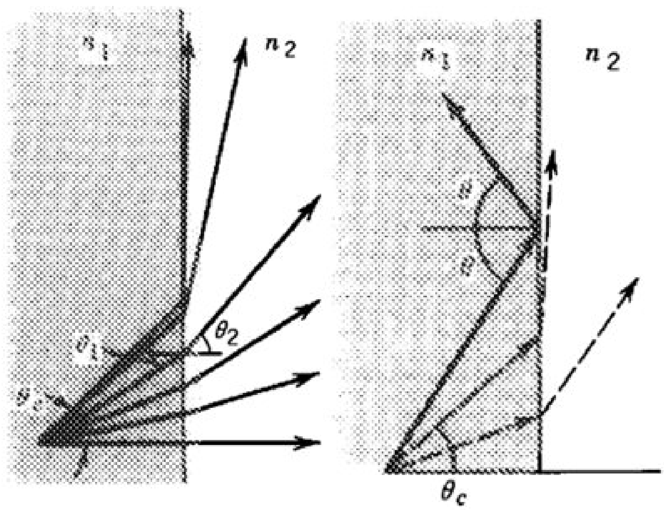

Figure 4.1: Angle of internal reflection on the inside of a optical fiber sensor [42]

4.2 Sensor types

There are two types of optical sensing: extrinsic, where the fiber is just the carrier of light, and the interaction with the environment takes place outside the fiber, and intrinsic, where the light does not leave the fiber, and the 'response' of the fiber due to the environmental influences itself, is measured. A lot of environmental parameters can have impact on the fiber. This makes an optical fiber suitable for measuring parameters like temperature, chemical changes, angles, vibrations etc. see Figure 4.2.

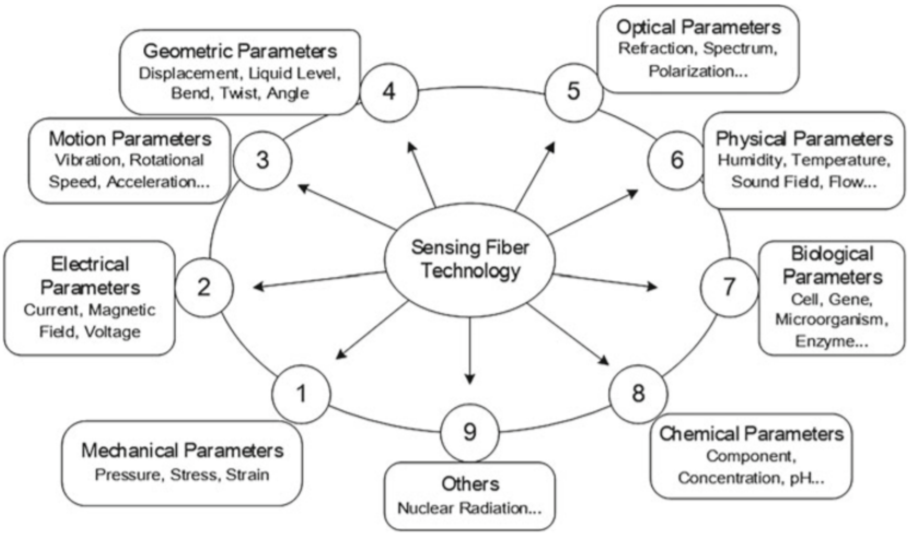

Figure 4.2: Types parameters which can be measured by OF [44]

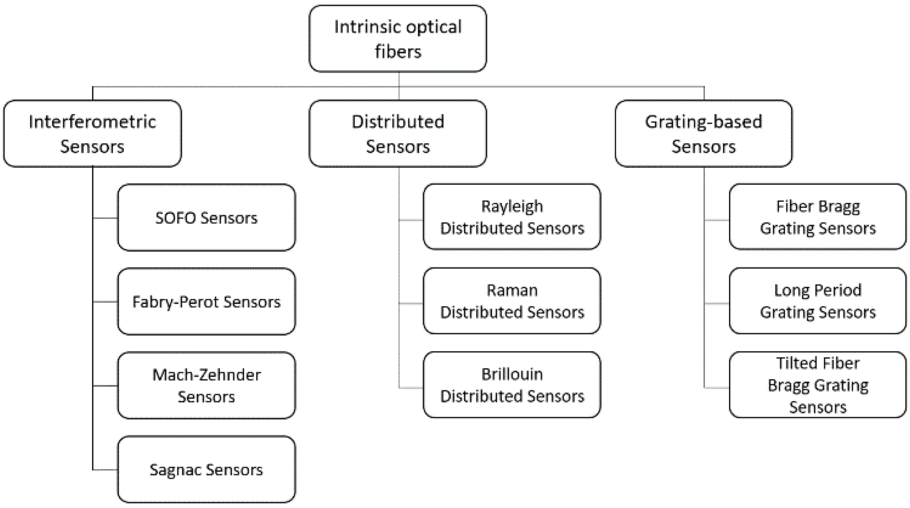

Figure 4.3: Types of optical fibers [44]

A great variety of optical sensors is available on the market. They all vary in which parameter is measured, and what type of acquiring technique is used. An overview of some intrinsic sensing techniques is given in Figure 4.3. Over the past decades, the optical fiber sensing technologies have been developed by the industry. Only the best techniques, or well-adapted solutions fitting with specifications remain economic to produce. Fabry-Perot interferometers is one example which are barely used anymore because the sensors are non-optically multiplexable. Another example is interferometry, which is very difficult to use in real applications and has non-constant sensitivity [44]. The most used technique is FBGs, which is a point sensor that can function as a quasi-distributed sensor. There are also quite popular fully distributed sensing techniques like Rayleigh, Raman and Brillouin. These are based on scattering phenomena in silica fibers [44].

There are several advantages to optical fibers, as compared to traditional measuring techniques including, but not limited to: small diameter, flexibility, wide bandwidth, low attenuation, immunity to electromagnetic interferences, resistance to ionizing radiations, resistance to water and humidity, metrological performances, multi-parameter sensing and wide and remote multiplexing [44]. Additionally, according to López-Higuera et al., optical fibers are the only technology which offers the possibility to perform integrated, quasi-distributed, and distributed measurements on or even within the structure [45].

4.3 Distributed sensing techniques

The distributed sensing techniques take the whole fiber as sensing unit. The sensing point is continuously distributed. The most commonly used distributed optical fiber sensing techniques are depending on the backscattering of light. This backscattering occurs because light waves are electromagnetic waves. When the incident wave interacts with the material of an optical fiber, the waves and medium molecules, create a scattering spectrum. When the light with angular frequency ω_0 is incident into the fiber, its scattering spectrum diagram is shown below.

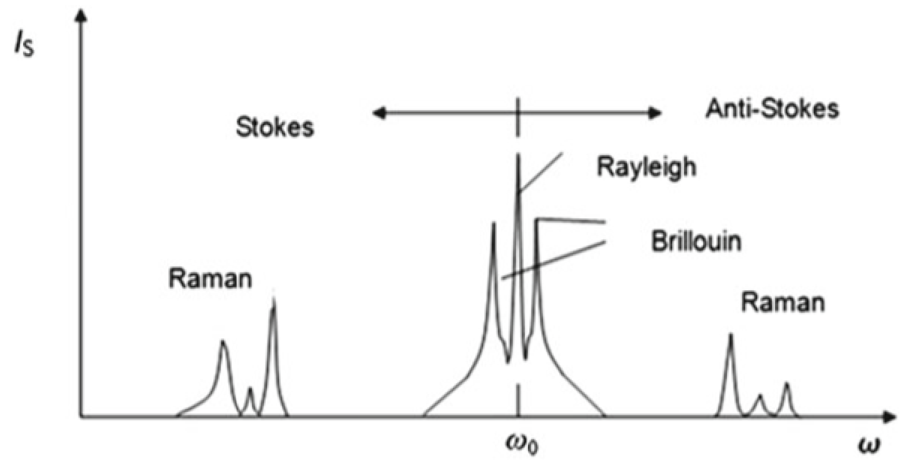

Figure 4.4: Types of backscattering [46]

Three types of backscattering are recognized. The first type is Rayleigh backscattering. This light has equal angular frequency as the incident light. This means that the photon energy is conserved. The Brillouin and Raman backscattering are caused by an inelastic scattering process. In terms of energy, Brillouin scattering describes the incident light (photons) to be influenced by the material within the fiber (phonons), as an interaction between two waves. Hence, wavelengths deviating from the incident wave arise. The Raman scattering is caused by energy conversion of the incident light to the electro structure of molecules or atoms.

These backscattering types can all be used to apply the optical fiber as a sensor. The Raman backscattering is sensitive to temperature, while the Brillouin and Rayleigh backscattering are sensitive to strain and temperature [47].

4.3.1 Raman Scattering sensors

The sensors based on Raman scattering often have a spatial resolution of 1m, but can be as low as 1cm [48]. The temperature resolution can be 2°C, and the integrating time is below 60 seconds [49]. This method can be used for lengths up to 15 km [47].

4.3.2 Brillouin scattering sensors

There are several sensing systems on the market which rely on Brillouin backscattering. The frequency shift of the Brillouin scattering is in the range of 10 Ghz and typically depends on temperature and stress in the fiber [43]. Two of those sensing systems, readily available to market, are Brillouin Optical Time Domain Analysis (BOTDA) and Brillouin Optical Frequency Domain Analysis (BOFDA). Both analyzing techniques need both ends of the fiber to function and allow for measurements up to 50 km. The BOTDA can reach accuracies up to 20 µstrain, with measurement times of 5 to 10 minutes while the BOFDA can reach higher accuracies but slower measuring speed [50]. Another sensing system readily available to market is Brillouin Optical Time Domain Reflectometry (BOTDR). This technique has lower accuracy of 50 to 100 µstrain, but can be done single ended, which is not possible with the other methods based on Brillouin scattering [47].

In general, readily available to market Brillouin based sensing systems reach spatial resolutions as small as 0.5 to 1m. There have already been several studies which invented methods to increase the specifications of the Brillouin based sensing systems like higher measuring frequency [51, 52, 53], higher accuracy, and better spatial resolution [49, 48]. These methods, however, decrease other specifications, and increase the costs of the interrogator.

4.3.3 Rayleigh scattering sensors

Optical Backscattered Reflectometer (OBR) systems use swept-wavelength coherent interferometry to measure Rayleigh backscattering as a function of position in the optical fiber. This technique is called Rayleigh based Optical Frequency Domain Reflectometry (OFDR). The Rayleigh backscattered profile of a specific optical fiber is a result of the heterogeneous reflective index of the latter (i.e. the imperfections), which is distributed randomly along the entire length of the fiber, establishing a fingerprint of each optical fiber as a result of its manufacturing process [54]. Changes in strain or temperature causes temporal and spectral shifts in the local Rayleigh backscatter pattern. These temporal and spectral shifts can be measured and scaled to give a distributed temperature or strain measurement [55]. A normal sampling rate for this method is 0.2 Hz [56] and a spatial resolution of 1cm is possible, over a maximum length of 70m [57].

4.4 Quasi distributed - FBG

A quasi distributed strain sensor can be obtained by using any point sensor with long gauge length. Then, the strain in between anchoring points is averaged and measured by the response of the point sensor. This measuring technique can be very efficiently obtained by the use of an optical fiber.

A Fiber Bragg Grating (FBG) is a narrow band filter or mirror in the core of an optical fiber. It can be produced by utilizing the photosensitivity of optical fiber materials. By exposing the optical fiber to external incident photons, a permanent change in refractive index is obtained. This change in refractive index causes the corresponding mode coupling of the light wave with a certain wavelength in the condition of fiber waveguide [46]. The specific wavelength a certain FBG reflects can be described by Equation (4.1).

$$\lambda_b = 2 * n_{eff} * \Lambda \tag{4.1}$$

Variable λ_b describes the specific wavelength, n_{eff} describes the effective (modified) refractive index in the grating and Λ describes the period of the grating. A theoretical explanation on the interaction between incident photons and the optical fiber can be found in Du [46].

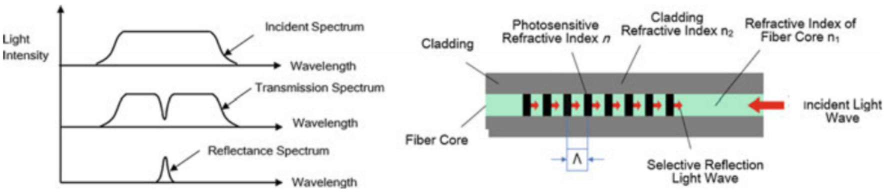

Figure 4.5: Principle of a FBG [46]

The principle of a FBG as a sensor is to measure the wavelength shift of the reflected light due to external influences. n_{eff} and Λ are varying due to thermal and strain changes. The relation between strain and wavelength shift, and between temperature and wavelength shift is linear. The theoretical backgrounds of these relations can be found in Du [46]. Specific scaling factors are delivered by manufacturers on delivery.

A typical FBG has a length of 5-10 mm. Multiple gratings can be present on one optical fiber. These must reflect different wavelengths, so that each reflected wavelength can be matched to the position along the fiber. The total domain of frequencies is divided over the gratings. Limitations on the total domain, and the frequency range needed per grating limit the number of gratings on one fiber to less than 100. The number of gratings that can be present on one fiber is dependent on the expected wavelength shift of the gratings in the fiber. If this shift is expected to be high, a lower number of FBGs can be present on one cable since the specific sensor will use more frequencies within the total domain and therefore a larger frequency spacing between individual sensors must be reserved.

To measure which wavelengths are reflected, a so-called interrogator unit is used. These wavelengths can be logged at speeds higher than 100 kHz [58]. An example of reflected wavelengths of a fiber optic cable with multiple FBGs connected to an interrogator is presented in Figure 4.6. The length of the FBG gives the lower boundary for the spatial resolution to be 5mm. The maximum spatial resolution is not limited, since FBGs with long gauge length are possible [59]. Typical resolution for FBGs is 1 $\mu\varepsilon$, or 0.1 °C, and has the possibility to measure wavelength shifts up to 10nm [58]. Typical sensitivities are 0.7 $pm/\mu\varepsilon$ and 17 pm/°C, but depend on specific sensor choice.

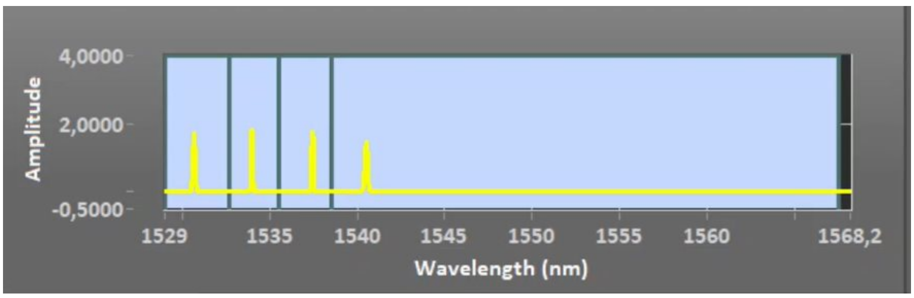

Figure 4.6: FBG peaks detected by a i4 interrogator

4.5 Applications of distributed sensing techniques

Optical fibers, and especially FBGs have been used a lot in taking measurements from concrete specimen. Applying glass fiber to measure reinforced concrete comes with its challenges. In this section these challenges are described so these can be implemented in the sensor design of the experiment.

If the optical fiber is longitudinally connected to the concrete specimen, by embedding or gluing in or onto the concrete. It causes the strain in the fiber to be equal to the strain in the concrete. This is ideal for measurement below the cracking point of the concrete. Above this point, the strain in the concrete is infinite at the location of the crack. The optical fiber is not able to equal this strain and will therefore also break. The signal of the sensor will therefore be lost. Several solutions to this problem are provided by literature and are explained below.

For embedded sensors, this issue is solved by strengthening the optical fiber cable with reinforcing cladding. This cladding protects the fiber and spreads out the strains over a larger length of the fiber. Since the bond of a cast in fiber is limited and the cladding is somewhat flexible, the anchorage length of the fiber around cracks is increased. This is a feasible method if only global strains are measured. When the structure is unloaded, the cracks close. This could cause compression to occur in the fiber, since it was pulled out during cracking. This can seriously influence the accuracy of the measurement for specific types of fiber optic measurements [46].

Alternatively, the sensors can be embedded in the reinforcement steel. Up until far beyond yielding, the steel will not fracture. This means a spreading of the strains by the fiber is not necessary. This is already achieved by the steel itself. In addition, it is often the strains in the steel that interests the engineers the most. When electrical and fiber optic sensors are embedded in the steel, it can be observed that the strain measured by the FBG is quite accurate. The observations reveal that the strains are a bit higher than the electrical strain gauges at a higher loading stage. This can however be explained by the location of the sensors in the rebar. The optical fiber is placed near the surface of the rebar in a small slot glued with epoxy, while the electrical strain gauges are located in the center of a splitted rebar [60]. Local higher stresses are to be expected near the surface [61].

For external sensors, full longitudinal gluing is an option [62]. The issue with the cracking of the concrete can then be solved by applying flexible glue. Around locations of concrete fracture the glue can plastically deform or debond. When the interaction between concrete, the fiber and the glue is known, it is possible to find crack widths with this method as shown in Figure 4.7 [63]. This method however, can fail at higher load levels with larger crack openings [64]. Also, problems occur when the cracks close during unloading [65, 56].

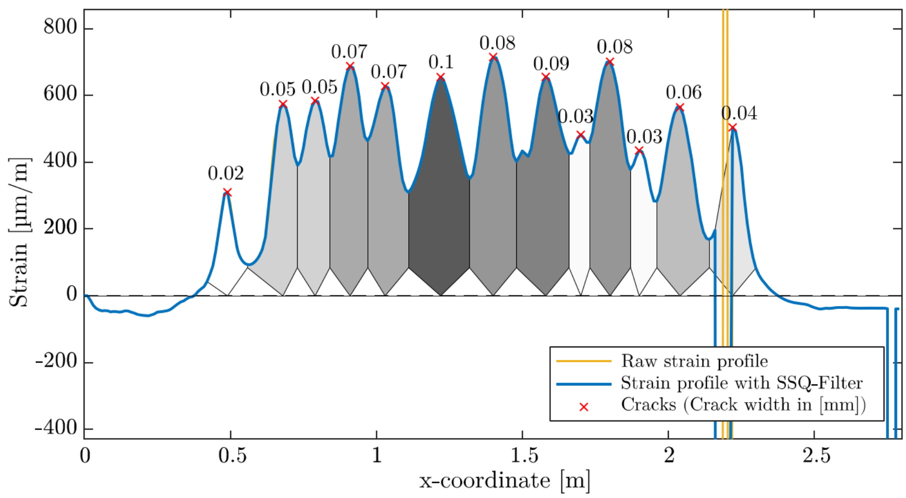

Figure 4.7: Crack widths determined by a distributed optical fiber sensor [63]

One method to sense strains of a cracked structure is to use long gauge measurements. This is a discrete method which averages the strain over the length in between two anchor points. When used with some pretension, the closure of the cracks can be measured. With FBG sensors it is possible to sense at a high frequency, but the localization of the damage is limited to the applied gauge length.

4.6 Conclusion

The application of optical fibers to cracking concrete surfaces can be problematic. Locally, cracking concrete leads to infinite strains. From previous studies it can be concluded that continuously gluing a fiber to a concrete structure can lead to undesirable issues after cracking of the specimen like breaking the fiber or affecting the measurement by deformation of the glue. Therefore it is recommended to use discrete, long gauge measurements to overcome an infinite strain at the point of cracking.

Table 4.1: Summary of fiber optic solution

Method	Precision $\mu\varepsilon$	Frequency	Type of measurement
FBG	1	1 khz	up until 30 sensors on one line; total lengths up until 10 km; single ended
Brillouin scattering (BOTDA, BOFDA, ...)	2-30	<0.1 hz	spatial resolution 0.2-1.0 m; total lengths up until 25 km; double ended
Rayleigh scattering (OBR)	1-5	0.2 hz	spatial resolution 2-20 mm; rang up until 70 m; single ended

An overview of the presented strain fiber optic measurement techniques is shown in Table 4.1. The execution of a proof load test, requires direct data visualization to determine if further loading is safe. This is only possible if the acquisition time is lower than 5 s. It is therefore advised to use either the OBR system or the FBG system.

The minimum gauge length for both systems is equal and the acquisition time to collect the data would both be fast enough. But The OBR system is relatively new compared to the FBG technique which has been used for decades by now. In addition, the OBR system seems to suffer some problems with alternating loads. These problems might be solved with applying prestress to the fiber. Applying prestress is never done before in combination with the OBR system and therefore it would introduce undesirable risks. Therefore the FBG method is applied in the measuring system.

5 Review and development of stop criteria

The currently available stop criteria are all based on the measurement techniques which have been used so far. Every stop criterion is determined for a certain setup of sensors, which all have varying precision and accuracy. The reliability of a stop criterion, is therefore linked to the sensor system it is measured with. This implies that when a new measurement system is designed, the feasibility of the current stop criteria to the newly designed system should be assessed. Moreover, new stop criteria which are specific to this sensing system could be developed and the current stop criteria could be optimized for the system. Within this chapter, the applicability of currently available stop criteria to distributed strain measurements on the longitudinal bottom side of the concrete is reviewed. The interpretation of the results of the proposed measuring system are discussed. The results can be subdivided into 2 groups; measurements that indicate flexural failure and measurements that indicate shear failure.

5.1 Conversion of strain results

Fiber optic measurement results in strain on the bottom side of the concrete slab. To interpret this strain in terms of stop criteria, the measured strain should be converted to a crack width, or a stiffness indicator. In this paragraph, the conversions between the measured strain, and desired quantities are described.

5.1.1 Strain to crack width

The strain, multiplied by the gauge length, gives an elongation. The amount of elongation that can be attributed to the crack width can be determined by the tension tie model as described in Section 3.1.1. The elongation (ΔL) can therefore be described by Equation (5.2)

$$\Delta L = w_{cr} + \varepsilon_{mean,concrete,gauge} l_{gauge} \tag{5.1}$$

For each particle of concrete is determined how much stress it experiences. This is based on its distance to a crack and the distance of cracks to each other. With the integral of the stress diagram and the E-modulus one can determine the strain in the concrete over a certain length. This is shown in Figure 5.1.

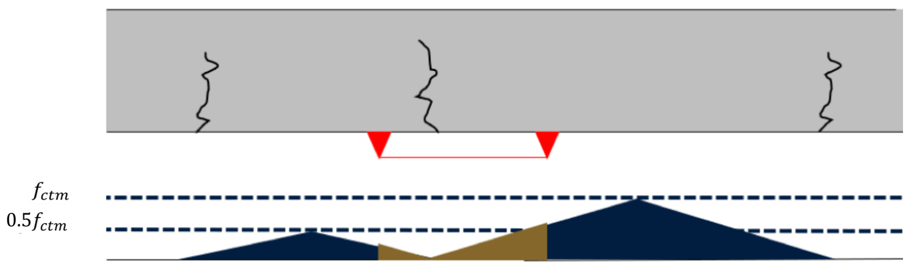

Figure 5.1: Concrete stress in between cracks

As can be concluded from above approach, the strain measured by a fiber-optic strain sensor is very dependent within the gauge length and how the cracks are located on this gauge length. To have an accurate estimation of the cracks and strains of the concrete, it should be known where the cracks are located in the gauge length. This approach should therefore be combined with an optical method of crack identification such as DIC.

A more practical method to reduce the sensitivity to the location of the cracks is to average out all the measurements over multiple cracks. Then, an average concrete strain can be determined for multiple cracks. This does however, reduce the accuracy of the measurement system. The average concrete strain can be determined by calculating the average stress in the concrete over multiple cracks which lays in between 0.25f_{ctm} and 0.5f_{ctm}. For a typical concrete slab bridge of C50, this would result in 30-45 $\mu\varepsilon$. This strain is in general less then 10% of proposed stop criteria.

In proof load testing a direct interpretation of the results is necessary. Therefore, a fictitious crack width is introduced. This ficticious crack width assumes an average number of cracks within the gauge length based on the calculated average crack spacing. The amount of concrete strain is neglected since the influence of the concrete strain will be below 10%. Then, the ficticious crack width can be calculated with the following formula:

$$w_{fict} = \frac{\varepsilon l_{gauge}}{s_{cr}} \tag{5.2}$$

5.1.2 Concrete strain to steel strain

In previous experiments, LVDTs on the bottom side of the concrete were used to measure the mean strain. The strain on the bottom side of the concrete is then interpolated to the strain in the reinforcement steel with help from the following formula:

$$\varepsilon_s = \frac{d-c}{h-c}\varepsilon_{c,bot} \tag{5.3}$$

The measured mean strain on the outside of the concrete over the gauge length might however not be representative for the strains of the reinforcing steel at high strains. At yielding strains the reinforcement anchors itself into the concrete over a length which is proportional to the diameter of the reinforcement and the quality of the bond. Therefore, the elongation of the steel within the crack, should be divided over the anchorage length of the steel. Hence, the strain on the outside is not representative for the strain in the steel way beyond yielding.

5.1.3 Steel strain to height of the compressive zone

The height of the compressive zone needs to be determined in two stages. The uncracked, and the cracked section. For both stages a calculation method is described in this paragraph. The calculation that must be used, is determined by the cracking strain. If the measured strain is higher than the cracking strain, the section can be assumed cracked. If the strain is lower, linear elastic material behavior is assumed.

For uncracked sections, the linear elastic theory is valid. This means that the height of the compressive zone can be determined by calculating the neutral axis. This can be done by the following formula:

$$y_{top} = \left(\frac{\left(A_c E_c \frac{h}{2} + A_s\left(E_s - E_c\right)d\right)}{\left(A_c E_c + A_s\left(E_s - E_c\right)\right)}\right) \tag{5.4}$$

The height of the compressive zone after cracking, can be determined based on Torenfeldts parabola Equations (3.15) to (3.21). When concrete properties and geometry are specified, a relation between the steel stress and the compressive zone height can be obtained.

5.1.4 Strain to curvature

To calculate the curvature, the steel strain and compressive height should be known. From Section 5.1.2, the strain in the steel can be calculated and from Section 5.1.3, the concrete compressive height can be calculated. The curvature follows from Equation (5.5):

$$\kappa = \frac{\varepsilon_s}{d - c} \tag{5.5}$$

5.1.5 Strain to section stiffness

The stiffness of a certain measuring section, is determined by the following formula:

$$k_{sec} = \frac{F_{applied}}{\varepsilon} \tag{5.6}$$

Over the full gauge length the development of the cracks is measured. By identifying the stiffness stage, the measuring point is in, it is maybe possible to identify critical positions over the length. In addition, it can be deduced if the full width is active, and it is possible to track the points in the slab where stiffness reductions develop.

1. Linear elastic behavior (pre-cracking)
2. Sudden development of a crack, including some permanent deformation
3. Linear elastic behavior with lower stiffness because the presence of a crack
4. Non-linear behavior of the crack due to yielding of the reinforcement

5.1.6 Strain to deflection

When the curvature over the full length of the beam is known following Section 5.1.4, this can be used to determine the shape of the slab. When the deflection at both ends is set to zero, the total deflection can be determined following the following protocol:

1. Multiply the curvature by the gauge length for every section to find the $\Delta\phi$ for every section
2. Introduce rotation at the support ($\phi_{support}$) as variable
3. The rotation for each section (ϕ_i) can be determined by $\phi_i = \phi_{support} + \sum_0^i \phi_{section}$
4. Calculate the deflection $w(l) = \sum_0^l \phi_i * l_{gauge}$
5. 5. $w(l) = 0$ Solve for $\phi_{support}$

5.2 Adaptation of current stop criteria for fiber optical measurements

In this section, an elaboration on the current stop criteria is given. The formulas of calculation are given and the adjustments to adapt to a measurement system with multiple longitudinal semi-continuous fiber optic measurements are presented.

5.2.1 Safety approach

To apply the in Chapter 3 selected stop criteria to a concrete slab bridge, a re-evaluation of the designed limits is presented in this section. The current approach is based on the used sensors during those tests, and were mainly focusing on beam behavior. For the application to a slab, redistribution of forces in the slab is expected, and the sensors are more distributed over the full length and width. Thus, it can be expected that if a specific stop criterion is reached straight underneath the load, the slab will have more capacity to redistribute forces after that point than a beam. This leads to higher margins of safety which can be used to improve the current stop criteria. The following three methods are considered:

Table 5.1: Three Methods to adjust the safety approach

	Method	Safety when loaded up to stop criteria
1	Loading with a safe margin to the plastic stage of the structure. Use the stop criteria for beams straight underneath the load at the critical location	Low chance of structural failure
2	Reduce the applied safety margin of 35% to a lower percentage	Moderate chance on structural failure. It is up to the engineer to decide if it is allowed to rely on alternative load-carrying paths
3	Loading with a safe margin to the plastic stage, apply stop criteria for beams at the governing yield line. Check for yielding on critical location	Moderate chance on structural failure. Test should justify this claim

Where option 1 would be overly conservative, option 2 decreases the total applied safety to the stop criteria. A high number of tests is required to prove that a reduction of the safety level is appropriate. Option 3 does not reduce the amount of safety on the stop criteria itself. It defines the critical point at another location. Therefore, the current level of safety can be maintained. The justification of this relocation of the critical measurement, can be proven with a lower number of tests than when a whole new safety analysis should be performed.

5.2.2 25% stiffness reduction

The stiffness of the structure is determined by the following formula:

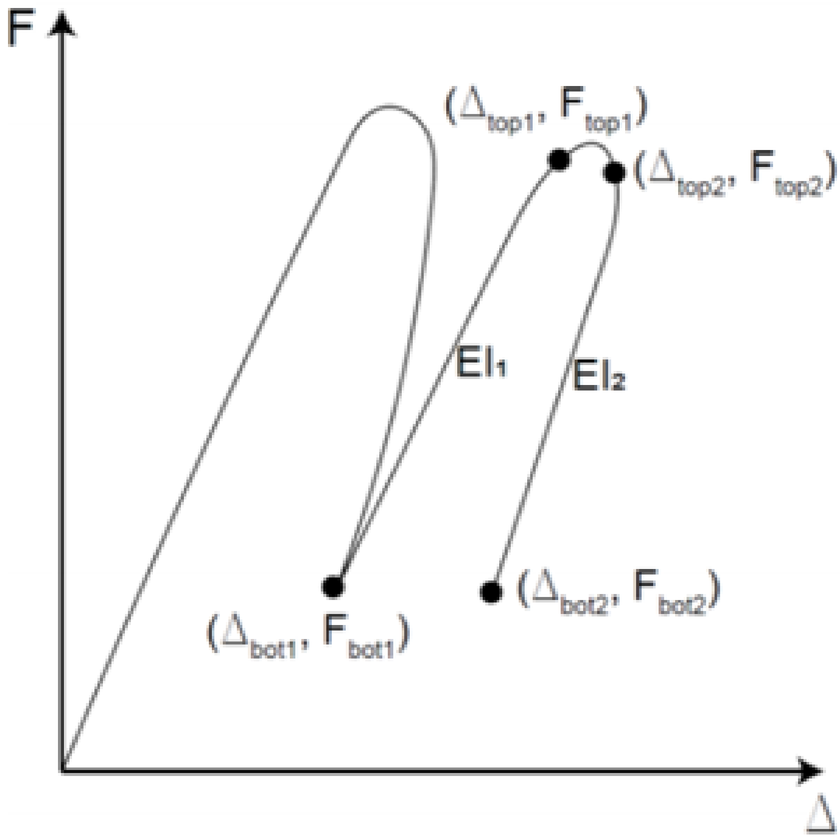

Figure 5.2: Method to determine stiffness of loading and unloading branch [5]

$$EI_{loading} = \frac{F_{top1} - F_{bot1}}{\Delta_{top1} - \Delta_{bot1}} \tag{5.7}$$

The force is a value obtained by the measurement setup. The deflection can be determined as described in Section 5.1.6. As soon as a reduction in stiffness of 25% is observed, the stop criterion is reached.

5.2.3 Deformation profiles

Using the integration of strains as explained in Section 5.1.6, a profile of deformation can be calculated. With this deformation profile on several load levels a qualitative analysis on the shape can be performed.

5.2.4 Flexural - ε_{stop}

The strain stop criterion is based on strain observations straight below the load. The theoretical derivation allows for 65% of the yielding strain to occur, before the stop criterion is reached, to account for uncertainties and have a safety margin. This stop criterion was developed for beam experiments.

Plate behavior provides the possibility to redistribute the forces over the full width of the slab. Redistribution from the middle of the slab to the outer edge happens beyond linear elastic deformations (after cracking moment). The steel rebars straight below the load, will reach yielding moment on a lower load then rebars closer to the edge; this guarantees some margin of safety. Hence, a new interpretation of the stop criterion is proposed.

As ε_{stop} has proven to be quite accurate for the beams. With a feasible margin of safety [10], the stop criterion is maintained. The difference, however, is where the strain is measured. Before flexural failure, steel over the full width of the slab will yield. Therefore, it will be justified, to measure the strain closer to the edge. If enough safety is guaranteed for the outer parts of the slab, the total safety of the slab is also guaranteed.

However, yielding of the reinforcement is undesirable. Therefore, an extra criterion is set for the strain which is measured straight below the load. The measured strain underneath the load may not be higher than 90% of the yielding strain. This criterion prevents permanent damage to the slab bridge.

5.2.5 Flexural - $w_{max} < w_{stop}$

The limit on crack width, can be measured by using the conversion from concrete strain to crack width following Section 5.1.1. The current crack width criteria was developed by Lantsoght et al. [10]. The calculation of the crack width is calculated by Frosch's approach. Based on beam experiments, Lantsoght proposed to calculate the crack width which corresponds to reinforcing steel which is stressed to 65% of the yielding strain. In contrary to Lantsoghts' proposal, the limiting crack width will not be compensated by the self-weight of the structure [21]. The self weight and the factored load are subjected to the structure at the moment of testing and will therefore be present in crack width.

The following calculation method is used to determine the stop criterion for the test specimen [21]:

$$w_{stop} = 2\frac{0.65 f_{ym}}{E_s}\beta_{fr}\sqrt{d_c^2 + (\frac{s}{2})^2} \tag{5.8}$$

5.2.6 Shear - ε_{CSDT}

The additional capacity which is developed when loads are redistributing are not considered in the CSDT. Conservatively, the slab can be assumed to be a wide beam. To account for the spreading of the force, the effective width can be determined. The stop criteria can then be calculated based on an one-dimensional force transfer mechanism such as CSDT. The procedure is described below:

1. Determining effective width with the French method.
2. Calculate the shear capacity according to the CSDT.
3. Calculate the corresponding bending moment underneath the load.
4. Find the corresponding curvature underneath the load.
5. Convert the curvature into a strain on the bottom of the specimen.
6. Find the stop criteria by reducing the strain by 35%, and subtracting the strain caused by permanent loads (Equation (5.9)).

$$\varepsilon_{lim,CSDT} < .65\varepsilon_{CSDT} - \varepsilon_{c0} \tag{5.9}$$

The measurements of the strain, located in the line between the load and the support will reach the stop criterion first, since it is the most heavily loaded area. The distribution of strains between the sensors underneath the load, and the sensors further away to the edge, can be calculated by linear elastic approach. Any deviation from these results means redistribution of forces.

5.2.7 Shear - $w_{max} < 0.4/0.75 w_{ai}$

w_{ai} estimates the crack width at which aggregate interlock will no longer be possible. The stop criterium can be calculated with the following formulas:

$$w_{ai} = \frac{0.03 f_c^{0.56} \frac{S_{cr}}{d} (978 {\Delta_{cr}}^2 + 85\Delta_{cr} - 0.27) R_{ai}}{\nu_{RBK}} + 0.01mm \tag{5.10}$$

With:

$$\nu_{RBK} = max\left(1.13 k_{slab} k \sqrt{\frac{f_c}{f_{ym}}}; 0.15 k_{slab} k (100 \rho_s f_c)^{1/3}\right) \tag{5.11}$$

$$k = 1 + \sqrt{\frac{200mm}{d}} \leq 2 \tag{5.12}$$

$$\Delta_{cr} = \frac{25d}{30610\phi} + 0.0022 \leq 0.025mm \tag{5.13}$$

$$R_{ai} = 0.85 \sqrt{\left(\frac{7.2}{f_{c-40} - 40} + 1\right)^2 - 1 + 0.34} \tag{5.14}$$

This stop criteria can directly be applied to the concrete slab. The cracks can be determined with the formulations in Section 5.1.1 for the shear tests. The measurements between the load and the support are then compared to this stop criterion.

5.3 New stop criteria

5.3.1 Flexural - Stiffness reduction per section

The current stop criterion for stiffness is dependent on the whole system and could therefore possibly perform inconsistent. This new stop criterion proposed here will monitor the stiffness reduction for every gauge length. It is proposed to measure the stiffness as determined in Equation (5.6).

The stop criterion will be reached when a 25% stiffness reduction is observed for at least one section near the critical location.

5.3.2 Shear - Critical shear crack theory

Where in theoretical calculations based on CSCT the strain at $0.6d$ is calculated based on the assumed strain at a critical location as can be calculated following Equation (3.8). In proof load testing there is the opportunity of measuring a value of which the strain at $0.6d$ can be deduced directly over the full length. This reduces the amount of assumptions, and therefore the uncertainty of the method. The ability to plot the force versus the strain in real time at all possible critical cracks, provides an opportunity to set a stop criterion at a factored CSCT limit. Prior to loading, the effective width can be determined by using the French method. With that value, the CSCT limit can be determined. This limit is reduced by a safety factor, for example 35%. This is implemented in the CSCT formula in Equation (5.15) From the external measurement, the steel strain, compressive height and strain at $0,6d$ can be determined through equivalent triangles. The strain at $0.6d$ can then be plotted against the force, and loading should be stopped when the target load is reached or when the factored CSCT limit is reached.

$$\frac{V_R}{bd\,(f_c)^{1/2}} = 0.65\frac{1}{6}\frac{2}{1+120\,[\varepsilon d/(d_{g,0}+d_g)]} \tag{5.15}$$

Since redistribution of shear forces is not desirable, it is proposed to measure this stop criterion over the full length on the shortest line between the load and the support. And to average the measured strain over a maximum of 1 major crack, as each of those cracks can develop into the critical shear crack [19].

5.3.3 Punching - Critical shear crack theory

As there are optimizations of the CSCT for punching failure, the above stop criterion is extended to punching failure as well. The stop criterion is presented in Equation (5.16). An initial safety margin of 35% is proposed.

$$\frac{V_R}{b_0 d\,(f_c)^{1/2}} = 0.65\frac{3/4}{1+15\,[\psi d/(d_{g,0}+d_g)]} \tag{5.16}$$

As stated in Section 3.1.3, the CSCT for punching is not based on the strain on a certain point, but on the rotation within the critical shear crack. In Figure 5.3 it is shown where the Inclinometers were located for deriving the CSCT on a 0.25 m thick slab of 3x3 m.

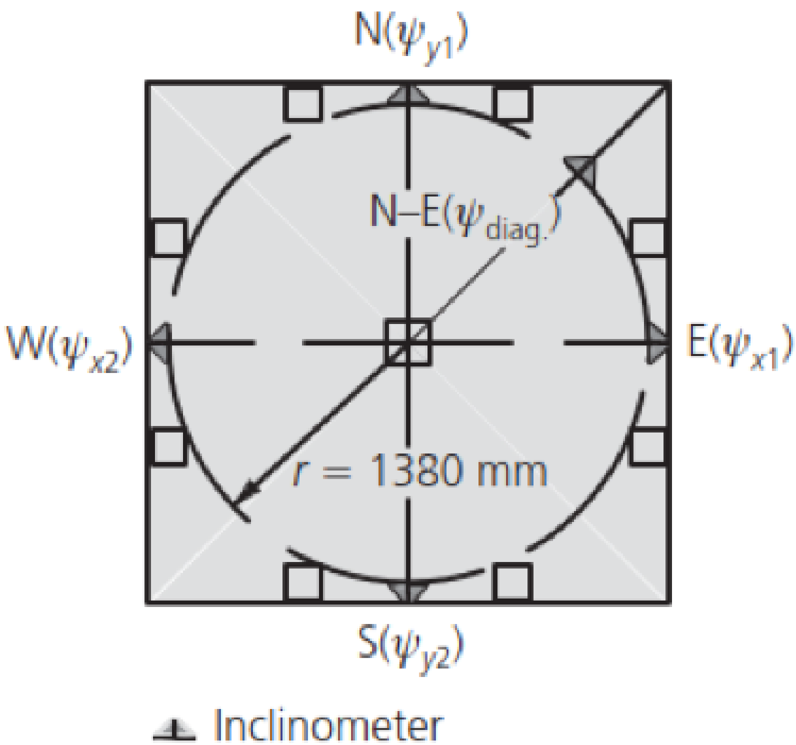

Figure 5.3: Location of the inclinometers for CSCT experiments with loading in the center of the concrete plate [30]

A conical deformation profile is assumed, which implies that all measured rotation is rotation form the critical shear crack. Thus, the global rotation is used. the rotation can be determined based on the deformation profile as elaborated on in Section 5.1.6

The continuous fiber optic measurement technique makes it possible to measure the actual rotation of the critical shear crack with a local measurement. This can be especially useful when flexural behaviour is present as the assumption on the conical deformation profile is not valid in that case.

It is proposed to keep track of the limit within the zone in which critical cracks can form a punching cone, in the longitudinal direction, as this direction will reach the limit first.

5.4 Overview of the stop criteria

An overview of the proposed stop criteria which can be measured by optical fibers is shown in Figure 5.4. The new investigated stop criteria are placed in an orange box. The equation numbers are indicated in the Figure.

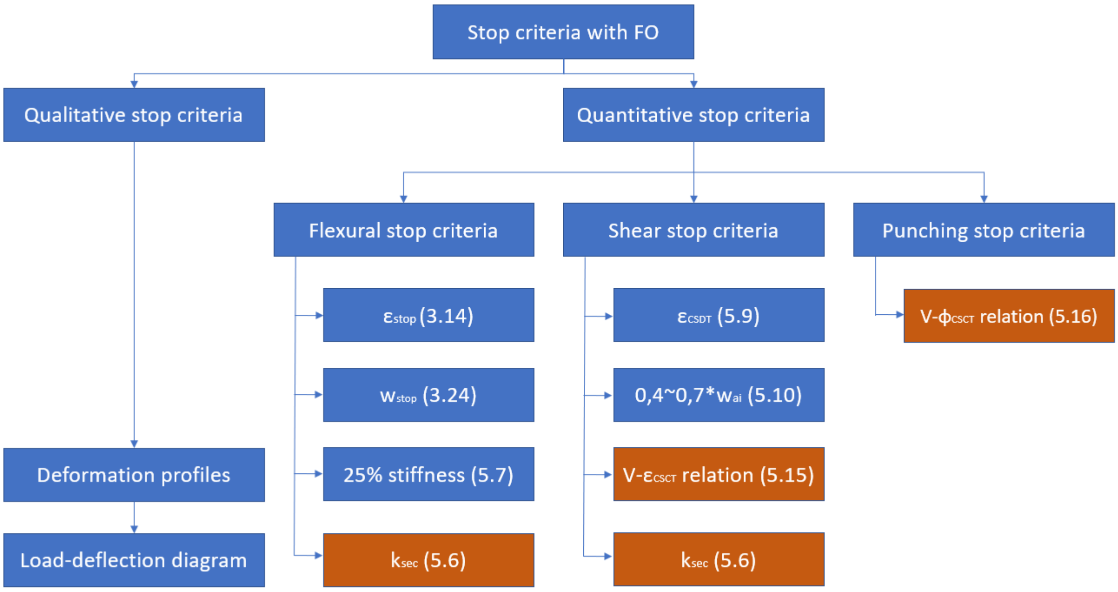

Figure 5.4: Overview over stop criteria

6 Fiber optical sensor design and accuracy

This chapter provides an insight in the development of the measurement system. First the design of the connection between concrete and fiber is elaborated on. A mechanical anchor is developed, and glue experiments are performed to ensure a reliable bond. Second, a proposal on designing the geometrical layout is shown. This proposal is based on sensor limitations and the proposed stop criteria. Lastly, a comparison between measurements from the optical fiber and from reference methods is presented to give more insight in the accuracy of the developed system.

6.1 Connection design

This section explains the design choices on the anchorage system for the fiber optic sensor system. This anchorage system ensures that the strains on the bottom of the concrete are transmitted to the optical fiber sensor. When an optical fiber experiences tensile strain, a tensile force developes. Since high strains are expected, the connection with the concrete needs to be tested to resist these forces, without too much deformation in the connection itself. The verification of this anchor can be subdivided into the following categories:

- Connection of the fiber to a steel part
- Connection of the steel parts to each other
- Connection of a steel part to the concrete

Where the first two parts were outsourced to a specialized company with experience in making these connections, the latter needed more investigation. The design by the external company is shown in Figure 6.1

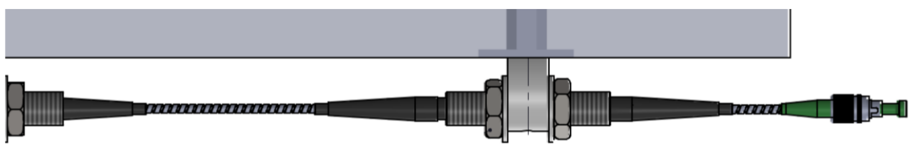

Figure 6.1: Design of the optical fiber connection

Normally a mechanical anchorage of the fiber to a object to be measured is preferable. This approach reduces the risk of creep. However, it is undesirable to damage the concrete of an existing bridge to mount anchors to it. Therefore a mechanical anchor is not possible. Thus, an experimental program was set up to select an appropriate glue based on strength and creep performance.

6.1.1 Dimensions of the gluing plate

Under normal circumstances, it would be preferred to first investigate the glue properties, and then determine the required gluing surface based on the tolerated deformation and the found stiffness. However, due to restraints in the planning, the gluing plates needed to be ordered before the glue experiment was possible. Therefore the dimensions of the gluing surface are determined beforehand based on a theoretical approach and assumptions. The dimensions of the gluing plate are dependant on the following variables:

- Minimum practical surface of 15 x 15 mm
- Minimum practical thickness of 10 mm, to apply screw thread
- Maximum tensile bond force

- Loads on the gluing plate

In addition, when a gluing plate is too big, cracks in the concrete will develop underneath the glued surface which can cause spalling. Another unknown is the behaviour when loads are present over longer periods of time.

From tensile tests of the applied fiber can be concluded that the maximum load the fiber can exert to the connection is 0.8 kN. This is the shear force the glue connection should resist. Therefore, the moment the glue connection should be able to resist can be seen in Figure 6.2.

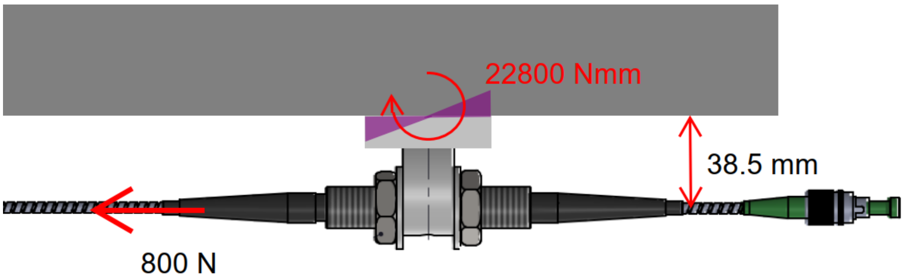

Figure 6.2: Force and moment applied to gluing plate

Assuming the glue will be stronger than the concrete and a square gluing plate, using linear elastic calculation of the stresses,the minimum dimensions of the gluing plate can be expressed as follows:

$$a_p = \sqrt[3]{\frac{6M}{f_{ctm;0.05}}} \tag{6.1}$$

Assuming a concrete strength class of C35/45, the concrete tensile strength can then be used to determine the minimum dimensions of the gluing plate based on tensile forces:

$$a_p = \sqrt[3]{\frac{622800}{2.25}} = 39.32 \text{ [N and mm]} \tag{6.2}$$

For practical applicability this is rounded off to a value of 40 by 40 mm, with a sandblasted gluing surface on the bottom side to increase the bond.

6.1.2 Glue strength

Five glues (A, B, C, D and E) were selected to investigate the strength. Starting point of this experiment was to load the plate in approximately the same way as it is loaded in the final application. Thus an M8 bolt was placed in the glued plate, which made it possible to introduce the shear force as well as the bending moment. For this test 2 techniques have been used to load the bolt. At first dead weight was used to load the bolt. As forces went beyond 150 kg, and the goal was to load up till failure, the method of loading by dead weight was not longer an option. Therefore the method of loading switched to a manual jack. The setup of both tests is shown in Figure 6.3.

The gluing plates were glued to a piece of concrete following the protocol as described below:

- Roughen up the concrete surface with a steel brush

(a) Loading by dead weight

(b) Loading by manual hydraulic jack

Figure 6.3: Loading methods to test the glued plates

(a) Tensile failure of the glue

(b) Failure of bond with the steel part

(c) Failure of the concrete

Figure 6.4: Three failure modes of the gluing plate

- Remove any dust
- Degrease the gluing plate and the gluing surface with acetone
- Apply a thin layer of glue on the gluing plate
- Let harden for the glue-specific prescribed hardening time

The average failure force of each glue is presented in Table 6.1. What can be observed is that glue D and E are underperforming significantly in comparison to the other glues. This is emphasised by the failure mechanism. Glue E left glue residue on both the concrete and the gluing plate. Therefore, it can be concluded that the glue itself failed in tension. Glue D only left residue on the concrete surface. It can thus be concluded that the bond between the glue and the gluing plate was not strong enough. For the other three glues (A, B and C) another failure mode was found. At failure, the concrete failed. A layer of 1 - 4 mm of concrete was still attached to the gluing plate. Therefore, these 3 glues complied with the assumption. An overview of the three failure mechanisms is presented in Figure 6.4. Although all five glues can hold the expected maximum load of 800N, the risk of detachments on glues D and E is judged too high because of the low sample size of this test.

Table 6.1: Results of failure test

Glue	Number of tests	Value
A	1	250 kg
B	1	270 kg
C	3	227 kg
D	2	159 kg
E	3	104 kg

6.1.3 Glue creep performance

Based on the results from the tensile test, only glue A, B and C were tested on behavior over time. For this test, a constant load of approximately 300 N was applied to the gluing plate using a bolt. The deformation of the gluing plate is measured over 17 hours with LVDTs. An overview of the setup can be seen in Figure 6.5.


Figure 6.5: Setup of the creep test

A few minutes after the test started, all plates glued with glue C failed. Therefore, this glue is unsuitable for this project. The failure occurred in the glue itself and left glue residue on both gluing plate and concrete. Because of this failure, no data is available for glue C under long term loading. The deformation under this constant load for glue A and B is plotted in Figure 6.6

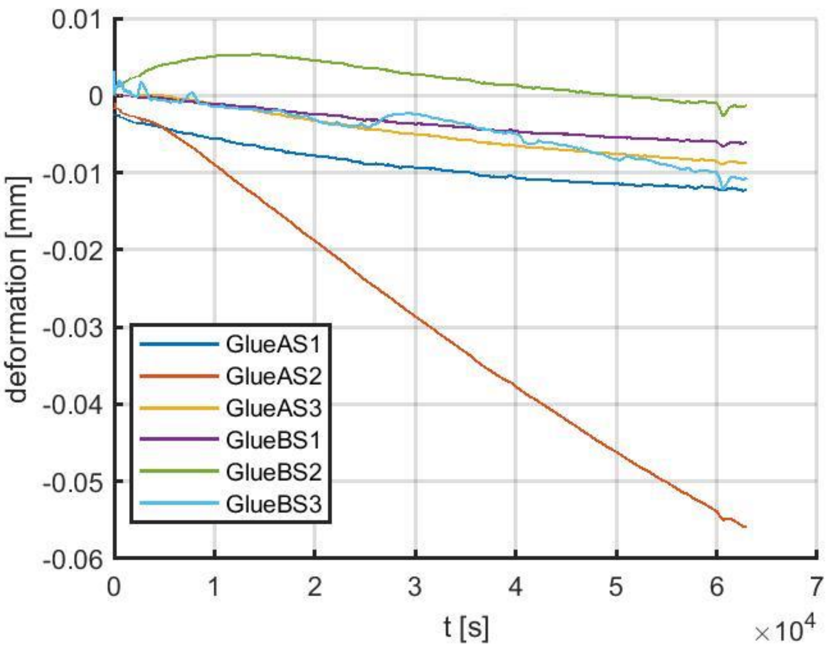

Figure 6.6: Displacement of steel plates during creep test, a comparison for 2 glues

It cannot be explained why certain specimen move in opposite direction as expected. To determine the deformation for each glue over the time frame, the minimum and maximum value are used to determine the stiffness over time. A summary of these stiffnesses is given in Table 6.2.

Experiment:	Creep:
Glue A S1	0.012328 mm
Glue A S2	0.055899 mm
Glue A S3	0.009393 mm
Average glue A	0.025873 mm
Glue B S1	0.006883 mm
Glue B S2	0.008060 mm
Glue B S3	0.015406 mm
Average glue B	0.010116 mm

Table 6.2: Glue creep values

Based on these results glue B is chosen, since it has the lowest average deformation over the full measuring period.

6.2 Layout design

Based on the literature review, the development of the stop criteria and the anchorage details a proposal for the location and spacing of the sensors is developed in this section. It is important that the optical fiber does not break under the exerted strain. The amount of strain in the fiber is dependent on the amount of cracks within the gauge length, the crack width and the gauge length itself. In this section, some tools are provided to perform the analysis on the gauge length and the location of the fibers.

6.2.1 Gauge length

The gauge length has influence on all results of the measurement system. Therefore it has to be chosen with care. All measurements within the gauge length are averaged. Thus, a shorter gauge length leads to higher accuracy of the measurement.

Because of the high FBG costs, during the design of the gauge length it must be kept in mind that the system is developed to be reusable in multiple projects. The gauge length should therefore not be optimized for one bridge, since it could compromise the re-usability of the system. It is therefore proposed to use a generic applicable gauge length.

With a short gauge length, the concrete strains can be monitored very precisely so that the exact moment of cracking can be identified. After cracking, if the gauge length is short enough to cover only one crack per anchor point, individual information on cracks can be gathered. If multiple cracks are present, the obtained crack width will always be an averaged value over the same amount of cracks. Another advantage on a short gauge length is a shorter dx for calculating the deformation profile as proposed in Section 5.1.6.

However, there are some limits to the minimum gauge length. The anchorage system needs a certain area to bind the gluing plates. These gluing plates cannot be glued right next to each other and should leave some unglued concrete in between the anchorage points. With the current anchorage method, 100 mm in between the anchors would be the bare minimum.

The second limiting factor is the expected maximum strain. This limit is the minimum value of the tensile strain limit in the fiber and the available optical bandwidth, which is explained in more detail in Section 6.2.2. The maximum strain the fiber will experience can be estimated by calculating the structural responses of the bridge. Here, an important distinction must be made between real proof load tests in the field, and a proof load test experiment in a laboratory. In a laboratory experiment, one of the goals is to determine the margin of safety on the stop criteria. Therefore the specimen will be tested up until failure. At, and just prior to actual failure, structural responses will be extremely high in comparison to a field application, which is not meant to reach this stage. Therefore, the required resistance to strain differs massively. The minimum gauge length following from the strain limit is given in Equation (6.3).

$$\frac{\sum_0^n w_{cr,m}}{l_{gauge}} < min(\varepsilon_t, \varepsilon_\lambda) \tag{6.3}$$

Apart from all above considerations, it must also be noted that with the FBG technique, every sensor costs a significant amount of money. It can therefore be financially appealing to apply the maximum gauge length which still provides acceptable results. As most of the proposed stop criteria for optical fibers are dependent on the behavior of the major cracks, and it is not desirable to have 2 major cracks in one span, this limits the maximum gauge length to the distance between 2 major cracks which can be determined by Equation (3.3).

6.2.2 Wavelength spacings

Each FBG reflects a certain wavelength. This wavelength differs when the FBG is subjected to strain or a temperature change. The FAZ i4 Interrogator which is used, scans all frequencies between 1529 and 1564 nm. Within this wavelength users can add up to 30 sensors on one channel. The amount of sensors which can be used is however limited by the amount of strain that is expected on a specific sensor. The more strain is expected on one sensor, the more the wavelength will shift, and therefore the more bandwidth this sensor will occupy. To calculate the maximum amount of sensors on one channel, one should divide the total scan bandwidth by the required bandwidth for one sensor. If the bandwidth is given, this can also be a limiting factor on the amount of strain that can be applied to the fiber. This maximum strain can be calculated by Equation (6.4). This equation relates change in strain ($\Delta\varepsilon$) and temperature (ΔT) to the shift of reflected wavelength ($\Delta\lambda$) trough fiber specific conversion factors for strain(A) and for temperature (B).

$$\Delta\varepsilon = \frac{\Delta\lambda - B\Delta T}{A} \tag{6.4}$$

6.2.3 Geometry

Based on the safety approach proposed in Section 5.2, multiple longitudinal optical fiber measurements can optimize the current flexural stop criteria for slab bridges. The positioning of these longitudinal sensors in the width direction needs to be determined based on the specific dimensions and failure mechanisms of the slab. For concrete slabs subjected to a concentrated load on a flexural-critical position, the reinforcement yields prior to failure. This leads to high deformations in the slab straight beneath the load. Due to cracking of the specimen, the stiffness of the structure will decrease in the loaded region.

The uncracked part or less cracked stiffer parts consequently starts to carry more of the applied load. This redistribution of forces in the transversal direction will eventually lead to a fully yielding middle cross section, if no other failure mechanism is critical before that stage. As proposed in the safety approach, the stop criteria can be measured at an offset from the direct line of force. This excludes peak values from the measurement and therefore more of the plate action can be used to prove structural resistance. Nonetheless, the strain straight underneath the load should still be monitored on stop criteria with a very low safety margin as proposed by Vos [22], since these criteria provide a high accuracy on structural responses very close to yielding. The positioning of the sensor should not be at the edge of the slab, as a typical concrete slab bridge will have a non-rectangular side face with edge reinforcement which can influence the results. If the measurement is too close to the load, it will not have beneficial effects. It is therefore proposed to have an additional measurement at 2.5*h from the load. This aligns with the definition between a beam and a slab, as slabs may be calculated as beams, as long as the slabs are not wider than 5*h. At this point, a decent amount of plate action is expected, while not moving away from the load significantly.

6.2.4 Application of internal sensors

To verify the results, and to gain more insight in structural behavior, it is possible to add FBGs within the concrete. These sensors are embedded in the reinforcement steel. Following Fugro's corporate procedure first a slot of 2 x 2 mm over the full length of the reinforcement bar is milled and the whole bar is sandblasted. Second, the slot and the fiber optic are cleaned thoroughly. Finally, the slot is filled with a selected epoxy and baked in an oven to reach maximum strength of the epoxy (see Figure 6.7).

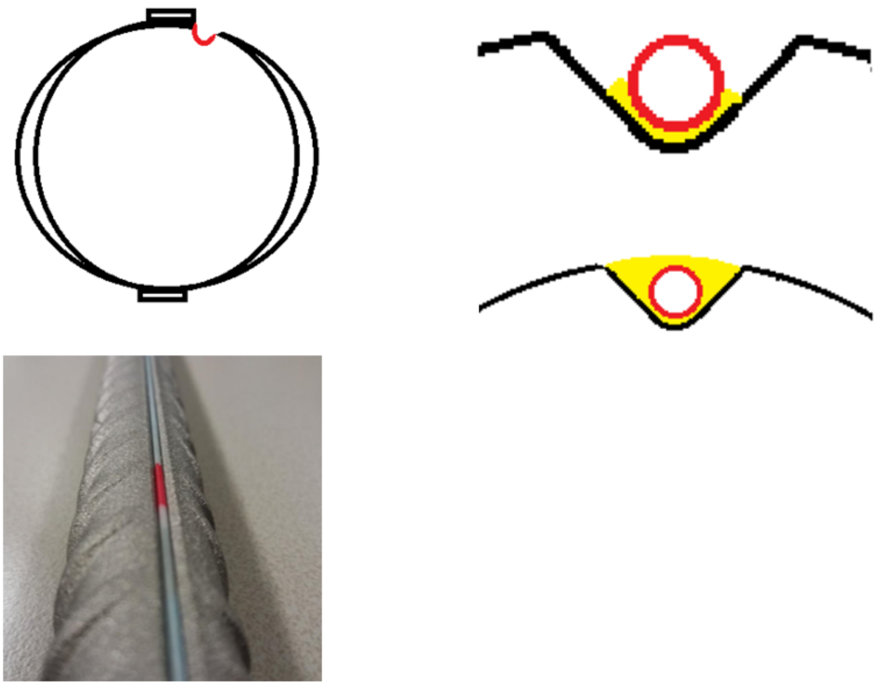

Figure 6.7: Cross-section of the reinforcement steel with a milled slot

In Appendix B tensile tests are shown that prove that the machining of these reinforcement bars does not influence the behaviour of the reinforcement much. The decrease in maximum force can be linearly related to the minor removal of material. However, this tensile test showed that the results of the internal sensors lose accuracy above the yielding point. From that point on, the epoxy cannot equal the developing strains in the reinforcement bars. Therefore the glue breaks at various locations. The results obtained from these sensors above yielding point should therefore be used with care. The cracking of the glue is shown in Figure 6.8.

Figure 6.8: Cracks in the glue after yielding

6.3 Accuracy and precision of the system

To check the accuracy of the measurement system, comparison measurements have been executed. This section provides an overview of the comparisons with other measurement methods and what this means for the accuracy and precision of the designed solution.

6.3.1 Small beam tests

Prior to the slab test, 2 shear-critical beams of 1400 x 100 x 200 mm (lwh) were tested to compare small-scale application of the fiber optic method to LVDTs. The beams were loaded with a point load, and spanned 1100 mm. 4 fiber optic sensors, and 4 LVDTs were placed to compare the results. An overview of the test setup is shown in Figures 6.9 and 6.10.

Figure 6.9: Setup of the small beam tests

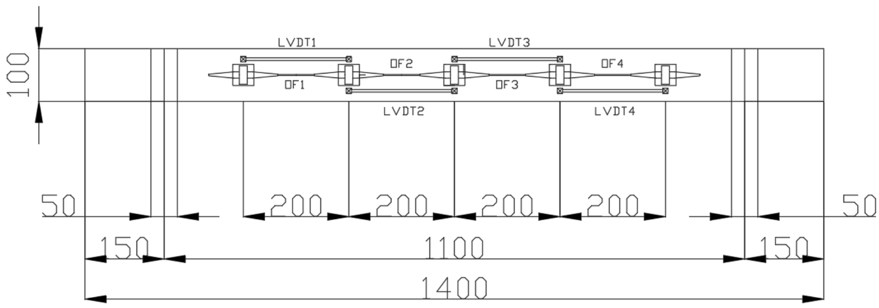

Figure 6.10: Bottom view of the beams with locatioins of the sensors

After reaching 2000$\mu\varepsilon$, the optical fibers were removed to prevent permanent damage to the sensors. The difference between the OF and the LVDT measurement was calculated as a percentage. In general, results of the optical fiber were within a 15% margin of the LVDT, as can be seen in Figure 6.11. In the beginning the percentage differences are high because of the extremely low absolute measured value. As the LVDT measurement and the OF measuremnet were not at exactly the same position, the observed 15% difference should be seen as an upper boundary for the accuracy. More details and graphs on these tests are presented in Appendix C.

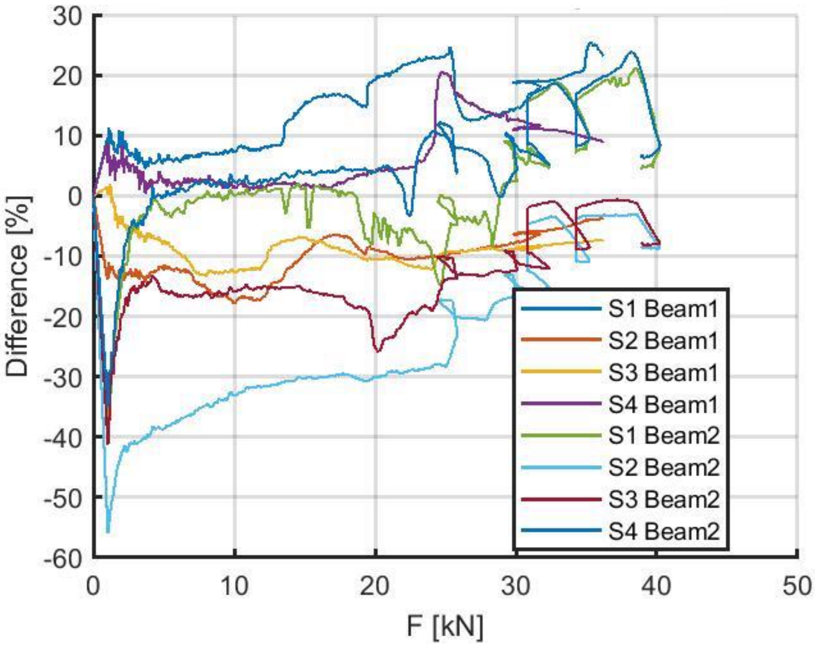

Figure 6.11: Difference on small beam experiments

A typical observation during this test was when a crack crossed a glued anchor location, the crack would run around the anchor as indicated in Figure 6.12. These local disturbances might have caused a larger error between the optical fiber and LVDT measurement.

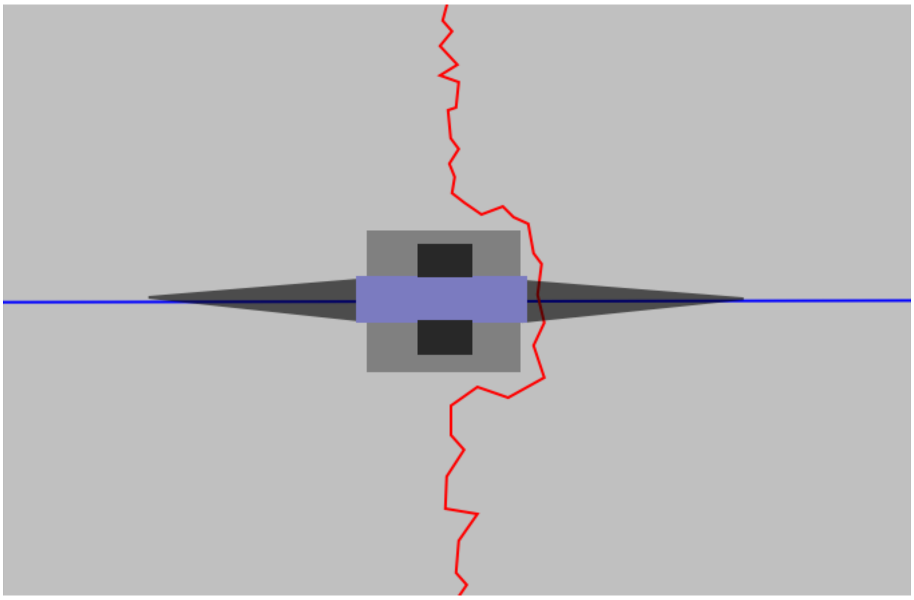

Figure 6.12: Typical observation on the cracking pattern on application of the glued anchor

6.3.2 LVDT comparison

During all slab tests, one LVDT was placed next to an optical fiber sensor to check the accuracy of the optic fiber system. The exact position of the LVDT varied between tests, so the location was near the loading point. An overview of the loading positions and location of the comparison sensor for each test are presented in Figure 6.13. For all three tests, the measured strain is is plotted over time in Figures 6.14 and 6.15.

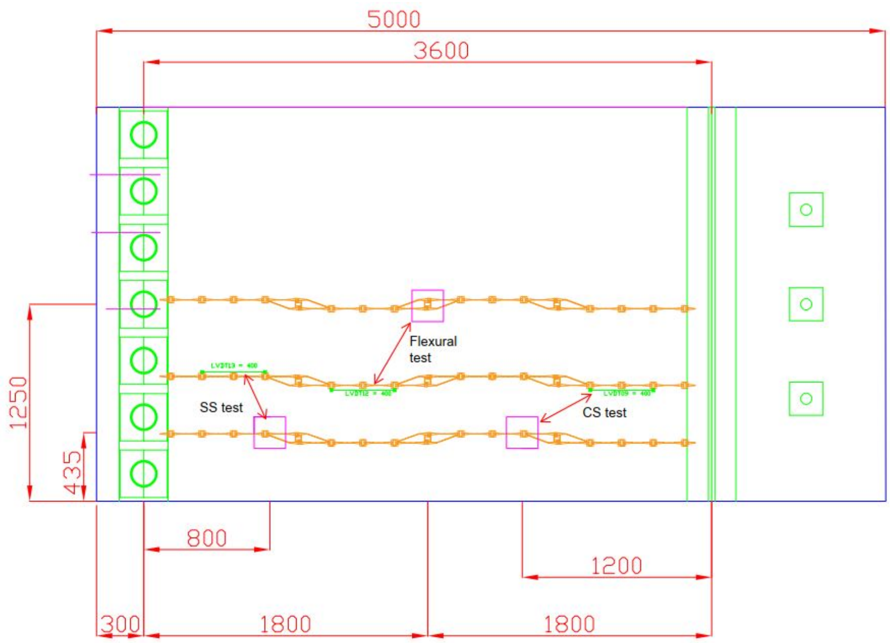

Figure 6.13: Loading position with comparison sensor

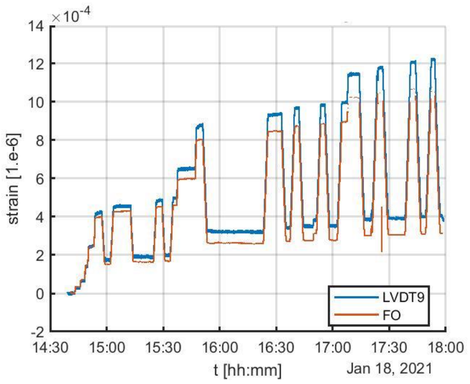

(a) LVDT vs FO flexural test day one

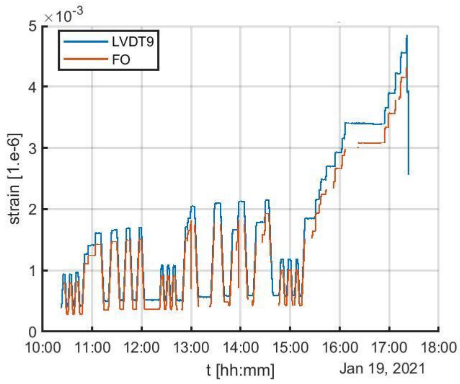

(b) LVDT vs FO flexural test day two

Figure 6.14: Loading of SR1M1

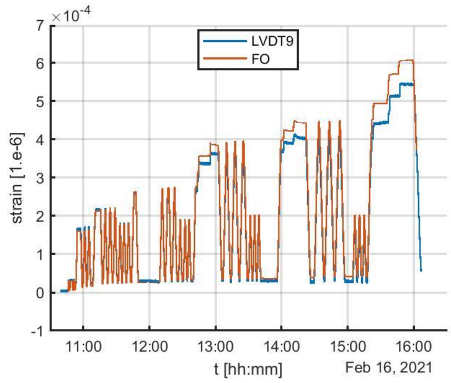

(a) LVDT vs FO during SR1E2

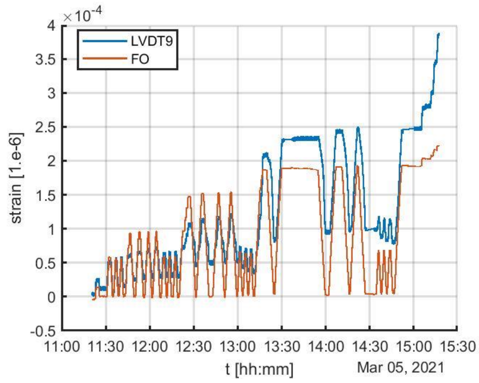

(b) LVDT vs FO during SR1E3

Figure 6.15: Strain comparison between OF and LVDT during Slab experiments

What can be observed from the first experiment, is that the measurement in the LVDT starts to deviate from the measurement with the FO. Over time this difference increases. The second experiment, however, indicates the exact opposite. The FO measurement is higher compared to the LVDT over time. The differences between the two measurements are quite high especially near the end of the test. During the third test, the LVDT provides a faulty result.

6.3.3 Creep test

Since there are some discrepancies between the LVDT measurement and the FO measurement, it was opted to check if creep occurred in the optical fiber. To check this, the sensors where tensioned with 0.1 kN and where observed for 72 hours. As the each fiber contains 4 sensors, the prestress was introduced on the outer two anchors. After the application of the prestress, the intermediate anchors were fastened. If any creep would occur, it is to be expected that the forces redistribute as shown in Figure 6.16.

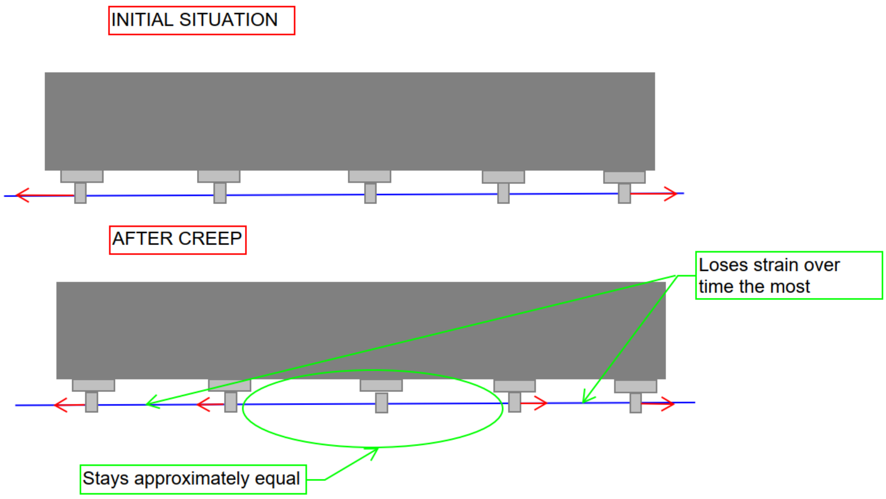

Figure 6.16: Creep test expectation

A typical result of the experiment is shown in Figure 6.17. The number in the legend corresponds to the distance of the sensor in meters from the simple support. The expectation of Figure 6.16 is therefore not present. The result shows that the strain in the middle of the slab decreases more than the strain near the support. This can be explained by the order of the tests. Just before the creep test started, one of the failure tests was executed. During this test the slab experienced higher moments at 1.9 m from the simple support than at 2.5 m from the simple support. During the weekend it is to be expected that the strains measured in the more heavily loaded area reduce more, as more changes to the local equilibrium are made because of new cracks. As the strength of concrete is lower when the load is applied over a longer time, some of the local stresses are relieved over the weekend.

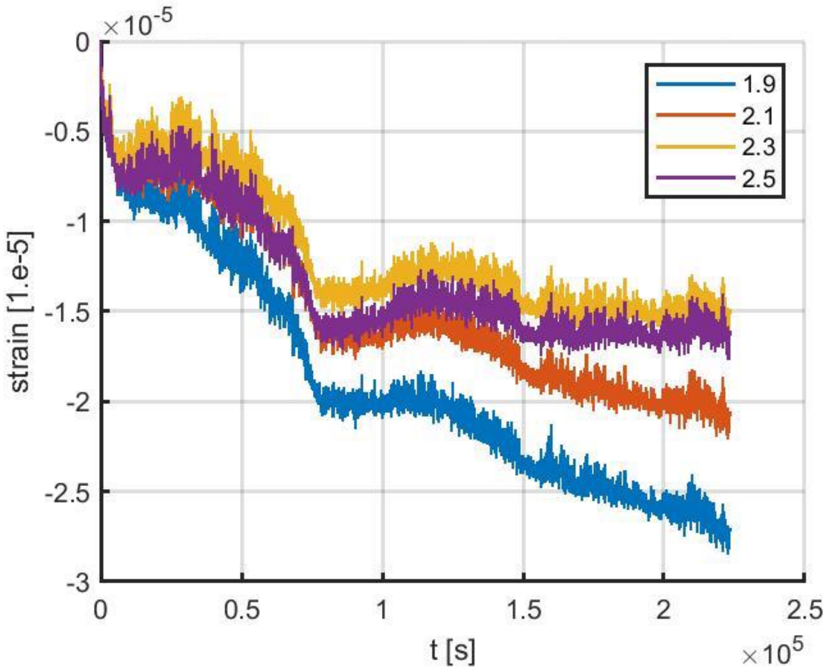

Figure 6.17: Typical result of creep test (middle line)

When the strains of a LVDT and an OF are compared during this creep test, it can be observed that the strain shifts of the OF and LVDT are approximately equal. Especially when the initial drop in the OF is set to zero in Figure 6.18. This initial drop is related to the temperature drop underneath the structure which is caused by shutting down the equipment after finishing the test on Friday.

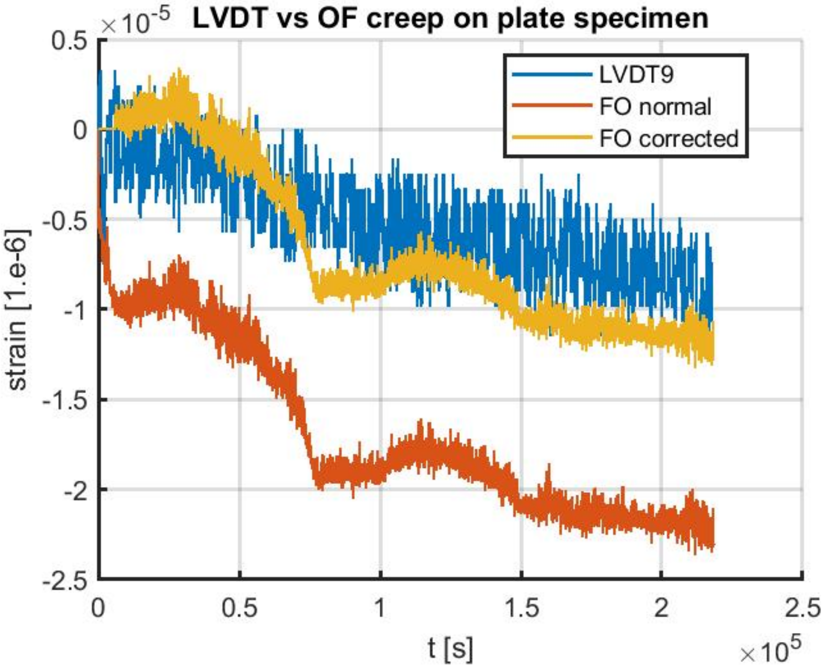

Figure 6.18: LVDT vs OF creep on slab specimen

6.4 Conclusion

Based on the above experimental program, glue 2 was used for gluing the anchor plates since it was more than capable of carrying the maximum force, and it is the stiffest glue. The possible time effects during constant loading are known, and can be compensated for if needed. Comparison of FO and LVDTs on beams suggest a general measuring difference of maximum 15%. These measurements were not taken at exactly the same location, which could also cause a difference. Comparisons on the slab lead to bigger differences between OF and LVDT. With help of a creep test, the time effect was excluded. When zooming in on the comparison areas, it turns out that some cracks cross the LVDT under a different angle. In addition, at some points the LVDT measured another number of cracks. This is a possible explanation of the difference. The inhomogeneity of the concrete leads to differences in measurements close to each other.

The milling of a slot and the sandblasting of a rebar are not significant to the performance of the rebar. Strains in the reinforcement can be measured up until the yielding strain, since the glue cracks after yielding. The results after that point are probably inaccurate.

7 Experiments with the developed fiber optical measurement system

In this chapter the results of the experiments on the half scale slab bridge are presented. As described in Chapter 2, the specimen is subjected to several tests. The main variable in these tests is the loading position. In contrary to the expectations, the first experiment (SR1M1) resulted in flexure induced punching failure. Therefore the loading positions on the subsequent tests were adjusted. Optic fiber measurements were performed on experiments SR1M1, SR1E2 and SR1E3. The loading positions on SR1E1 and SR1E4 did not show meaningful results on the OF sensors because of the loading position. First the application of the design method from Chapter 6 is applied to the specimen. Second, an overview of the measured material properties and experiment results are given. In subsequent sections these results are interpreted with help of theoretical approaches and the stop criteria are evaluated.

7.1 Application of the design to the Delft university of technology experimental program

To gather data with a FO measurement system for a proof load test, the proposed design recommendations from Chapter 6 are applied to the half-scale proof load test as elaborated on in Chapter 2. This section elaborates on the slab-specific design choices which were influenced by the specimen properties, but also by limited availability of sensors.

7.1.1 Gauge length

The gauge length applied in the measuring system is determined by the availability of sensors within Fugro. The feasibility of the available sensors are checked by maximum and minimum values for strain, cracking distance and practical recommendations. The system should comply to the following points:

- The maximum calibrated strain of the available sensors is 7500 $\mu\varepsilon$, strains of interest should not be higher than that value. The strain of interest is the characteristic value of the maximum crack width(1.43 mm)(Appendix A).
- The initial crack is determined to be ≈ 0.03 mm. The sensor system should be able to measure this.

The developed system provides the best results if each gauge length measures exactly one crack. However, considering that the maximum strain will probably be the limiting factor, one could opt for optimizing the amount of measured strain. Following Figure 3.6, not all cracks are equally big. If every sensor would measure a maximum of one major crack, the design would be optimal in terms of measured strains. The design specimen has a theoretical major crack spacing of 204 mm. Within Fugro, sensors with gauge lengths of 150 mm, 200 mm and 250 mm are available. The precision of these sensors is approximately 1 $\mu\varepsilon$. In Table 7.1 the 3 options are evaluated.

Table 7.1: Gauge length

Gauge length [mm]	150	200	250
Maximum crack width (1.43 mm) leads to the following strain	**9585**	**7189**	**5751**
Error percentage based on Minimum crack width (0.03 mm)	0.46 %	0.62 %	0.78 %
Chance of having two major cracks within gauge length	**low**	**moderate**	**high**

From this comparison can be concluded that the best option is to have a gauge length of 200 mm. The available sensors with this spacing have 4 sensors on one fiber.

7.1.2 Geometry

The spacing in between the connection points to the structure is known. The total length which can be measured can now be calculated. The number of external sensors is limited to approximately 50. Therefore, the total length which can be measured is 50 x 200 mm = 10.000 mm. Since within the current design, the sensors are not able to cross each other, three lines of measurement are possible on the bottom side of the concrete. The following question is where to place the strings of optical fibers onto the concrete. The slab will be loaded in the middle of the width. This is the first location for one of the measuring lines. The following points are considered in the placing of these further two lines.

- The lines may not be next to each other, since it would disturb the DIC results.
- The slab is expected to fail in shear at a loading position of a = 800 mm. This gives an effective width of 1900 mm. It would be interesting to see how strains develop within this effective width.
- The results are expected to be approximately symmetrical over the width, with the loading point as symmetry axis. Therefore, measuring on one side of the load would give more information about the strain distributions.

To get a clear view on how strains develop within the effective width, it is proposed to place one line at the outer boundary of the effective width, 1900 / 2 = 950 mm from the middle point. This line can then also be used as a measurement point of the flexural stop criteria as proposed in Section 6.2.3. To see how the stresses distribute in between the line of the load and the outer boundary, the other line is placed in the middle between these lines. The measurements will be verified by OF measurements within the reinforcing steel. Therefore, the exact position of the sensors is changed to the closest reinforcing bar, from the position determined above. Since one anchor point needs to hold the end of one fiber, and hold the starting point of one other fiber, a slight jump in the width direction is introduced of 58 mm. This ensures that both the fibers have the same anchoring point, and results can be interpreted as such. A drawing of the final setup can be seen in Figure 7.1.

The applied sensors for this project have a wavelength spacing of 2.5 - 3 nm. The sensitivity of the used fibers is 788 $\mu\varepsilon/$nm. This means that a change in strain can be observed up untill 2000 $\mu\varepsilon$ before the wavelengths start to overlap. If higher strains occurred, the measurement was stopped, the bandwidth declared to a specific FBG was manually changed, and then the measurement could continue. This is however very unpractical with a high amount of sensors. A full overview of all the sensors and base wavelengths can be found in Appendix D.

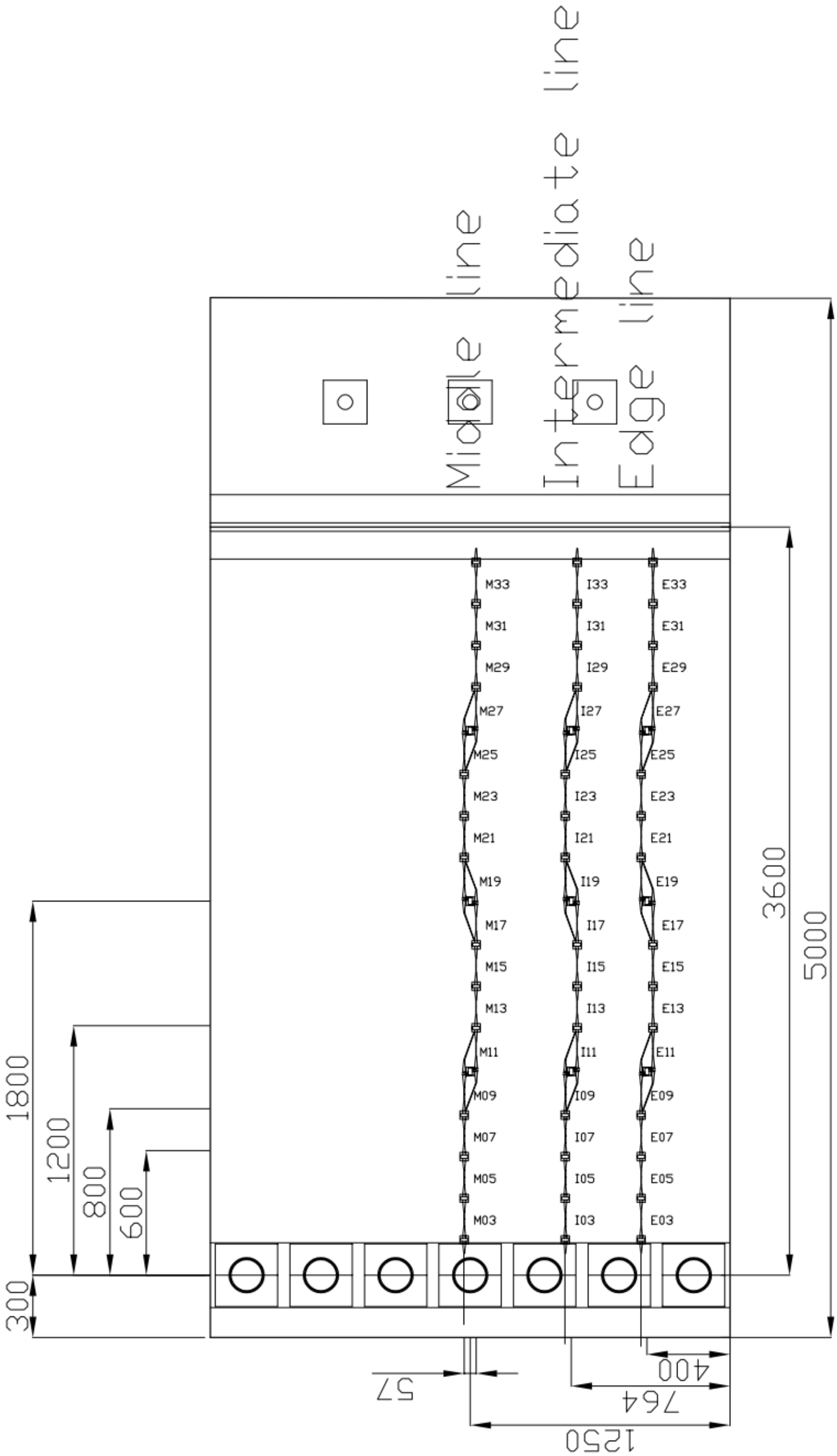

Figure 7.1: Final design of the sensors

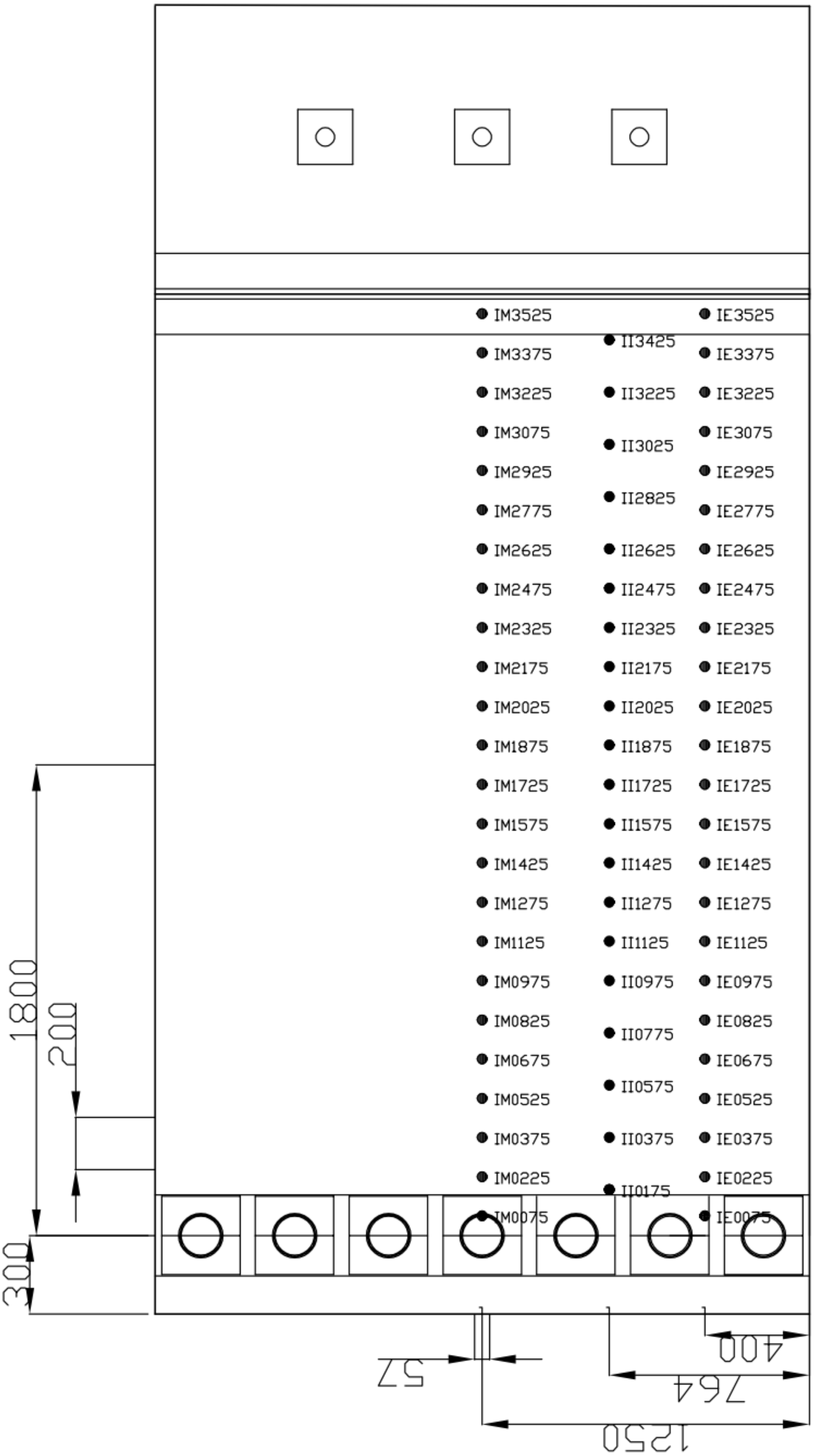

Figure 7.2: All internal sensor locations

7.1.3 Internal sensors

Following the protocol described in Section 6.2.4, three longitudinal bottom reinforcement bars were prepared with FBG sensors. The sensors are located every 150 mm. The reinforcement bars are placed in the reinforcement cage before casting. The bars are located at the same location as the external sensors. An overview of all the internal sensor locations is given in Figure 7.2.

7.1.4 Sensor names

As can be observed in Figures 7.1 and 7.2, there is logic in naming the sensors. All sensors on the middle line, contain an M in the sensor name, all sensors on the intermediate line contain an I in the sensor name, and all sensors on the edge line contain an E in the sensor name.

All external sensors' names consist of one letter and a two number digit. This digit is the distance from the simple support in decimetres.

All internal sensors' names consist of two letters and a four number digit. All internal sensors have an I in front of the letter which indicates the line on which the sensor is on. The four number digit is the distance of the sensor from the simple support in mm.

7.1.5 Practical application of the sensor system

If the optical fibers are not applied in a perfectly straight line, tensioning them will cause the angle between the anchor points to form a narrow curve. This can lead to loss of signal, or even failure of the optical fiber. Thus, it is very important to align the anchor points in a perfectly straight line. To ensure a straight line between the anchor points, a poisoning tool (Figure 7.3) was developed. This positioning tool can be used to determine the exact location of the anchor. Additionally, a plate can be screwed on the positioning tool, to ensure pressure onto the gluing plate during the hardening of the glue (24 h). The positioning tool can be clamped to the bridge by struts. In Figure 7.3 two pictures of the positioning tool are shown. Around the edges of the gluing location, Teflon and grease is applied to prevent the glue from bonding to the positioning tool.

Figure 7.3: Pictures of the positioning tool

The total measurement setup involved 21 fiber optic cables. These are each connected to an interrogation channel. As each interrogator has 4 channels, 6 interrogators were combined to form the measurement system as shown in Figure 7.4

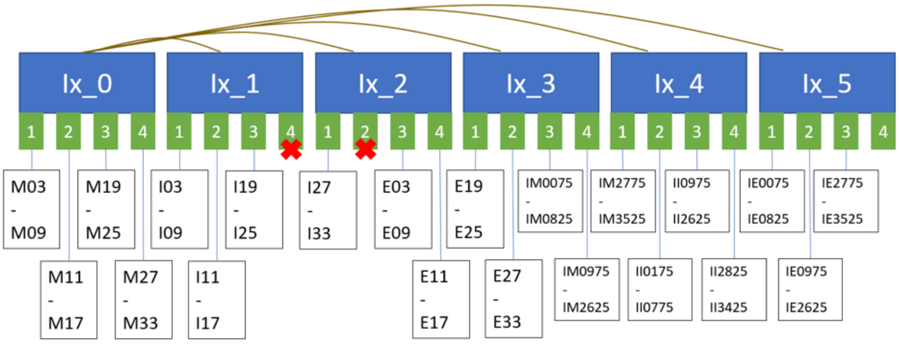

Figure 7.4: Interrogator configuration to sensors

To make sure that the system measures accurately from the start, some minor pretension was applied by screwing the threated anchor a bit more while watching the reflecting wavelengths from the sensor. The applied pretension is approximately 0.5 nm

7.2 Description of the experiments

This section provides more details on the performed tests. An overview of the loading positions, and accompanying test numbers are presented in Figure 7.5.

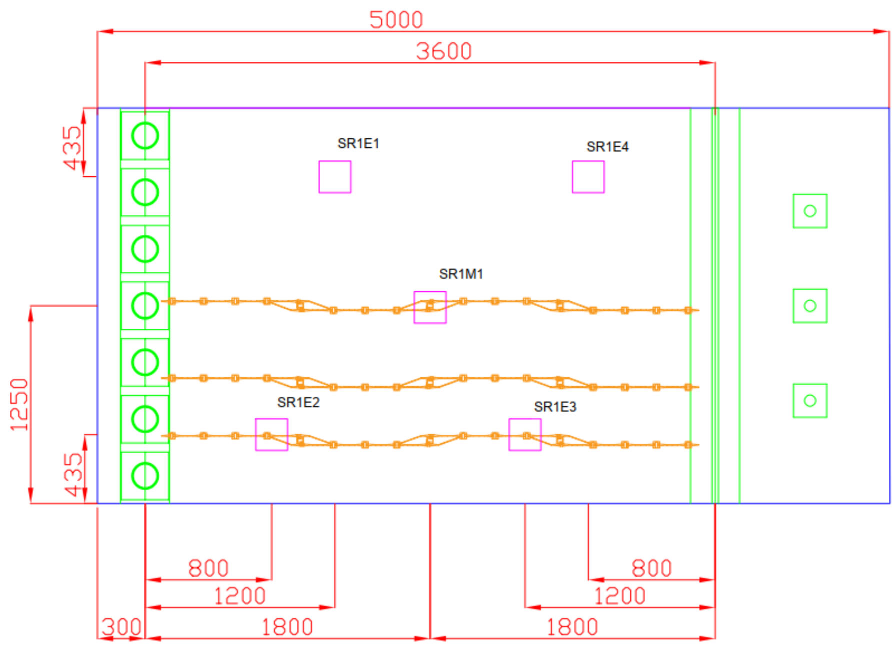

Figure 7.5: Final loading positions

7.2.1 Material properties

The specimen was cast on 01-10-2020. Concrete cubes were tested to follow the strength development over time. The average cube compressive strength at 28 days was 51.74 MPa. The experiments on the slab started on day 115 after casting. By then, the mean cube compressive strength has increased up to 58.73 MPa. The development of the strength is shown in Figure 7.6.

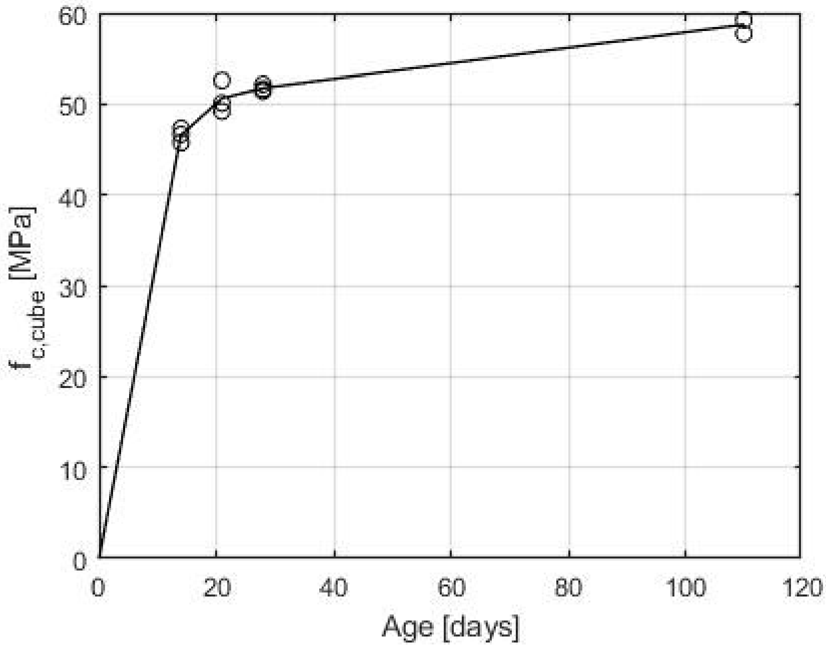

Figure 7.6: Cube compressive strength development over time [66]

The steel material properties can be deduced from Appendix B. The mean yielding stress is 585 N/mm^2.

7.2.2 SR1M1

Experiment SR1M1 was performed on 19-01-2021. The loading protocol is shown in Figure 7.7. The load-deflection diagram is shown in Figure 7.8. Internal sensors indicated yielding of the reinforcement around 900 kN. At 1125 kN, the slab failed in flexure induced punching failure. The final failure can be seen in Figure 7.9.

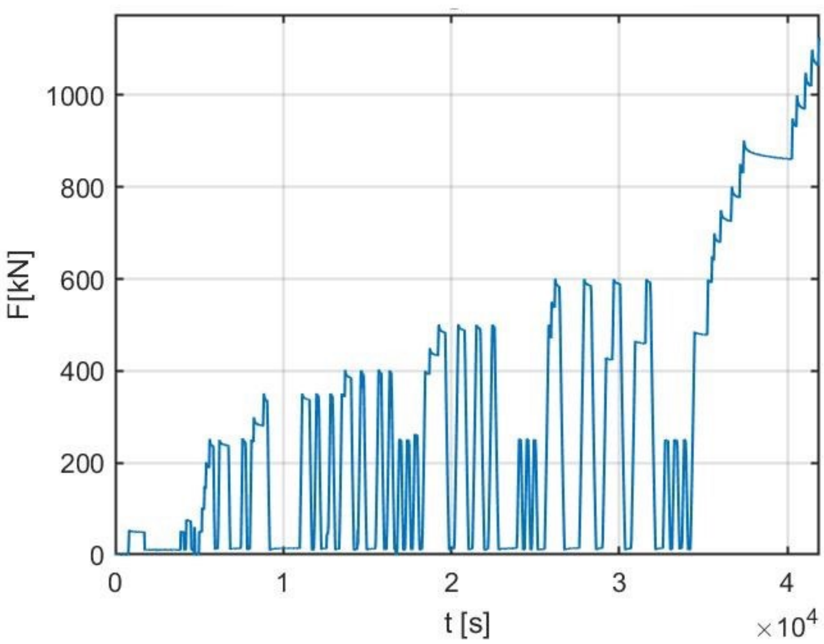

Figure 7.7: Loading protocol SR1M1

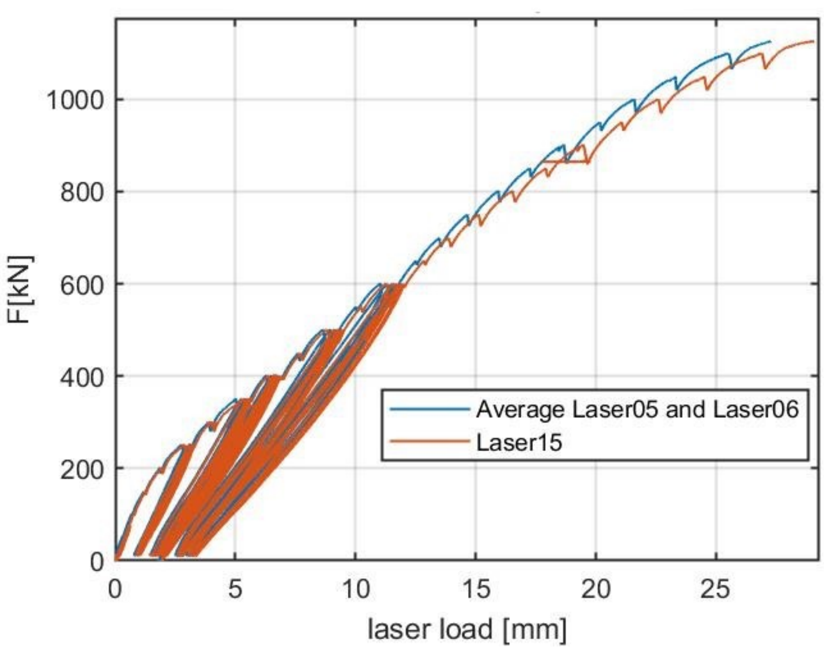

Figure 7.8: Load deflection diagram SR1M1

Figure 7.9: DIC image of flexure induced punching failure of SR1M1

7.2.3 S1E2

Experiment S1E2 was performed on 16-02-2021. The loading protocol is shown in Figure 7.10. The load-deflection diagram is shown in Figure 7.11. At 726 kN, a shear crack developed and the slab failed in shear. The final failure can be seen in Figure 7.12.

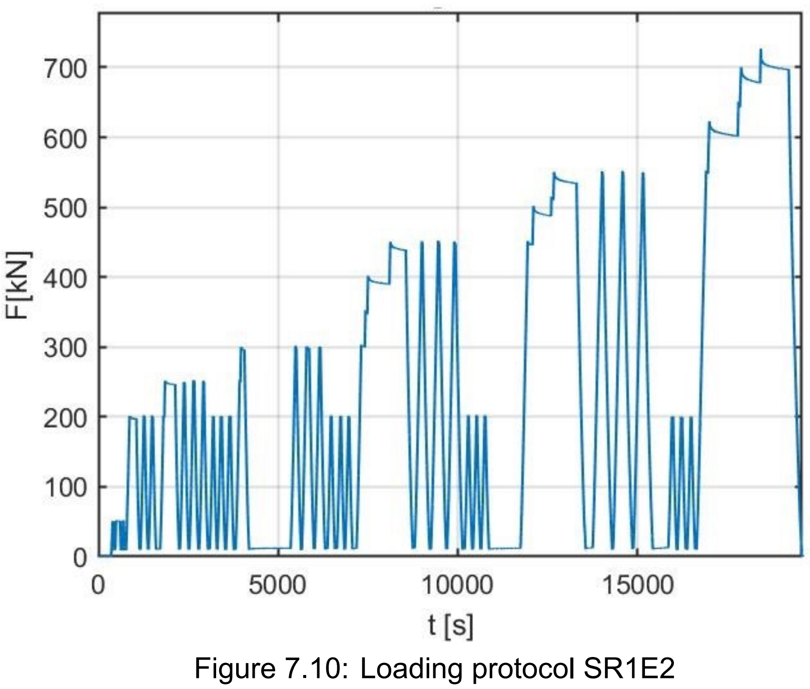

Figure 7.10: Loading protocol SR1E2

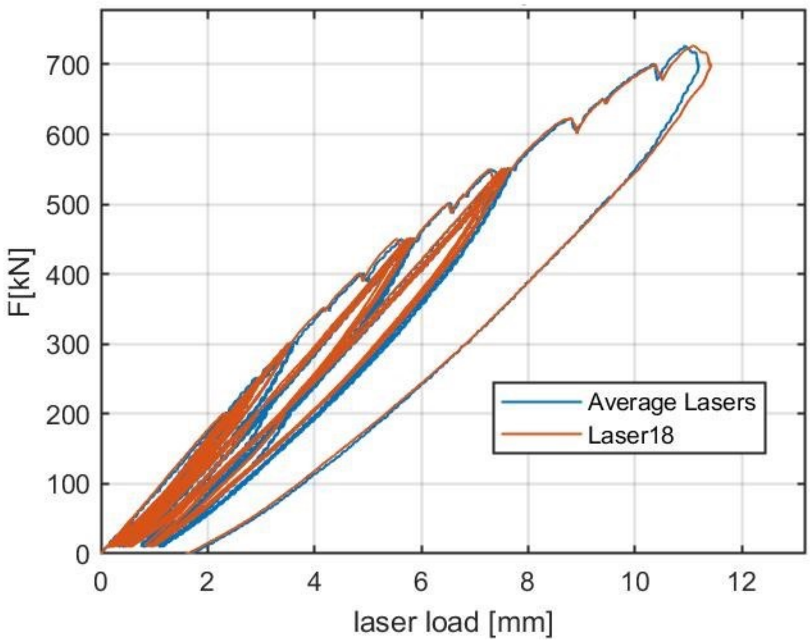

Figure 7.11: Load deflection diagram SR1E2

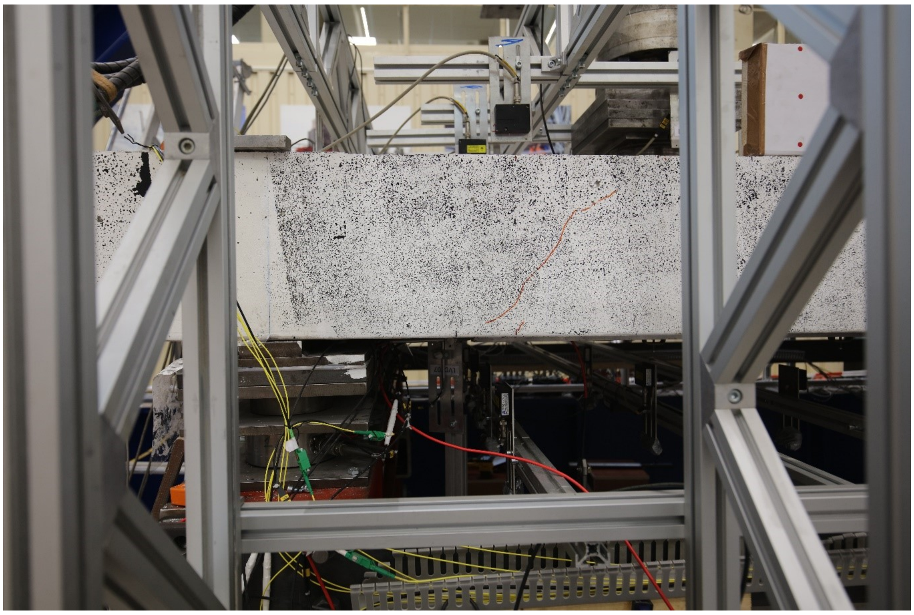
Figure 7.12: Picture of shear crack S1E2

7.2.4 S1E3

Experiment S1E3 was performed on 05-03-2021. The loading protocol is shown in Figure 7.13. The load-deflection diagram is shown in Figure 7.14. At 624 kN, a shear crack developed and the loading was stopped. The shear crack can be seen in Figure 7.15.

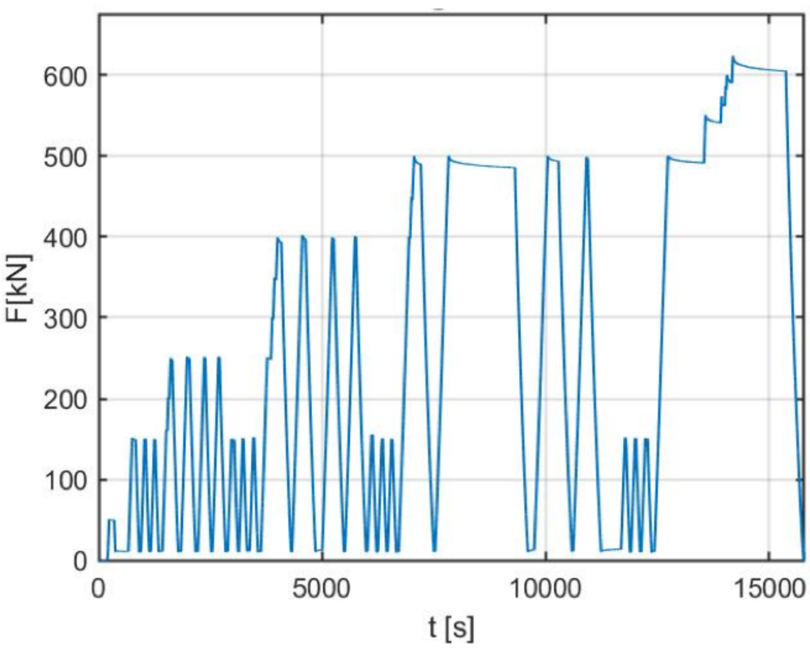

Figure 7.13: Load protocol SR1E3

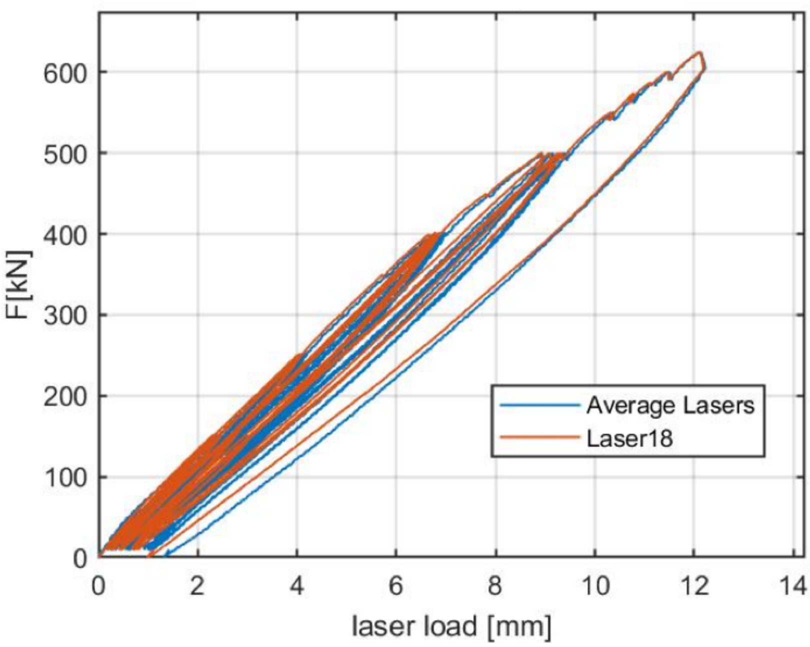

Figure 7.14: Load deflection diagram SE1E3

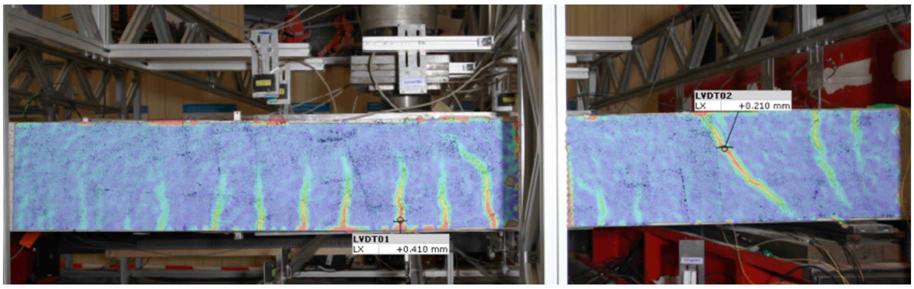

Figure 7.15: Failure of S1E3

7.3 Evaluation of the cracking indicator

For an uncracked specimen (SR1M1), the measurement system provides the possibility to locate the formation of cracks within the concrete. This section elaborates on the theoretical background of crack detection and shows the performance of the measurement system during the first stages of SR1M1 by comparing the results to DIC measurements.

7.3.1 Theoretical approach of measuring cracking by averaged strain measurements

As the measuring method averages the strain result on the bottom side of the specimen, and is not in direct contact with the surface, the characteristic infinite strain cannot be measured at cracking location. Hence, a more theoretical approach is needed to find a value on which it can be assumed that the concrete has cracked.

Following the tensile tie model, the initiation of a crack happens when the concrete reaches the cracking strain. Generally the initiation causes a sudden increase in the measured strain. Therefore, the cracking strain can serve as an indicator value for cracks. Dependent on the specific application, one can choose for a characteristic or an average value for the tensile strength of concrete. For applications in bending, it is proposed to use the flexural bending strength, as the inhomogeneity of the concrete leads to a lower strength with axial forces. The indicator value should be reduced by the strain present in the structure because of the self-weight. The limit value can be determined by Equation (7.1)

$$\varepsilon_{cr} = \frac{f_{ctm;fl}}{E_{c,m}} - \varepsilon_{sw} \tag{7.1}$$

Since the difference between the characteristic value for concrete tensile strength and the average tensile strength is 30%, the results compared to this indicator are expected to show quite some scatter, as the formulation cannot be more accurate as the scatter is in concrete itself.

7.3.2 Application of the cracking indicator

By calculation from Eurocode NEN-EN 1992-1-1 the flexural mean tensile strength of the concrete $f_{ctm,fl} = 4.62N/mm^2$ as the concrete cube compressive strength of the lab specimen is 58.73N/mm2. Since the ε_{sw} is dependent on the location on the span, the indicator for the slab experiment varies over the length of the slab. The ε_{sw} is calculated in Appendix A.

7.3.3 Comparison of the crack indicator with DIC results

As DIC is proven to be an accurate method to identify cracks, the strain results with indicator are compared with DIC results for experiment SR1M1. As the DIC did not cover the whole slab, the comparison is presented for the sensors within the grey shaded area in Figure 7.16.

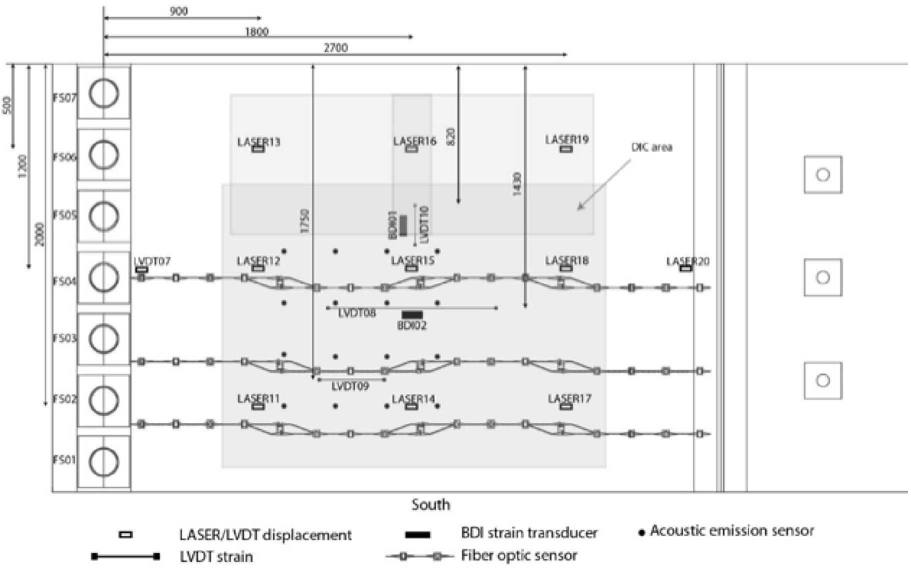

Figure 7.16: DIC range [66]

DIC pictures were taken every load increment of 50 kN. The visual comparison between DIC and the indicator with FO strains is given in Figures 7.17 to 7.19. For clear comparison, The DIC picture is cropped, so only the comparison results remain on the picture. The bar chart is located such that the strain at the chart location is located above the same segment in the DIC picture. A crack in the DIC picture can be identified by green/yellow/red lines. The cracking indicator is shown as a blue line in the bar chart. In Figure 7.17 no cracks can be detected on the DIC picture and the cracking limit is not reached in any of the sections. In Figure 7.18 the first cracks start to become visible on the DIC picture and the cracking limit is reached in two sections. There are two sections which are close to the cracking limit. In one section there is a crack, and in the other section there is no crack. In Figure 7.19 the most sections are already cracked, and this can also be seen by the bar charts which exceed the cracking limit.

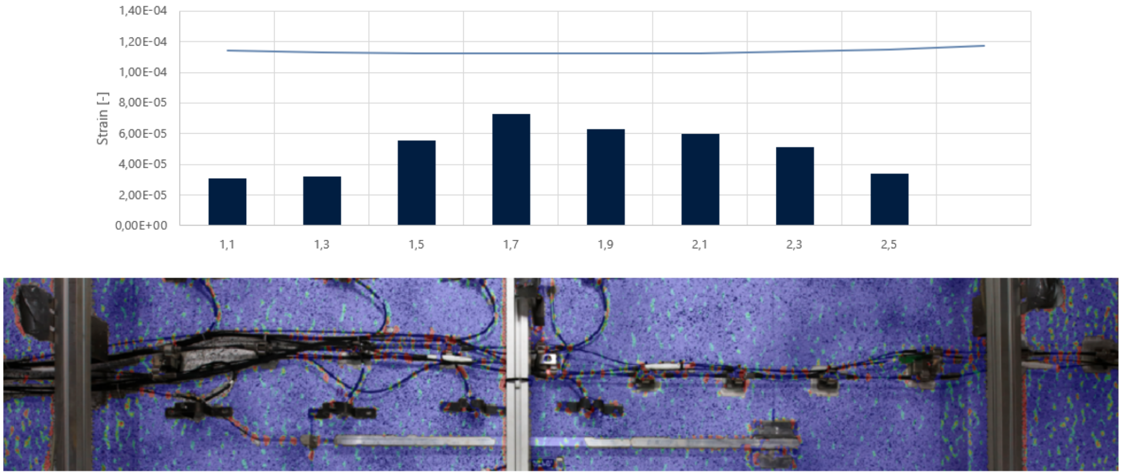

Figure 7.17: Strains at 100 kN

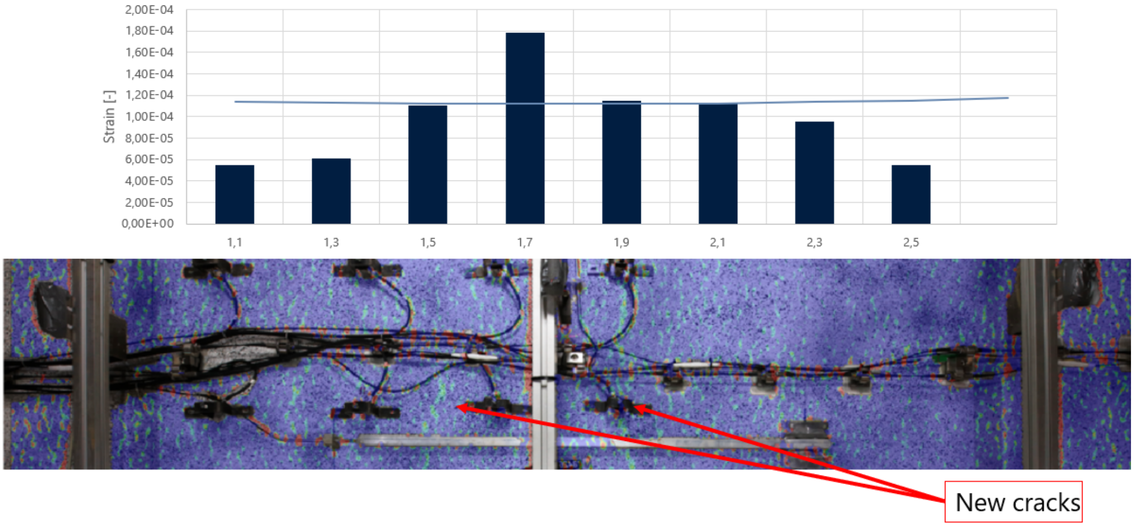

Figure 7.18: Strains at 150 kN

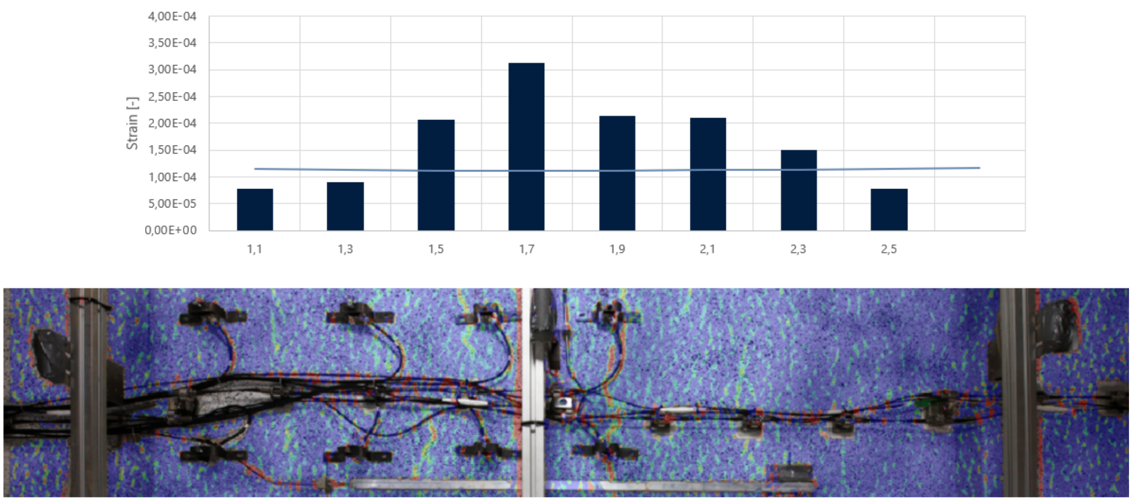

Figure 7.19: Strains at 200 kN

A comparison for all sensors within the DIC range which cracked before 200 kN, is provided in Table 7.2. In column two and three, the load level at cracking is noted down. If cracking is observed with both measuring methods, the same load level is provided in both columns. If only one of the two methods indicates cracking, in column 5, the difference between the strain measurement and the cracking indicator is given. The sign ”-” indicates that no cracking occurred during the analyzed loadsteps. For locations M17, I17 and E17 the installation of other sensors made it impossible for the DIC measurement to determine if any cracks were present. Hance, a NaN value is presented for those locations.

The first crack in the concrete is also confirmed by the internal steel strains measured by the internal sensors. In Figure 7.20, the measured steel strains are compared to an expected value by linear elastic calculation. it can be seen that the linear elastic strains are exceeded at 1.575 m from the support. This corresponds to the result from the external sensors in Figure 7.18

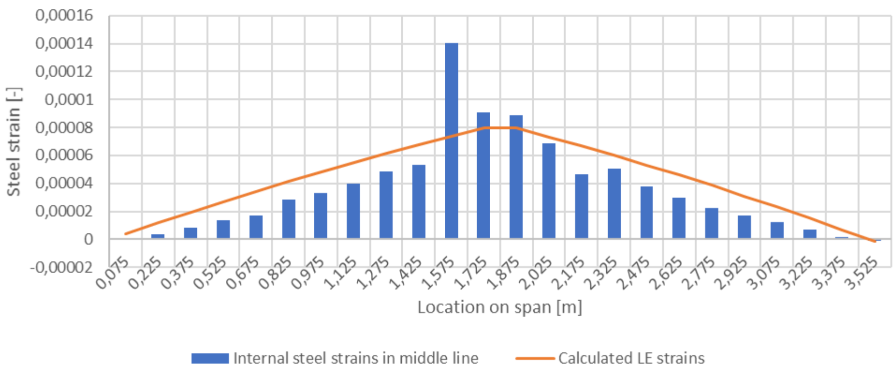

Figure 7.20: Steel strains at 150 kN during SR1M1

It can be concluded from these results that this cracking indicator performs extremely well. For all considered sensors only one has a noticeable difference between the cracking indicator and the actual cracking point measured by DIC.

7.4 Flexural stop criteria

In Figure 7.21, the critical reinforcement strains are plotted for the 3 rebars equipped with FO measurements. It can be observed that the middle rebar started yielding at 831 kN, the intermediate rebar at 982 kN and the edge rebar at 1115 kN. From this it can be concluded that the results can be used to check the performance of the flexural stop criteria since these stop criteria should prevent yielding of the reinforcement.

Table 7.2: Results of cracking indicator

Sensor number	Cracking load DIC [kN]	Cracking load OF [kN]	Match	Difference [%]
M11	-	-	yes	
M13	-	-	yes	
M15	150		no	-2%
M17	NaN	150	NaN	
M19	150	150	yes	
M21	200	200	yes	
M23		200	no	30%
M25	-	-	yes	
I11	-	-	yes	
I13	200	200	yes	
I15	150	150	yes	
I17	NaN	200	yes	
I19	150	150	yes	
I21	200	200	yes	
I23	200	200	yes	
I25	-	-	yes	
E11	200	200	yes	
E13	200	200	yes	
E15	150	150	yes	
E17	NaN	200	NaN	
E19	150	150	yes	
E21	200	200	yes	
E23	200	200	yes	
E25	-	-	yes	

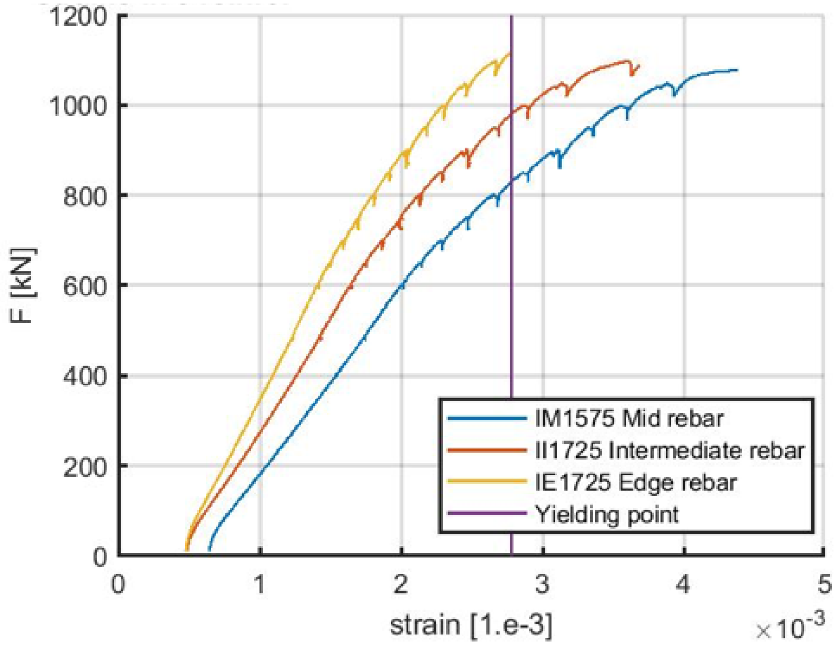

Figure 7.21: Reinforcement strains during failure part of SR1M1

7.4.1 Interpretation of the FO results

In Figure 7.22, results of the middle sensors of all lines are shown during SR1M1. A remarkable thing about these results is that the further away from the load the strains are measured, the more consistent the results get. This is because of spreading in the plate and because the results are less disrupted by the local point load.

As already pointed out in Section 5.2, the bridge must yield over the full width before it fails to flexural failure. Hence, it is proposed to measure the stop criterion at 2.5h in transversal direction away from the load. An additional benefit from this approach can be observed. The results become consistent, so that the gauge length has less influence on the measurement. This observation is emphasized by the internal steel strain results at 600 kN (Figure 7.23).

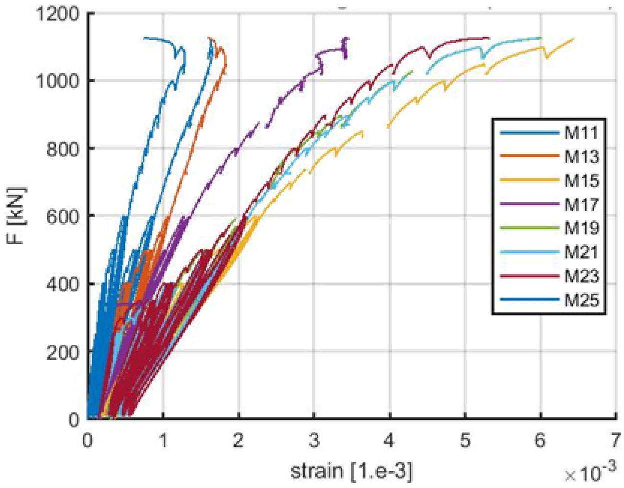

(a) Sensors M11-M25 during flexural test (middle line)

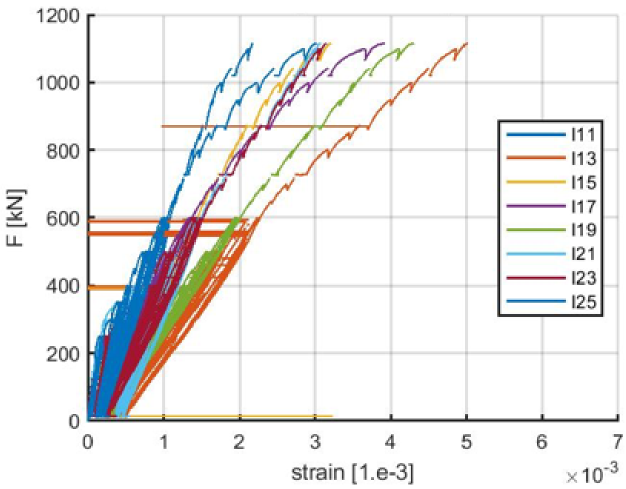

(b) Sensors I11-I25 during flexural test (intermediate line)

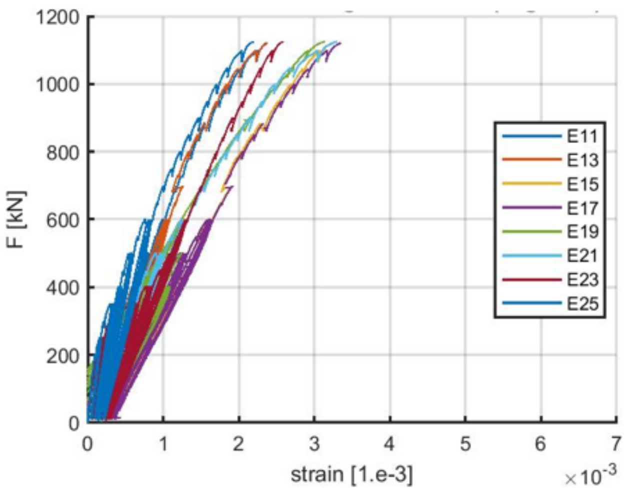

(c) Sensors E11-E25 during flexural test (edge line)

Figure 7.22: Strain results during SR1M1

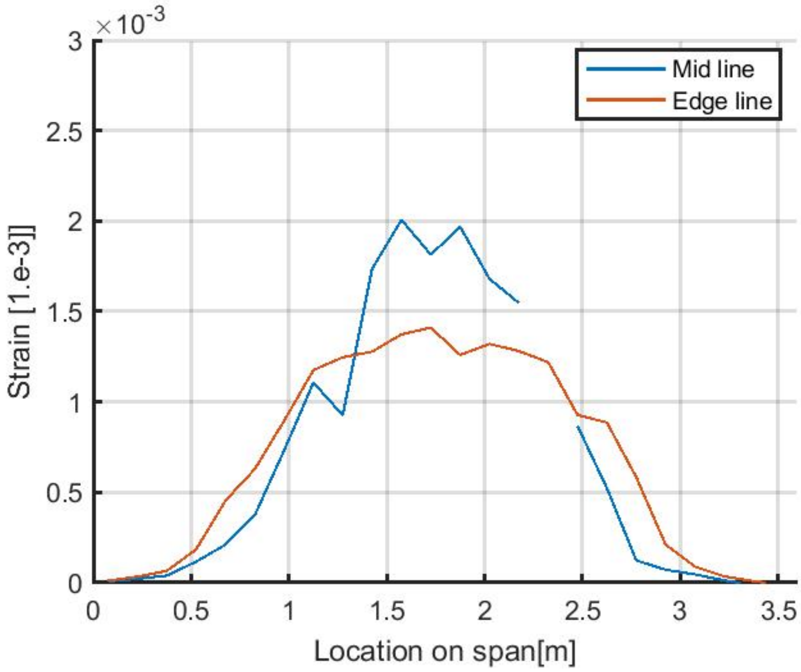

Figure 7.23: Internal strain during SR1M1 at 600kN

The steel strain results are approximately equal over more than 1 m length. Hence, If it is possible to find stop criteria for the location $2.5h$ from the load, there is less chance of missing the critical position as can happen with single sensors straight underneath the load. This benefit makes the total evaluation more safe, which can lead to a lower required safety factor on the stop criteria. Additionally, the decreasing influence of the gauge length can lead to optimizations in the sensor system itself, and make it easier to apply the same sensor to multiple projects.

Where, up till now, the stop criteria are mainly analyzed for beams, in this section an analysis on the performance of the stop criteria for concrete slabs loaded with concentrated loading is performed. One of the goals of stop criteria is to prevent plastic deformations such as yielding of the reinforcement. For beams, yielding of the reinforcement is often considered the failure point of the beam. Hence, to define the performance of a stop criterion, one can simply compare the point of reaching the stop criterion to the point of failure. The difference between these values is the safety of the method.

For slabs, yielding is still undesirable behavior. However, this point does not coincide with the failure of the slab. After initial yielding, decrease in local stiffness causes redistribution of stresses to occur. The stiffer parts start to carry more force. Hence, the total capacity of a concrete slab is generally much higher than the initial yielding point. Although this extra capacity reduces the chance of a collapse during a proof load test significantly, it is not a desirable stress state of the bridge because of the plastic deformations. Hence, it is important that the stop criteria prevent any yielding of the reinforcement. Therefore, the flexural stop criteria will be compared to the onset of yielding in the structure.

As many of the stop criteria currently have a theoretical basis for the development of the stop criterion, these stop criteria imply a relation between external measurements and the stress within the reinforcement. Since the results from laboratory testing provide measurements of the strain in the reinforcement, this relation can be checked. It is studied how well these relations approximate the stress state of the reinforcing steel. Especially near stop criteria levels, an error between the reinforcement stress and the approximation from external sensor is provided.

Since the sensors were not specifically ordered for this project, fiber optical sensors already available within Fugro were used to apply to this project. As calculated in chapter 7 the bandwidth of the available sensor is small for the high strain application. This caused the sensors to run out of boundaries above certain load levels. By stopping the measurement and resetting the boundaries, it is attempted to keep the measurements running. However, some of the peaks caused by running out of boundaries are still visible in the data. These spikes should be ignored as they will not be present when enough optical bandwidth is available.

Since the fiber is mounted 28 mm beneath the concrete surface, the measurement will be amplified by the rotations of the sections. Hence, the stop criterion for optical fiber should be slightly larger than the stop criterion for the LVDT, which is mounted 10 mm beneath the concrete surface, which is larger than a stop criterion measured on the concrete surface. To avoid multiple stop criteria, in all graphs presented in this chapter, the presented measurement will be factored to show an equivalent strain on the concrete surface, or at reinforcement level. This ensures a clear comparison between the various methods, as well as that for all methods the same stop criterion can be checked. The calculation is shown in Equation (7.2).

$$\varepsilon_{reinf;equivalent} = \frac{h-c}{d-c}\varepsilon_{c,bot} = \frac{h-c+a_m}{d-c}\varepsilon_{sensor} \tag{7.2}$$

7.4.2 Strain

The strain stop criterion for the slab is $2165\mu\varepsilon$ calculated by Equation (3.14). This stop criterion is checked in Figure 7.24 for measurements taken with LVDT and with a FO. The presented results are reduced by Equation (7.2), to account for the magnification of the measured value due to the distance between the slab and the measurement. It can be observed that the stop criterion is reached at 604 kN for the LVDT, and at 649 kN for the single optical fiber.

Section 7.4.2 gives a better insight in how the stop criterion actually performs, as the strain at the bottom of the concrete is converted to a fictitious reinforcement strain, using Equation (7.2). The main difference between Figure 7.25a and Figure 7.25b, is the presentation of the measured strain in the reinforcement by the OF. For Figure 7.25a the critical (one-sensor) measuring point is shown, while for Figure 7.25b the average steel strain over 1,05 m is shown. Since the stop criterion is based on $0.65 * \varepsilon_y = 0.65 * 0.002781 = 1808$ $\mu\varepsilon$, this line is also plotted in the graphs. It can be observed that especially at the $65\%\varepsilon_y$, the measurements from the LVDT, the FO in the reinforcement and the single external FO sensor are all on one line. The averaged FO measurement is a bit off. The explanation of this difference is presented in Figure 7.25b, as that graph shows that if the strain on the external sensors is averaged over a longer length, better results are obtained if the internal sensors are also averaged over a longer length.

LVDT08 is a sensor close to the presented fiber optical results. The slightly different location can explain the difference between the averaged optical fiber result and the result from the LVDT.

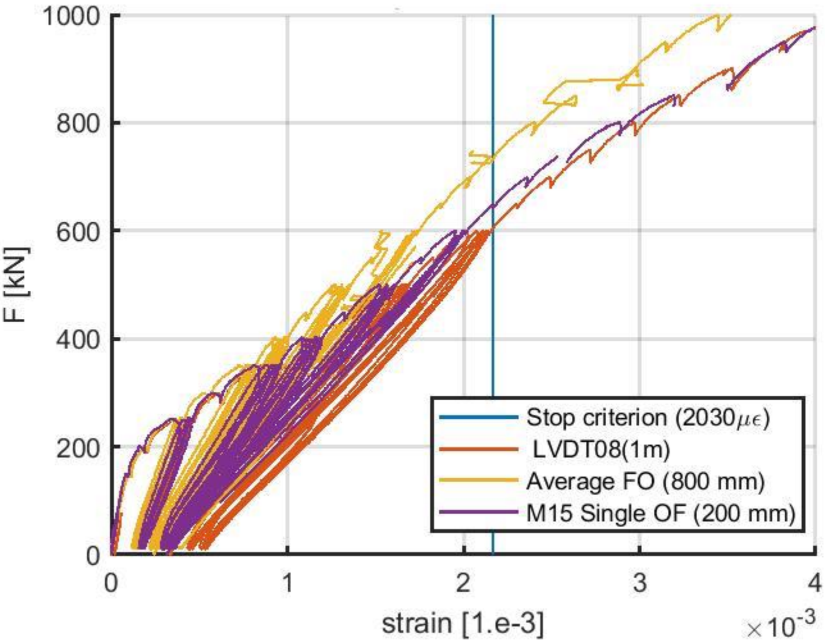

Figure 7.24: Evaluation of the flexural strain stop criterion for external measurements during SR1M1

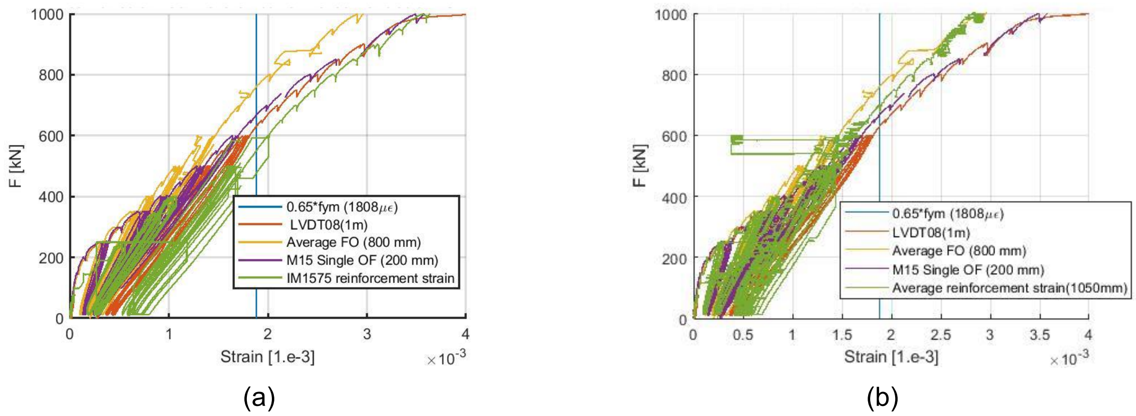

Figure 7.25: SR1M1 External strains converted to reinforcement strains compared to reinforcement strain in one sensor (a) and compared to the average of multiple reinforcement sensors (b)

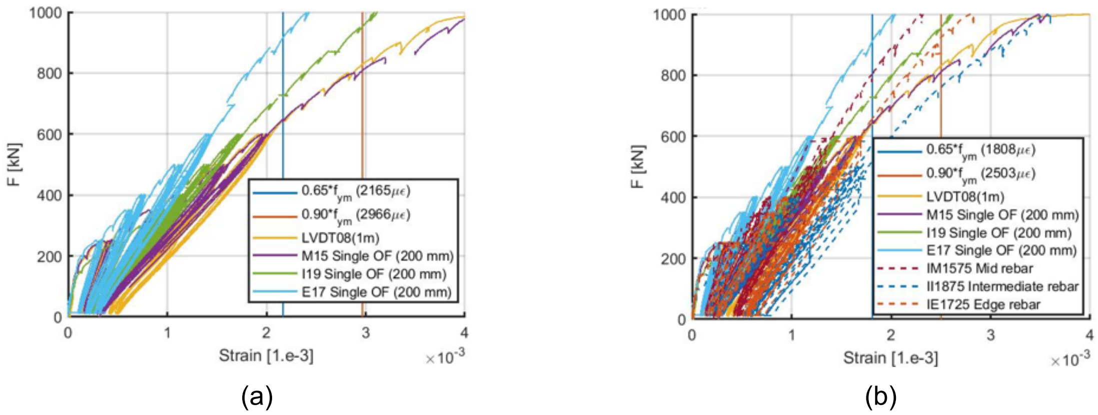

Figure 7.26: SR1M1 External strains compared to the 90% stop criterion adjustment at the bottom of the concrete level (a) and at the reinforcement level (b)

The adjustment made to this stop criterion in Chapter 5 seems to perform well. In Figure 7.26 the 90% value of the stop criterion is presented. For this test, this criterion was reached on 802 kN at sensor M15. Which is close to the actual yielding point. An overview of the comparisons at proposed stop criterion is given in Table 7.3. In the first column, it is shown at what load the stop criterion is violated. In the second column, this is compared to the initial yielding point (831 kN). In the third column, the reinforcement results are checked, and the force at which ideally the stop criterion should have warned following the theoretical approach is provided. In the fourth column, the difference between the achieved result and the ideal result is shown.

Measurement (stop criterion)	Force @ stop criterion	% of F_y	Force @ stop criterion reinforcement strain	Error
Mid line FO (65%)	649	78%	459	41%
LVDT08 (65%)	604	73%	459	32%
Intermediate line (65%)	726	87%	657	11%
Edge line (65%)	917	110%	800	15%
Mid line FO (90%)	802	97%	760	6%

Table 7.3: overview of the strain stop criterion results

From these results it can be observed that the 65% limit on the edge line provides an unsafe result in comparison to the onset of yielding. This indicates that the 2.5h distance of this sensor to make use of the redistribution is probably slightly too high. The intermediate line of sensors however, provides a safe result which does use a bit of the load spreading in the slab. The correctness of the result does increase when moving further away from the load. This might be the case because this is further away from the point load which gives a higher scatter in the results. Additionally, it is found that decreasing the applied safety to the stop criterion results in a high correctness of the steel stress calculation from the external sensors. Using a low safety to have a low error is also something [22] found success with.

7.4.3 Crack width

The sum of the crack width within one measuring segment, can be calculated by rewriting Equation (6.3), and implementing Equation (7.2) to get Equation (7.3).

$$\sum_{0}^{n} w_{cr} = \frac{h-c}{h-c+a_m} * \varepsilon_{sensor} * l_{gauge} \text{ for n is the number of cracks} \tag{7.3}$$

The first crack can be determined by the method described in Section 7.3.3. However, the second crack cannot be identified by studying OF results, thus an alternative method is necessary to determine number of cracks within one measuring segment.

For the examination of the experimental setup as presented in Chapter 2, the results from the DIC measurements were mostly able to identify the amount of cracks. In Figure 7.27 a DIC result from test SR1M1 is shown. In Table 7.4, the interpretation of the number of cracks is shown. Although DIC provides a very good insight on the cracking pattern, there are some blind spots because of the frame for the lasers and the limited angle of the camera. After the final test on the specimen, all measuring equipment was removed, to analyze the full slab with DIC while loaded. These results (Appendix E) show a combined cracking pattern from all executed tests on the specimen. Hence, not all cracks from SR1M1 could be counted accurately.

M03	M05	M07	M09	M11	M13	M15	M17	M19	M21	M23	M25	M27	M29	M31	M33
NaN	NaN	NaN	1	1	2	2	1	2	2	2	1	2	NaN	NaN	NaN
I03	I05	I07	I09	I11	I13	I15	I17	I19	I21	I23	I25	I27	I29	I31	I33
NaN	NaN	NaN	1	1	2	1,5	2	2	2	2	2	2	NaN	NaN	NaN
E03	E05	E07	E09	E11	E13	E15	E17	E19	E21	E23	E25	E27	E29	E31	E33
NaN	NaN	NaN	2	2	3	2	2	2	2	2	2	2	NaN	NaN	NaN

Table 7.4: number of cracks for each sensor during SR1M1

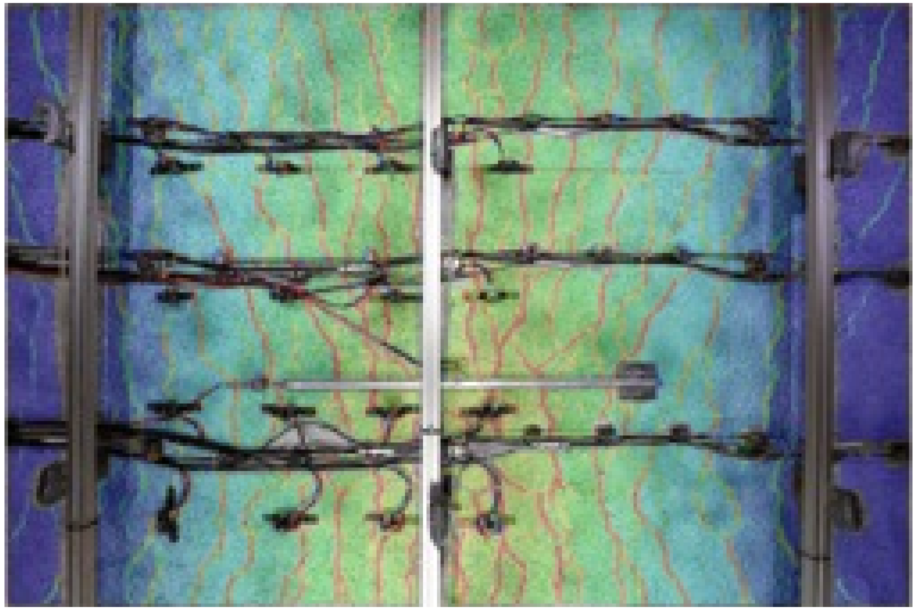

Figure 7.27: DIC result

To calculate the average crack width, the sum of the crack widths is divided by the number of cracks within the measuring segment. For multiple cracks, this will always be a underestimation of the actual crack width, as two cracks never have exactly the same width. In contrary, following the approach elaborated in Section 3.1.2, one of the cracks will definitely grow higher, and therefore it will also have a higher crack width.

The stop criterion for crack widths can be calculated by Equation (5.8) and is 0,28 mm. In Figure 7.28 some average crack widths at critical locations are plotted, and it can be seen that the stop criterion of 65% of the yielding strain is reached at 680 kN by sensor M17. However, since the distribution of the crack widths is not equal between the cracks, one other sensor might have reached the crack width at an earlier stage but this is not viable because of the averaged value.

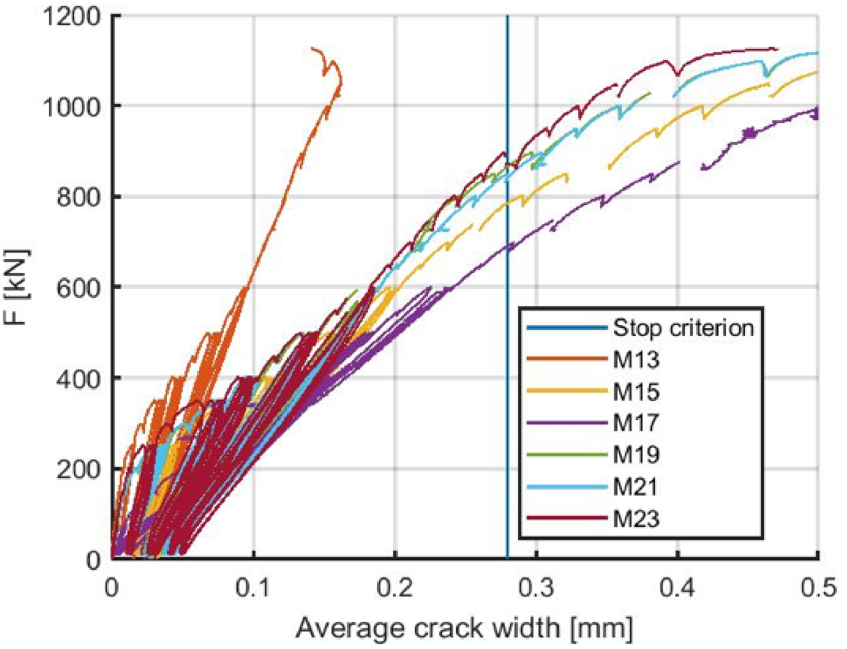

Figure 7.28: Crack widths for middle line

A better understanding of the error margin, mainly caused by the method of measuring the crack, can be obtained by analysing the measured external strains at the stop criterion. In Table 7.5, the force at 65% of the yielding strain measured within the internal sensors in the reinforcement is shown. At this force level, the values of the external sensors are provided. From this strain, the minimum and maximum crack width can be determined. These crack widths can then be compared to the stop criterion (0,28 mm). Hence, an error bandwidth is obtained in the final column. The results show that the crack widths might be a well performing stop criterion, when the number of cracks and the ratio between them are known. However, with the current measurement setup, these amount of errors cause that the results cannot be used for further analysis on the stop criteria. A lower error can be obtained by measuring one crack per gauge length or by adding information about the distribution of the crack widths among the gauge length.

Based on these results it would be wise to consider different cracking theories which use the distance between cracks as input. The input of the distance between the cracks can then be set as a fictitious length between the cracks, which can equal the gauge length.

	F at $0,65$ $*\varepsilon_y$[kN]	$\mu\varepsilon_{external}$ at loadlevel [-]	min. crack width [mm]	max. crack width [mm]	Error [%]
Mid line	517	1660/951	0,190	0,332	-32% - 18%
Intermediate	677	2226	0,222	0,445	-21% - 58%
Edge	800	1960	0,196	0,392	-30% - 39%

Table 7.5: results of error analysis crack width stop criterion

7.4.4 Sectional stiffness

Based on the formulation in Equation (5.6), the sectional stiffness has been monitored throughout experiment SR1M1. As taking the direct derivative of the measurement gives strange results due to the application of loadsteps and pauses, the stiffness is calculated for each load step. The sectional stiffness for several critical measuring segments on the measuring lines is shown in Figure 7.29.

In the results it can be seen that the sectional stiffness is continuously reducing for all sections. No big abnormalities occur during this decrease of stiffness. By looking at the repeated load level of 250 kN presented in Table 7.6, it can be observed that the sectional stiffness reduction can be considered permanent damage, as the stiffness at the repeated 250 kN approximately equals the lowest previous stiffness at a higher load level.

The stop criterion proposed in Chapter 5 does not provide any opportunity because of the ongoing decrease in stiffness. A typical stop criterion has a safety margin of 35%, so should ideally warn around $0.65\% * f_{ym}$. If a critical initial stiffness$(50$kN: $5.49 * 10^{-7})$ is compared to the value of the critical stiffness at $0.65\% * f_{ym}$ $(500$kN: $2.97 * 10^{-6})$, it can be observed that the stiffness decreased with a factor 6. Accounting for above consideration about permanent damage, this value is heavily dependent on previous load levels to the bridge. Hence, the amount of stiffness reduction compared to the initial stiffness does not provide a feasible stop criterion.

However, during proof load testing, it can be advantageous to know up till which level the structure has been loaded before the proof load testing. From above results it is to be expected that the sectional stiffness can help determine historical load levels. As a decrease of stiffness will only be observed at higher loads compared to historical loads.

7.4.5 Deformation profiles and 25% stiffness reduction

The deformation profiles for SR1M1 are monitored with laser deflection measurements. As deformation profiles is a qualitative stop criterion, abnormalities in the deformation profiles were searched. This is usually done by connecting the point measurements with lines, and to evaluate the changing angles of those lines in relation to the applied load. This process can be executed for SR1M1 based on Figure 7.30. However, for this test no abnormality was found, and the deformation profile stop criterion was not reached. Hence, no data can be gathered on the performance of optical fiber measurements on the stop criterion deformation profiles.

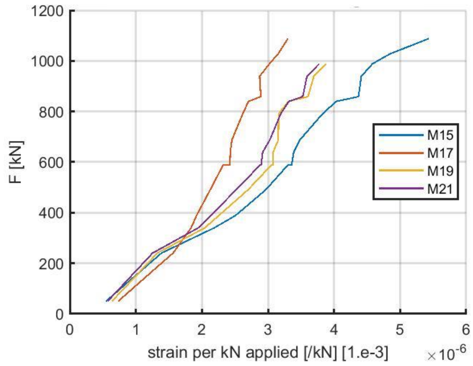

(a) Stiffness in middle line during SR1M1

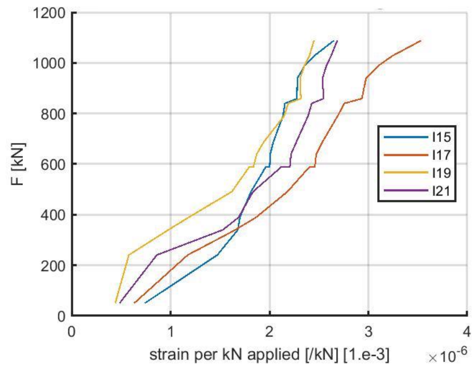

(b) Stiffness in intermediate line during SR1M1

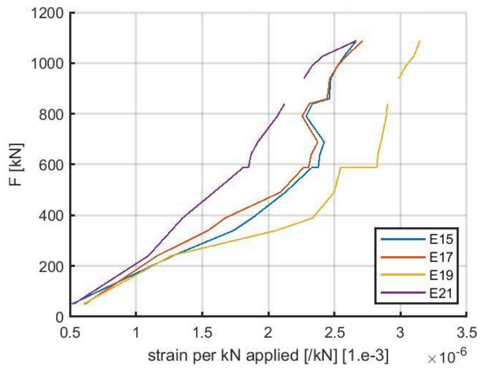

(c) Stiffness in edge line during SR1M1

Figure 7.29: Sectional stiffness for all FO measuring lines during SR1M1

Load level chronological	M15	M17	M19	M21
-50,157807	-5,5E-07	-7,3E-07	-6,4E-07	-5,7E-07
-240,6062503	-1,4E-06	-1,6E-06	-1,3E-06	-1,3E-06
-340,0813596	-2,2E-06	-1,8E-06	-2E-06	-1,9E-06
-389,2700793	-2,5E-06	-1,9E-06	-2,3E-06	-2,1E-06
-243,436912	-2,7E-06	-2E-06	-2,5E-06	-2,2E-06
-490,7364263	-3E-06	-2,1E-06	-2,7E-06	-2,5E-06
-241,4705743	-3E-06	-2,2E-06	-2,8E-06	-2,4E-06
-587,810968	-3,3E-06	-2,3E-06	-3E-06	-2,9E-06
-237,9268447	-2,8E-06	-2E-06	-2,8E-06	-2,2E-06
-588,345767	-3,4E-06	-2,4E-06	-3,1E-06	-2,9E-06
-639,168115	-3,4E-06	-2,4E-06	-3,1E-06	-2,9E-06
-688,434689	-3,5E-06	-2,5E-06	-3,2E-06	-3E-06
-790,468402	-3,8E-06	-2,6E-06	-3,2E-06	-3,2E-06
-839,799845	-4E-06	-2,7E-06	-3,3E-06	-3,3E-06
-858,858252	-4,4E-06	-2,9E-06	-3,6E-06	-3,5E-06
-939,046204	-4,4E-06	-2,9E-06	-3,7E-06	-3,6E-06
-988,831471	-4,6E-06	-3E-06	-3,9E-06	-3,8E-06
-1027,402102	-4,8E-06	-3,2E-06		
-1088,207591	-5,4E-06	-3,3E-06	-4,6E-06	-4,5E-06

Table 7.6: Sectional stiffness fore external sensors over chronological load steps

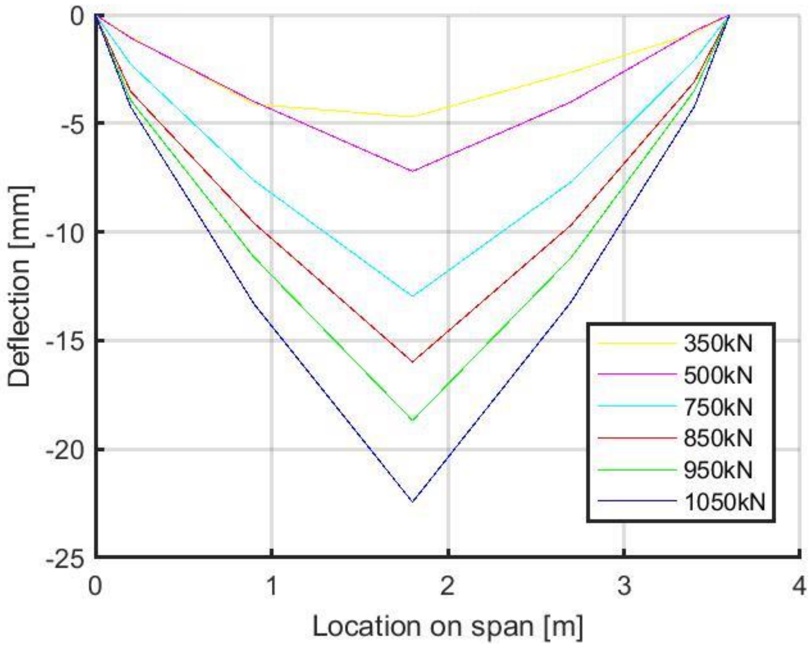

Figure 7.30: Longitudinal deflection profile from lasers

However, what can be examined is how accurate the deformation profile can be simulated by optical fibers. These deformation profiles can be calculated by using Section 5.1.6 The results of this calculation are shown in Figure 7.31. In this figure also the laser measurements are shown as markers to compare the profiles.

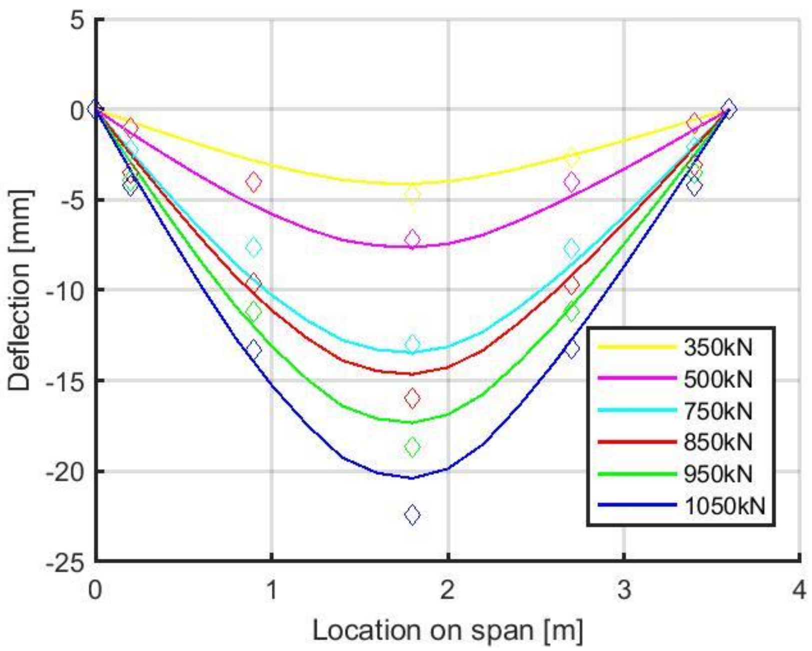

Figure 7.31: Longitudinal deflection profile from FO

From the results it can be seen that the deformation profiles are really close to the laser measurements which are represented by markers in the plot. The difference at midspan has a standard deviation of less then 7%. Hence, this method of integration might be used to calculate live deflection of the slab.

Since the external sensors can be used to calculate the deflection, the same result can also be used to determine the reduction in stiffness. However, for evaluation of this stop criterion, the results from the lasers is used.

In Figure 7.32, for each load step the stiffness is calculated. The graph shows that the stiffness is continuously decreasing, and does not reach any plateau at which it stays constant. When lower load levels are repeated, it is found that the stiffness stays equal to the stiffness observed at the highest load up until that point.Hence, when a structure has been loaded up until a certain point in the past, up until this point the stiffness will remain the same. The stiffness starts to change beyond this point. Considering these results it is likely that the stop criterion is triggered when the load onto the structure is increased further than historical loads.

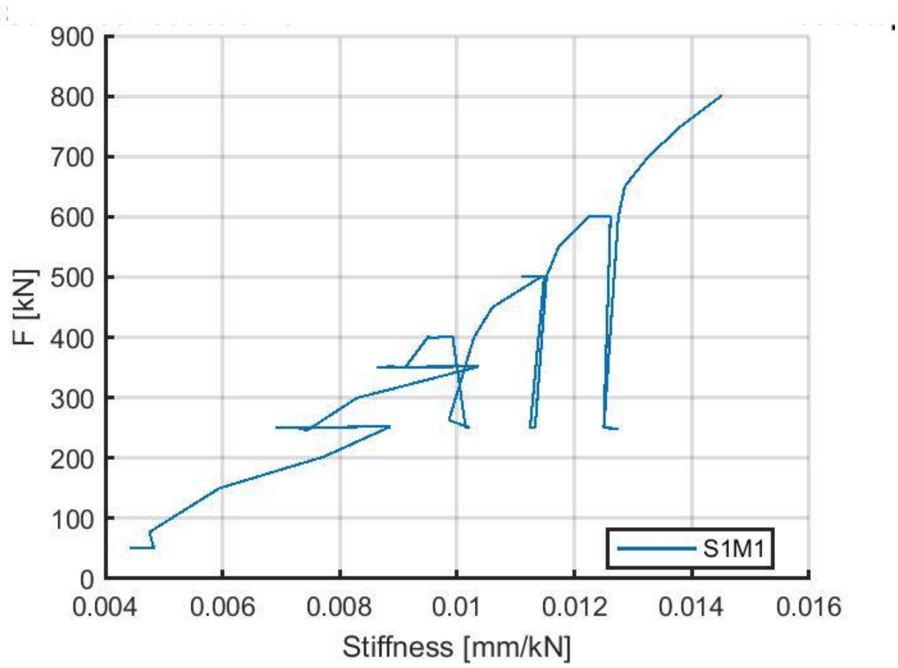

Figure 7.32: Stiffness measurement on SR1M1

7.5 Flexure induced punching with CSCT for punching shear

As the first experiment failed in flexure induced punching failure, the results of this test are compared to the critical shear crack theory for punching. The CSCT limit can be determined by using the properties of the slab and calculated with Equation (3.12).

7.5.1 Rotation results

For the slabs used to derive the CSCT, the measured rotations are added up between the loading point and the measuring point. From calculation follows that the measurement points (inclinometers) used to derive the CSCT, are located around the support line at approximately 6.5*d to 7*d. As for the slab in this study the load is placed at 6,8*d from the support, it is comparable to measure the rotation above the support. With the current sensor layout, two methods are available to determine the rotation above the support. With help of the integrations shown in Section 5.1.6, the deformation profile and slab rotations can be calculated from the external optical fibers. The rotation can also be determined by combining the deflection laser above, and very close to the support to deduce the angle. In addition to this approach, the rotation of the actual shear crack can be measured based on the approach shown in Section 5.1.6. This can be done by taking the external sensors, and by taking the internal sensors. All four results are shown in Figure 7.33 and plotted against the CSCT limit.

The angle in transversal direction is not specifically measured. The method to derive the angle is by using the deflection at 3 points (from lasers) in transversal direction and assuming a parabolical shape of deflection in transversal direction. This parabolical shape then leads to an angle. The development of the angle is shown in Figure 7.34

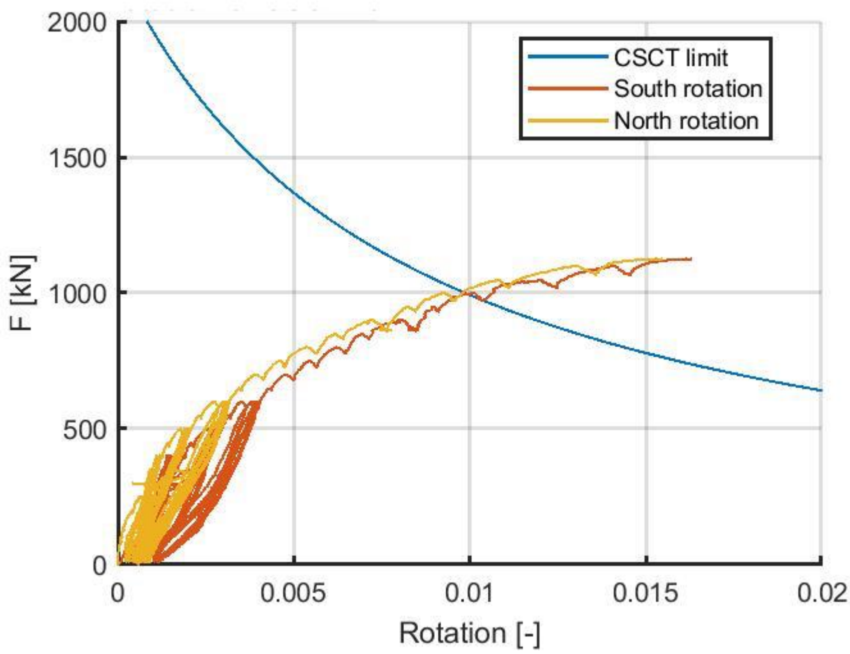

Figure 7.34: Transversal rotations based on laser results during SR1M1

The CSCT stop criterion (Section 3.1.3) for two way shear is applied to SR1M1 to check the performance. The results of this analysis is shown in Figure 7.35. Following the analysis of Chapter 7 the most accurate measurement of the rotation is at the critical shear crack itself. The stop criterion is reached at 86% of the failure load.

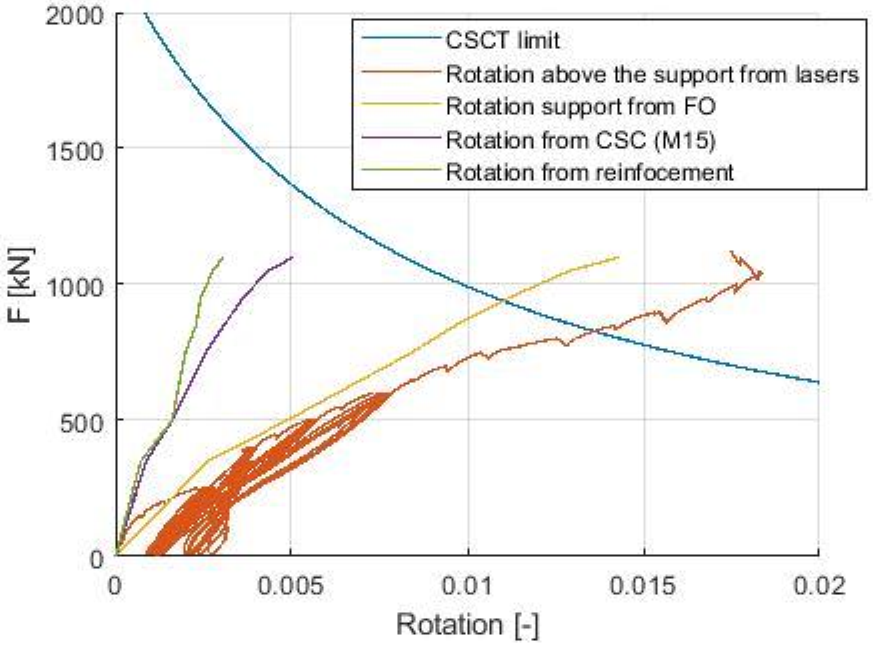

(a)

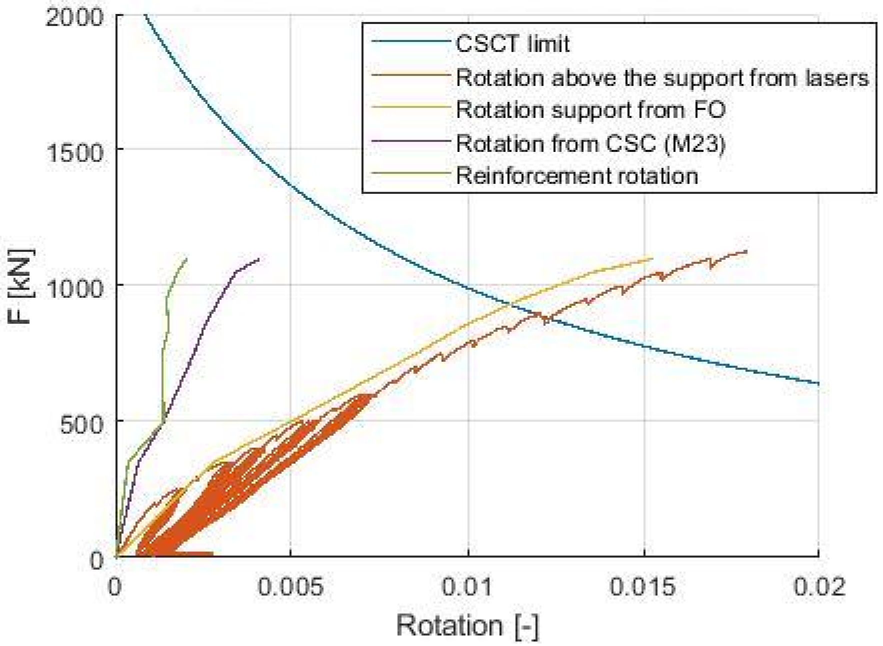

(b)

Figure 7.33: Rotation measurements on simple (a) and continuous (b) support during SR1M1

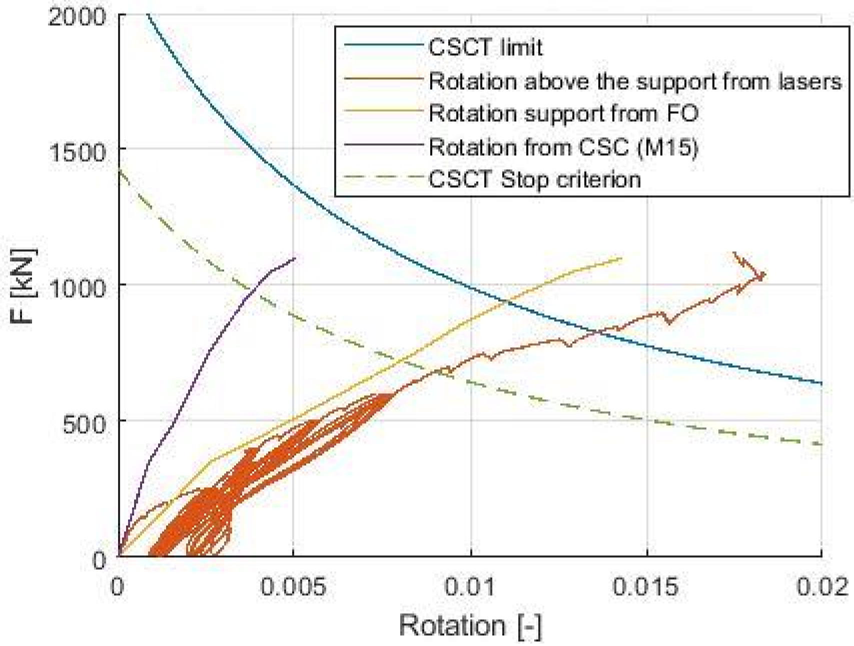

Figure 7.35: Stop criterion for punching CSCT

7.5.2 Influence of flexural behavior

When comparing the internal and external sensors, it can be observed that the results show almost equal results up until 500 kN. Above that point, the reinforcement result starts to deviate from the external result. This can be explained by the bond-slip relation of the steel. When higher forces in the steel are present, the steel starts to slip trough the concrete. Hence, the steel strain at one point can no longer be linearly related to the crack width or crack rotation. Thus, the reinforcement result will start to deviate. As the CSCT is based on the rotation of the crack, the focus should be on the external sensor data. From the results can be observed that the direct measurement on the critical shear crack lead to a failure point close to the CSCT limit. This is not the case for the angle measurements from the support. Force/rotation relations which are way higher than the CSCT limit are present. It can be noted that this observation is not on its own when looking at the failure criterion and experimental data from symmetrical tests (database from Muttoni [25]). Many of the experiments with rotations higher than $\frac{0.15*\phi_{max}*d}{16+d_g}$, fail above the CSCT limit. A possible explanation for this could be, that flexural bending is more present, which is especially the case for one-way slabs. This causes the assumption of a conical deflection to be less accurate. Local measurements like the currently applied optical fiber system, could reduce the flexural influences, and keep track of the live actual rotation of every crack which can develop into a critical shear crack.

7.5.3 Redistribution in transversal direction

Based on the literature review in Section 3.1.3, it is to be expected that the concrete reaches the failure criterion first in the span orientation and then distributes to the transversal direction. As the reinforcement ratio in the transversal direction is only 0.21%, it is not to be expected that a big increase in punching shear capacity is possible in that direction as typical slabs with those reinforcement ratios have high rotations on low load levels. In contrary to the experiments of Sagasta, the non-critical direction is following a force-rotation branch with a significant lower stiffness. Hence, this branch may not be able to carry more force than the capacity reduction caused by the softening. This is emphasized by the transversal direction almost fully flattening out and also exceeding the CSCT limit. Even when the transversal rotation is compared to the rotation of the actual critical shear crack it loses capacity very rapidly as can be seen in Figure 7.36. Hence it seems like the critical rotation should be measured in the longitudinal direction.

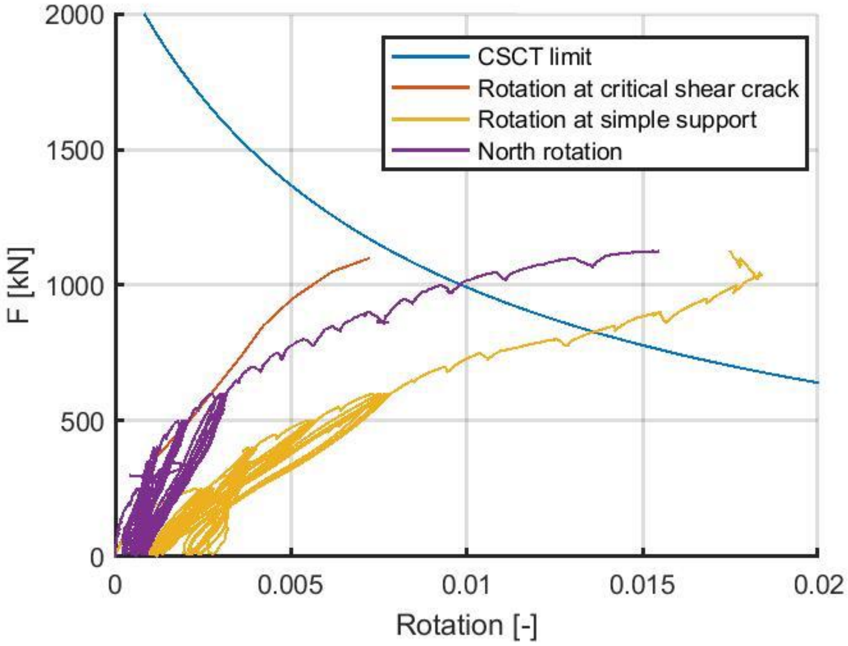

Figure 7.36: Combination of x and y direction of rotations during SR1M1

7.6 Determining one-way or two-way shear

To evaluate the results from experiment S1E2 and S1E3, which failed in shear, it must first be determined if the type of failure is mainly related to one-way or to two-way shear.

Shear theories in general are dependent on parameters such as concrete strength, effective depth, crack height and critical shear displacement. These parameters do not vary much within the same slab. As indicated in the previous section, the slab became punching critical after the occurrence of high rotations due to yielding of the reinforcement at the location of the critical shear crack. When rewriting Equation (3.12), one can find the relation shown in Equation (7.4). It can be observed that the right part of the equation is constant within the same specimen, and can serve as a failure criterion for punching shear.

$$V_r + 15 * V_r * \psi * (\frac{d}{d_{g,0} + d_g}) = 3/4 * b_0 * d * (f_c)^{1/2} \tag{7.4}$$

Hence, for the flexure induced punching failure in SR1M1, this constant value is determined by solving the left side of the equation based on the rotation measurements prior to punching failure:
$1125 + 15 * 1125 * 0.00521846265/(16 + 16) = 1854kN$

This can be compared to the theoretical value which can be determined by the right side of Equation (7.4):
$3/4 * 1617 * 265 * (48.73)^{1/2} * 10^{-3} = 2243kN$

The difference between the theoretical and the measured value is 17%, which seems reasonable.

Now the constant value has been determined for this slab, it can be checked with the measurements from S1E2 and S1E3, if the left side of Equation (7.4) for these tests, come close to the punching failure value determined above:
S1E2:
$725 + 15 * 725 * 0,00156256 * 265/(16 + 16) = 865kN$
S1E3
$625 + 15 * 625 * 0,00296249 * 265/(16 + 16) = 855kN$
Although this method will not be very accurate without calibration, there is a major difference between the left part of Equation (7.4) for the verified punching failure in SR1M1, and the load locations near the supports in S1E2 and S1E3. This indicates that punching failure is not the main failure type at these locations. Hence, in evaluation of these experiments, one dimensional theories for shear will be made use of.

7.7 Shear stop criteria

The previous section determined that both S1E2 and S1E3 failed mainly in one-way shear failure. This section elaborates on the comparison of the failure point to the CSCT failure slope for one-way shear failure. With the effective width determined by the French method, the CSCT limit can be determined by substituting the effective width and other properties of the slab into Equation (3.7). When analyzing the in this section presented results one may note that the slopes up until approximately 500 kN are quite straight. This is because only the failure test is presented. Before this test the slab has been loaded at the same location with loads up until 500 kN.

As S1E2 and S1E3 both failed in shear failure, in this section the stop criteria proposed in Chapter 5 evaluated. All shear stop criteria are measured on the fiber the closest to the direct line of force between the load and the support as this is expected to be the critical line.

7.7.1 Critical section

Before comparing strain results to the CSCT, it must be determined which measurements are most relevant to analyze, and which section is the critical cross section. For beams subjected to concentrated loads, Muttoni states that the critical cross section is $d/2$ away from the load, as shear forces are equal over the full length between the force and the support, and because closer to the support, a higher moment is present, which causes higher crack widths decreasing the shear capacity [25]. For beams subjected to distributed loads, it is more complicated since the shear force increases when moving closer to the support. However, also the capacity increases because of the lower crack width. For those cases it is advised to check at $d/2$ and $L/6$ from the support [25]. Above statements yields for calculations of members assessed with the CSCT, but can this approach also be used for monitoring strains on the bottom side of the concrete? This seems not to be the case, as any flexural crack can develop into the critical shear crack. Although the crack tip is likely to be near this critical section. The distance between this point and where the critical shear crack is located on the bottom face can actually be any distance between load and support. Hence, all cracks between $d/2$ from load initiation and support should be checked for the CSCT limit. In Figure 7.37 an overview of the critical zone is given for the external sensors. In Figure 7.38 this overview is provided for internal sensors.

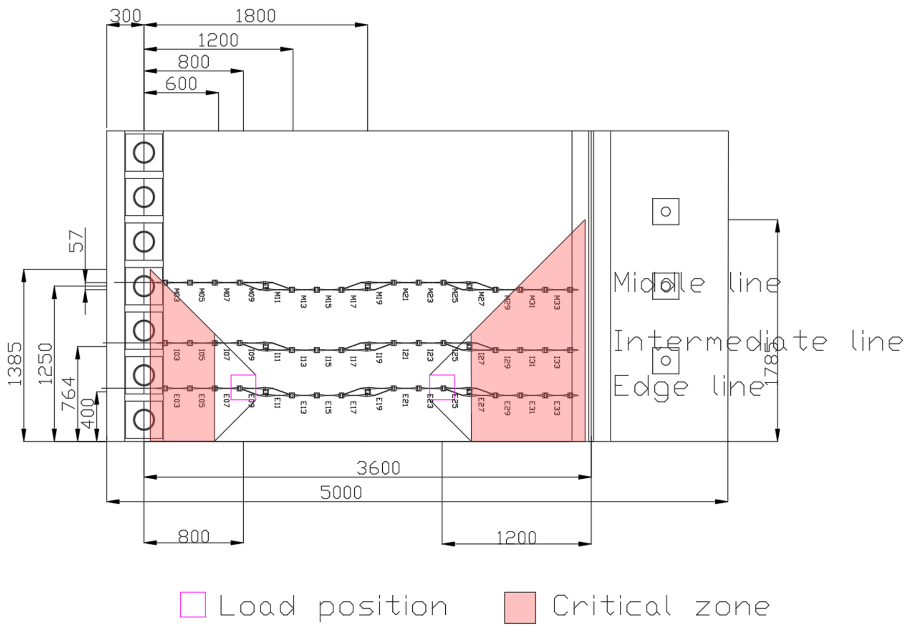

Figure 7.37: Critical zone for shear with external sensors

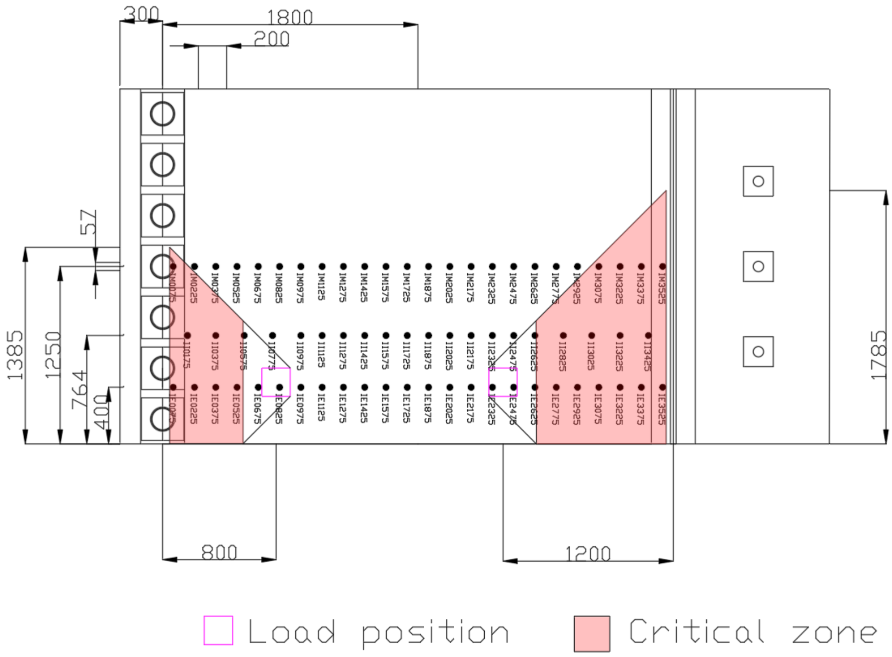

Figure 7.38: Critical zone for shear with internal sensors

7.7.2 Interpretation of the OF results

In this section, the results are presented, and relations to the theory are shown.

Results of S1E2

On this experiment, the slab was loaded 800 mm away from the simple support. The most important sensors for this loading position are the sensors straight in between the load and the simple support. By using the external sensors to determine the reinforcement strain and height of the compressive zone following Section 5.1, the strain at 0.6*d can be found. These results are plotted against the CSCT limit in Figure 7.39.

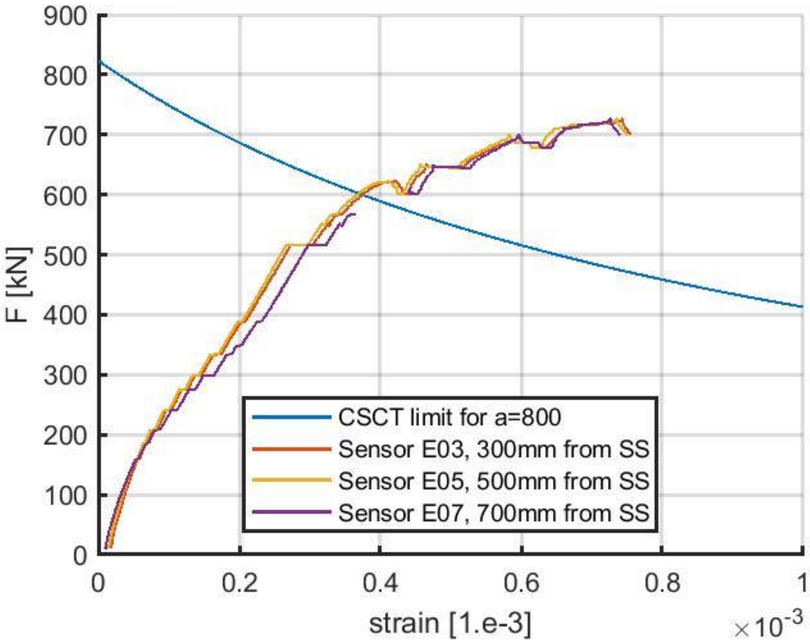

Figure 7.39: Strain at 0.6d from external FO sensors during SR1E2

By making use of the internal sensors, a more direct measurement can be performed. The assumed relation between external strain and steel strain is avoided. In addition, locations closer to the support can be measured. The strain at 0.6*d can be calculated by first calculating the height of the compressive zone. The results are shown in Figure 7.40.

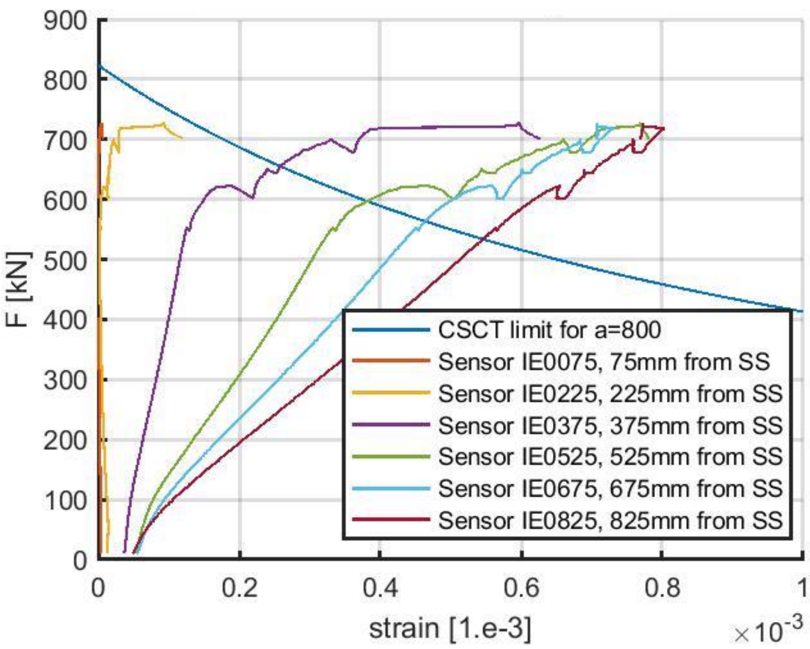

Figure 7.40: Strain at 0.6d from internal FO sensors during SR1E2

From the internal and external results can be observed that the results from the internal and external sensors are quite similar, although we see a higher difference during the strain development stage between the individual internal sensors. The force-rotation line exceeds the CSCT limit at multiple points for both internal and external sensors. This can indicate arching action, as that is one of the known mechanisms which can cause concrete members to exceed the CSCT limit [25].

Results of S1E3

For this experiment, the load was placed 1200 mm from the continuous support. Following the same procedure as described in Section 7.7.2, the results from the external sensors are presented in Figure 7.41 and the results from the internal sensors are presented in Figure 7.42.

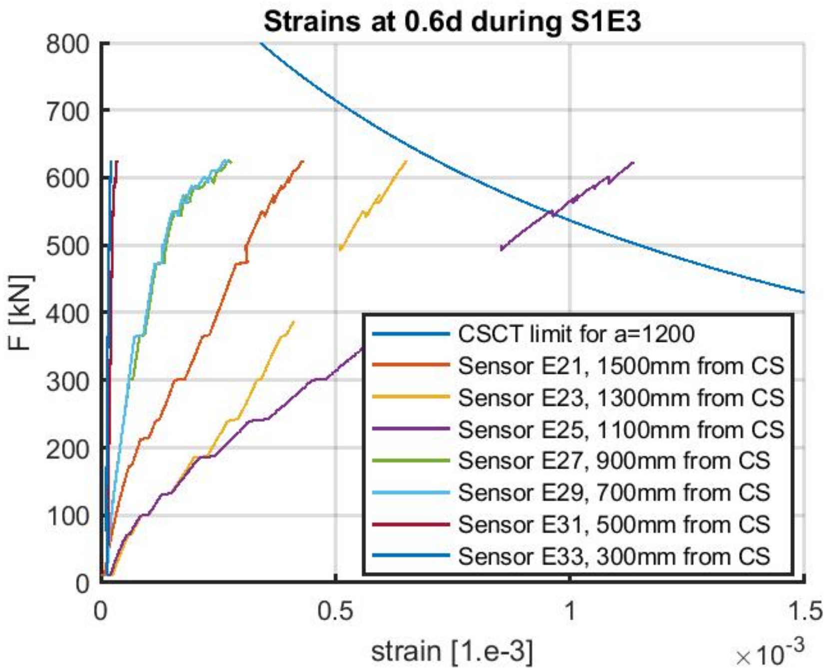

Figure 7.41: Strain at 0.6d from external FO sensors during SR1E3

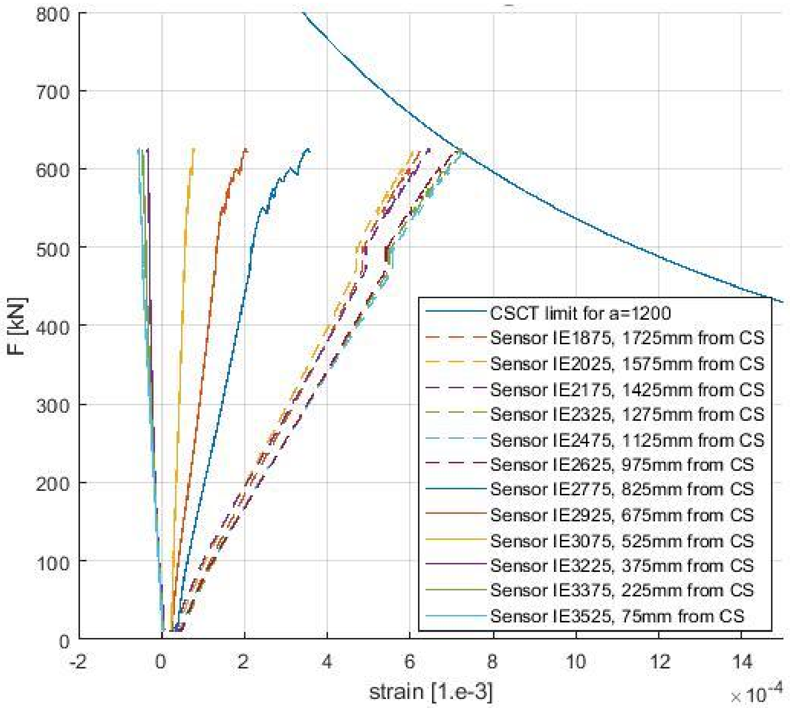

Figure 7.42: Strain at 0.6d from internal FO sensors during SR1E3

The continuous support can be clearly recognized in the results, since the first 500 mm, no strain, or a negative strain is noticeable in the graph. Therefore, the point of contra flexure will lay around 500 mm away from the continuous support. Within the graphs, there are lines which are very close or exceeding the CSCT limit. However, only one sensor (IE2625) is within the critical zone. All other locations which reach the CSCT limit, are not in between the critical zone as defined in Section 7.7.1. The critical zone for the test of the continuous support is in between 0 and 1068 mm from the support. For the sensors between 600 and 900 mm from the continuous support, the external results give a similar result as the reinforcement sensors. All external sensors within the critical zone are still quite below the CSCT limit. This can be explained because, after removal of all sensors, this load position was tested again, and it showed still more capacity than was applied in the test. The specimen failed in shear failure at 750 kN. When looking at the slope of the graph, it is obvious that at 750 kN, multiple sensors would have reached the CSCT limit.

Difference on analyzing the performance of shear stop criteria for beams and for slabs

As it was found that arching action occurred during S1E2, it would not be realistic to compare the stop criteria for this experiment to the actual failure force, as arching action is not considered in the theories to determine the stop criteria. Hence, when comparing the force at the stop criterion with the failure force of S1E2, the failure force will be assumed around 600kN, as this is the approximate point from where arching action carried a significant amount of force.

7.7.3 ε_{CSDT}

Following Section 5.2.6, the shear force according to the CSDT is determined. To account for loading at the edge, the effective width is calculated with the French method.

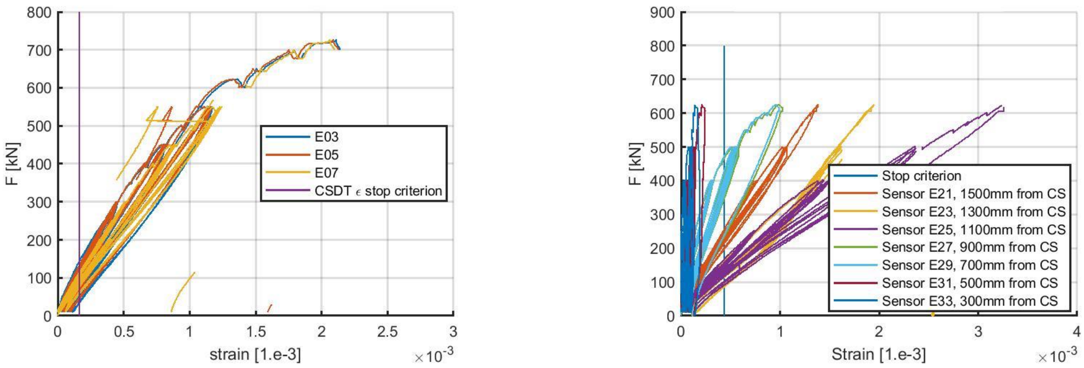

Figure 7.43: Comparison of external strain sensors to CSDT strain stop criterion

To calculate the according moment, the slab was modeled in a SCIA model. With this moment and M-K diagram based on the sectional properties the ε_{CSDT} is determined. This is reduced by the safety margin of 35%. For both loading positions the results are summarized in Table 7.7

Table 7.7: results of CSDT stop criterion calculation

Exp.	b_{eff} [mm]	V_{CSDT} [kN]	M_{CSDT} [kNm/m]	φ_{CSDT} [mm]	ε_s [-]	ε_{bot} [-]	ε_{stop} [-]
S1E2	1385	461.71	210	1.49E-06	0.000199	0.000251	0.000163
S1E3	1785	623.39	333	4E-06	0.000536	0.000675	0.000439

The stop criteria are compared to the measured external strains in Figure 7.43. The results are summarized and compared to reinforcement results in Table 7.8.

Exp.	F at stop criterion [kN]	% of failure force	F at ε_{CSDT} in reinf [kN]	Error
S1E2	110	18%	119	-8%
S1E3	432	58%	207	109%

Table 7.8: Error analysis of the CSDT

From the results it can be observed that for experiment S1E2 the stop criterion does not provide a feasible stop criterion, since it is reached at 18% of the modified failure load. In S1E3, a better result is found based on the CSDT limit. However, there is a big discrepancy between the point at which the external sensors indicate the stop criterion is reached, based on concrete strains and the actual steel strain within the slab. 65% of the steel limit as displayed in Table 7.7, was reached at 207 kN. This might be caused by simplifying the slab as if it was a beam using the French method.

7.7.4 w_{ai}

Similarly to Section 7.4.3, the crack widths for tests S1E2 and S1E3 are determined. In Figure 7.44 the average crack width is shown. The stop criterion can be determined with Equation (5.10) and for this specimen is 0.095 mm.

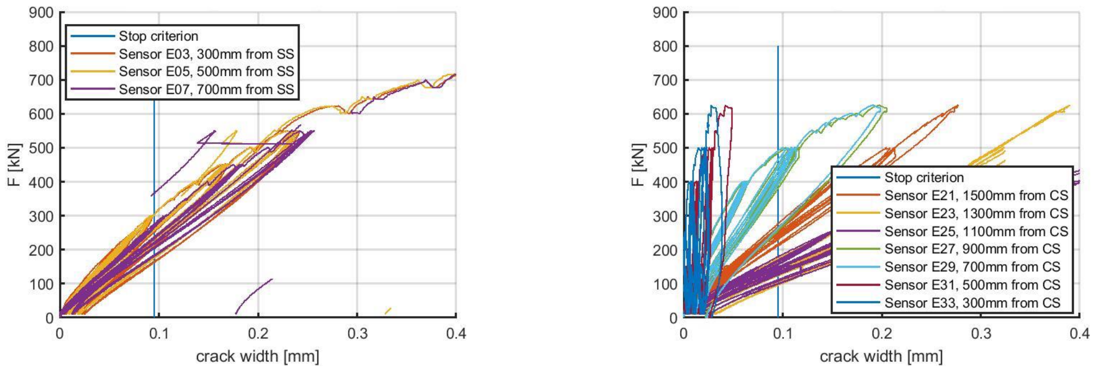

Figure 7.44: Comparison of crack widths to aggregate interlock crack stop criterion

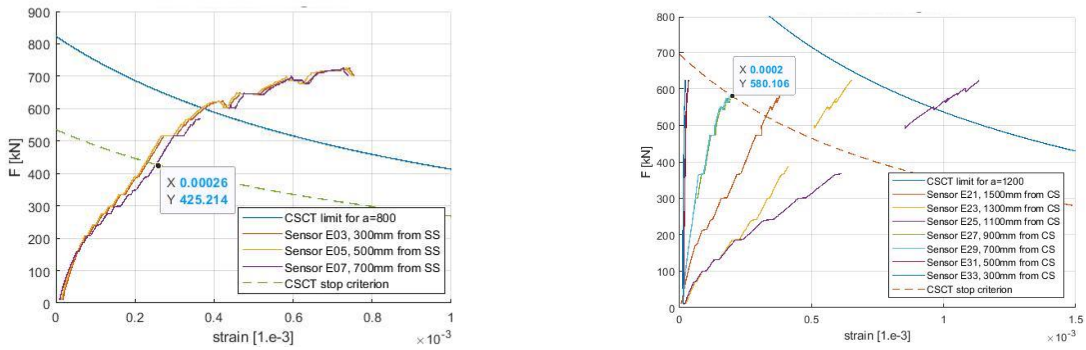

Figure 7.45: Comparison of strains to the CSCT stop criterion

From the results it can be observed that the stop criterion is first reached at 277 kN for S1E2 and 485 kN for S1E3. This is at 46% and 65% of the failure load which provides a significant amount of safety without being overly conservative.

7.7.5 ε_{CSCT}-Force relation for one way shear

The proposed stop criterion of the CSCT limit reduced by 35%, can be calculated by Equation (3.7). In Figure 7.45, the performance of the stop criteria on S1E2 and S1E3 is shown.

S1E2, reached the stop criterion at 70% of the failure load and S1E3 reached the stop criterion in a shear-critical sensor (E27) at 77% of the failure load. The observed margin in comparison to the failure load seems in relation to the applied safety margin. Hence, the CSCT performed well as a stop criterion to the shear failures of this slab.

7.7.6 Sectional stiffness

The sectional stiffness of critical sensors during S1E2 and S1E3 are shown in Figures 7.46 and 7.47. Just as for the flexural analysis of the sectional stiffness, a 25% stiffness reduction stop criterion would not perform well with the presented results, as the stiffness is constant, constantly decreasing, or sometimes stabilizing after a initial decrease.

The sudden drop in stiffness for the sensors close to the supports of experiment S1E2, can be explained by cracking at those locations due to activation of the full effective width. But as these drops are close to the failure point, and can be directly related to cracking of the slab at those locations, the added value of the actual number of the stiffness cannot be proven. For S1E3, such a drop was not observed.

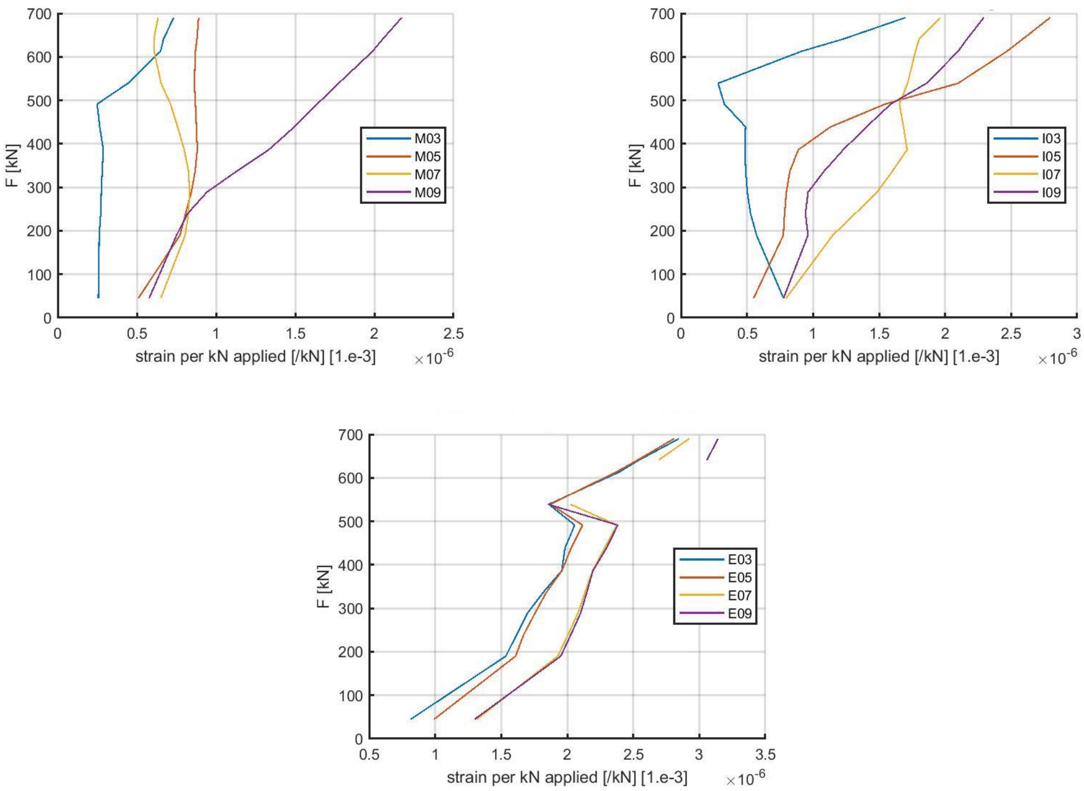

Figure 7.46: Sectional stiffness for all FO measuring lines during SR1M1

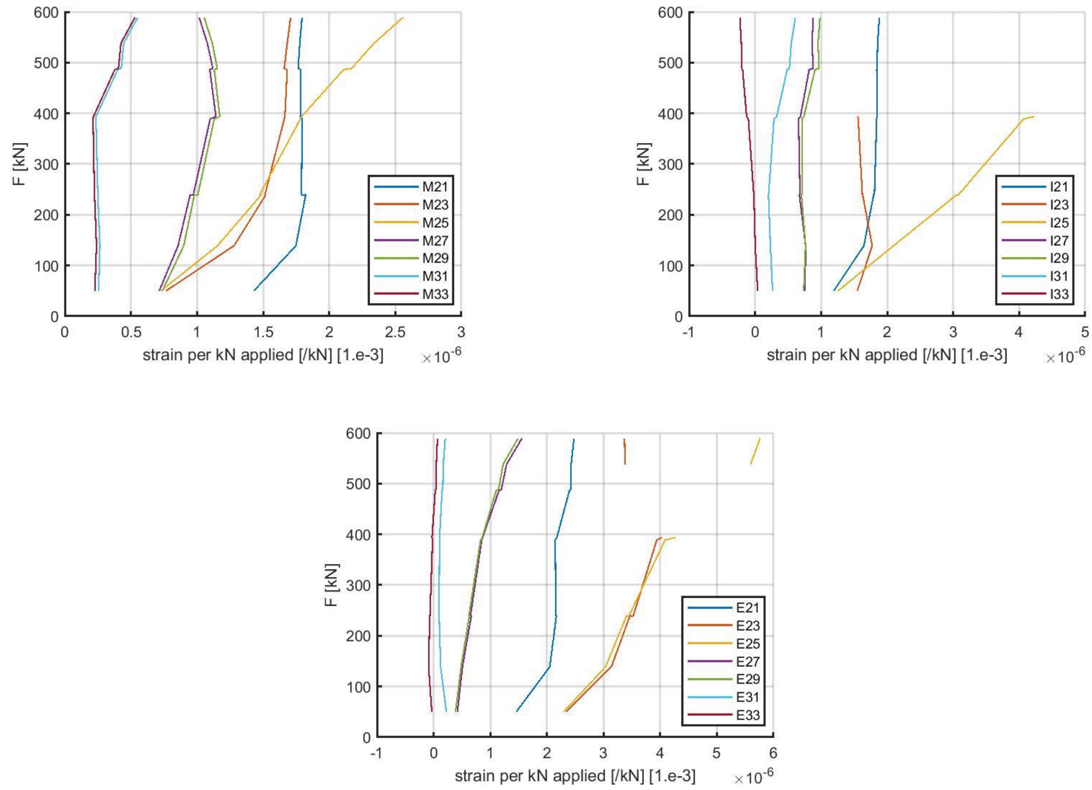

Figure 7.47: Sectional stiffness for all FO measuring lines during SR1M1

7.8 Conclusion

A summary of the flexure and shear stop criteria are given in Tables 7.9 and 7.10. For flexure, it can be observed that the criteria on strain and crack width have a feasible amount of safety compared to the yielding load. The criteria on the stiffness reduction were reached in the first load step and do not provide useful results. The deformation profiles did not show any abnormalities so the stop criterion based on the deformation profiles was never reached. Based on the analysis of internal strains, the strain stop criterion has a higher accuracy in comparison to the steel strain at locations further away from the load.

The best performing stop criterion for shear was the newly derived stop criterion based on the relation between allowable shear force and rotation of the critical shear crack, measured by external strains. Another criterion which provided good results was the stop criteria based on crack width for aggregate interlock. As this stop criterion does not account for other shear carrying mechanisms it is logical that the margin of safety is bigger. The sectional stiffness criterion was reached at the first load step. Therefore, this is not a good stop criterion. The stop criterion based on maximum strain calculated by the CSDT provides inconsistent results. When compared to the internal sensors, the strain in the reinforcement steel shows high differences from the theoretical approach. Hence, this is not yet a good stop criterion.

As these results are obtained for a sample size of 1 (for flexural failure and flexure induced punching failure) or 2 (for shear failure), one can imagine the number of data points is small. However, the results on the stop criteria can give a first insight on how the current proposal performs on a slab. The significance increases even further as the internal strains on the reinforcement can also be monitored. These measurements can provide insight into the performance of stop criteria with a theoretical basis on steel strain.

Criterion:	F_{stop} [kN]	F_y [kN]	F_{stop}/F_y
Deformation profile	$> F_{max}$	831	$> F_{max}$
ε_{stop}	649	831	79%
w_{stop}	680	831	81%
25% Stiffness reduction	150	831	18%
k_{sec}	251	831	30%

Table 7.9: Summary of the performance of the flexural stop criteria

Criterion	F_{stop} E2	F_{arch} E2	F_{stop} E3	F_{fail} E3	F_{stop}/F_{arch} E2	F_{stop}/F_{fail} E3
ε_{CSDT}	110	600	432	750	18 %	58%
w_{ai}	277	600	485	750	46%	65%
$V-\varepsilon_{CSCT}$	425	600	580	750	70%	77%
k_{sec}	100	600	100	750	17%	13%

Table 7.10: Summary of the performance of the shear stop criteria

8 Discussion

The lack of validated stop criteria for shear failure, a standardized sensor layout approach, and the high amount of single sensors are all causes why proof load testing is not regularly used commercially. In this thesis, research has been conducted to take away a few of these objections by applying longitudinal long gauge fiber optical measurements. In this chapter, the significance of the findings is elaborated on, as well as limitations to interpreting those findings.

8.1 Limitations in followed procedure

The experiments executed in this research have provided data on flexural behavior, shear behavior, and punching behavior. The data is gathered on a 1:2 scale version of a bridge that has been designed to represent the results from a full-scale experiment as accurately as possible. However, this does not exclude the risk of size effects on the gathered data. In further research, a full scale experiment can be conducted to verify the stop criteria for higher effective depths.

The final sensor layout provided measurements over almost the full length. The supports of the slab made it impossible to extend the optical fiber sensors to the middle point of the support. Hence, the strain on the first and last 200 mm of the slab was not measured. These results were needed for the integration to determine the deformation profile. Hence these results were linearly extrapolated. In future applications, the FO system can be designed more shallow to make sure that the optical fiber can measure up until the center of the support.

In experiment SR1M1, the slab was loaded in the middle of the span. After executing the proof load testing load protocol, the slab was loaded up until failure. From the internal sensors it could be concluded that first, yielding of the reinforcement steel occurred, after which the slab failed in flexure induced punching failure.

For experiment SR1E2 and SR1E3, the slab was loaded near the supports. These tests failed in shear failure. Whether the data on experiment SR1E2 and SR1E3 are fully representative for a general case is uncertain, as the pushed out punching cone damage might have influenced the structural responses. However, when looking at the results of SR1E2 and SR1E3, no unexpected behavior can be found.

After removal of all the sensors, additional testing showed that there was residual capacity at the loading point of SR1E3. This makes interpretation of the results more difficult, as for the final 125kN, no sensor data is gathered and the structural responses after reaching 625kN can only be guessed.

By interpreting findings of this study, it should be noted that these findings are not generally applicable as the properties of concrete slabs differ between various slabs (e.g. steel yielding strain, concrete compressive strength, maximum aggregate size etc.). The obtained results are solely based on one specimen. Variations on the shown properties are not studied within this thesis.

8.2 FO compared to currently applied sensor setup for proof load testing

Initial cracking is an important point in the analysis of an uncracked concrete slab bridge. The developed sensing system is able to very accurately determine the first crack in a measured section by use of the cracking indicator. An advantage of the FO measurement system is that it measures over the full length of the bridge. Hence, the critical location cannot be missed, as is the case with single sensors. In addition, the detection of the cracks can be done automatically, where in normal circumstances visual inspection is necessary to locate cracks. As visual inspection is not desirable underneath a proof loaded structure the FO sensors are able to provide more insight to the structure. The results found in this study were verified by DIC results. In 21 of the 23 sections the DIC and OF cracking indicator showed cracks at the same load level. The used load levels had increments of 50 kN. To determine the exact accuracy of the cracking indicator, a load increment of 1 kN could be used.

Many of the flexural stop criteria are related to steel strains [10]. During the flexural test, comparison of the external and internal strains demonstrate that the external sensors can roughly estimate the internal reinforcement strains. The conversion from external to internal strains is done by assuming a linear strain distribution in the concrete section, and by iterating the compressive zone height. The accuracy on this conversion from external to internal strain increases on the intermediate and edge sensor line, as the results are more equally spread out in the longitudinal direction. This is to be expected as the results are less disturbed by the point load, and the forces are already spread out more. As the results get more consistent further away from the load, this also provides an opportunity to investigate if it is possible to find stop criteria for locations further away from the load. This leads to a stop criteria which is less vulnerable to gauge length changes. In addition, it is less likely to miss the critical location when choosing the location of single sensors.

Another parameter which can be used as a local stop criterion is based on the crack width. It has been proven a challenge to determine crack widths from the obtained results if there is more than one crack within the gauge length. In that case an average crack width is obtained. However, the crack width stop criterion is based on the maximum crack width. Thus, a ratio between the cracks is required to be able to still use a crack width stop criterion. This ratio might be obtained by DIC analysis, or by the use of another FO technique [56]. Another option is to not solve this challenge, as the strain stop criteria perform quite consistent and therefore the crack with stop criterion can become unnecessary. The consistent results should however be verified by more experiments.

By numerical integration of the strain results the deformation profile can be calculated. This deformation profile has similar results on the comparison locations where lasers measured the deflection. This method can thus be used to describe the longitudinal deflection of slab bridges. This method might be used instead of lasers. The advantage of this method is that the whole deflection profile can be known, compared to only point measurements which are able with lasers. The disadvantage of the OF method is some loss in accuracy and it is uncertain if stop criteria based on deflection profiles can be noticed, similar to examples in literature ([67]). This could not be verified as the deflection profile stop criteria were not reached during the experiments.

The FO sensor setup is even more relevant in proof load experiments related to shear. When the shear capacity of structures is calculated, in theory, very exact points exist, at which the maximum shear force coincides with the location with the lowest strength. This can for instance be seen in the application of the one-dimensional CSCT, for which is suggested to check the capacity at 0.5d from the loading point [25]. In practice however, the strength of concrete is very inhomogeneous. The actual crack path of the crack that in the end leads to shear failure can propagate up until over the full length between the load initiation and the support [27]. Hence, on the bottom face of the slab each crack in between these two points might be the critical shear crack, and should therefore be monitored (the exact definition of the critical zone can be found in Chapter 7). The critical location can therefore not be determined on beforehand. The developed FO measurement system is able to keep track of this full critical zone. During loading, the highest value can be selected as the critical location.

Following the obtained data on SR1E2 clearly showed a force-strain relation which exceeded the one-dimensional CSCT limit. As the force-strain relation is clearly flattening after reaching the CSCT limit, it is assumed that arching action occurred. As arching action is not included in the CSCT [30], the presence of arching action makes it possible to exceed the CSCT limit. Experiment SR1E3 does not show a shear-critical sensor reach the CSCT limit. This might be caused because measurements were stopped 125 kN before failure. When the rotation of the force-strain relation of critical sensors and the additional 125 kN are considered, it becomes clear that a failure close to the CSCT limit happened. This can however not be validated due to the fact that there is no sensor data. Now initial experience on this stop criterion produces hopeful results, more experiments can be conducted to find a feasible level of safety, as the for this study applied 65% level is an arbitrary safety level.

For the development of the stop criterion for flexure induced punching also the developed FO sensing system is used. From experiments it became clear that the angle of the punching cone can vary widely [30]. Hence, it is only possible to keep track of the critical shear crack when a critical zone is defined.

One of the observations during the analysis of this stop criterion is the difference in how the rotation for evaluation of the CSCT is determined. During development of the punching CSCT theory, inclinometers were used to determine the rotations at the critical shear crack. This was possible under the assumption of a conical deformation profile, with all rotation to be assumed in the critical shear crack. For flexure induced punching, this assumption does not seem to hold as a lot of rotation is generated by flexural behaviour. During this study, it was found that measuring the actual rotation in the critical shear crack by the developed OF measurement system does provide results closer to the CSCT limit than the measurement of the global rotations. For ductile shear failures it might thus be beneficial to measure the critical shear crack itself. As this is an observation on only one test, more research should be done to verify this claim. Usually the global rotations are done with inclinometers. As these sensors were not available, a rotation is obtained by using the deflection results from the lasers around the support. This might have caused an error compared to the standard inclinometer technique.

As there is a method available to account for non-axis symmetric conditions for punching with the CSCT, the results of redistribution in the transversal direction was investigated. Results from literature show that if a concrete plate is spanning in one direction, the critical shear crack in this direction grows significantly more compared to the crack which is not in the spanning direction. Furthermore, it is to be expected that if a concrete plate has a lower reinforcement level in one of the two spreading directions, the amount of redistribution is limited. Hence, in this study, the critical (longitudinal) direction is measured, and not much redistribution to the transversal direction is expected as a flatter force-rotation curve is expected in this direction. As explained above, the critical crack in longitudinal direction causes failure close to the CSCT limit. The interpretation of the combination of these two non-axis symmetrical conditions combined needs further study to be verified, as no literature was found in which these two non-axis symmetrical conditions were combined.

8.3 Application of FO measurements in proof load testing in the field

The developed optical fiber sensing system has great potential to be applied during proof load tests in the field. This study has shown that optical fibers can provide more information on the structure than conventional sensing methods and that stop criteria for shear based on the CSCT limit, which need this sensing setup, are very promising. Because of the long gauge application with low pretension, the sensors are able to measure during loading and unloading of the slab, without loss of accuracy as is the case for continuously glued sensors [61].

For application of the sensing system to a proof load field test, several design aspects should be considered. As the distance between the major cracks is bigger for full scale structures [19] it is necessary to check if the gauge length can also be adjusted. The gauge length almost has a linear relation with the final price of the measurement solution because of the price for each single sensor.

For this study, only a conclusion about the upper boundary of the exact accuracy of the sensing system can be made. As the measured value has only been compared to one other sensing method, with a slight distance between the measurements. This distance could have caused the value that should be measured to differ in between sensing systems. Hence, more research is necessary to determine the exact accuracy of the system.

From the results on the stop criteria, it can be concluded that for flexural proof load tests the best performing stop criterion is the ε_{stop}. This stop criterion can be combined with the qualitative stop criteria and the stop criterion for flexure induced punching. For shear proof load tests the w_{ai} and the newly derived CSCT stop criterion provided the best results. In combination with the qualitative stop criteria these criteria can form a set to prevent shear failure.

One of the upcoming challenges in applying the optical fiber to a bridge is the temperature sensitivity of the sensors and the compensation of temperature difference. As the applied sensors are very vulnerable to temperature changes [46], it should be determined in practice how many temperature sensors should be used to compensate accurately for the temperature change, as in outdoor applications the temperature can differ over the full length of the slab. There are multiple methods available to compensate for the temperature [46].

For a typical load test, sensors like load cells, strain sensors, deflection measurements and acoustic emission can be used [11]. All these type of sensors can be based on FBG fiber optical measurements. If the gauge length is chosen so the sensor will measure only one crack, or if this challenge is solved with another measuring method, all most important structural responses can be measured with optical fibers and the system can function as an all in one solution for proof load testing. One of the main advantages of using optical fibers for this application is that the sensors are multiplexable, which reduces the amount of cables significantly. In addition, the strains can be measured over the full length, semi continuously, which reduces the risk of missing a critical location, such as the critical shear crack. All these features contribute to simplification of the sensor setup, which makes the method of proof load testing more economically viable [32].

The influence of the application of an internal sensor to a reinforcement bar is investigated by doing tensile tests on reinforcement bars with a grinded slot. These tests show that the influence on the reinforcement bar can be linearly related to the removed material to grind the slot. For three tests, the slot was filled with the glue which was also used to glue the optical fiber sensor in. The chosen glue is a stiff glue. This ensures that the strain present in the rebar is transferred to the sensor without spreading on the glue. During the tensile tests it was observed that as soon as the reinforcement bar reached strains around the yielding point, the glue started to crack. Hence, the measurement from the internal sensors are not trustworthy after the rebar has reached its yielding strain at the sensor location. This can be optimized by investigating more anchorage possibilities from the sensor to the reinforcement steel. Up until the yielding point, the sensors gave great insight in the behavior of the slab. They were able to observe cracking and to check theories with the gathered data. Hence, this is a technique which could be used for structural health monitoring on new bridges, as is currently already frequently done in China [44]. Before applying this into new structures it would be necessary to investigate the long term effects and to investigate more about how the results should be interpret during these type of applications.

The application technique of using a positioning tool to determine the exact locations of the anchors has worked out well. This method makes it possible to glue the anchors way in advance, on exactly the right location. As the glued plates are quite shallow, the reduction in free height underneath the bridge will almost be negligible.

9 Conclusion and further research

9.1 Summary and conclusion

During this study, a method has been determined for measuring stop criteria by means of fiber optical sensors during proof load testing. First the requirements for a longitudinal measurement system during proof load testing were investigated from literature. It was concluded that to improve the applicability of proof load testing as an assessment method, it would be desirable to develop a continuous longitudinal measurement of the structural responses. Important structural responses for stop criteria are strain, crack widths and deformations of the structure. In Chapter 4 several fiber optic measurement systems were considered to fulfill this desire. One concession about using optical fibers for this purpose was that a fully continuous measurement is not possible in combination with alternating loads. Thus, a semi-continuous system has been developed. It was shown that the FBG and the OBR technique both were possible. As the OBR technique is relatively new compared to the more mature FBG technique, this technique was chosen to design a measurement system with.

With the knowledge on which fiber optic sensor to use, and the choice for a semi-continuous design, current stop criteria could be adjusted so they could be measured with the proposed sensing system. In addition, it is proposed to measure the strain at a distance from the load to investigate how this would influence the results. Stop criteria which can be measured with the FO measuring system are presented in Chapter 5. Then, in Chapter 6, a method of installation was determined and the accuracy of the sensing system was determined. It was made sure that the anchorage to the concrete would not influence the results.

This system was applied to a 1:2 scale proof load test in Chapter 7. Within this chapter the results from this test were analyzed. It was shown that the system is capable of determining initial cracking. The flexural stop criterion based on measuring strain performed well, and is also verified by measuring steel strains. For shear failure, the crack width stop criterion showed good results. The newly derived stop criterion based on the CSCT also showed promising results. For the flexure induced punching, it was found that to determine the rotation of the critical shear crack it is probably better to measure at local level instead of the global rotation, as the flexural rotations are more present.

The developed measurement system is able to provide a combination of global and local information. In addition, other types of sensors which are often used or which are currently under development for proof load testing can be part of an optical fiber sensing system. Therefore, the optical fiber sensing system could provide an all in one solution for proof load testing of concrete slab bridges. Which is advantageous in many ways such as data structure, cabeling, and required skill level of the proof load testing staff. Below, the main findings are listed.

Measuring system

- The measurement system functions as designed, and produces relevant results.
- The results acquired by optical fiber sensors are generally within a 15% margin when compared to LVDT measurements close to the optical fiber.
- The anchorage design of the fiber optic sensor does not show significant creep deformations which influence the result of the sensors.
- Cracking of the concrete structure can be detected by applying the cracking limit to the results from fiber optical sensors.
- Internal sensors are able to measure actual steel strains, which can be used to verify assumptions in applied theories.

- The main advantage of using the designed fiber optical sensors is that the structural responses can be monitored semi continuously during a load protocol related to a proof load test, without having to connect each separate sensor to the loggerbox (multiplexibility).

Stop criteria

- The flexural stop criterion based on maximum strain (ε_{stop}) performed well as it provided a sufficient amount of safety. With the proposed adjustments this criterion seems to benefit from slab load distribution.
- The results from the flexural crack width stop criterion (w_{stop}) are still inconclusive, as the bandwidth of result interpretation is too wide to determine the error of the criterion.
- The adjustments to the shear stop criterion baed on the CSDT (ε_{CSDT}) does not make it a good stop criterion for concrete slabs as its results are inconsistent for the executed tests.
- The shear stop criterion based on crack width (w_{ai}) performed well on the test as it provides a safety margin in line with the theory.
- The newly proposed strain stop criterion for one way shear based on the ε-force relation performs well as is provided a sufficient amount of safety on the tested slab. More research is necessary to verify if this criterion is valid for other circumstances.
- The newly proposed strain stop criterion for two way shear based on the ψ-force relation performs well as is provided a sufficient amount of safety on the tested slab. More research is necessary to verify if this criterion is valid for other circumstances.
- All stop criteria based on global or sectional stiffness does not provide promising results as the stiffness is continuously decreasing for an increasing load.

Concrete slab

- For flexural failure: more consistent strain results are obtained when measuring further away in transversal direction from the point load. By measuring a stop criterion for such a location, the measurement system becomes less dependent on the applied gauge length which can be a beneficial feature as the same sensors can be used on multiple projects.
- The shear failures found during the experimental program show agreement with the CSCT failure criterion.
- With the developed measurement system it was possible to measure the flexure induced punching critical shear crack and obtain more accurate results according to the CSCT, than the rotations measured above the support. This indicates that the assumption of a conical deformation profile might not be valid for low reinforced slabs and that the current measurement method is an improvement to determine punching failure.
- For the CSDT, high discrepancies were found between the assumptions from the theory and the actual measured value within the reinforcement. Hence, it indicates that compensation for the effective width is not enough to apply this theory to concrete slabs.
- The integration of the fiber optical strain results over the full length of the slab is able to describe the deflection with a low error in comparison to the laser deflection results.

9.2 Recommendations for practice

- It is recommended to use and further optimize the developed measuring system as a monitoring system for stop criteria during proof load tests
- For direct interpretation of the results, a dashboard should be developed which can give an overview of all applied sensors. This dashboard should also detect critical locations. It should be able to select each individual sensor to check not only the current value, but also the historic data. Such a dashboard is needed as the amount of applied sensors of such a application is very high.
- The positioning tool used for accurately placing and gluing the sensors can be improved so application in practice can be executed faster.
- Altough it is very labour intensive and costly, it is recommended to replace electrical sensors for strain, load cells, acoustic emission sensors and inclinometers to equivalent sensors based on optical fiber (FBG) technique. This simplifies the acquisition of data as only one type of loggerbox (interrogator) is needed. This simplifies the data structure and reduces requirements on the staff. This all simplifies the measurement setup.
- As FOS are very resistant to environmental influences, long term measuring with this technique is an option. This makes it possible to combine the proof load test with a permanent SHM system. This should however be investigated further.

9.3 Further research

- To verify the work of this thesis the fiber optical measurement system should be applied on full scale and at more bridges with other properties, to ensure a decent sample size.
- The one thing withholding the sensor system from being an all in one solution is the determination of the ratio between multiple cracks within one section length. Hence it is useful to search for a method which can fulfill this required measurement.
- This study found an upper bound for the accuracy. For future applications it is useful to determine the exact accuracy of the measurement system with straight up comparisons between sensors.
- The current sensing method for FBG's glued in the reinforcement can be improved by making the results valid for strains after yielding. To achieve this, more research is needed on the connection between the fiber and the steel.
- The redistribution of a typical punching failure for a bridge, has not yet been investigated for the CSCT. It would be valuable to investigate redistribution of the force in the less reinforced and not span direction.
- Because of the high performance of the internal sensors, it is interesting to investigate this system as a structural health monitoring system for new structures.

Bibliography

[1] E. O.L. Lantsoght et al. “Stop criteria for proof load tests verified with field and laboratory testing of the Ruytenschildt Bridge”. In: *IABSE Conference, Copenhagen 2018: Engineering the Past, to Meet the Needs of the Future - Report* (2018), pp. 79–86.
[2] Fib. *Model code 2010: final draft*. Tech. rep. 2012.
[3] G Zarate and E.O.L. Lantsoght. *Stevin Report 25.5-20-01 Measuring techniques*. Tech. rep. 2019.
[4] Branko Glisic et al. “Damage detection and characterization using fiber optic sensors”. In: *Sensors and Smart Structures Technologies for Civil, Mechanical, and Aerospace Systems* (2013).
[5] E.O.L. Lantsoght et al. *Stevin Report 25.5-16-06 Analysis of beam experiments for stop criteria*. Tech. rep. 2016.
[6] S.A.A.M. Fennis et al. “Proefbelasting viaduct Vlijmen-Oost”. In: *Cement* (2014), pp. 40–45.
[7] D.A. Fennis S.A.A.M.and Hordijk. *Stevin report 25.5-14-05 Proefbelasting Halvemaansbrug Alkmaar*. Tech. rep. 2014.
[8] E.O.L. Lantsoght et al. “Towards standardisation of proof load testing pilot test on viaduct Zijlweg”. In: (2017).
[9] E.O.L. Lantsoght et al. “Pilot Proof-Load Test on Viaduct De Beek: Case Study”. In: (2017).
[10] G. I. Zarate and E.O.L. Lantsoght. “Stevin Report 25.5-19-05 Verification of stop criteria”. In: (2019).
[11] G Zarate and E.O.L. Lantsoght. *Stevin Report 25.5-20-03 Preparation of experiments*. Tech. rep. 2020.
[12] E.O.L. Lantsoght. “Proof load testing of reinforced concrete bridges : Experience from a program of testing in the Netherlands”. In: *In 1er Congreso Iberamericano de Ingenieria Civil: Quito, Ecuador* (2017).
[13] CEN. *Eurocode 1: Actions on structures-Part2: Traffic loads on Bridges, in NEN-EN 1991-2.* Tech. rep.
[14] E.O.L. Lantsoght et al. “Applying Experimental Results to the Shear Assessment Method for Solid Slab Bridges”. In: (2010).
[15] dr. ir. drs. C.R. Braam and ir. P. Lagendijk. *Constructieleer gewapend beton*. 2011.
[16] dr. ir drs. braam et al. *basiskennis beton*. 2015.
[17] Bažant and Wahab. “Stability of parallel cracks in solids reinforced by bars”. In: (1980), pp. 97–105.
[18] Bažant. “stability conditions for propagation of a system of cracks in a brittle solid”. In: 5 (1977), pp. 353–366.
[19] Y Yang. “Shear Behaviour of Reinforced Concrete Members without Shear Reinforcement”. PhD thesis. 2014.
[20] Robert J Frosch. “Another Look at Cracking and Crack Control in Reinforced Concrete”. In: (2000), pp. 437–442.
[21] E.O.L. Lantsoght et al. “Stop Criteria for Flexure for Proof Load Testing of Reinforced Concrete Structures”. In: (2019).
[22] Werner Vos. “Stop criteria for proof loading”. In: (2016).
[23] G. I. Zarate and E.O.L. Lantsoght. “Stevin report 25.5-20-02 Literature review on shear cracking and shear mechanism in RC slab bridges”. In: (2020).

[24] Aurelio Muttoni and Joseph Schwartz. “Behavior of Beams and Punching in Slabs without Shear Reinforcement”. In: *IABSE Colloquium* (1991), pp. 703–708.
[25] Aurelio Muttoni and Miguel Fernández Ruiz. “Shear strength of members without transverse reinforcement as function of critical shear crack width”. In: *ACI Structural Journal* (2008), pp. 163–172.
[26] Rui V A Z Rodrigues. “shear strength of reinforced concrete bridge deck slabs”. PhD thesis. 2007.
[27] E.O.L. Lantsoght. *Shear in Reinforced Concrete Slabs under Concentrated Loads close to Supports*. 2013.
[28] Rijkswaterstaat. *Richtlijnen Beoordeling Kunstwerken - beoordeling van de constructieve veiligheid van een bestaand kunstwerk bij verbouw, gebruik en afkeur*. Tech. rep.
[29] Aurelio Muttoni and Andor Windisch. “Punching shear strength of reinforced concrete slabs without transverse reinforcement”. In: *ACI Structural Journal* (2009), p. 381.
[30] Juan Sagaseta et al. “Non-axis-symmetrical punching shear around internal columns of RC slabs without transverse reinforcement”. In: *Magazine of Concrete Research* (2011), pp. 441–457.
[31] *TRB e-circular*. Tech. rep. November. 2019.
[32] E.O.L.; Lantsoght et al. “State-of-the-art on load testing of concrete bridges”. In: *Engineering Structures* (2017).
[33] ACI committee 437. *Code requirenments for Load Testing of Existing Concrete Structures (ACI 437.2M- 13) and Commentary.* Tech. rep. 2013.
[34] NCHRP. “Manual for Bridge Rating through Load Testing”. In: *V. NCHRP Project 12-28(13)A* (1998), p. 152.
[35] U A Bewertung. “DAfStb-Richtlinie Belastungsversuche an Betonbauwerken (Entwurf)”. In: (2019), pp. 1–24.
[36] van Leeuwen. “OVER DE SCHEURVORMING IN PLATEN”. In: (1962), pp. 50–62.
[37] Th. Monnier. “The moment curvature relation of reinforced concrete”. In: *Heron 17.2* (1970).
[38] K Benitez and Y Yang. “Development of a Stop Criterion for Load Tests based on the Critical Shear Displacement Theory”. In: (2014).
[39] J.C. Walraven. “AGGREGATE INTERLOCK: A theoretical and experimental analysis”. In: (1980).
[40] Rijkswaterstaat. *Inventarisatie kunstwerken*. Tech. rep. 2007.
[41] B.D. Gupta. “Fiber Optic Sensors: Principles and Applications”. In: (2006), p. 294.
[42] Bahaa E. A. Saleh and Malvin Carl Teich. *Photons in Semiconductors*. 2003, pp. 542–591.
[43] Sylvain Lecler and Patrick Meyrueis. “Intrinsic Optical Fiber Sensor”. In: (2012).
[44] Pierre Ferdinand. “The Evolution of Optical Fiber Sensors Technologies During the 35 Last Years The Evolution of Optical Fiber Sensors Technologies During the 35 Last Years and Their Applications in Structure Health Monitoring”. In: (2016).
[45] José Miguel López-higuera et al. “Fiber Optic Sensors in Structural Health Monitoring”. In: (2011), pp. 587–608.
[46] Yanliang Du et al. *Optical Fiber Sensing and Structural Health Monitoring Technology*. 2019.
[47] Gust Van Lysebetten and Noël Huybrechts. “DISTRIBUTED STRAIN / TEMPERATURE SENSING : RECENTE ERVARINGEN”. In: *Geotechniek* November (2019).

[48] Michael G. Tanner et al. “High-resolution single-mode fiber-optic distributed Raman sensor for absolute temperature measurement using superconducting nanowire single-photon detectors”. In: *Applied Physics Letters* (2011).
[49] R Feced et al. “Advances in high resolution distributed temperature sensing using the time-correlated single photon counting technique”. In: *IEE* (1997).
[50] Noël Huybrechts, Gust Van Lysebetten, and Monica de Vos. “Advanced monitoring techniques for a wide range of geotechnical applications Techniques de monitoring avancées pour un large domaine d ’ applications géotechniques”. In: (2017), pp. 2781–2784.
[51] Dexin Ba et al. “Distributed measurement of dynamic strain based on multi-slope assisted fast BOTDA”. In: (2016), pp. 1229–1235.
[52] Yosuke Mizuno et al. “Ultrahigh-speed distributed brillouin reflectometry”. In: *Light: Science and Applications* June (2016), pp. 1–8.
[53] “Single-shot BOTDA based on an optical chirp chain probe wave for distributed ultrafast measurement”. In: *Light: Science and Applications* 1 (2018), pp. 26–32. DOI: 10.1038/s41377-018-0030-0.
[54] J. H. L. Grave. “Measuring changing strain fields in composites with Distributed Fiber-Optic Sensing using the optical backscatter reflectometer”. In: *Composites Part B: Engineering* (2015), pp. 138–146.
[55] Dirk Samiec. “Distributed fibre-optic temperature and strain measurement with extremely high spatial resolution”. In: (2011).
[56] Gerardo Rodriguez, Joan R Casas, and Sergi Villalba. “Shear crack width assessment in concrete structures by 2D distributed optical fiber”. In: *Engineering Structures* May (2019), pp. 508–523.
[57] António Barrias et al. “Application of distributed optical fiber sensors for the health monitoring of two real structures in Barcelona”. In: *Structure and Infrastructure Engineering* (2018), pp. 1–19.
[58] Honglei Guo et al. “Fiber Optic Sensors for Structural Health Monitoring of Air Platforms”. In: (2011), pp. 3687–3705.
[59] Whitten L. Schulz, Joel P. Conte, and Eric Udd. “Long-gage fiber optic Bragg grating strain sensors to monitor civil structures”. In: *Smart Structures and Materials 2001: Smart Systems for Bridges, Structures, and Highways* July 2001 (2001), pp. 56–65.
[60] Gintaris Kaklauskas, Aleksandr Sokolov, and Regimantas Ramanauskas. “Reinforcement Strains in Reinforced Concrete Tensile Members Recorded by Strain Gauges and FBG Sensors : Experimental and Numerical Analysis”. In: (2019), pp. 1–13.
[61] António Barrias, Joan R. Casas, and Sergi Villalba. “Embedded Distributed Optical Fiber Sensors in”. In: (2018), pp. 1–22.
[62] V Villalba and Joan R Casas. “Application of OBR fiber optic technology in the Structural Health Monitoring of the Can Fatjó Viaduct (Cerdanyola del Vallés - Spain)”. In: (2012), pp. 498–501.
[63] Oliver Fischer, Sebastian Thoma, and Simone Crepaz. “Distributed fiber optic sensing for crack detection in concrete structures”. In: July (2019), pp. 97–105.
[64] Sebastian Felix Gehrlein and Oliver Fischer. “Full-scale shear capacity testing of an existing prestressed concrete bridge Testing concept , experimental set-up , measuring technique , and essential findings”. In: (2019), pp. 64–73.
[65] Gerardo Rodríguez, Joan R Casas, and Sergi Villaba. “Cracking assessment in concrete structures by distributed optical fiber”. In: (2015).
[66] G Zarate. *Stevin Report 25.5-14-09 Measurement report of reinforced concrete slabs*. Tech. rep. 2021.

[67] E.O.L. Lantsoght. *Stevin Report 25.5-17-05 Beams from Ruytenschildt Bridge: Analysis of stop criteria*. Tech. rep. 2017.

A Slab calculations

A.1 Initial calculations

Crack width:

$w_{max} = \frac{1}{2}\frac{f_{ctm}}{\tau_{bm}}\frac{\Phi}{\rho_{eff}}\frac{1}{E_s}(\sigma_s - \alpha\sigma_{sr} = \frac{1}{2}\frac{3.21}{6.42}\frac{20}{0.01}\frac{1}{200000}(560 - 0.5 * 48 = 1.34mm)$

A.2 Shear strength

$$V_{R,c} = b_{eff}d(C_{R,c}k_h(100\rho_l f_c)^{1/3}) \tag{A.1}$$

with:

$$k_h = 1 + \sqrt{\frac{200mm}{d}} \leq 2 \tag{A.2}$$

gives $1 + \sqrt{\frac{200mm}{265}} = 1.87$

for $b_{eff} = 1385$ mm $V_{R,c} = 1385 * 265 * (0.15 * 1.875(100 * 0.00996 * 43)^{1/3}) = 361$ kN

for $b_{eff} = 1785$ mm $V_{R,c} = 1785 * 265 * (0.15 * 1.875(100 * 0.00996 * 43)^{1/3}) = 465$ kN

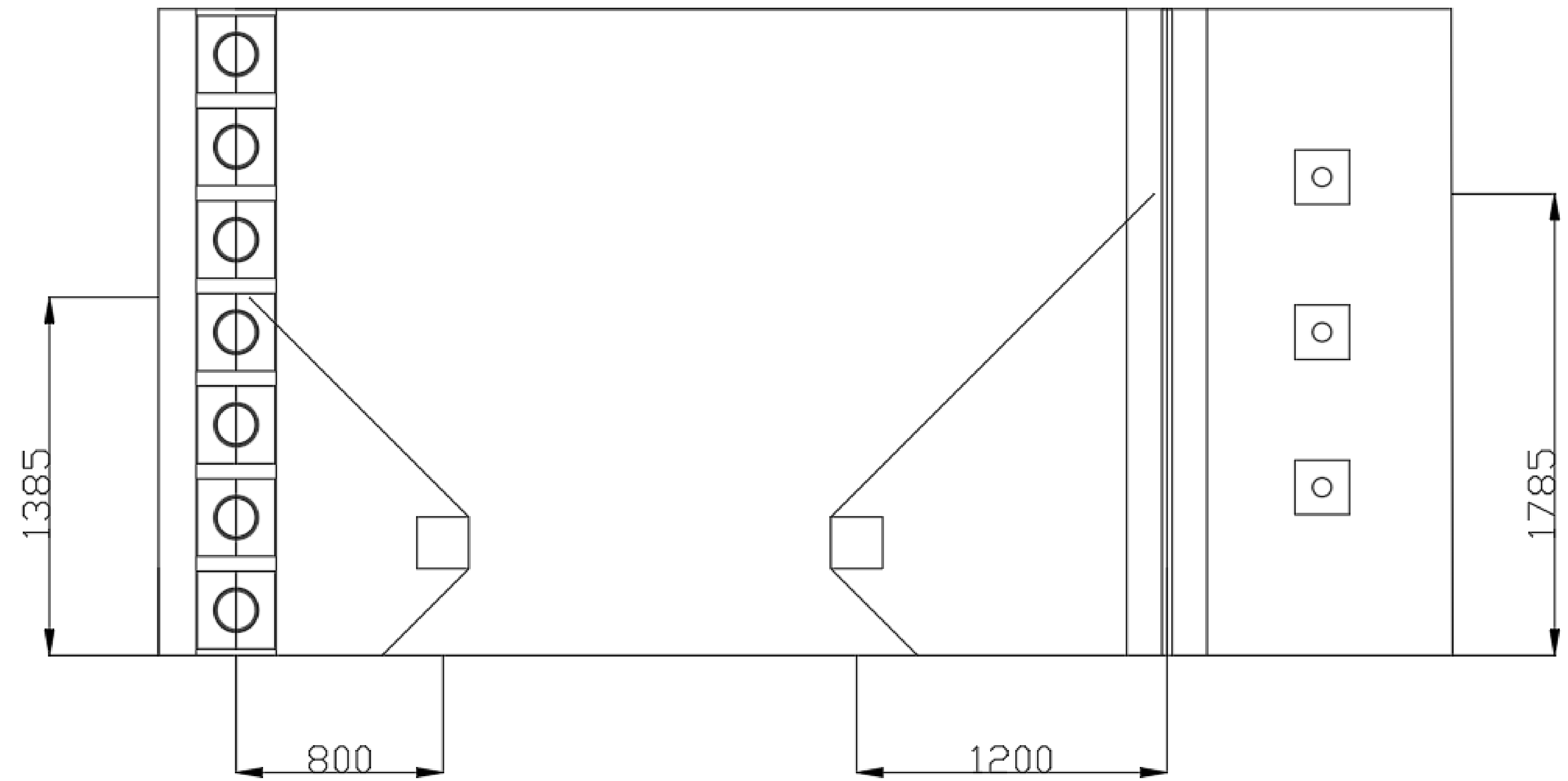

A.3 Calculation of self weight strains

location	0	0,3	0,5	0,7	0,9	1,1	1,3	1,5	1,7	1,8	1,9	2,1	2,3	2,5	2,7	2,9	3,1	3,3	3,5	3,6
M	-0,84	7,56	12,23	16,15	19,31	21,73	23,40	24,31	24,48	24,28	23,90	22,56	20,48	17,65	14,06	9,73	4,65	-1,19	-7,77	-11,34
sigma	-0,02	0,18	0,30	0,39	0,47	0,52	0,57	0,59	0,59	0,59	0,58	0,55	0,49	0,43	0,34	0,24	0,11	-0,03	-0,19	-0,27
με	-0,60	5,36	8,66	11,44	13,68	15,39	16,57	17,22	17,34	17,20	16,93	15,98	14,51	12,50	9,96	6,89	3,29	-0,84	-5,50	-8,04

A.4 Calculation of deflection by numerical integration

350 kN

Measured external strain

		0,3	0,5	0,7	0,9	1,1	1,3	1,5	1,7	1,9	2,1	2,3	2,5	2,7	2,9	3,1	3,3		[m]
		3,39885E-05	5,27E-05	8,00005E-05	0,000267	0,000365	0,000354	0,000965	0,000749	0,000883	0,000865	0,000707	0,00017	0,000100651	6,7E-05	3,52E-05	1,25E-05		[-]

Measured internal strain

		0,075	0,225	0,375	0,525	0,675	0,825	0,975	1,125	1,275	1,425	1,575	1,725	1,875	2,025	2,175	2,325	2,475	2,625	2,775	2,925	3,075	3,225	3,375	3,525		[m]
		1,25291E-06	9,58E-06	2,15846E-05	3,83E-05	4,84E-05	9,22E-05	0,000147	0,000257	0,000393	0,000655	0,000898	0,000641	0,00086061	0,000584	0,000494	0,000328	0,000161274	0,000101	5,42E-05	3,78E-05	2,32E-05	9,57E-06	-3E-06	-1,2E-05		[-]

Internal strain avaraged at locations external strain

		0,3	0,5	0,7	0,9	1,1	1,3	1,5	1,7	1,9	2,1	2,3	2,5	2,7	2,9	3,1	3,3		[m]
		1,5583E-05	3,55E-05	5,574E-05	0,00012	0,000239	0,000437	0,000776	0,000683	0,000814	0,000539	0,000355	0,000151	7,78231E-05	4,05E-05	2,1E-05	3,3E-06		[-]

Deflection calculation external sensors

Iterate compressive zone following Thornfelds parabola based on steel stress:

		131	131	131	131	131	131	106	113	108	109	112	131	131	131	131	131		[mm]
		4,855007056	7,530885	11,42748973	38,10776	52,13879	50,55259	145,1701	111,1585	132,3143	129,4414	105,1325	24,30057	14,37727773	9,574015	5,02239	1,790368		[N/mm2]

Calculate curvature:

		0,3	0,5	0,7	0,9	1,1	1,3	1,5	1,7	1,9	2,1	2,3	2,5	2,7	2,9	3,1	3,3		[m]
		1,7253E-07	2,68E-07	4,06094E-07	1,35E-06	1,85E-06	1,8E-06	4,35E-06	3,48E-06	4,01E-06	3,95E-06	3,27E-06	8,64E-07	5,1092E-07	3,4E-07	1,78E-07	6,36E-08		

Calculate ΔPhi

	0,1	0,3	0,5	0,7	0,9	1,1	1,3	1,5	1,7	1,9	2,1	2,3	2,5	2,7	2,9	3,1	3,3	3,5	[m]
	1,54878E-05	3,45061E-05	5,35E-05	8,12188E-05	0,000271	0,000371	0,000359	0,00087	0,000696	0,000803	0,00079	0,000654	0,000173	0,000102184	6,8E-05	3,57E-05	1,27E-05	-1,0246E-05	

Determine initial phi, such that deflection is 0 at simple support (red cell)

	0	0,2	0,4	0,6	0,8	1	1,2	1,4	1,6	1,8	2	2,2	2,4	2,6	2,8	3	3,2	3,4	[m]
	-0,002615495	-0,00260001	-0,00257	-0,00251198	-0,00243	-0,00216	-0,00179	-0,00143	-0,00056	0,000136	0,000939	0,001729	0,002383	0,002555978	0,002658	0,002726	0,002762	0,002774628	

Determine deflection

0	0,2	0,4	0,6	0,8	1	1,2	1,4	1,6	1,8	2	2,2	2,4	2,6	2,8	3	3,2	3,4	3,6	[m]
0	-0,52309906	-1,04310057	-1,5562	-2,05859626	-2,54475	-2,97673	-3,3346	-3,62061	-3,73271	-3,70552	-3,5178	-3,17203	-2,69538	-2,18417992	-1,65255	-1,10731	-0,55493	-3,3307E-15	[mm]

Deflection calculation internal sensors

Iterate compressive zone following Thornfelds parabola based on steel stress:

		131	131	131	131	122,5	127,6	112	115,7	111	122,5	131	131	131	131	131	131		[mm]
		2,225923995	5,077528	7,962054088	17,11632	34,82331	62,88963	115,4653	100,9375	121,3794	78,46718	50,76476	21,61209	11,11645881	5,790143	2,994765	0,471777		[N/mm2]

Calculate curvature:

		0,3	0,5	0,7	0,9	1,1	1,3	1,5	1,7	1,9	2,1	2,3	2,5	2,7	2,9	3,1	3,3		[m]
		7,91018E-08	1,8E-07	2,82944E-07	6,08E-07	1,16E-06	2,18E-06	3,59E-06	3,22E-06	3,75E-06	2,62E-06	1,8E-06	7,68E-07	3,95041E-07	2,06E-07	1,06E-07	1,68E-08		

Calculate ΔPhi

	0,1	0,3	0,5	0,7	0,9	1,1	1,3	1,5	1,7	1,9	2,1	2,3	2,5	2,7	2,9	3,1	3,3	3,5	[m]
	-4,44691E-06	1,58204E-05	3,61E-05	5,65889E-05	0,000122	0,000233	0,000436	0,000719	0,000644	0,000751	0,000524	0,000361	0,000154	7,90082E-05	4,12E-05	2,13E-05	3,35E-06	-1,4579E-05	

Determine initial phi, such that deflection is 0 at simple support (red cell)

	0	0,2	0,4	0,6	0,8	1	1,2	1,4	1,6	1,8	2	2,2	2,4	2,6	2,8	3	3,2	3,4	[m]
	-0,00204205	-0,0020465	-0,00203	-0,00199459	-0,00194	-0,00182	-0,00158	-0,00115	-0,00043	0,000215	0,000966	0,00149	0,001851	0,002004397	0,002083	0,002125	0,002146	0,002149195	

Determine deflection

0	0,2	0,4	0,6	0,8	1	1,2	1,4	1,6	1,8	2	2,2	2,4	2,6	2,8	3	3,2	3,4	3,6	[m]
0	-0,40841	-0,81770938	-1,22384	-1,62276248	-2,01036	-2,37363	-2,69035	-2,91989	-3,00569	-2,9627	-2,76959	-2,47159	-2,10143	-1,70055186	-1,28387	-0,85896	-0,42979	4,80414E-05	[mm]

500 kN																									
Measured external strain																									
		0,3	0,5	0,7	0,9	1,1	1,3	1,5	1,7	1,9	2,1	2,3	2,5	2,7	2,9	3,1	3,3		[m]						
		0,000117891	0,000142	0,000125322	0,000667	0,00065	0,00082	0,001821	0,001053	0,001611	0,001595	0,001594	0,000359	0,000207363	9,23E-05	3,48E-05	9,09E-06		[-]						
Measured internal strain																									
		0,075	0,225	0,375	0,525	0,675	0,825	0,975	1,125	1,275	1,425	1,575	1,725	1,875	2,025	2,175	2,325	2,475	2,625	2,775	2,925	3,075	3,225	3,375	3,525
		7,46707E-06	2,06E-05	3,63352E-05	9,55E-05	0,000122	0,00027	0,000518	0,000808	0,001125	0,001442	0,001676	0,001451	0,001694046	0,00138	0,001236	0,000936	0,00063669	0,000316	9,87E-05	6,5E-05	3,9E-05	1,59E-05	-4,5E-06	-1,9E-05
Internal strain avaraged at locations external strain																									
		0,3	0,5	0,7	0,9	1,1	1,3	1,5	1,7	1,9	2,1	2,3	2,5	2,7	2,9	3,1	3,3		[m]						
		2,84461E-05	8,56E-05	0,00014659	0,000394	0,00076	0,001178	0,001559	0,001488	0,001642	0,001308	0,000986	0,000583	0,000207239	7,06E-05	3,52E-05	5,69E-06		[-]						
Deflection calculation external sensors																									
Iterate compressive zone following Thornfelds parabola based on steel stress:																									
		131	131	131	115,7	115,7	111	101,6	104	94,5	94,5	94,5	131	131	131	131	131		[mm]						
		16,83987769	20,26887	17,90131992	98,48597	95,93784	122,1629	275,9813	158,9554	247,0624	244,5962	244,3863	51,25328	29,62026756	13,17747	4,977282	1,298343		[N/mm2]						
Calculate curvature:																									
		0,3	0,5	0,7	0,9	1,1	1,3	1,5	1,7	1,9	2,1	2,3	2,5	2,7	2,9	3,1	3,3		[m]						
		5,98432E-07	7,2E-07	6,36152E-07	3,14E-06	3,06E-06	3,78E-06	8,04E-06	4,7E-06	6,9E-06	6,83E-06	6,83E-06	1,82E-06	1,0526E-06	4,68E-07	1,77E-07	4,61E-08								
Calculate ΔPhi																									
	0,1	0,3	0,5	0,7	0,9	1,1	1,3	1,5	1,7	1,9	2,1	2,3	2,5	2,7	2,9	3,1	3,3	3,5	[m]						
	9,53155E-05	0,000119686	0,000144	0,00012723	0,000628	0,000612	0,000755	0,001609	0,00094	0,00138	0,001366	0,001365	0,000364	0,000210521	9,37E-05	3,54E-05	9,23E-06	-1,692E-05							
Determine initial phi, such that deflection is 0 at simple support (red cell)																									
	0	0,2	0,4	0,6	0,8	1	1,2	1,4	1,6	1,8	2	2,2	2,4	2,6	2,8	3	3,2	3,4	[m]						
	-0,004870344	-0,00477503	-0,00466	-0,00451128	-0,00438	-0,00376	-0,00314	-0,00239	-0,00078	0,000161	0,001541	0,002907	0,004272	0,004636194	0,004847	0,00494	0,004976	0,004984974							
Determine deflection																									
0	0,2	0,4	0,6	0,8	1	1,2	1,4	1,6	1,8	2	2,2	2,4	2,6	2,8	3	3,2	3,4	3,6	[m]						
0	-0,974068787	-1,92907448	-2,86014	-3,76239983	-4,63921	-5,39037	-6,01914	-6,49681	-6,65276	-6,62066	-6,31255	-5,73118	-4,8768	-3,94956104	-2,98022	-1,99214	-0,99699	-2,2204E-15	[mm]						
Deflection calculation internal sensors																									
Iterate compressive zone following Thornfelds parabola based on steel stress:																									
		131	131	131	131	113	102,8	95	96,5	94	100,4	106	120,8	131	131	131	131		[mm]						
		4,063312439	12,2322	20,93926147	56,25301	112,7908	178,171	238,7976	227,4703	251,9281	198,6107	148,3357	85,23352	29,60260685	10,08559	5,022015	0,813461		[N/mm2]						
Calculate curvature:																									
		0,3	0,5	0,7	0,9	1,1	1,3	1,5	1,7	1,9	2,1	2,3	2,5	2,7	2,9	3,1	3,3		[m]						
		1,44396E-07	4,35E-07	7,4411E-07	2E-06	3,53E-06	5,23E-06	6,69E-06	6,43E-06	7,02E-06	5,75E-06	4,44E-06	2,81E-06	1,05198E-06	3,58E-07	1,78E-07	2,89E-08								
Calculate ΔPhi																									
	0,1	0,3	0,5	0,7	0,9	1,1	1,3	1,5	1,7	1,9	2,1	2,3	2,5	2,7	2,9	3,1	3,3	3,5	[m]						
	-2,91796E-05	2,88793E-05	8,69E-05	0,000148822	0,0004	0,000707	0,001046	0,001338	0,001286	0,001403	0,001149	0,000889	0,000563	0,000210395	7,17E-05	3,57E-05	5,78E-06	-2,413E-05							
Determine initial phi, such that deflection is 0 at simple support (red cell)																									
	0	0,2	0,4	0,6	0,8	1	1,2	1,4	1,6	1,8	2	2,2	2,4	2,6	2,8	3	3,2	3,4	[m]						
	0,005108011	0,005078831	0,005108	0,005194649	0,005343	0,005743	0,00645	0,007496	0,008834	0,01012	0,011523	0,012672	0,01356	0,014123348	0,014334	0,014405	0,014441	0,014446899							
Determine deflection																									
0	0,2	0,4	0,6	0,8	1	1,2	1,4	1,6	1,8	2	2,2	2,4	2,6	2,8	3	3,2	3,4	3,6	[m]						
0	1,02160221	2,037368498	3,058911	4,097840407	5,166535	6,31519	7,605188	9,104417	10,87121	12,89513	15,19968	17,73406	20,44615	23,27081751	26,13757	29,01865	31,90687	34,79625418	[mm]						

750 kN																									
Measured external strain																									
		0,3	0,5	0,7	0,9	1,1	1,3	1,5	1,7	1,9	2,1	2,3	2,5	2,7	2,9	3,1	3,3		[m]						
		0,000201271	0,000154	0,000408068	0,001415	0,00116	0,001385	0,003163	0,001897	0,002684	0,002833	0,00272	0,000763	0,000562073	0,000216	4,42E-05	-2,9E-06		[-]						
Measured internal strain																									
		0,075	0,225	0,375	0,525	0,675	0,825	0,975	1,125	1,275	1,425	1,575	1,725	1,875	2,025	2,175	2,325	2,475	2,625	2,775	2,925	3,075	3,225	3,375	3,525
		6,31969E-06	2,36E-05	4,63499E-05	0,000148	0,000376	0,000503	0,000993	0,001495	0,001454	0,002192	0,002595	0,002359	0,002505782	0,002154	0,001813	0,001482	0,001151731	0,000772	0,000202	9,59E-05	5,14E-05	7,88E-06	-2,1E-05	-4,6E-05
Internal strain avaraged at locations external strain																									
		0,3	0,5	0,7	0,9	1,1	1,3	1,5	1,7	1,9	2,1	2,3	2,5	2,7	2,9	3,1	3,3		[m]						
		3,49977E-05	0,000131	0,000397067	0,000748	0,001411	0,001577	0,002393	0,002398	0,002447	0,001984	0,001537	0,001088	0,000486785	0,000114	4,42E-05	-6,5E-06		[-]						
Deflection calculation external sensors																									
Iterate compressive zone following Thornfelds parabola based on steel stress:																									
		131	131	129,3	97,5	112	98	82,2	91	84	83,6	84	113	120,8	131	131	131		[mm]						
		28,75005592	22,06385	58,52390849	215,9774	172,5152	211,1084	494,0078	292,4561	418,0543	441,5858	423,6651	113,3079	82,14615276	30,80725	6,30656	-0,41227		[N/mm2]						
Calculate curvature:																									
		0,3	0,5	0,7	0,9	1,1	1,3	1,5	1,7	1,9	2,1	2,3	2,5	2,7	2,9	3,1	3,3		[m]						
		1,02168E-06	7,84E-07	2,05369E-06	6,14E-06	5,37E-06	6,02E-06	1,29E-05	8E-06	1,1E-05	1,16E-05	1,11E-05	3,55E-06	2,71271E-06	1,09E-06	2,24E-07	-1,5E-08								
Calculate ΔPhi																									
	0,1	0,3	0,5	0,7	0,9	1,1	1,3	1,5	1,7	1,9	2,1	2,3	2,5	2,7	2,9	3,1	3,3	3,5	[m]						
	0,000251857	0,000204336	0,000157	0,000410737	0,001228	0,001074	0,001204	0,002574	0,001601	0,0022	0,002318	0,002229	0,00071	0,000542541	0,000219	4,48E-05	-2,9E-06	-5,0683E-05							
Determine initial phi, such that deflection is 0 at simple support (red cell)																									
	0	0,2	0,4	0,6	0,8	1	1,2	1,4	1,6	1,8	2	2,2	2,4	2,6	2,8	3	3,2	3,4	[m]						
	-0,0084198	-0,00816794	-0,00796	-0,00780679	-0,0074	-0,00617	-0,00509	-0,00389	-0,00132	0,000284	0,002484	0,004802	0,007032	0,007741538	0,008284	0,008503	0,008548	0,008544928							
Determine deflection																									
0	0,2	0,4	0,6	0,8	1	1,2	1,4	1,6	1,8	2	2,2	2,4	2,6	2,8	3	3,2	3,4	3,6	[m]						
0	-1,68396	-3,31754862	-4,91027	-6,47162855	-7,95084	-9,18445	-10,2033	-10,9813	-11,2446	-11,1878	-10,691	-9,73052	-8,3242	-6,77589468	-5,11908	-3,41847	-1,7089	8,56083E-05	[mm]						
Deflection calculation internal sensors																									
Iterate compressive zone following Thornfelds parabola based on steel stress:																									
		131	131	129,3	114	98	95	87	87	86,4	89,8	96	104	125,9	131	131	131		[mm]						
		4,999161169	18,73951	56,94621607	110,8472	215,1478	241,619	371,2072	371,9991	379,9042	306,3746	235,1724	164,2797	70,35859691	16,21528	6,311078	-0,93382		[N/mm2]						
Calculate curvature:																									
		0,3	0,5	0,7	0,9	1,1	1,3	1,5	1,7	1,9	2,1	2,3	2,5	2,7	2,9	3,1	3,3		[m]						
		1,77653E-07	6,66E-07	1,99832E-06	3,5E-06	6,13E-06	6,77E-06	9,93E-06	9,95E-06	1,01E-05	8,33E-06	6,63E-06	4,86E-06	2,40863E-06	5,76E-07	2,24E-07	-3,3E-08								
Calculate ΔPhi																									
	0,1	0,3	0,5	0,7	0,9	1,1	1,3	1,5	1,7	1,9	2,1	2,3	2,5	2,7	2,9	3,1	3,3	3,5	[m]						
	-6,21264E-05	3,55306E-05	0,000133	0,000399665	0,000699	0,001227	0,001354	0,001986	0,00199	0,002026	0,001665	0,001325	0,000972	0,000481727	0,000115	4,49E-05	-6,6E-06	-5,8129E-05							
Determine initial phi, such that deflection is 0 at simple support (red cell)																									
	0	0,2	0,4	0,6	0,8	1	1,2	1,4	1,6	1,8	2	2,2	2,4	2,6	2,8	3	3,2	3,4	[m]						
	-0,00703405	-0,00709618	-0,00706	-0,00692746	-0,00653	-0,00583	-0,0046	-0,00325	-0,00126	0,000728	0,002754	0,00442	0,005745	0,006716742	0,007198	0,007314	0,007359	0,007351934							
Determine deflection																									
0	0,2	0,4	0,6	0,8	1	1,2	1,4	1,6	1,8	2	2,2	2,4	2,6	2,8	3	3,2	3,4	3,6	[m]						
0	-1,40681	-2,82604528	-4,23817	-5,62366606	-6,92922	-8,09496	-9,0153	-9,66492	-9,91731	-9,77163	-9,22078	-8,33685	-7,18786	-5,84450872	-4,40482	-2,94207	-1,47036	2,89156E-05	[mm]						

850 kN																									
Measured external strain																									
		0,3	0,5	0,7	0,9	1,1	1,3	1,5	1,7	1,9	2,1	2,3	2,5	2,7	2,9	3,1	3,3		[m]						
		0,000212994	0,000161	0,00048024	0,001643	0,001335	0,001524	0,003813	0,002271	0,003208	0,003318	0,003101	0,000878	0,000663676	0,000261	4,02E-05	-1,5E-05		[-]						
Measured internal strain																									
		0,075	0,225	0,375	0,525	0,675	0,825	0,975	1,125	1,275	1,425	1,575	1,725	1,875	2,025	2,175	2,325	2,475	2,625	2,775	2,925	3,075	3,225	3,375	3,525
		3,83197E-06	2,23E-05	4,73461E-05	0,000173	0,000468	0,000609	0,001187	0,001759	0,00183	0,002544	0,003047	0,002753	0,002906516	0,002548	0,002101	0,001728	0,001355639	0,000935	0,000259	0,000113	4,79E-05	-1,9E-06	-3,4E-05	-6,4E-05
Internal strain avaraged at locations external strain																									
		0,3	0,5	0,7	0,9	1,1	1,3	1,5	1,7	1,9	2,1	2,3	2,5	2,7	2,9	3,1	3,3		[m]						
		3,48343E-05	0,000152	0,000491313	0,000898	0,001663	0,001949	0,002795	0,002802	0,002847	0,002325	0,001791	0,001286	0,000597306	0,000137	3,96E-05	-1,8E-05		[-]						
Deflection calculation external sensors																									
Iterate compressive zone following Thornfelds parabola based on steel stress:																									
		131	131	125,9	94	99,2	95,5	81	87,6	82	82	82,4	109	117,4	131	131	131		[mm]						
		30,4245609	22,97827	69,41266946	252,0973	203,147	233,3112	596,46	351,892	501,137	518,3691	484,1478	131,3677	97,6794731	37,27343	5,736243	-2,14707		[N/mm2]						
Calculate curvature:																									
		0,3	0,5	0,7	0,9	1,1	1,3	1,5	1,7	1,9	2,1	2,3	2,5	2,7	2,9	3,1	3,3		[m]						
		1,08119E-06	8,17E-07	2,37625E-06	7,02E-06	5,83E-06	6,55E-06	1,54E-05	9,45E-06	1,3E-05	1,35E-05	1,26E-05	4,01E-06	3,15136E-06	1,32E-06	2,04E-07	-7,6E-08								
Calculate ΔPhi																									
	0,1	0,3	0,5	0,7	0,9	1,1	1,3	1,5	1,7	1,9	2,1	2,3	2,5	2,7	2,9	3,1	3,3	3,5	[m]						
	0,00026916	0,000216237	0,000163	0,00047525	0,001404	0,001167	0,001311	0,003087	0,001889	0,002608	0,002698	0,002525	0,000802	0,000630271	0,000265	4,08E-05	-1,5E-05	-7,1289E-05							
Determine initial phi, such that deflection is 0 at simple support (red cell)																									
	0	0,2	0,4	0,6	0,8	1	1,2	1,4	1,6	1,8	2	2,2	2,4	2,6	2,8	3	3,2	3,4	[m]						
	-0,009665611	-0,00939645	-0,00918	-0,0090169	-0,00854	-0,00714	-0,00597	-0,00466	-0,00157	0,000317	0,002925	0,005622	0,008148	0,008949584	0,00958	0,009845	0,009886	0,00987028							
Determine deflection																									
0	0,2	0,4	0,6	0,8	1	1,2	1,4	1,6	1,8	2	2,2	2,4	2,6	2,8	3	3,2	3,4	3,6	[m]						
0	-1,93312221	-3,81241236	-5,64846	-7,45183503	-9,16016	-10,5877	-11,7818	-12,7138	-13,0283	-12,9649	-12,38	-11,2555	-9,62601	-7,83608904	-5,92012	-3,95116	-1,97406	-6,6613E-15	[mm]						
Deflection calculation internal sensors																									
Iterate compressive zone following Thornfelds parabola based on steel stress:																									
		131	131	124,2	109	94	91,8	83,6	83,6	83,5	87,4	92,2	99,8	125,9	131	131	131		[mm]						
		4,975819789	21,70705	71,28136521	134,2889	255,2599	300,1731	435,6759	436,7328	443,7812	360,3549	275,5667	195,4434	86,33299577	19,59697	5,65527	-2,57869		[N/mm2]						
Calculate curvature:																									
		0,3	0,5	0,7	0,9	1,1	1,3	1,5	1,7	1,9	2,1	2,3	2,5	2,7	2,9	3,1	3,3		[m]						
		1,76824E-07	7,71E-07	2,41076E-06	4,1E-06	7,11E-06	8,25E-06	1,14E-05	1,15E-05	1,16E-05	9,66E-06	7,59E-06	5,63E-06	2,9555E-06	6,96E-07	2,01E-07	-9,2E-08								
Calculate ΔPhi																									
	0,1	0,3	0,5	0,7	0,9	1,1	1,3	1,5	1,7	1,9	2,1	2,3	2,5	2,7	2,9	3,1	3,3	3,5	[m]						
	-8,35495E-05	3,53647E-05	0,000154	0,000482152	0,00082	0,001422	0,001651	0,002287	0,002293	0,002329	0,001932	0,001519	0,001127	0,000591099	0,000139	4,02E-05	-1,8E-05	-7,6849E-05							
Determine initial phi, such that deflection is 0 at simple support (red cell)																									
	0	0,2	0,4	0,6	0,8	1	1,2	1,4	1,6	1,8	2	2,2	2,4	2,6	2,8	3	3,2	3,4	[m]						
	-0,0081856	-0,00826915	-0,00823	-0,00807951	-0,0076	-0,00678	-0,00536	-0,00371	-0,00142	0,000875	0,003204	0,005136	0,006655	0,00778157	0,008373	0,008512	0,008552	0,008533818							
Determine deflection																									
0	0,2	0,4	0,6	0,8	1	1,2	1,4	1,6	1,8	2	2,2	2,4	2,6	2,8	3	3,2	3,4	3,6	[m]						
0	-1,63712	-3,2909499	-4,93771	-6,553608	-8,07308	-9,42858	-10,4998	-11,2408	-11,5244	-11,3494	-10,7087	-9,68145	-8,35048	-6,7941652	-5,11963	-3,41724	-1,70681	-4,8478E-05	[mm]						

950 kN																									
Measured external strain																									
		0,3	0,5	0,7	0,9	1,1	1,3	1,5	1,7	1,9	2,1	2,3	2,5	2,7	2,9	3,1	3,3		[m]						
		0,000221384	0,000182	0,000588122	0,001882	0,001538	0,001702	0,00457	0,002698	0,003897	0,003905	0,003645	0,001038	0,000805546	0,000332	3,51E-05	-2,9E-05		[-]						
Measured internal strain																									
		0,075	0,225	0,375	0,525	0,675	0,825	0,975	1,125	1,275	1,425	1,575	1,725	1,875	2,025	2,175	2,325	2,475	2,625	2,775	2,925	3,075	3,225	3,375	3,525
		6,22125E-07	1,72E-05	3,06747E-05	0,000187	0,000532	0,00066	0,001343	0,002005	0,001177	0,002671	0,003261	0,002941	0,003008793	0,002696	0,002007	0,001719	0,001430391	0,001052	0,000314	0,000137	3,85E-05	-1,5E-05	-5,3E-05	-8,6E-05
Internal strain avaraged at locations external strain																									
		0,3	0,5	0,7	0,9	1,1	1,3	1,5	1,7	1,9	2,1	2,3	2,5	2,7	2,9	3,1	3,3		[m]						
		2,39428E-05	0,000161	0,000553129	0,001002	0,001894	0,001426	0,002966	0,002994	0,002957	0,002351	0,001767	0,001367	0,000683078	0,000166	2,97E-05	-3,4E-05		[-]						
Deflection calculation external sensors																									
Iterate compressive zone following Thornfelds parabola based on steel stress:																									
		131	131	120,8	91	95,5	93	75	84	80	80	81	104	111	131	131	131		[mm]						
		31,6231267	26,04111	85,95328304	290,2338	235,5348	261,5351	720,7165	420,342	610,4895	611,7401	570,1917	156,7256	120,0523915	47,41349	5,012491	-4,19402		[N/mm2]						
Calculate curvature:																									
		0,3	0,5	0,7	0,9	1,1	1,3	1,5	1,7	1,9	2,1	2,3	2,5	2,7	2,9	3,1	3,3		[m]						
		1,12378E-06	9,25E-07	2,83843E-06	7,94E-06	6,62E-06	7,24E-06	1,81E-05	1,11E-05	1,57E-05	1,57E-05	1,48E-05	4,64E-06	3,7122E-06	1,68E-06	1,78E-07	-1,5E-07								
Calculate ΔPhi																									
	0,1	0,3	0,5	0,7	0,9	1,1	1,3	1,5	1,7	1,9	2,1	2,3	2,5	2,7	2,9	3,1	3,3	3,5	[m]						
	0,000264429	0,000224756	0,000185	0,000567686	0,001589	0,001323	0,001448	0,003613	0,002212	0,003143	0,003149	0,002951	0,000927	0,000742439	0,000337	3,56E-05	-3E-05	-9,5242E-05							
Determine initial phi, such that deflection is 0 at simple support (red cell)																									
	0	0,2	0,4	0,6	0,8	1	1,2	1,4	1,6	1,8	2	2,2	2,4	2,6	2,8	3	3,2	3,4	[m]						
	-0,011158987	-0,01089456	-0,01067	-0,01048472	-0,00992	-0,00833	-0,00701	-0,00556	-0,00194	0,000267	0,00341	0,00656	0,009511	0,01043791	0,01118	0,011517	0,011553	0,011523149							
Determine deflection																									
0	0,2	0,4	0,6	0,8	1	1,2	1,4	1,6	1,8	2	2,2	2,4	2,6	2,8	3	3,2	3,4	3,6	[m]						
0	-2,231797329	-4,41070888	-6,54467	-8,64161319	-10,625	-12,2907	-13,6917	-14,8031	-15,192	-15,1385	-14,4564	-13,1445	-11,2423	-9,1547574	-6,91869	-4,61522	-2,30463	-4,885E-15	[mm]						
Deflection calculation internal sensors																									
Iterate compressive zone following Thornfelds parabola based on steel stress:																									
		131	131	122,5	106	91	97	83	82,8	83	87,2	82,2	98	115,7	131	131	131		[mm]						
		3,420046502	23,0092	80,54682625	150,6474	292,0739	217,7656	462,6705	467,1874	461,2366	364,5933	275,9015	208,4881	100,8786679	23,76569	4,240257	-4,80259		[N/mm2]						
Calculate curvature:																									
		0,3	0,5	0,7	0,9	1,1	1,3	1,5	1,7	1,9	2,1	2,3	2,5	2,7	2,9	3,1	3,3		[m]						
		1,21537E-07	8,18E-07	2,69162E-06	4,51E-06	7,99E-06	6,17E-06	1,21E-05	1,22E-05	1,21E-05	9,76E-06	7,19E-06	5,94E-06	3,21751E-06	8,45E-07	1,51E-07	-1,7E-07								
Calculate ΔPhi																									
	0,1	0,3	0,5	0,7	0,9	1,1	1,3	1,5	1,7	1,9	2,1	2,3	2,5	2,7	2,9	3,1	3,3	3,5	[m]						
	-0,000114919	2,43074E-05	0,000164	0,000538325	0,000902	0,001599	0,001234	0,002421	0,002442	0,002414	0,001953	0,001437	0,001189	0,000643502	0,000169	3,01E-05	-3,4E-05	-9,8404E-05							
Determine initial phi, such that deflection is 0 at simple support (red cell)																									
	0	0,2	0,4	0,6	0,8	1	1,2	1,4	1,6	1,8	2	2,2	2,4	2,6	2,8	3	3,2	3,4	[m]						
	-0,0083202	-0,00843512	-0,00841	-0,00824728	-0,00771	-0,00681	-0,00521	-0,00397	-0,00155	0,00089	0,003303	0,005256	0,006694	0,007882624	0,008526	0,008695	0,008725	0,008691041							
Determine deflection																									
0	0,2	0,4	0,6	0,8	1	1,2	1,4	1,6	1,8	2	2,2	2,4	2,6	2,8	3	3,2	3,4	3,6	[m]						
0	-1,66404	-3,35106381	-5,03323	-6,68268172	-8,22447	-9,58579	-10,6274	-11,4221	-11,7325	-11,5546	-10,894	-9,84271	-8,50398	-6,92746007	-5,22223	-3,48323	-1,73819	1,56551E-05	[mm]						

1050 kN																										
Measured external strain																										
		0,3	0,5	0,7	0,9	1,1	1,3	1,5	1,7	1,9	2,1	2,3	2,5	2,7	2,9	3,1	3,3		[m]							
		0,000221607	0,000229	0,000693432	0,002091	0,001705	0,001917	0,005703	0,003246	0,004835	0,004848	0,004329	0,00135	0,000924496	0,00043	3,45E-05	-4E-05		[-]							
Measured internal strain																										
		0,075	0,225	0,375	0,525	0,675	0,825	0,975	1,125	1,275	1,425	1,575	1,725	1,875	2,025	2,175	2,325	2,475	2,625	2,775	2,925	3,075	3,225	3,375	3,525	
		2,70427E-06	2,67E-05	1,37411E-05	0,00023	0,000636	0,00081	0,001848	0,002551	0,001116	0,003343	0,003456	0,003569	0,00371955	0,003436	0,002418	0,002056	0,001693414	0,001273	0,000455	0,000226	3,57E-05	-2,7E-05	-7,8E-05	-0,00013	
Internal strain avaraged at locations external strain																										
		0,3	0,5	0,7	0,9	1,1	1,3	1,5	1,7	1,9	2,1	2,3	2,5	2,7	2,9	3,1	3,3		[m]							
		2,02387E-05	0,000194	0,000664822	0,001329	0,002433	0,001487	0,003399	0,003551	0,003672	0,002927	0,002116	0,001623	0,000864073	0,000264	2,54E-05	-5,2E-05		[-]							
Deflection calculation external sensors																										
Iterate compressive zone following Thornfelds parabola based on steel stress:																										
		131	131	114	88	92,2	89,4	65	82	70,8	70,8	75	98	106	127,6	131	131		[mm]							
		31,65496097	32,67951	102,7511188	323,8203	262,4205	296,3519	910,7148	507,087	766,6576	768,6832	682,6607	205,9102	139,049175	61,908	4,930712	-5,70812		[N/mm2]							
Calculate curvature:																										
		0,3	0,5	0,7	0,9	1,1	1,3	1,5	1,7	1,9	2,1	2,3	2,5	2,7	2,9	3,1	3,3		[m]							
		1,12491E-06	1,16E-06	3,24034E-06	8,71E-06	7,23E-06	8,04E-06	2,17E-05	1,32E-05	1,88E-05	1,88E-05	1,71E-05	5,87E-06	4,1644E-06	2,15E-06	1,75E-07	-2E-07									
Calculate ΔPhi																										
	0,1	0,3	0,5	0,7	0,9	1,1	1,3	1,5	1,7	1,9	2,1	2,3	2,5	2,7	2,9	3,1	3,3	3,5	[m]							
	0,0002177	0,000224982	0,000232	0,000648068	0,001742	0,001446	0,001607	0,004337	0,002639	0,00376	0,00377	0,003422	0,001174	0,000832879	0,000429	3,5E-05	-4,1E-05	-0,00011618								
Determine initial phi, such that deflection is 0 at simple support (red cell)																										
	0	0,2	0,4	0,6	0,8	1	1,2	1,4	1,6	1,8	2	2,2	2,4	2,6	2,8	3	3,2	3,4	[m]							
	-0,0128989	-0,0126812	-0,01246	-0,01222395	-0,01158	-0,00983	-0,00839	-0,00678	-0,00244	0,000196	0,003956	0,007725	0,011147	0,012321492	0,013154	0,013583	0,013619	0,013577958								
Determine deflection																										
0	0,2	0,4	0,6	0,8	1	1,2	1,4	1,6	1,8	2	2,2	2,4	2,6	2,8	3	3,2	3,4	3,6	[m]							
0	-2,57978	-5,11601996	-7,60726	-10,0520544	-12,3672	-14,3339	-16,0114	-17,3674	-17,856	-17,8168	-17,0257	-15,4806	-13,2512	-10,786877	-8,156	-5,43931	-2,7156	-8,9172E-06	[mm]							
Deflection calculation internal sensors																										
Iterate compressive zone following Thornfelds parabola based on steel stress:																										
		131	131	117,4	99,2	86,4	96,5	82	82	82	83,1	88,4	94,5	110	131	131	131		[mm]							
		2,890956472	27,6732	97,84819046	202,2446	377,7615	227,2776	531,0506	554,6577	573,6966	456,615	327,5678	248,9174	129,0163978	37,71547	3,622807	-7,47245		[N/mm2]							
Calculate curvature:																										
		0,3	0,5	0,7	0,9	1,1	1,3	1,5	1,7	1,9	2,1	2,3	2,5	2,7	2,9	3,1	3,3		[m]							
		1,02735E-07	9,83E-07	3,1568E-06	5,81E-06	1,01E-05	6,42E-06	1,38E-05	1,44E-05	1,49E-05	1,2E-05	8,83E-06	6,95E-06	3,96364E-06	1,34E-06	1,29E-07	-2,7E-07									
Calculate ΔPhi																										
	0,1	0,3	0,5	0,7	0,9	1,1	1,3	1,5	1,7	1,9	2,1	2,3	2,5	2,7	2,9	3,1	3,3	3,5	[m]							
	-0,000155588	2,0547E-05	0,000197	0,00063136	0,001162	0,002014	0,001285	0,002764	0,002887	0,002986	0,002391	0,001767	0,00139	0,000792727	0,000268	2,57E-05	-5,3E-05	-0,00013197								
Determine initial phi, such that deflection is 0 at simple support (red cell)																										
	0	0,2	0,4	0,6	0,8	1	1,2	1,4	1,6	1,8	2	2,2	2,4	2,6	2,8	3	3,2	3,4	[m]							
	-0,00992449	-0,01008008	-0,01006	-0,00986285	-0,00923	-0,00807	-0,00606	-0,00477	-0,00201	0,00088	0,003865	0,006256	0,008022	0,00941288	0,010206	0,010474	0,010499	0,010446303								
Determine deflection																										
0	0,2	0,4	0,6	0,8	1	1,2	1,4	1,6	1,8	2	2,2	2,4	2,6	2,8	3	3,2	3,4	3,6	[m]							
0	-1,984898	-4,00091368	-6,01282	-7,9853898	-9,83169	-11,4456	-12,6567	-13,6109	-14,0123	-13,8364	-13,0633	-11,8121	-10,2076	-8,32505449	-6,28393	-4,1892	-2,08932	-5,7512E-05	[mm]							

1123 kN																									
Measured external strain																									
		0,3	0,5	0,7	0,9	1,1	1,3	1,5	1,7	1,9	2,1	2,3	2,5	2,7	2,9	3,1	3,3		[m]						
		0,000216296	0,000253	0,000766045	0,002176	0,001696	0,001712	0,006767	0,003613	0,006199	0,006162	0,005367	0,000918	0,000924969	0,000494	3,17E-05	-6,1E-05		[-]						
Measured internal strain																									
		0,075	0,225	0,375	0,525	0,675	0,825	0,975	1,125	1,275	1,425	1,575	1,725	1,875	2,025	2,175	2,325	2,475	2,625	2,775	2,925	3,075	3,225	3,375	3,525
		6,90637E-06	3,47E-05	1,54775E-05	0,000265	0,000671	0,000897	0,002137	0,002831	0,002009	0,003709	0,003818	0,003927	0,0040979	0,003802	0,002854	0,002358	0,001860915	0,001361	0,000529	0,000269	4,41E-05	-2,6E-05	-8,2E-05	-0,00014
Internal strain avaraged at locations external strain																									
		0,3	0,5	0,7	0,9	1,1	1,3	1,5	1,7	1,9	2,1	2,3	2,5	2,7	2,9	3,1	3,3		[m]						
		2,51039E-05	0,000223	0,000708478	0,001517	0,002716	0,002293	0,003763	0,003909	0,004049	0,003328	0,00244	0,001778	0,000945271	0,000312	3,25E-05	-5,4E-05		[-]						
Deflection calculation external sensors																									
Iterate compressive zone following Thornfelds parabola based on steel stress:																									
		131	131	111	87,4	92,2	91,8	60	82	63	63	67	106	106	124,7	131	131		[mm]						
		30,896338	36,17835	114,1653509	337,3705	260,9853	263,5589	1087,018	564,4535	992,2569	986,3909	855,0488	138,0514	139,12036	71,53817	4,52699	-8,70864		[N/mm2]						
Calculate curvature:																									
		0,3	0,5	0,7	0,9	1,1	1,3	1,5	1,7	1,9	2,1	2,3	2,5	2,7	2,9	3,1	3,3		[m]						
		1,09795E-06	1,29E-06	3,53016E-06	9,05E-06	7,19E-06	7,25E-06	2,53E-05	1,47E-05	2,34E-05	2,33E-05	2,06E-05	4,13E-06	4,16653E-06	2,43E-06	1,61E-07	-3,1E-07								
Calculate ΔPhi																									
	0,1	0,3	0,5	0,7	0,9	1,1	1,3	1,5	1,7	1,9	2,1	2,3	2,5	2,7	2,9	3,1	3,3	3,5	[m]						
	0,000182049	0,00021959	0,000257	0,000706032	0,001809	0,001438	0,001449	0,00505	0,002938	0,004678	0,004651	0,004113	0,000827	0,000833306	0,000486	3,22E-05	-6,2E-05	-0,00015596							
Determine initial phi, such that deflection is 0 at simple support (red cell)																									
	0	0,2	0,4	0,6	0,8	1	1,2	1,4	1,6	1,8	2	2,2	2,4	2,6	2,8	3	3,2	3,4	[m]						
	-0,01431075	-0,0141287	-0,01391	-0,01365198	-0,01295	-0,01114	-0,0097	-0,00825	-0,0032	-0,00026	0,004417	0,009067	0,01318	0,014006982	0,01484	0,015326	0,015358	0,015296181							
Determine deflection																									
0	0,2	0,4	0,6	0,8	1	1,2	1,4	1,6	1,8	2	2,2	2,4	2,6	2,8	3	3,2	3,4	3,6	[m]						
0	-2,86215	-5,68789016	-8,46971	-11,2001082	-13,7893	-16,0167	-17,9563	-19,6062	-20,246	-20,2983	-19,415	-17,6015	-14,9655	-12,1640882	-9,19603	-6,13085	-3,05924	7,21985E-07	[mm]						
Deflection calculation internal sensors																									
Iterate compressive zone following Thornfelds parabola based on steel stress:																									
		131	131	114	96	84	87,6	82	80	79	82	86,4	92,2	107	131	131	131		[mm]						
		3,585910911	31,88815	104,9804976	232,0421	423,0335	355,2786	587,8882	612,2903	635,0823	519,9009	378,8521	273,5681	141,9190114	44,60834	4,636854	-7,7112		[N/mm2]						
Calculate curvature:																									
		0,3	0,5	0,7	0,9	1,1	1,3	1,5	1,7	1,9	2,1	2,3	2,5	2,7	2,9	3,1	3,3		[m]						
		1,27431E-07	1,13E-06	3,31064E-06	6,54E-06	1,11E-05	9,54E-06	1,53E-05	1,58E-05	1,63E-05	1,35E-05	1,01E-05	7,54E-06	4,27725E-06	1,59E-06	1,65E-07	-2,7E-07								
Calculate ΔPhi																									
	0,1	0,3	0,5	0,7	0,9	1,1	1,3	1,5	1,7	1,9	2,1	2,3	2,5	2,7	2,9	3,1	3,3	3,5	[m]						
	-0,000175667	2,54862E-05	0,000227	0,000662129	0,001308	0,002226	0,001907	0,00306	0,003152	0,003252	0,002706	0,00202	0,001508	0,000855449	0,000317	3,3E-05	-5,5E-05	-0,00014257							
Determine initial phi, such that deflection is 0 at simple support (red cell)																									
	0	0,2	0,4	0,6	0,8	1	1,2	1,4	1,6	1,8	2	2,2	2,4	2,6	2,8	3	3,2	3,4	[m]						
	-0,0107272	-0,01090287	-0,01088	-0,01065074	-0,00999	-0,00868	-0,00646	-0,00455	-0,00149	0,001664	0,004916	0,007621	0,009642	0,011149389	0,012005	0,012322	0,012355	0,012300033							
Determine deflection																									
0	0,2	0,4	0,6	0,8	1	1,2	1,4	1,6	1,8	2	2,2	2,4	2,6	2,8	3	3,2	3,4	3,6	[m]						
0	-2,14544	-4,32601337	-6,50149	-8,63163777	-10,6294	-12,3656	-13,6566	-14,5661	-14,8638	-14,531	-13,5478	-12,0236	-10,0952	-7,86535072	-5,46438	-3,00001	-0,52904	1,93096808	[mm]						

B Steel tensile tests

As the installation of internal optic fiber sensors required grinding a slot in the reinforcement steel and sandblasting the surface, The influence of machining these reinforcement bars has been investigated. In this appendix, the result of 12 tensile tests is shown. These 12 experiments consists out of 3 experiments on reinforcement bars which were not machined, 3 experiments on sandblasted reinforcement, 3 experiments on reinforcement bars which were sandblasted and with a slot milled in it and 3 experiments on a sandblasted reinforcement bar with a milled slot filled with glue.

Test setup

The experiment setup consist out of a tensil testing machine, which clamps the specimen with two hydrolic clamps. a picture of the measurement setup is shown in fig. B.1. All experiments were executed on 05-11-2020. The loading speed for all experiments was set to 0.04mm/s. below, a short description for each experiment is given.

Reinforcement without modification T1-3

T1 T1 had a span of 230mm between the clamps. A overview picture of the specimen in the test setup is shown in fig. B.1. The failure of the specimen can be seen in fig. B.2. The force-strain diagram is presented in fig. B.3.

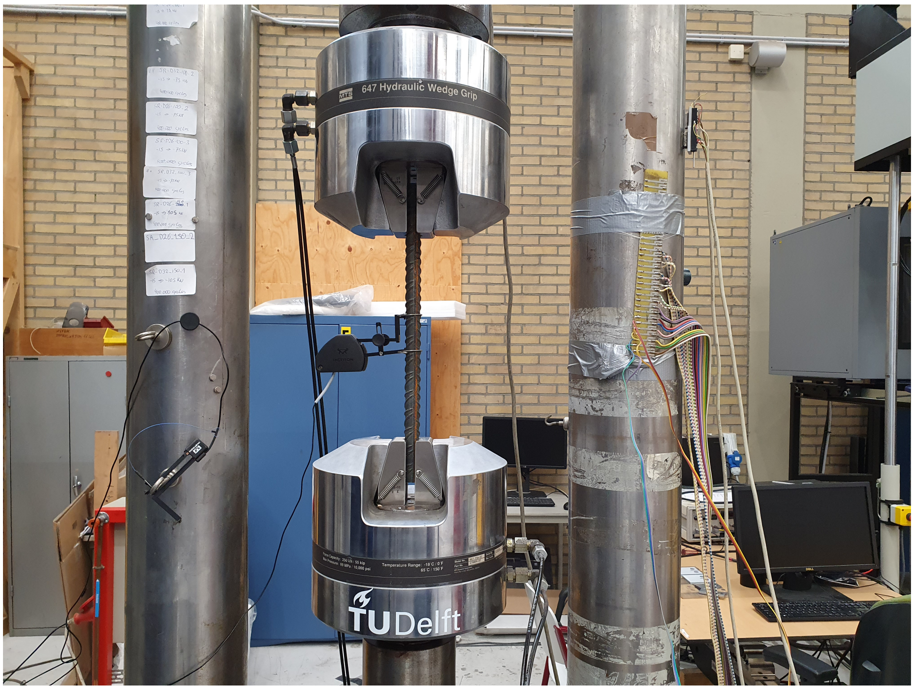

Figure B.1: specimen T1

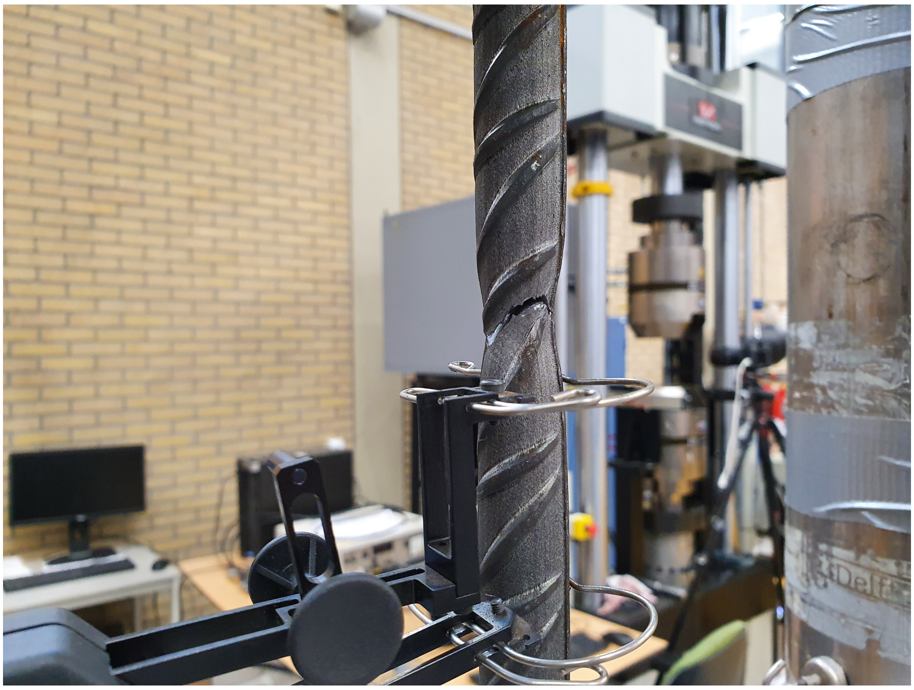

Figure B.2: failure T1

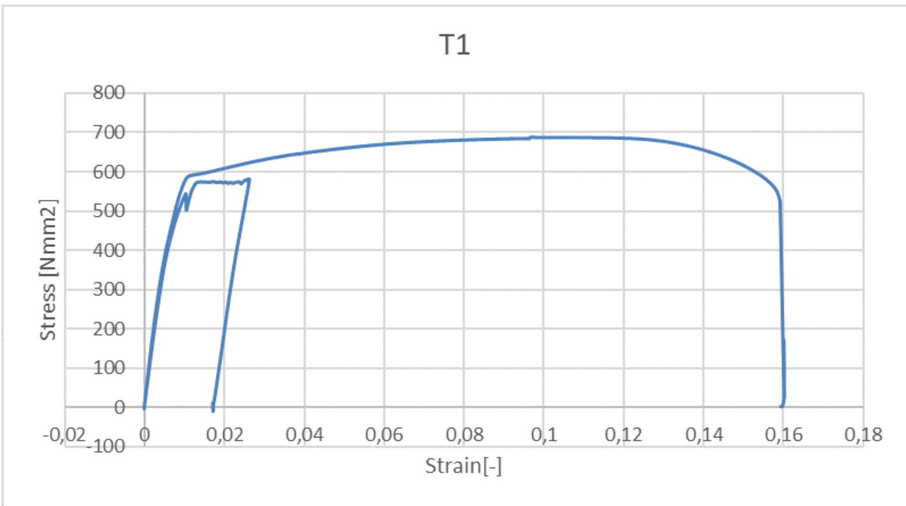

Figure B.3: Stress-strain diagram T1

T2 T1 had a span of 230mm between the clamps. A overview picture of the specimen in the test setup is shown in fig. B.4. The failure of the specimen can be seen in fig. B.5. The force-strain diagram is presented in fig. B.6.

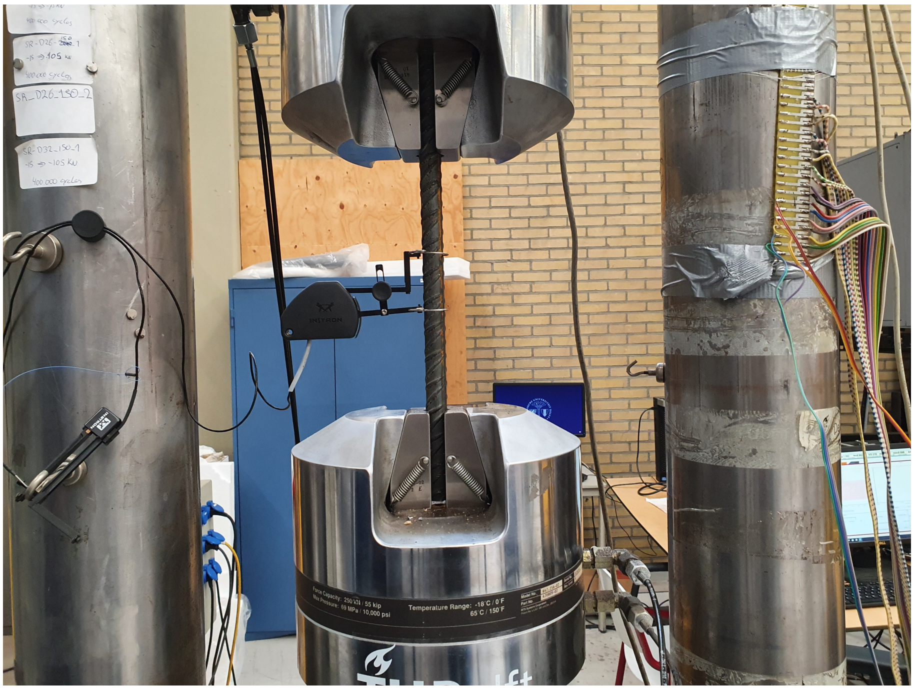

Figure B.4: specimen T2

Figure B.5: failure T2

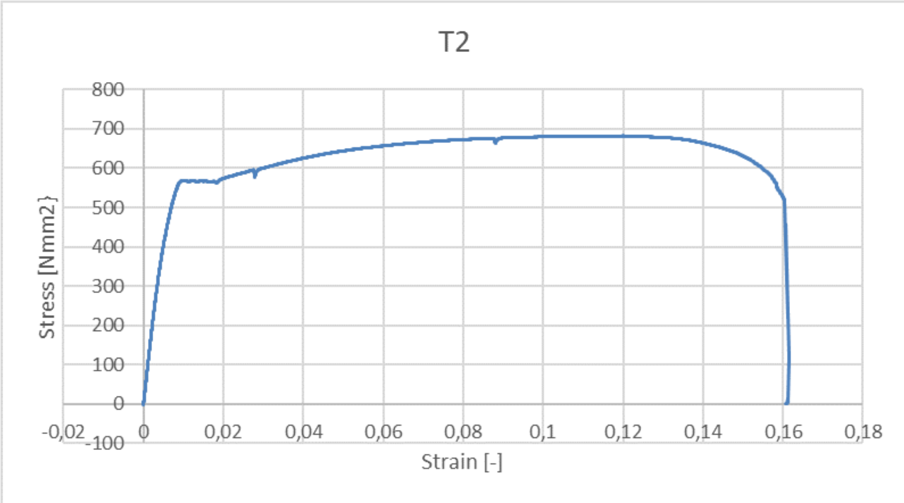

Figure B.6: Stress-strain diagram T2

T3 T1 had a span of 230mm between the clamps. A overview picture of the specimen in the test setup is shown in fig. B.7. The force-strain diagram is presented in fig. B.8.


Figure B.7: specimen T3

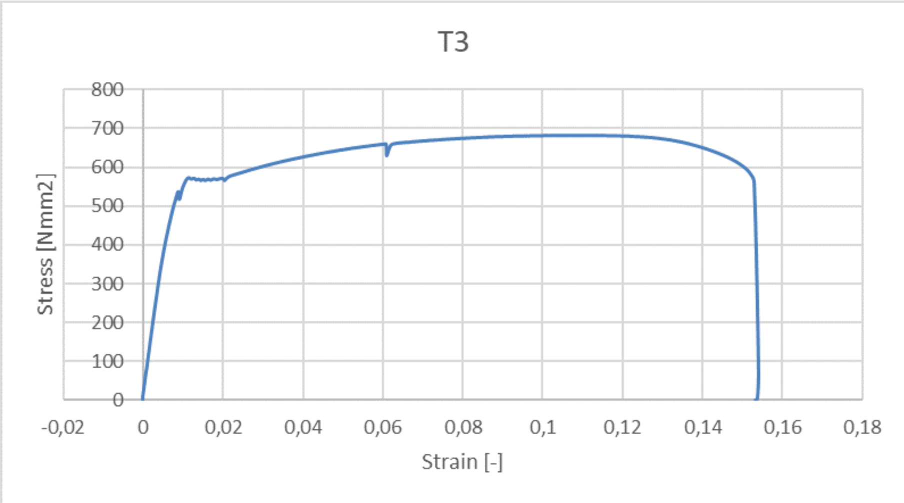

Figure B.8: Stress-strain diagram T3

Sandblasted reinforcement T4-6

T4 T1 had a span of 234mm between the clamps. A overview picture of the specimen in the test setup is shown in fig. B.9. The failure of the specimen can be seen in fig. B.10. The force-strain diagram is presented in fig. B.11.

Figure B.9: specimen T4

Figure B.10: failure T4

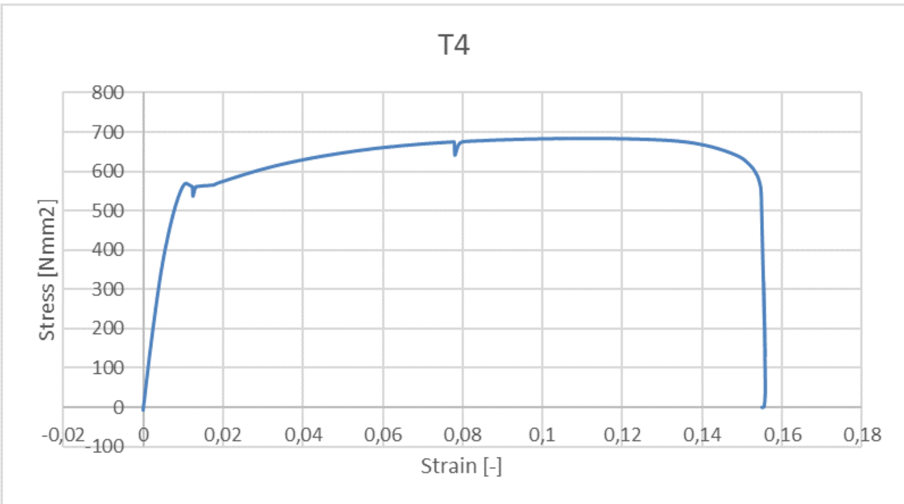

Figure B.11: Stress-strain diagram T4

T5 T1 had a span of 242mm between the clamps. A overview picture of the specimen in the test setup is shown in fig. B.12. The failure of the specimen can be seen in fig. B.13. The force-strain diagram is presented in fig. B.14.

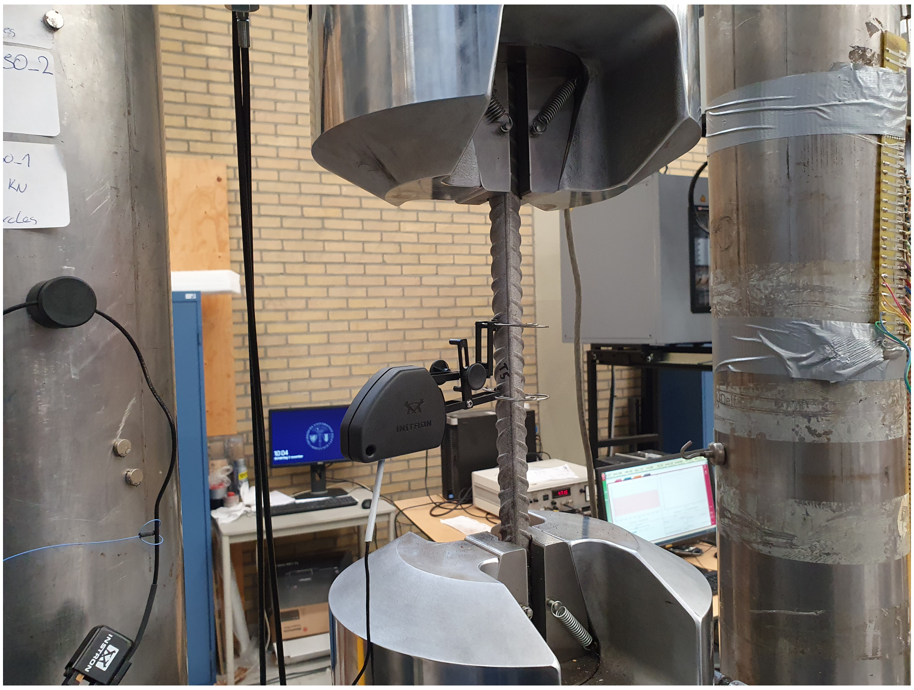

Figure B.12: specimen T5

Figure B.13: failure T5

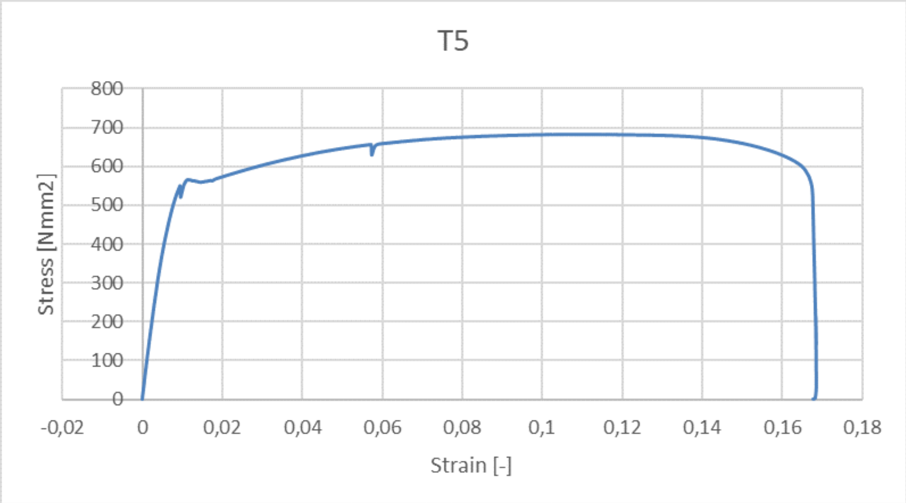

Figure B.14: Stress-strain diagram T5

T6 T1 had a span of 232mm between the clamps. A overview picture of the specimen in the test setup is shown in fig. B.15. The failure of the specimen can be seen in fig. B.16. The force-strain diagram is presented in fig. B.17.

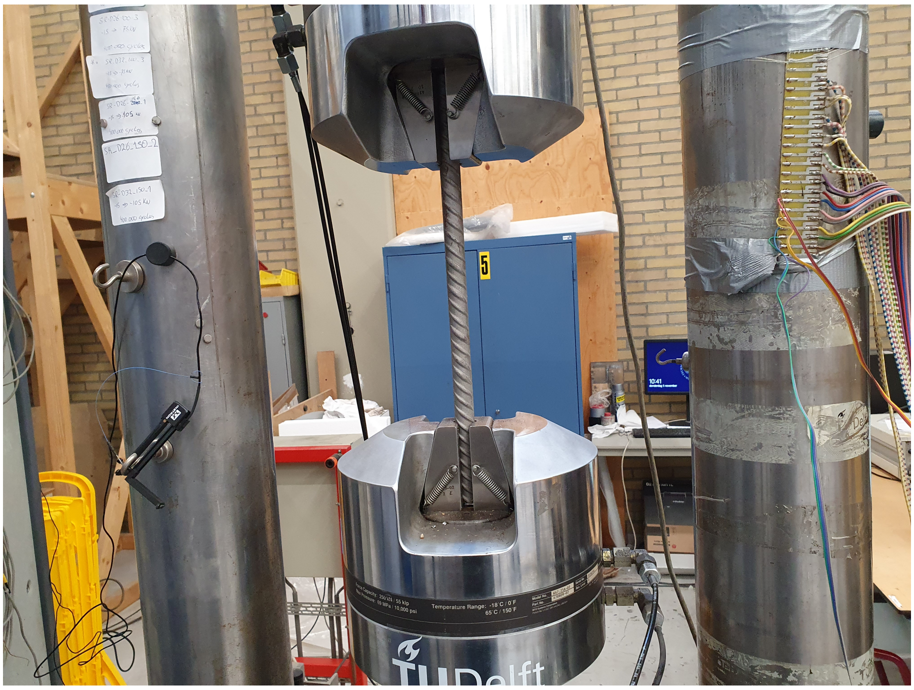

Figure B.15: specimen T6

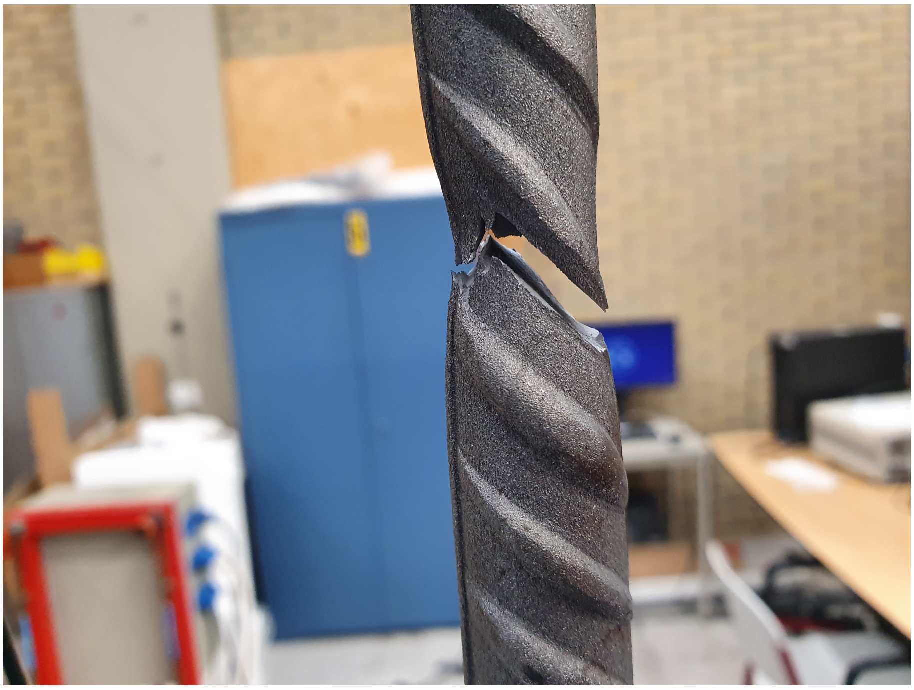

Figure B.16: failure T6

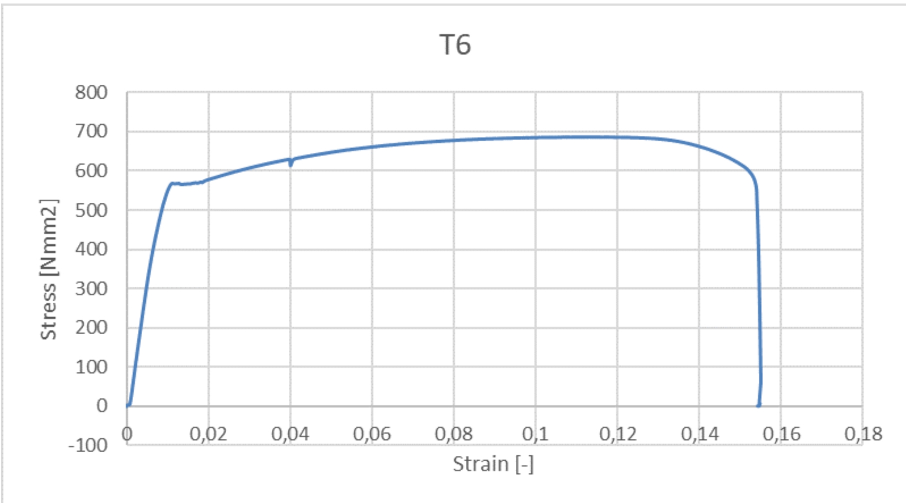

Figure B.17: Stress-strain diagram T6

Sandblasted and slotted reinforcement T7-9

T7 T1 had a span of 230mm between the clamps. A overview picture of the specimen in the test setup is shown in fig. B.18. The failure of the specimen can be seen in fig. B.19. The force-strain diagram is presented in fig. B.20.

Figure B.18: specimen T7

Figure B.19: failure T7

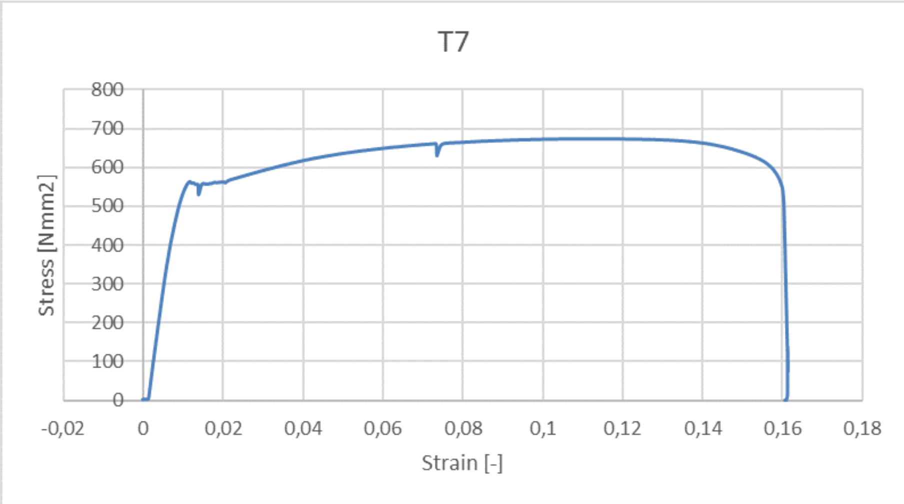

Figure B.20: Stress-strain diagram T7

T8 T1 had a span of 229mm between the clamps. A overview picture of the specimen in the test setup is shown in fig. B.21. The failure of the specimen can be seen in fig. B.22. The force-strain diagram is presented in fig. B.23.

Figure B.21: specimen T8

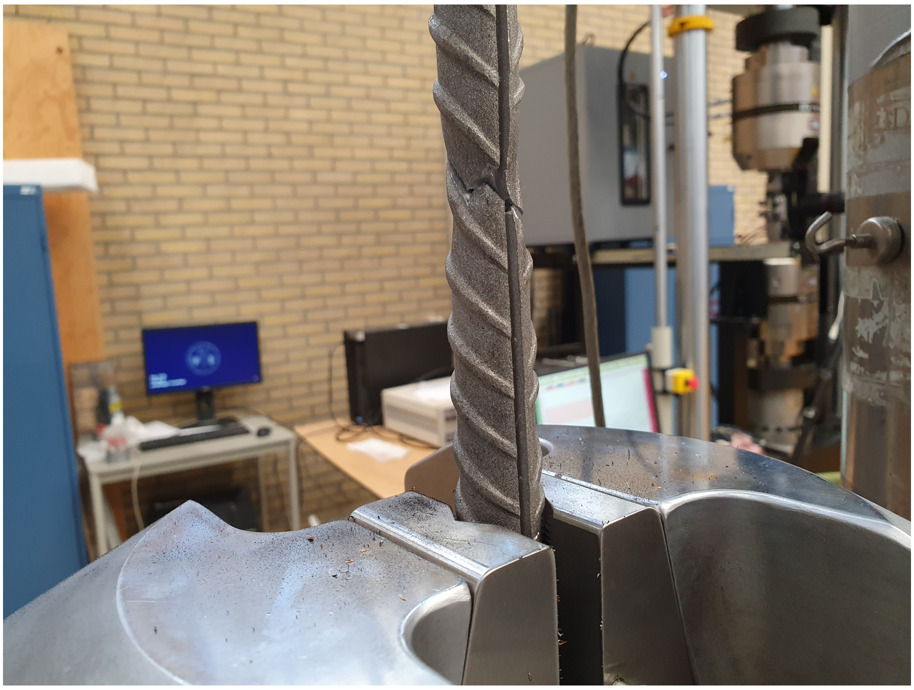

Figure B.22: failure T8

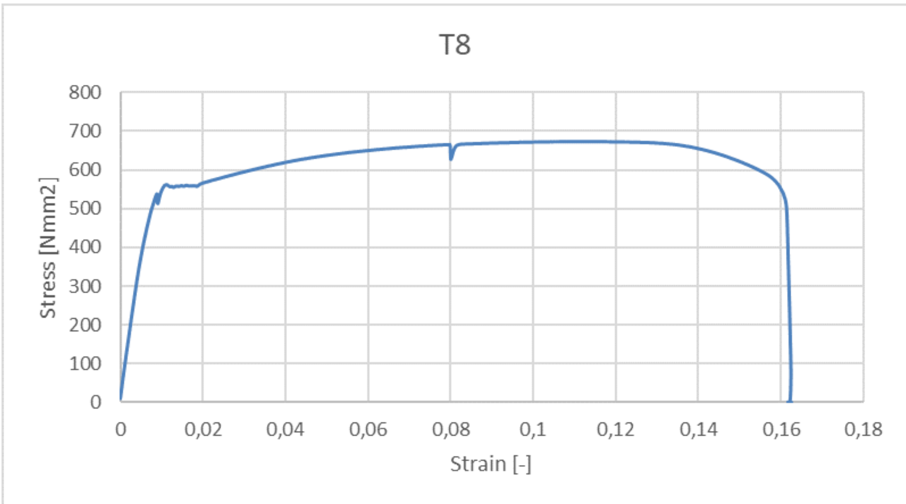

Figure B.23: Stress-strain diagram T8

T9 T1 had a span of 231mm between the clamps. A overview picture of the specimen in the test setup is shown in fig. B.24. The failure of the specimen can be seen in fig. B.25. The force-strain diagram is presented in fig. B.26.

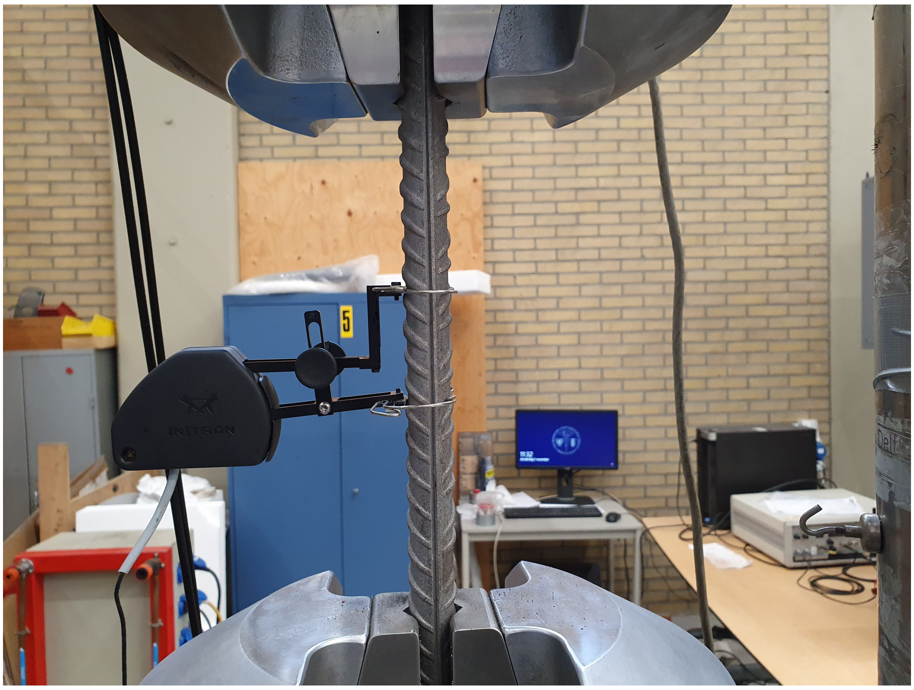
Figure B.24: specimen T9


Figure B.25: failure T9

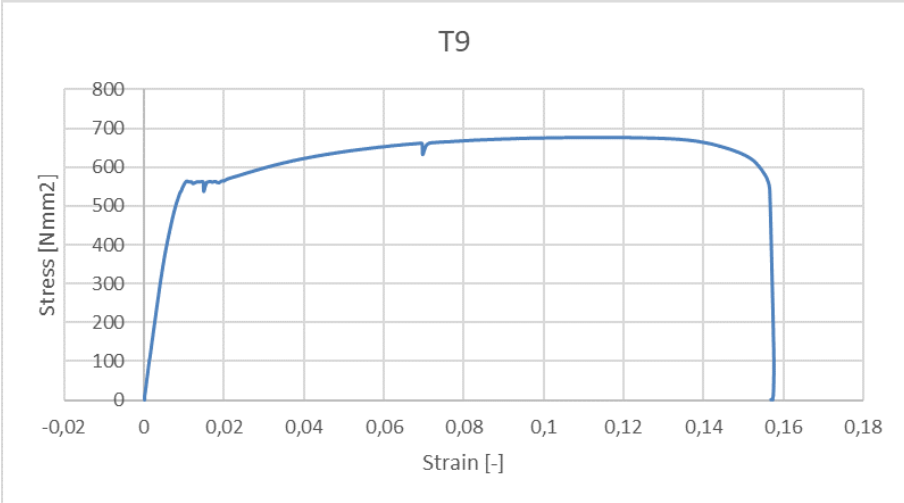

Figure B.26: Stress-strain diagram T9

Sandblasted and slotted reinforcement with glue T10-12

T10 T1 had a span of 229mm between the clamps. A overview picture of the specimen in the test setup is shown in fig. B.27. The failure of the specimen can be seen in fig. B.28. The force-strain diagram is presented in fig. B.29.

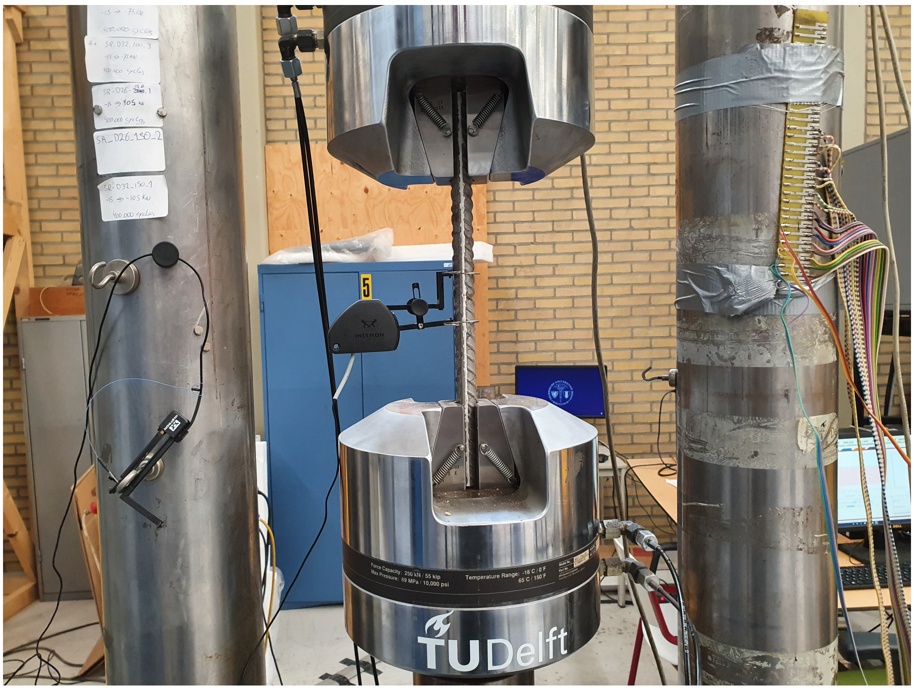

Figure B.27: specimen T10

Figure B.28: failure T10

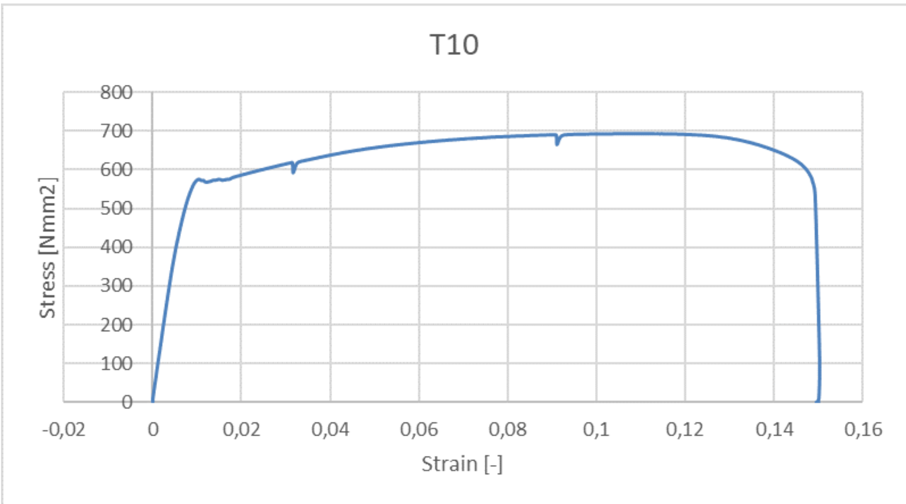

Figure B.29: Stress-strain diagram T10

T11 T1 had a span of 229mm between the clamps. A overview picture of the specimen in the test setup is shown in fig. B.30. The failure of the specimen can be seen in fig. B.31. The force-strain diagram is presented in fig. B.32.

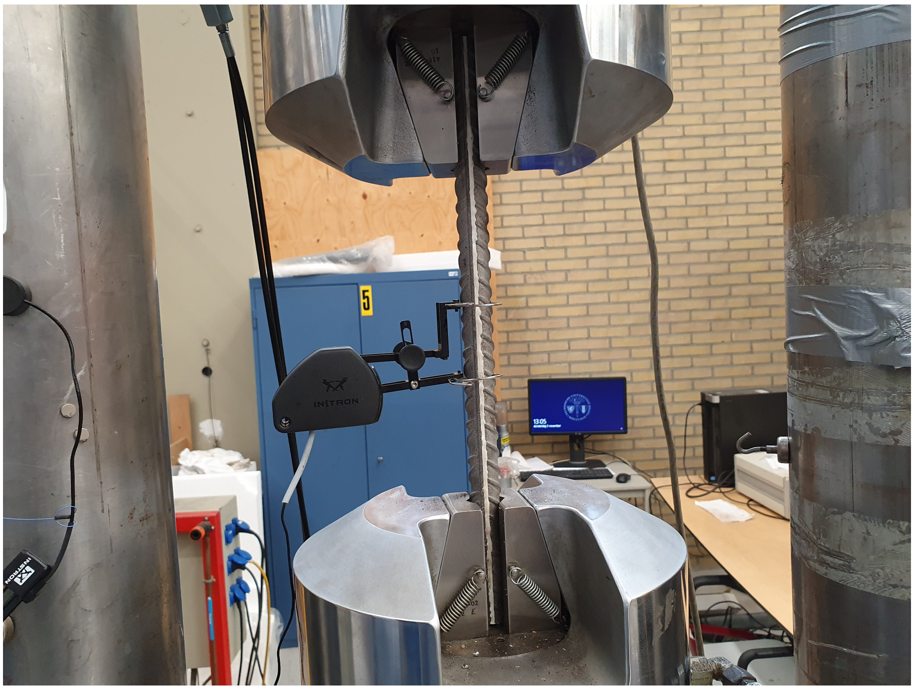

Figure B.30: specimen T11

Figure B.31: failure T11

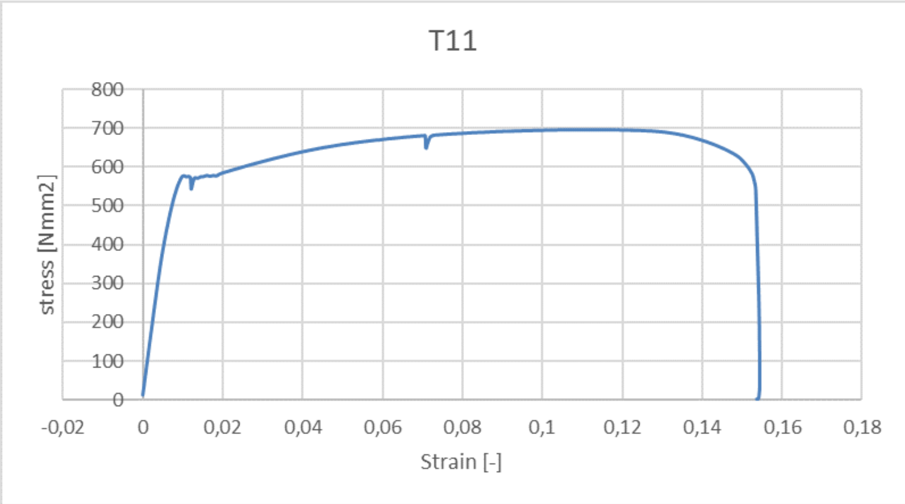

Figure B.32: Stress-strain diagram T11

T12 T1 had a span of 231mm between the clamps. A overview picture of the specimen in the test setup is shown in fig. B.33. The failure of the specimen can be seen in fig. B.34. The force-strain diagram is presented in fig. B.35.

Figure B.33: specimen T12

Figure B.34: failure T12

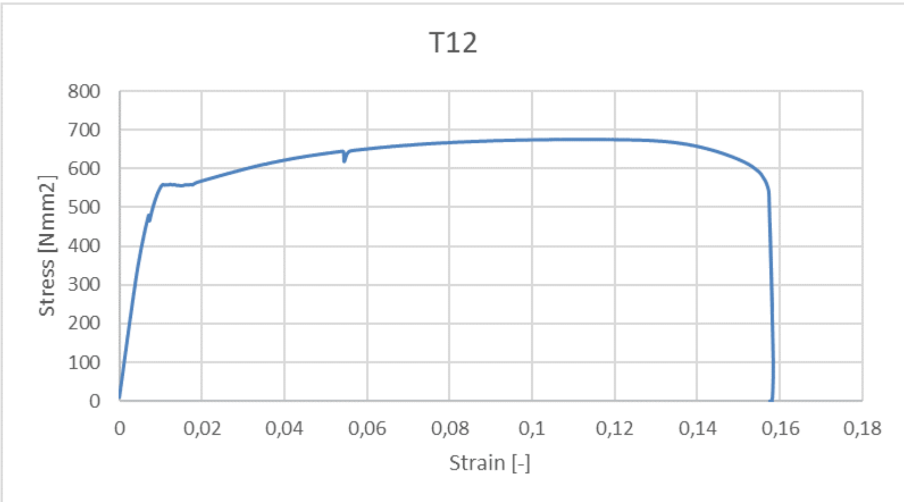

Figure B.35: Stress-strain diagram T12

Analysis of the results
a summary of the results is given in table B.1. The avarage yielding stress from all tests is 585 N/mm^2. No significant Difference between the machined reinforcement bars can be observed other than the linearly decreased surface which leads to a slightly lower ultimate force. From the reinforcement bars with the glue in the slots, it became clear that the results of the optical fiber sensor should not be trusted beyond yielding strain, as of that point the glue started to crack.

No.	F_y[kN]	F_{max}[kN]	D[mm]	f_y[N/mm^2]	f_u[N/mm^2]	
1	185.67	222.54	20	591	708	
2	179.24	221.47	20	570	705	Regular
3	184.17	220.59	20	586	702	
4	184.69	221.7	20	588	706	
5	183.41	221.24	20	584	704	Sandblasted
6	183.75	222.2	20	585	708	
7	181.89	218.45	19.87	587	705	Sandblasted
8	182.1	218.16	19.87	588	704	& milled slot of approx. 4mm
9	182.37	219.06	19.87	588	707	
10	180.86	218.22	19.87	583	704	Sandblasted
11	180.8	218.12	19.87	583	704	& milled slot of approx. 4mm
12	180.82	218.41	19.87	583	705	Slot filled with epoxy

Table B.1: Summary of steel tensile tests

C Beam tests

To acquire some experience with the measurement system and to check its accuracy, 3 beams were casted in the Stevin laboratory. After Hardening, four fiber optic sensors were installed. The results are compared to LVDT's next to the optical fiber measurements.

C.0.1 Production

Production of the beams took place on 01-10-2020. An overview of the reinforcement is shown in fig. C.1.

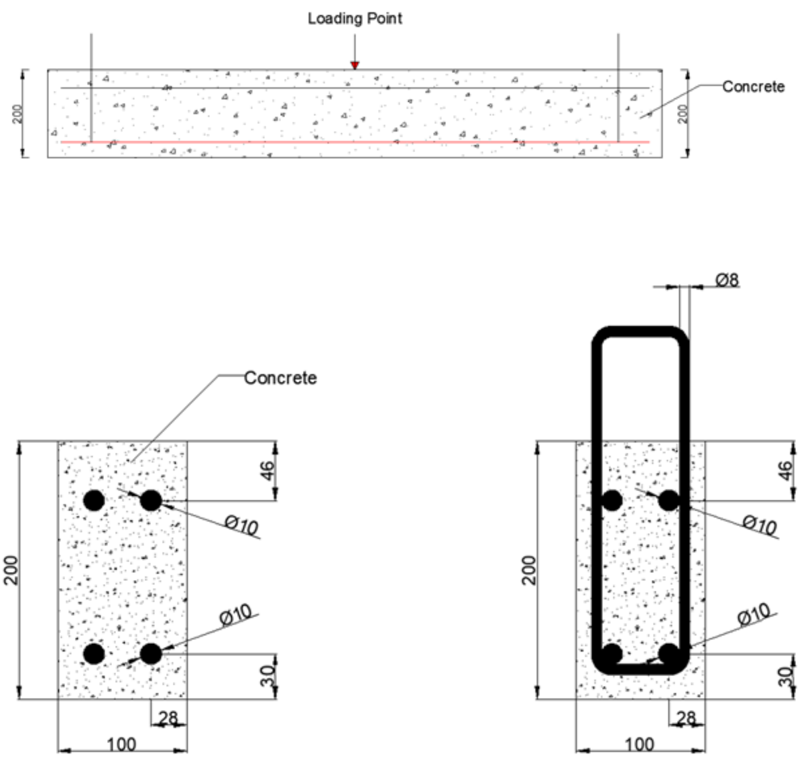

Figure C.1: foto production

two photos of production are presented in figs. C.2 and C.3

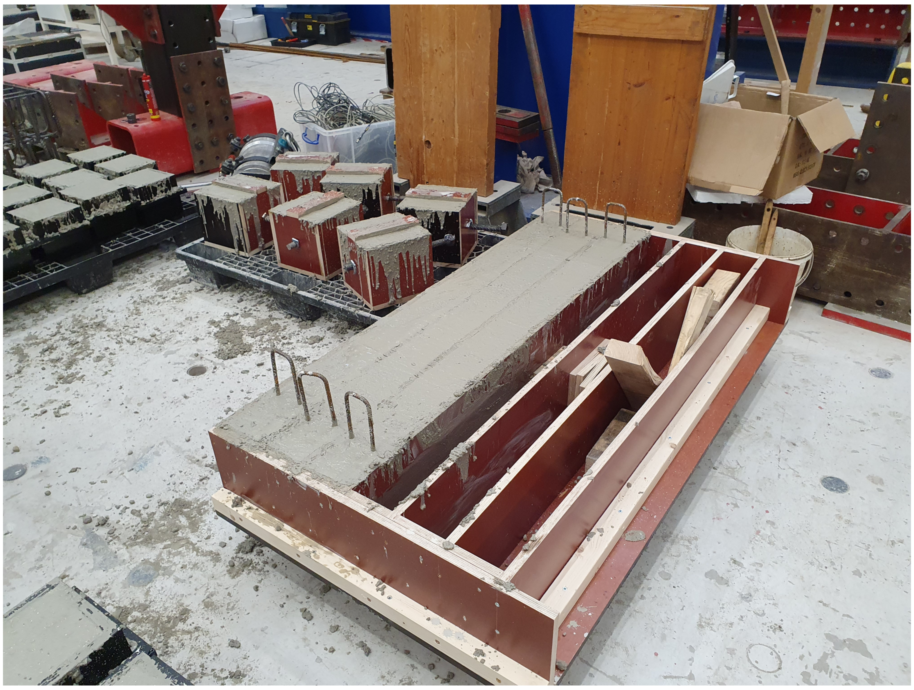

Figure C.2: Photo production

Figure C.3: Photo production

Test setup

The beam was placed between two support so it spanned 1100mm. The beam is loaded with a point load in the middle of the span. An overview of the test setup can be seen in fig. C.4. The beams were equipped with fiber optic and with LVDT sensors. An overview of the sensor layout on the bottom is provided in fig. C.5. The gluing plates were installed with 3 different glues. Beam one with glue 1, beam two with glue 2 and beam 3 with glue

3. As the results on the third beam were very different from the other 2 beams, and later tests showed that glue 3 was not able to resist constant load, the results from this beam were omitted for the comparison between fiber optic and LVDT.

Figure C.4: Test setup

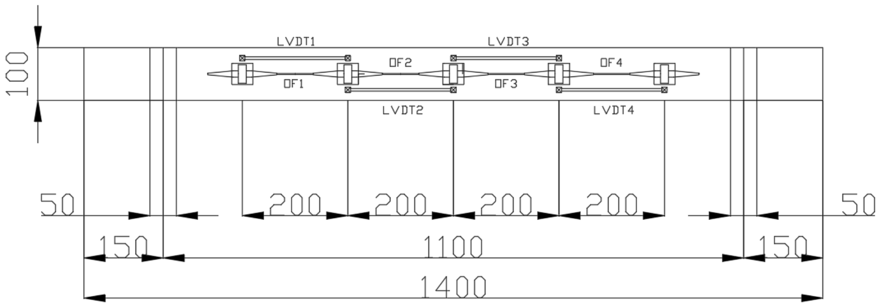

Figure C.5: Test setup

Comparison of the results

The beams were loaded up until failure. However, the sensors were removed at reaching 2000$\mu\varepsilon$ as it was not desirable to break one. The results from beam one and two can be found in figs. C.6 and C.7

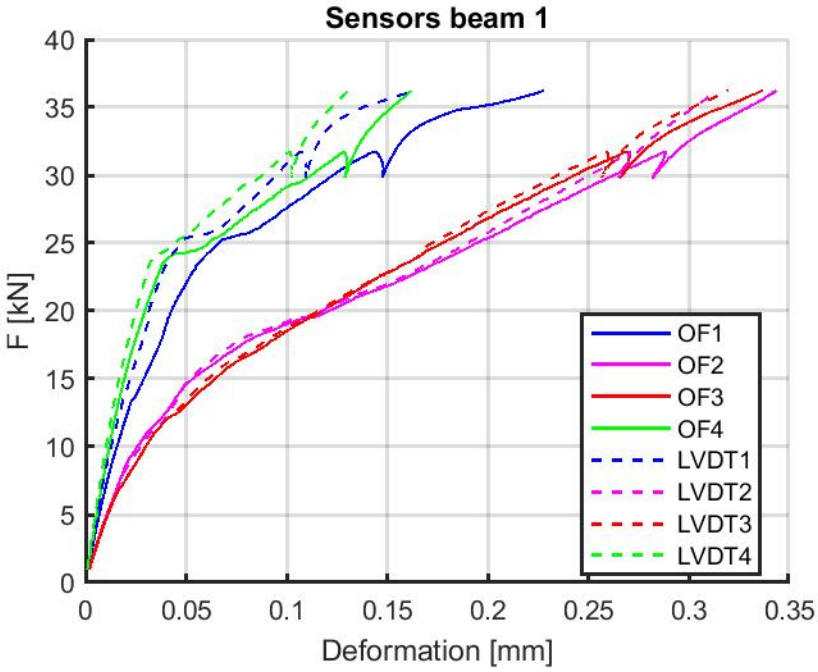

Figure C.6: Results of beam 1

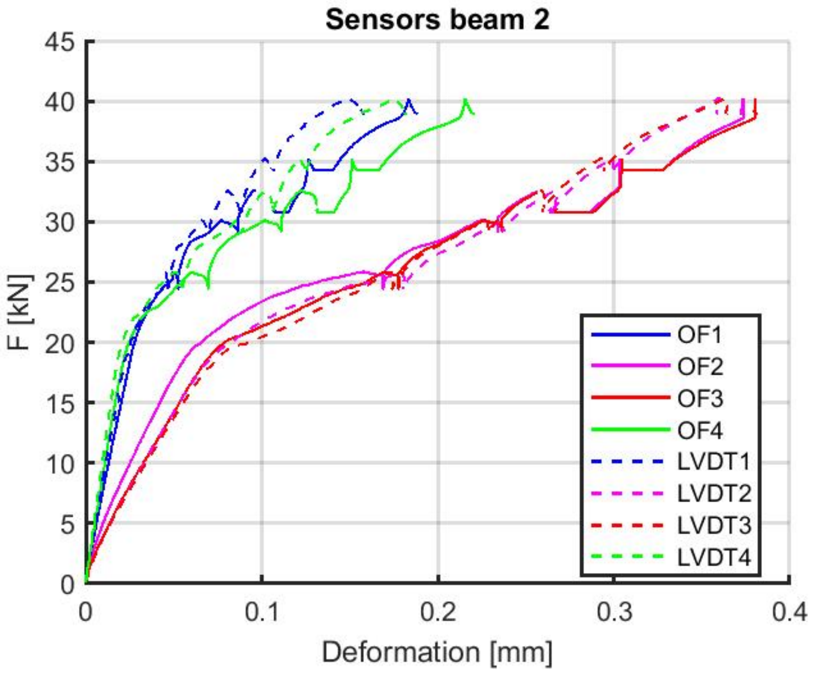

Figure C.7: Results of beam 2

D Base wavelengths

Below, for each sensor the base wavelength is presented.

Location name	Data name	Base wavelength [m]
M03	Ix_0_Channel _Sensor 1.bin	1.529501400E-06
M05	Ix_0_Channel _Sensor 2.bin	1.533302865E-06
M07	Ix_0_Channel _Sensor 3.bin	1.536296584E-06
M09	Ix_0_Channel _Sensor 4.bin	1.539164269E-06
M11	Ix_0_Channel 2_Sensor 1.bin	1.540071583E-06
M13	Ix_0_Channel 2_Sensor 2.bin	1.543092278E-06
M15	Ix_0_Channel 2_Sensor 3.bin	1.547386180E-06
M17	Ix_0_Channel 2_Sensor 4.bin	1.550039949E-06
M19	Ix_0_Channel 3_Sensor 1.bin	1.538777481E-06
M21	Ix_0_Channel 3_Sensor 2.bin	1.536005897E-06
M23	Ix_0_Channel 3_Sensor 3.bin	1.533033379E-06
M25	Ix_0_Channel 3_Sensor 4.bin	1.529752824E-06
M27	Ix_0_Channel 4_Sensor 1.bin	1.549302108E-06
M29	Ix_0_Channel 4_Sensor 2.bin	1.546338817E-06
M31	Ix_0_Channel 4_Sensor 3.bin	1.543704024E-06
M33	Ix_0_Channel 4_Sensor 4.bin	1.540441514E-06
I03	Ix_1_Channel 1_Sensor 1.bin	1.540552236E-06
I05	Ix_1_Channel 1_Sensor 2.bin	1.544143363E-06
I07	Ix_1_Channel 1_Sensor 3.bin	1.546918292E-06
I09	Ix_1_Channel 1_Sensor 4.bin	1.550010578E-06
I11	Ix_1_Channel 2_Sensor 1.bin	1.540660315E-06
I13	Ix_1_Channel 2_Sensor 2.bin	1.543903230E-06
I15	Ix_1_Channel 2_Sensor 3.bin	1.546941745E-06
I17	Ix_1_Channel 2_Sensor 4.bin	1.551018184E-06
I19	Ix_1_Channel 3_Sensor 1.bin	1.539120994E-06
I21	Ix_1_Channel 3_Sensor 2.bin	1.536132239E-06
I23	Ix_1_Channel 3_Sensor 3.bin	1.532838233E-06
I25	Ix_1_Channel 3_Sensor 4.bin	1.529887670E-06
I27	Ix_2_Channel 1_Sensor 1.bin	1.538849201E-06
I29	Ix_2_Channel 1_Sensor 2.bin	1.536193151E-06
I31	Ix_2_Channel 1_Sensor 3.bin	1.533232578E-06
I33	Ix_2_Channel 1_Sensor 4.bin	1.529523715E-06
E03	Ix_2_Channel 3_Sensor 1.bin	1.540429328E-06
E05	Ix_2_Channel 3_Sensor 2.bin	1.543129468E-06
E07	Ix_2_Channel 3_Sensor 3.bin	1.546372304E-06
E09	Ix_2_Channel 3_Sensor 4.bin	1.549520753E-06
E11	Ix_2_Channel 4_Sensor 1.bin	1.529348799E-06
E13	Ix_2_Channel 4_Sensor 2.bin	1.532558324E-06
E15	Ix_2_Channel 4_Sensor 3.bin	1.535454751E-06
E17	Ix_2_Channel 4_Sensor 4.bin	1.538428771E-06
E19	Ix_3_Channel 1_Sensor 1.bin	1.550358566E-06
E21	Ix_3_Channel 1_Sensor 2.bin	1.547042580E-06
E23	Ix_3_Channel 1_Sensor 3.bin	1.543992618E-06
E25	Ix_3_Channel 1_Sensor 4.bin	1.540858398E-06
E27	Ix_3_Channel 2_Sensor 1.bin	1.549648866E-06
E29	Ix_3_Channel 2_Sensor 2.bin	1.547293986E-06
E31	Ix_3_Channel 2_Sensor 3.bin	1.544261312E-06
E33	Ix_3_Channel 2_Sensor 4.bin	1.540235134E-06

Location name	Data name	Base wavelength [m]
IM0075	Ix_3_Channel 3_Sensor 1.bin	1.564348377E-06
IM0225	Ix_3_Channel 3_Sensor 2.bin	1.561345464E-06
IM0375	Ix_3_Channel 3_Sensor 3.bin	1.558517714E-06
IM0525	Ix_3_Channel 3_Sensor 4.bin	1.555583234E-06
IM0675	Ix_3_Channel 3_Sensor 5.bin	1.552756412E-06
IM0825	Ix_3_Channel 3_Sensor 6.bin	1.549939495E-06
IM0975	Ix_3_Channel 4_Sensor 1.bin	1.559809526E-06
IM1125	Ix_3_Channel 4_Sensor 2.bin	1.557334710E-06
IM1275	Ix_3_Channel 4_Sensor 3.bin	1.554792043E-06
IM1425	Ix_3_Channel 4_Sensor 4.bin	1.552149770E-06
IM1575	Ix_3_Channel 4_Sensor 5.bin	1.549581234E-06
IM1725	Ix_3_Channel 4_Sensor 6.bin	1.546912240E-06
IM1875	Ix_3_Channel 4_Sensor 7.bin	1.544286182E-06
IM2025	Ix_3_Channel 4_Sensor 8.bin	1.541689294E-06
IM2175	Ix_3_Channel 4_Sensor 9.bin	1.539117599E-06
IM2325	Ix_3_Channel 4_Sensor 10.bin	1.536315918E-06
IM2475	Ix_3_Channel 4_Sensor 11.bin	1.533760050E-06
IM2625	Ix_3_Channel 4_Sensor 12.bin	1.531115188E-06
IM2775	Ix_4_Channel 1_Sensor 1.bin	1.549633867E-06
IM2925	Ix_4_Channel 1_Sensor 2.bin	1.552533860E-06
IM3075	Ix_4_Channel 1_Sensor 3.bin	1.555534630E-06
IM3225	Ix_4_Channel 1_Sensor 4.bin	1.558357391E-06
IM3375	Ix_4_Channel 1_Sensor 5.bin	1.561292842E-06
IM3525	Ix_4_Channel 1_Sensor 6.bin	1.564092195E-06
II0175	Ix_4_Channel 2_Sensor 1.bin	1.539388369E-06
II0375	Ix_4_Channel 2_Sensor 2.bin	1.542380947E-06
II0575	Ix_4_Channel 2_Sensor 3.bin	1.545433593E-06
II0775	Ix_4_Channel 2_Sensor 4.bin	1.548654970E-06
II0975	Ix_4_Channel 3_Sensor 1.bin	1.531396739E-06
II1125	Ix_4_Channel 3_Sensor 2.bin	1.533907161E-06
II1275	Ix_4_Channel 3_Sensor 3.bin	1.536519589E-06
II1425	Ix_4_Channel 3_Sensor 4.bin	1.539170238E-06
II1575	Ix_4_Channel 3_Sensor 5.bin	1.541752696E-06
II1725	Ix_4_Channel 3_Sensor 6.bin	1.544178549E-06
II1875	Ix_4_Channel 3_Sensor 7.bin	1.546662962E-06
II2025	Ix_4_Channel 3_Sensor 8.bin	1.549337181E-06
II2175	Ix_4_Channel 3_Sensor 9.bin	1.551938428E-06
II2325	Ix_4_Channel 3_Sensor 10.bin	1.554497935E-06
II2475	Ix_4_Channel 3_Sensor 11.bin	1.557015053E-06
II2625	Ix_4_Channel 3_Sensor 12.bin	1.559624386E-06
II2825	Ix_4_Channel 4_Sensor 1.bin	1.546667590E-06
II3025	Ix_4_Channel 4_Sensor 2.bin	1.544039049E-06
II3225	Ix_4_Channel 4_Sensor 3.bin	1.542642849E-06
II3425	Ix_4_Channel 4_Sensor 4.bin	1.539634057E-06

Location name	Data name	Base wavelength [m]
IE0075	lx_5_Channel 1_Sensor 1.bin	1.549735336E-06
IE0225	lx_5_Channel 1_Sensor 2.bin	1.552908972E-06
IE0375	lx_5_Channel 1_Sensor 3.bin	1.555623465E-06
IE0525	lx_5_Channel 1_Sensor 4.bin	1.558648020E-06
IE0675	lx_5_Channel 1_Sensor 5.bin	1.561683433E-06
IE0825	lx_5_Channel 1_Sensor 6.bin	1.564563196E-06
IE0975	lx_5_Channel 2_Sensor 1.bin	1.559850356E-06
IE1125	lx_5_Channel 2_Sensor 2.bin	1.557257720E-06
IE1275	lx_5_Channel 2_Sensor 3.bin	1.554871469E-06
IE1425	lx_5_Channel 2_Sensor 4.bin	1.552268620E-06
IE1575	lx_5_Channel 2_Sensor 5.bin	1.549610801E-06
IE1725	lx_5_Channel 2_Sensor 6.bin	1.546846990E-06
IE1875	lx_5_Channel 2_Sensor 7.bin	1.544427407E-06
IE2025	lx_5_Channel 2_Sensor 8.bin	1.541826669E-06
IE2175	lx_5_Channel 2_Sensor 9.bin	1.539153880E-06
IE2325	lx_5_Channel 2_Sensor 10.bin	1.536573110E-06
IE2475	lx_5_Channel 2_Sensor 11.bin	1.533946869E-06
IE2625	lx_5_Channel 2_Sensor 12.bin	1.531252934E-06
IE2775	lx_5_Channel 3_Sensor 1.bin	1.564588383E-06
IE2925	lx_5_Channel 3_Sensor 2.bin	1.561616140E-06
IE3075	lx_5_Channel 3_Sensor 3.bin	1.558404993E-06
IE3225	lx_5_Channel 3_Sensor 4.bin	1.555502978E-06
IE3375	lx_5_Channel 3_Sensor 5.bin	1.552617763E-06
IE3525	lx_5_Channel 3_Sensor 6.bin	1.549782825E-06

E DIC results

To provide some more background to the optical fiber strain measurements, in this appendix a summary of the DIC results on the slab is provided for each test. These results indicate which cracks the optical fiber measurement system was measuring and might explain questions which arise when interpreting the optical fiber results.

E.0.1 S1M1

In fig. E.1 the range of the DIC measurement on the slab is indicated. Below, the DIC results for S1M1 are shown.

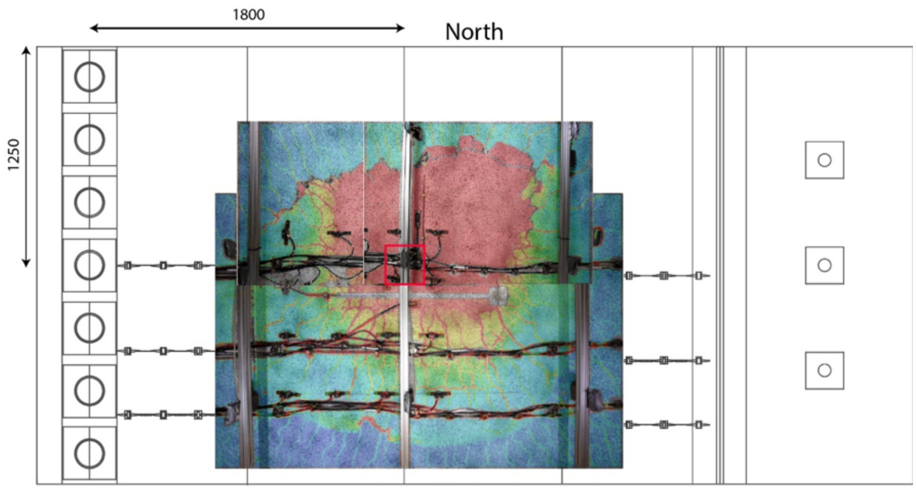

Figure E.1: overview of the DIC range for S1M1 [66]

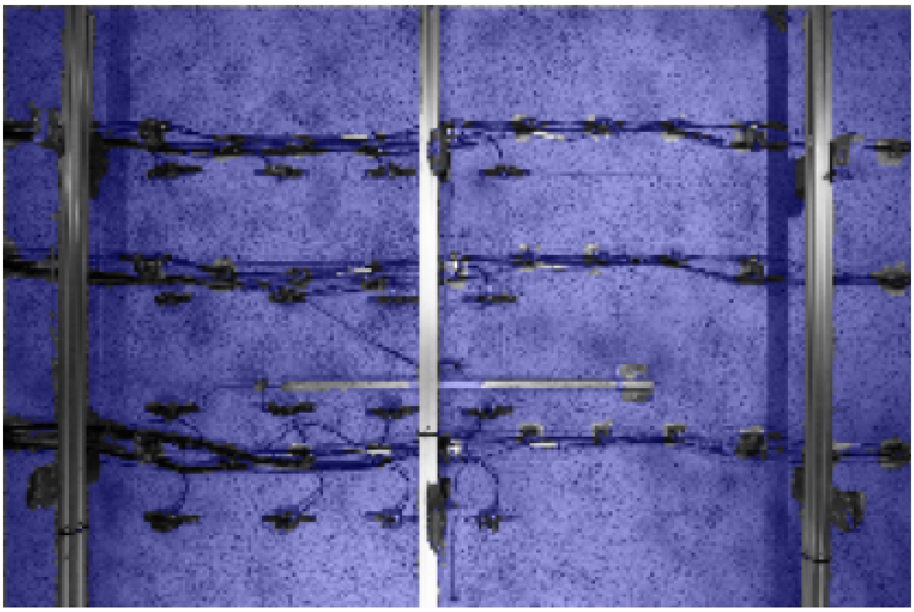

Figure E.2: 0kN [66]

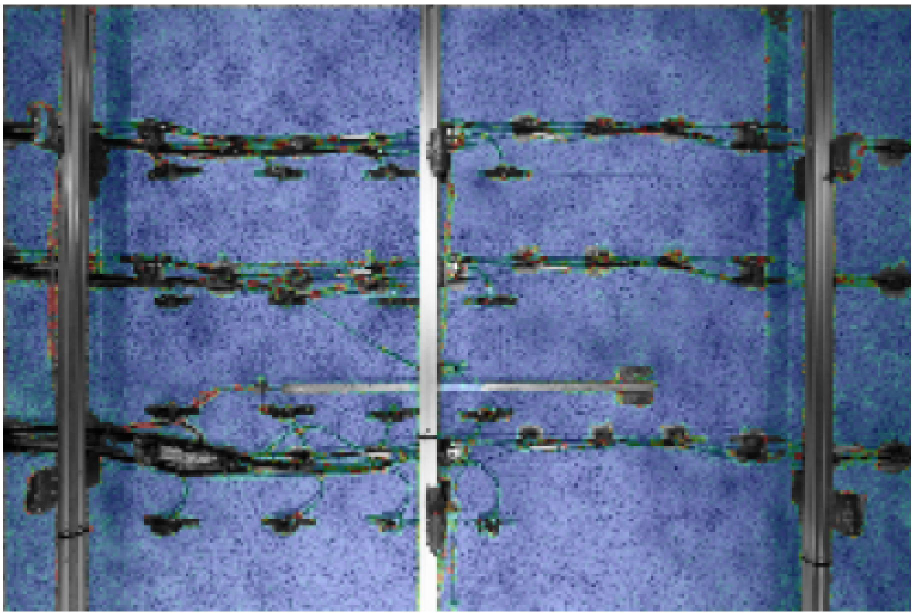
Figure E.3: 50kN [66]

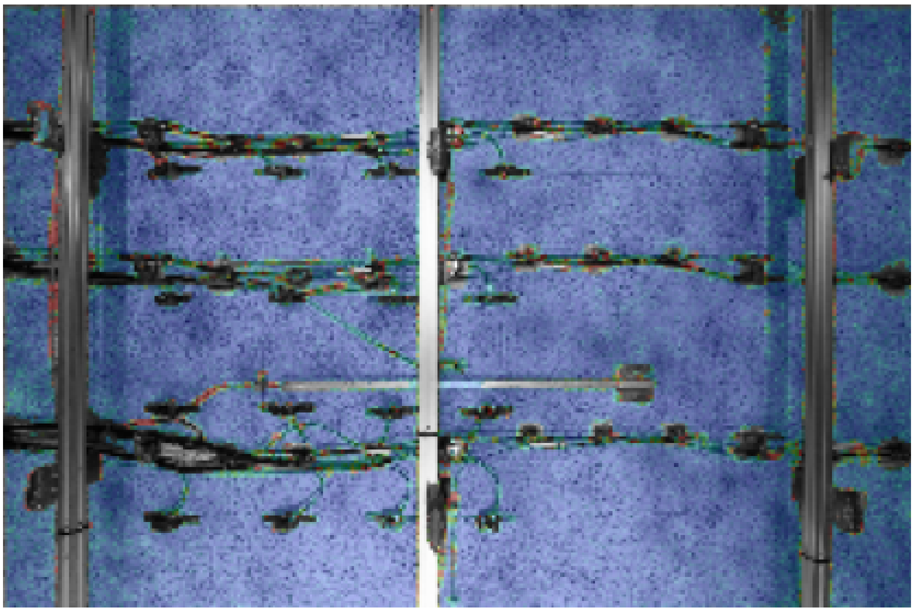
Figure E.4: 100kN [66]

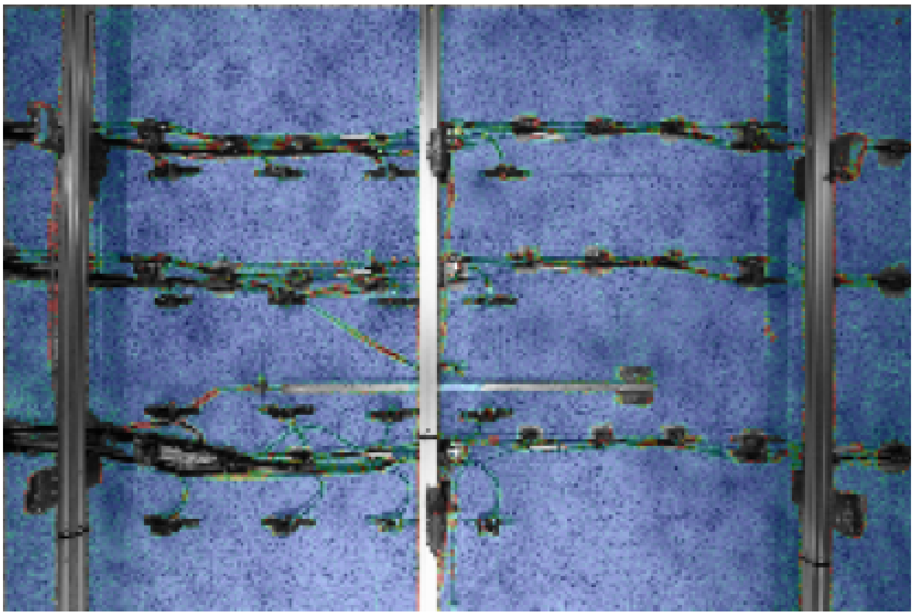

Figure E.5: 150kN [66]

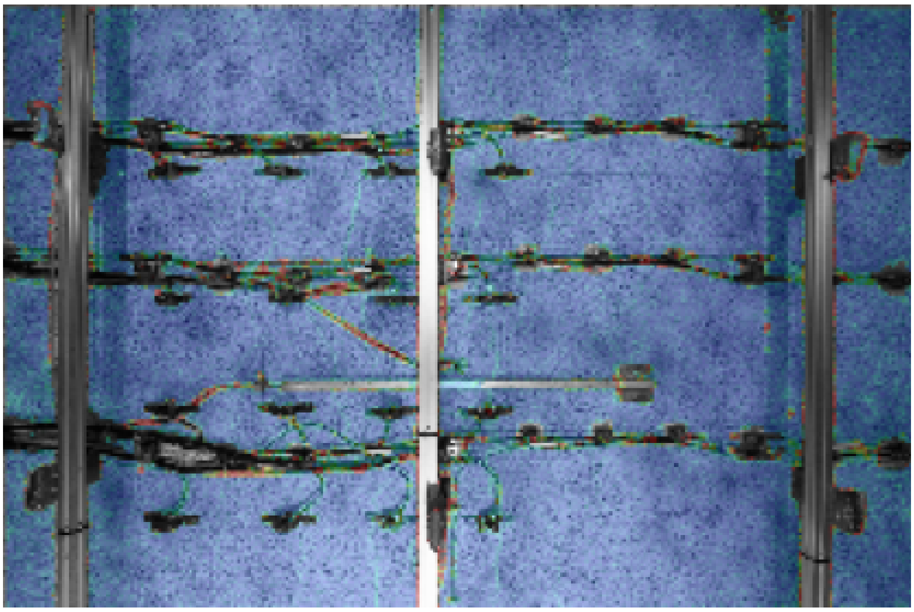

Figure E.6: 200kN [66]

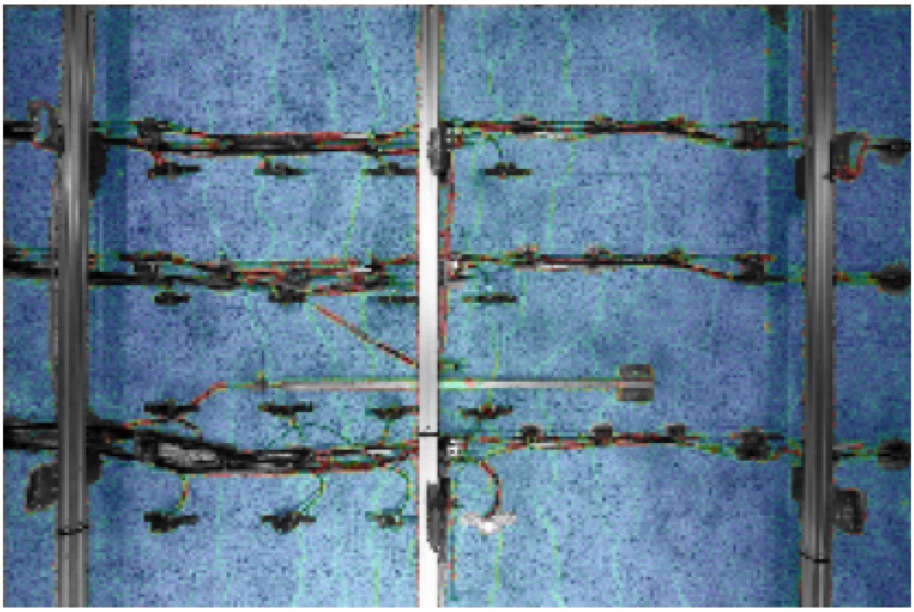
Figure E.7: 300kN [66]

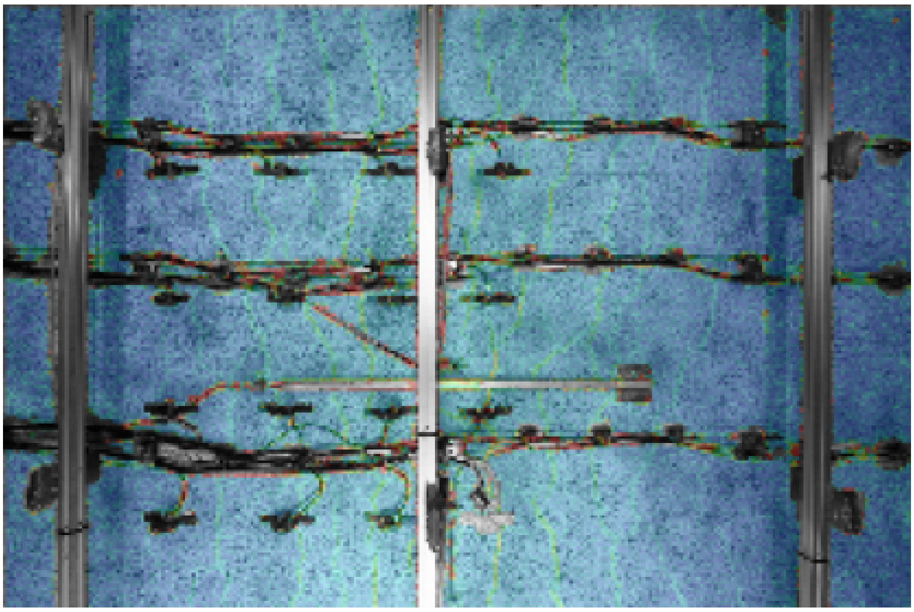
Figure E.8: 350kN [66]

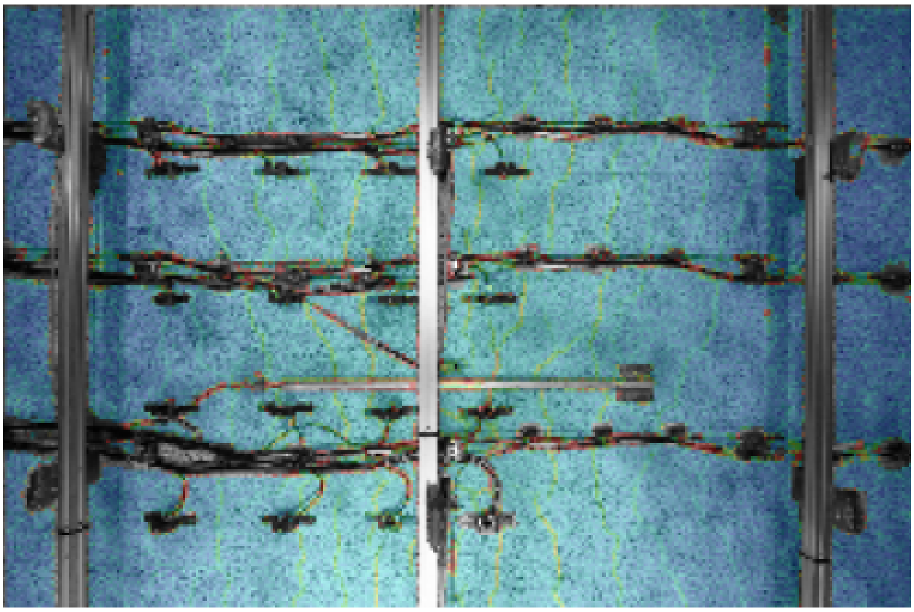

Figure E.9: 400kN [66]

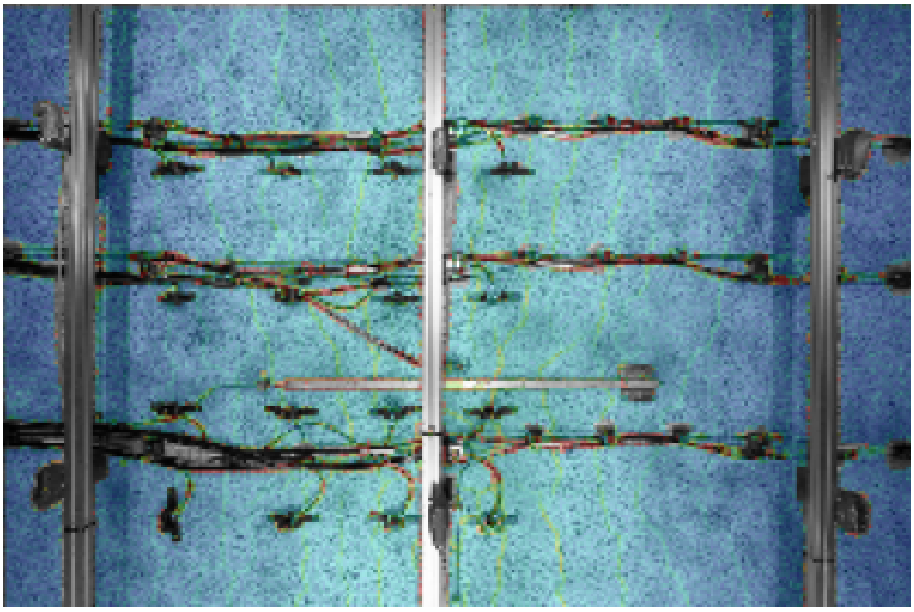

Figure E.10: 450kN [66]

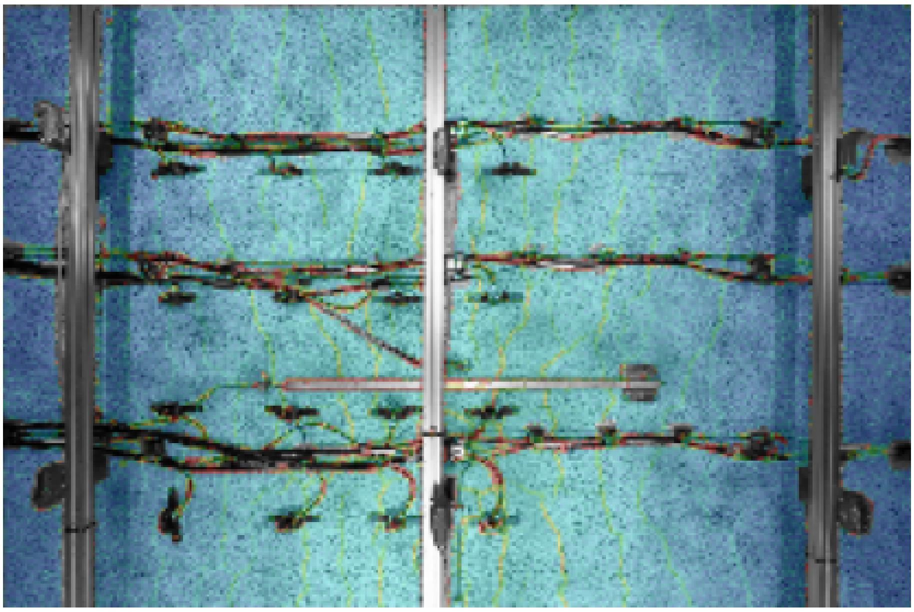

Figure E.11: 500kN [66]

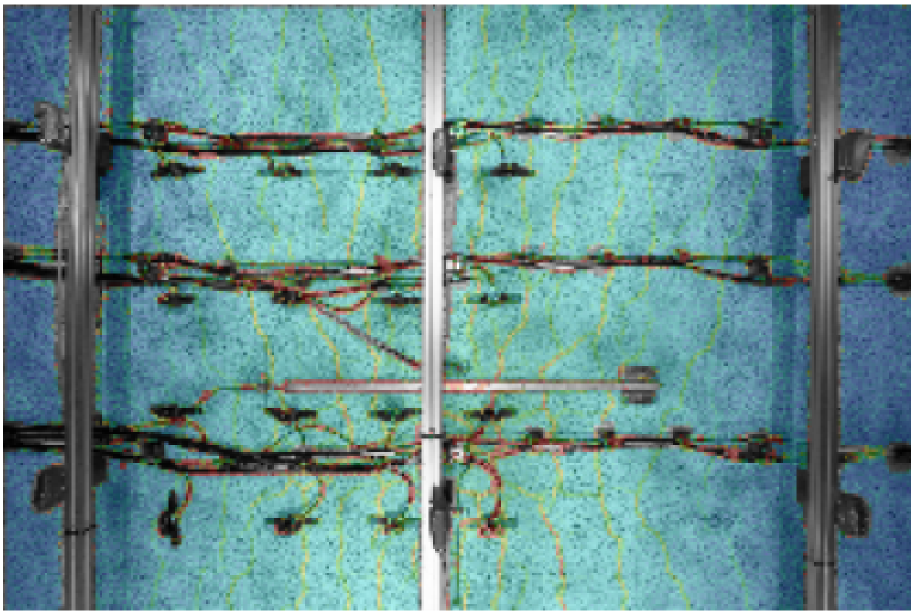

Figure E.12: 550kN [66]

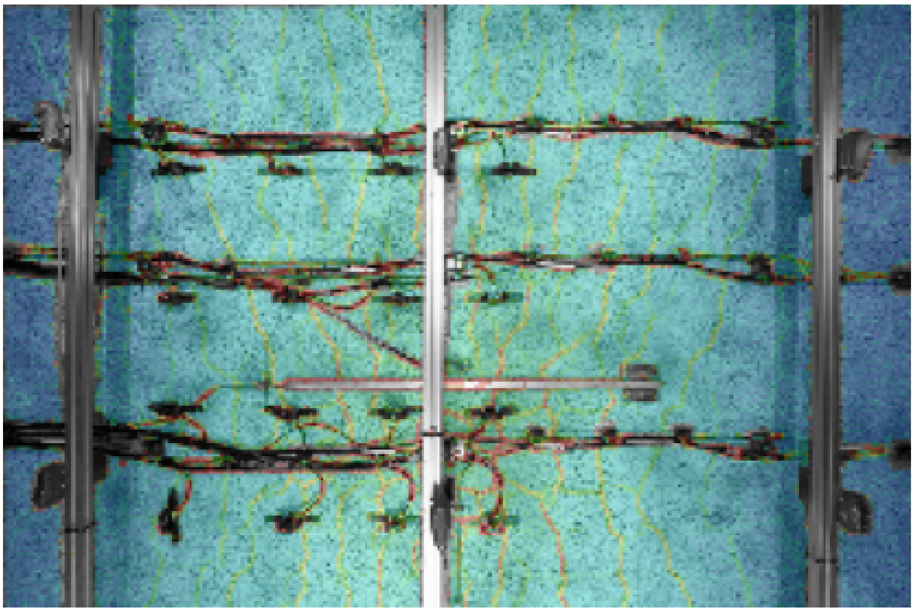

Figure E.13: 600kN [66]

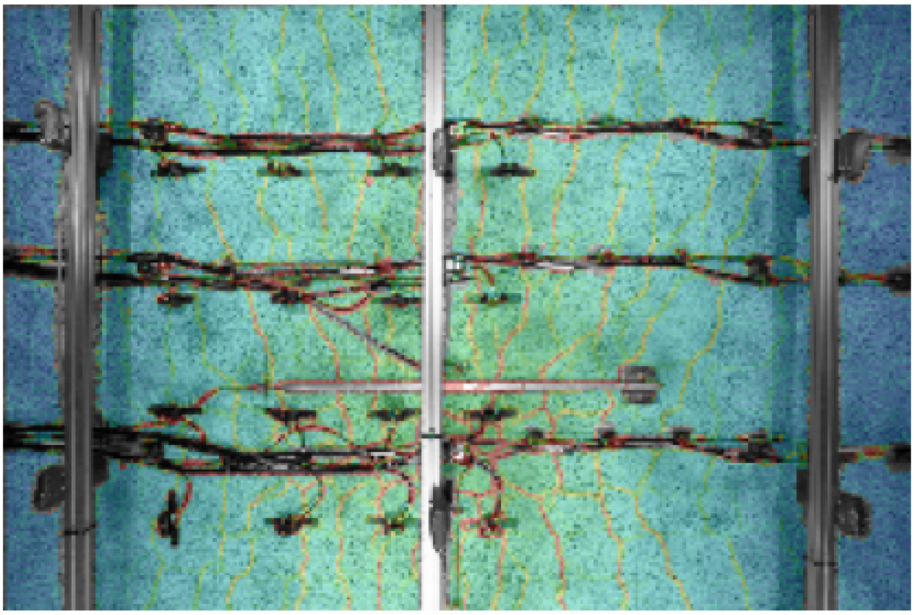

Figure E.14: 650kN [66]

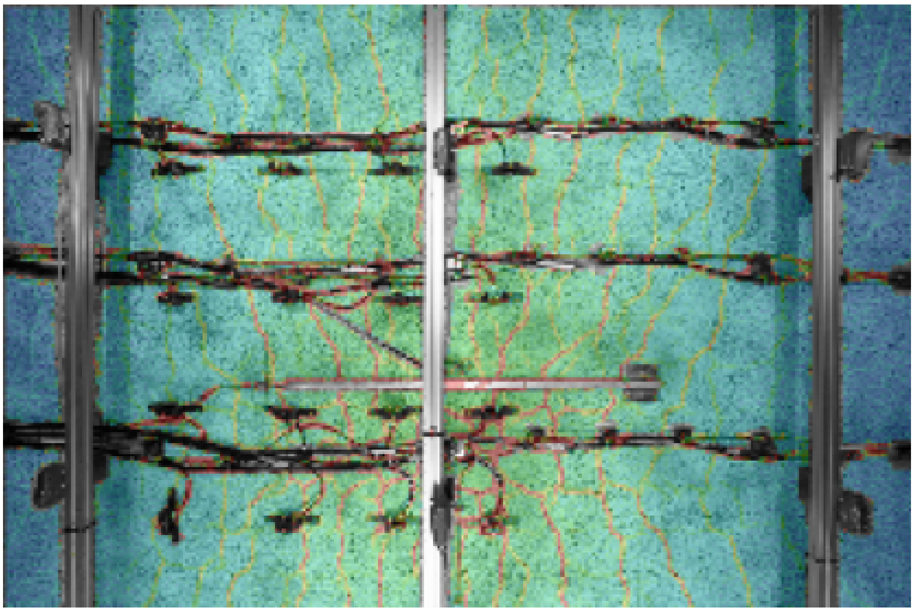

Figure E.15: 700kN [66]

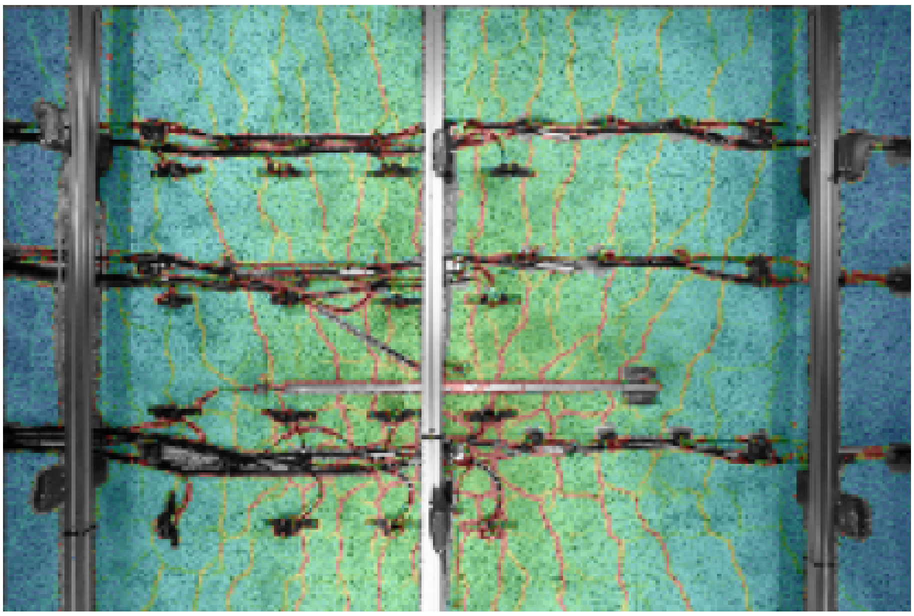

Figure E.16: 750kN [66]

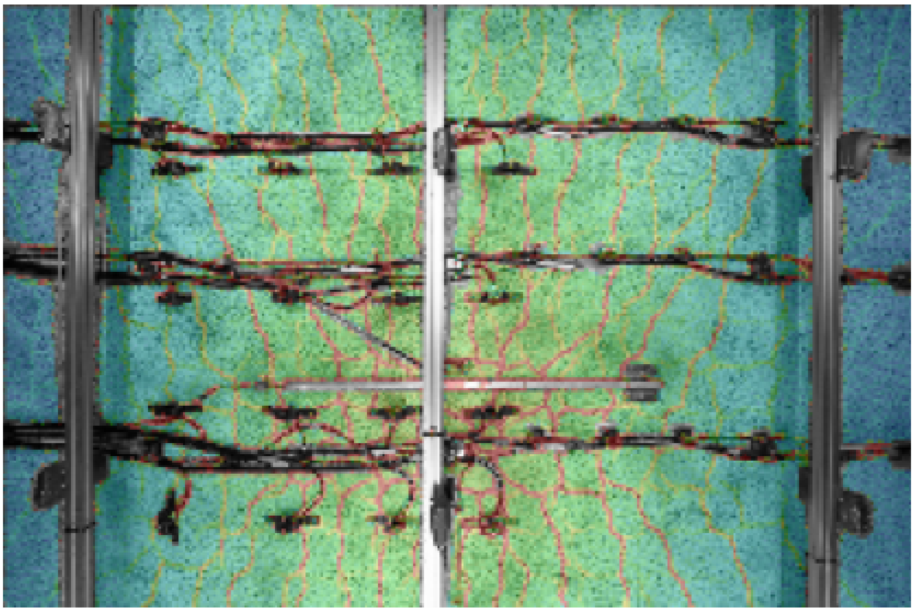

Figure E.17: 800kN [66]

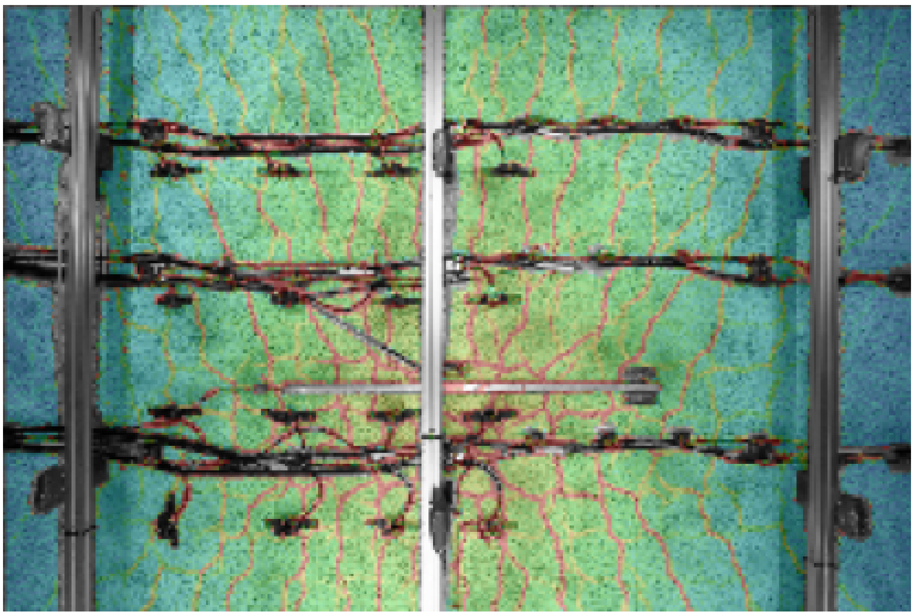

Figure E.18: 850kN [66]

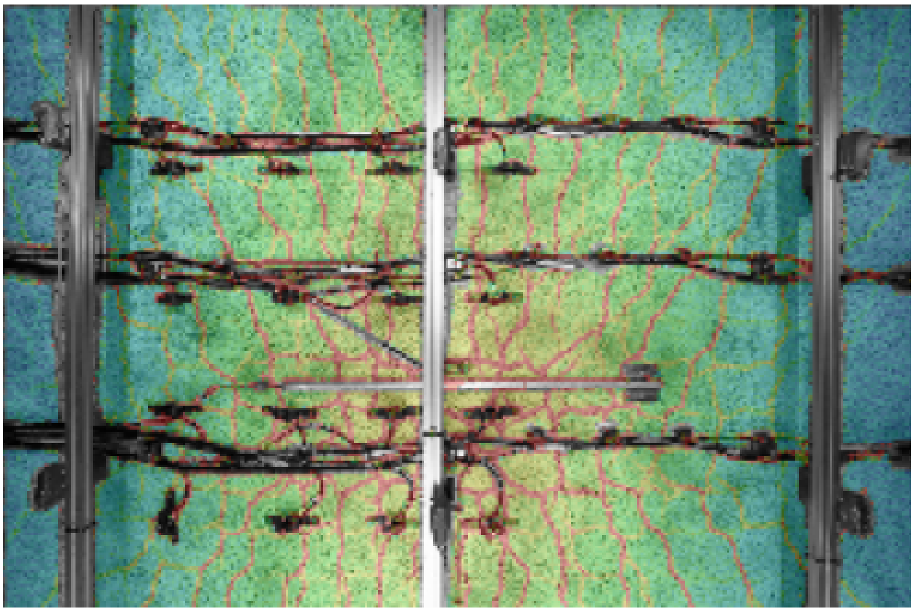
Figure E.19: 900kN [66]

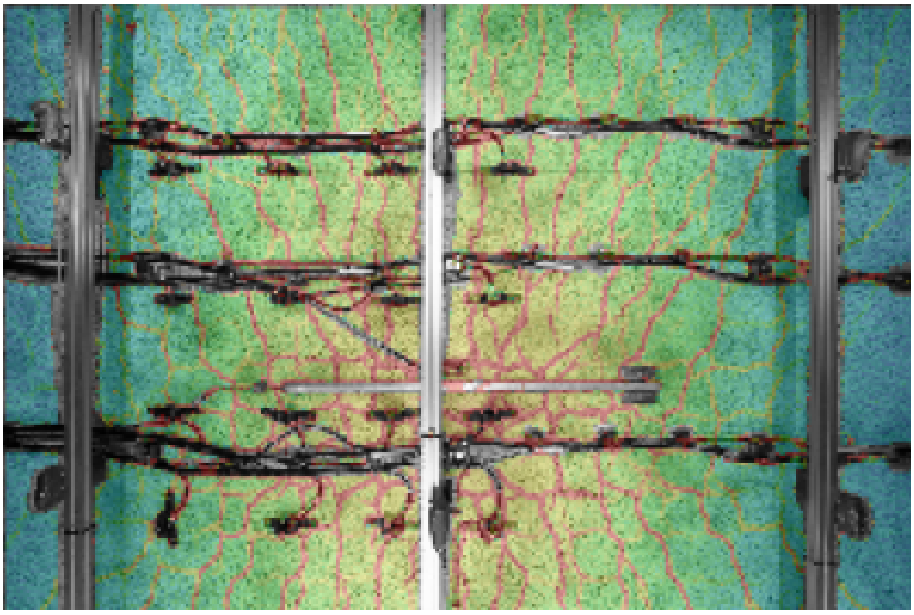
Figure E.20: 950kN [66]

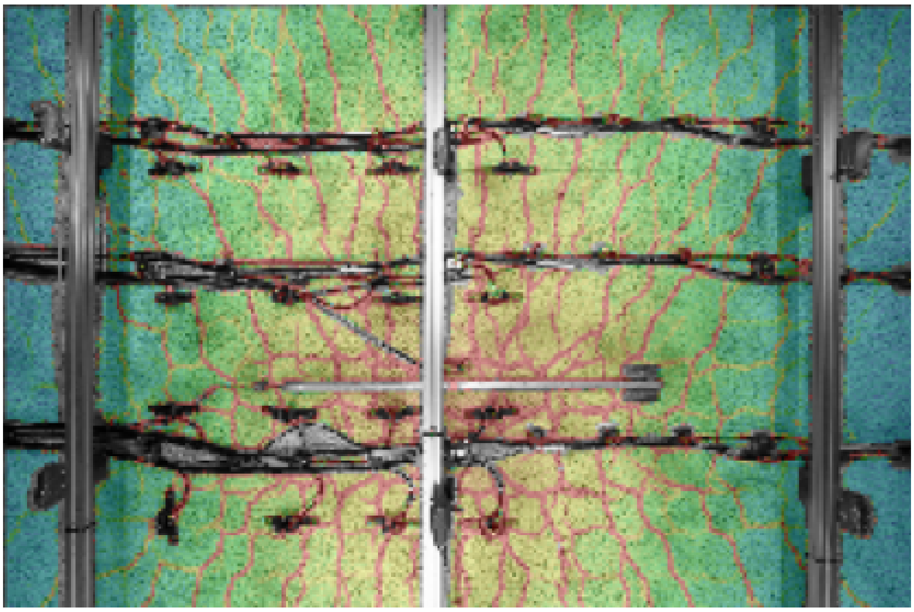
Figure E.21: 1000kN [66]

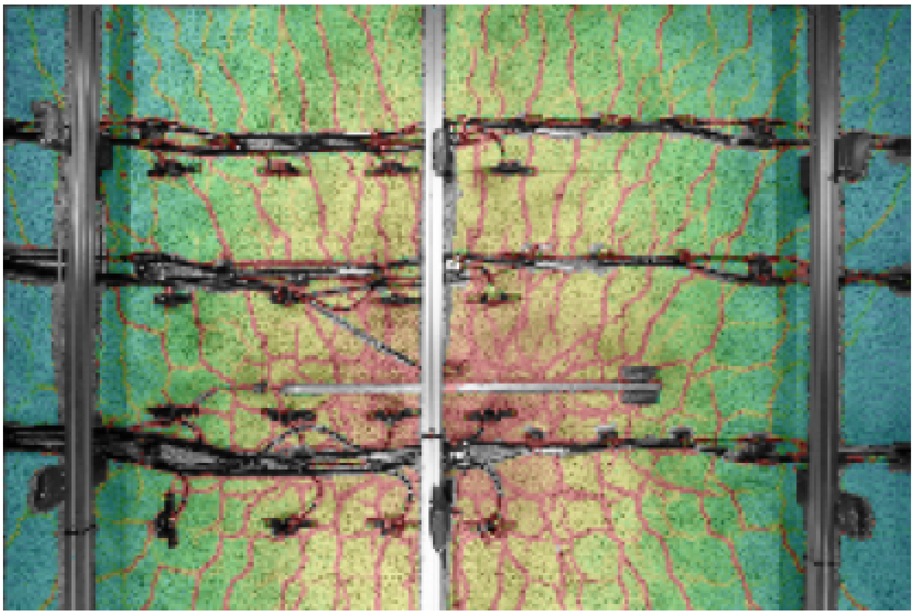
Figure E.22: 1050kN [66]

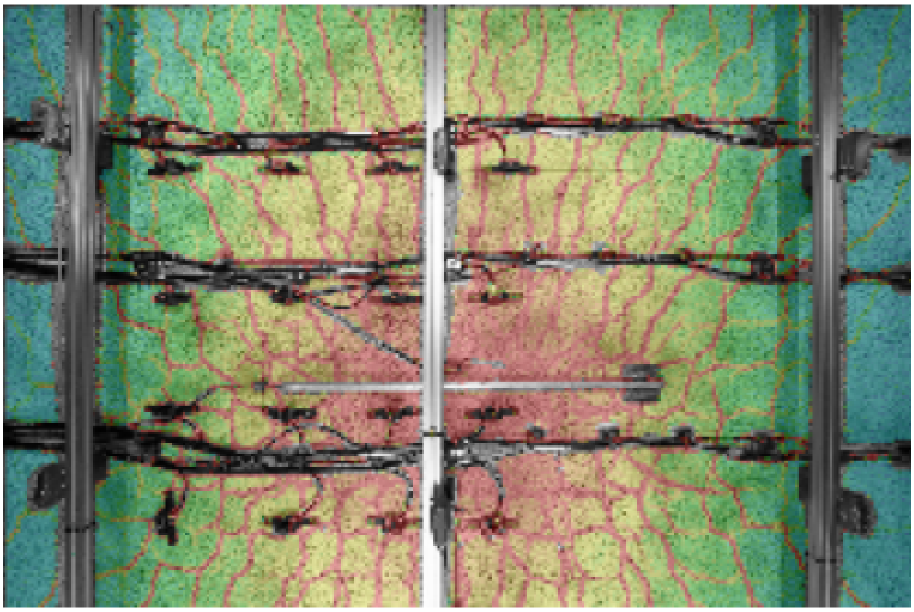

Figure E.23: 1100kN [66]

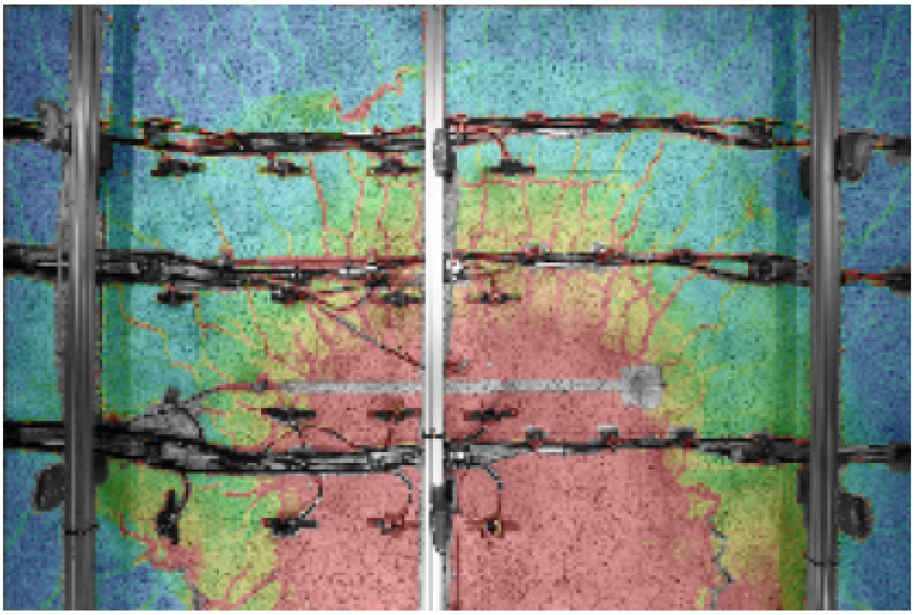

Figure E.24: after failure [66]

E.0.2 S1E2

In cref the range of the DIC measurement on the slab is indicated. Below, the DIC results for S1E2 are shown.

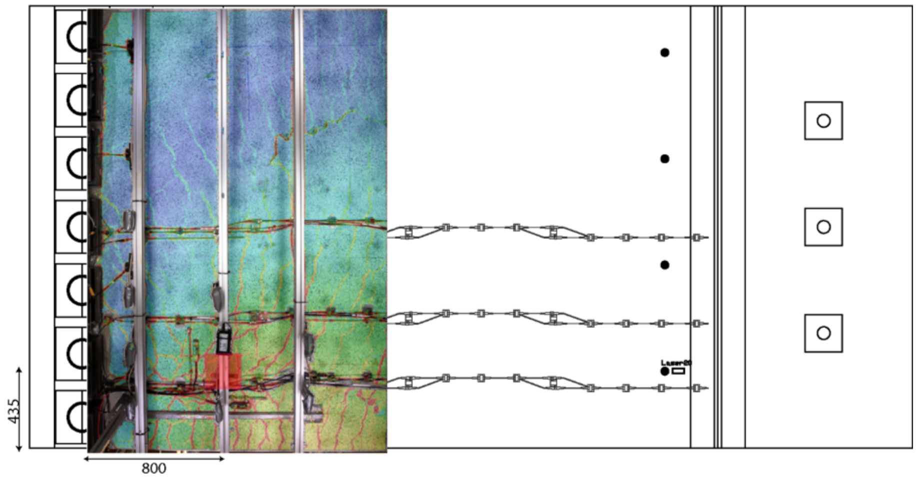

Figure E.25: overview of the DIC range for S1E2 [66]

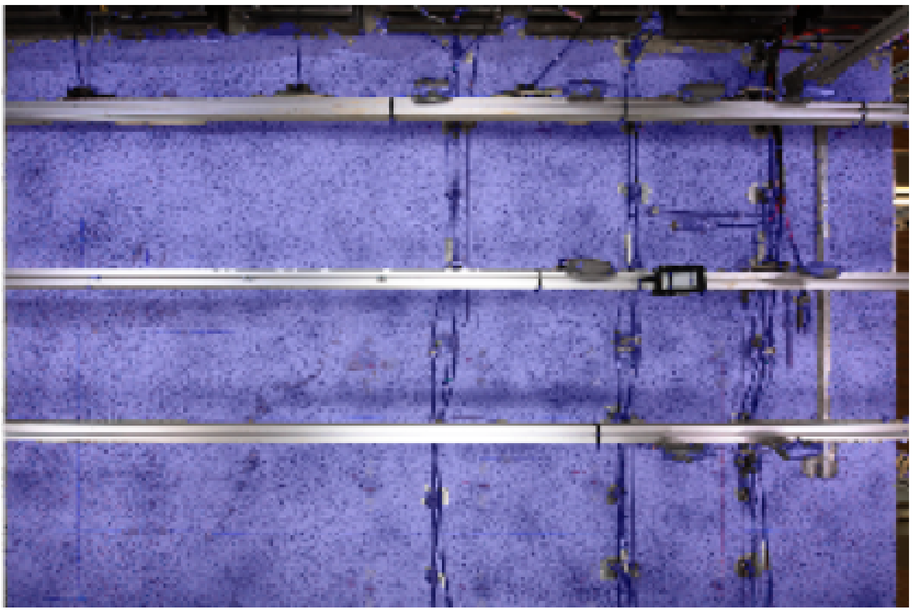

Figure E.26: 0kN [66]

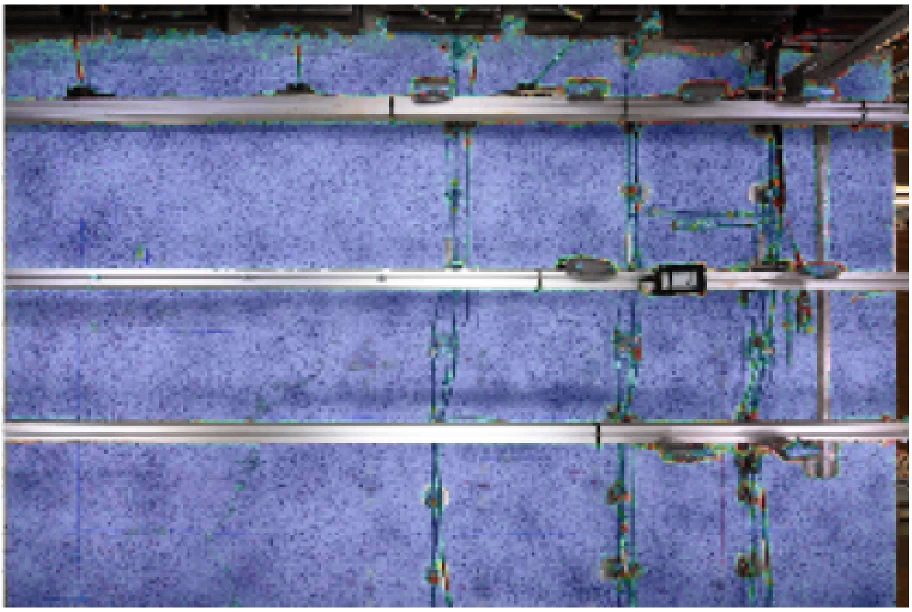
Figure E.27: 50kN [66]

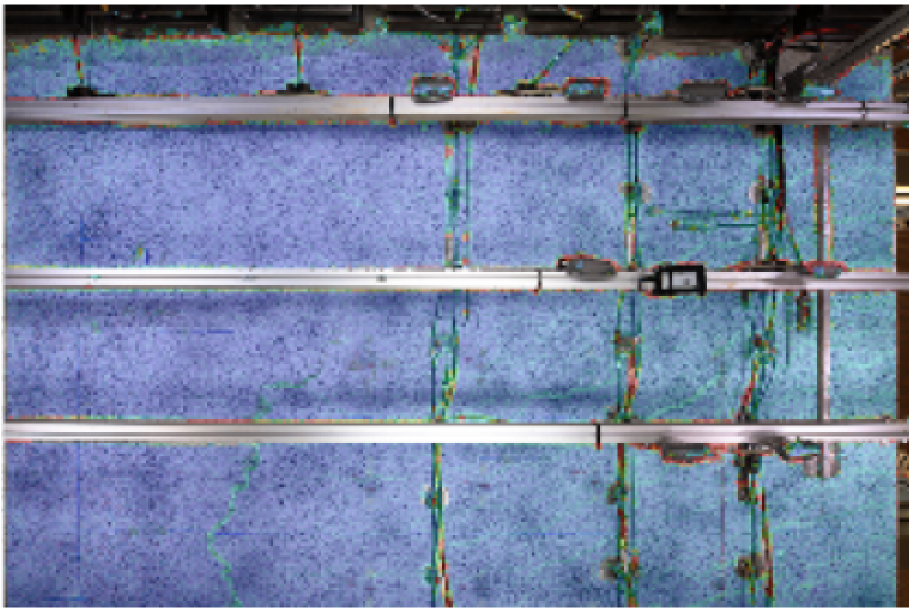
Figure E.28: 200kN [66]

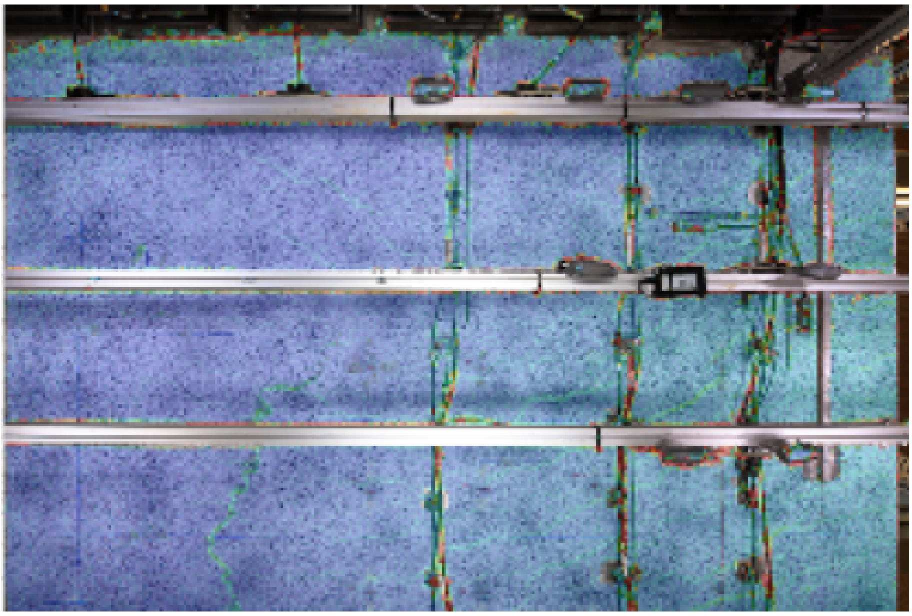

Figure E.29: 250kN [66]

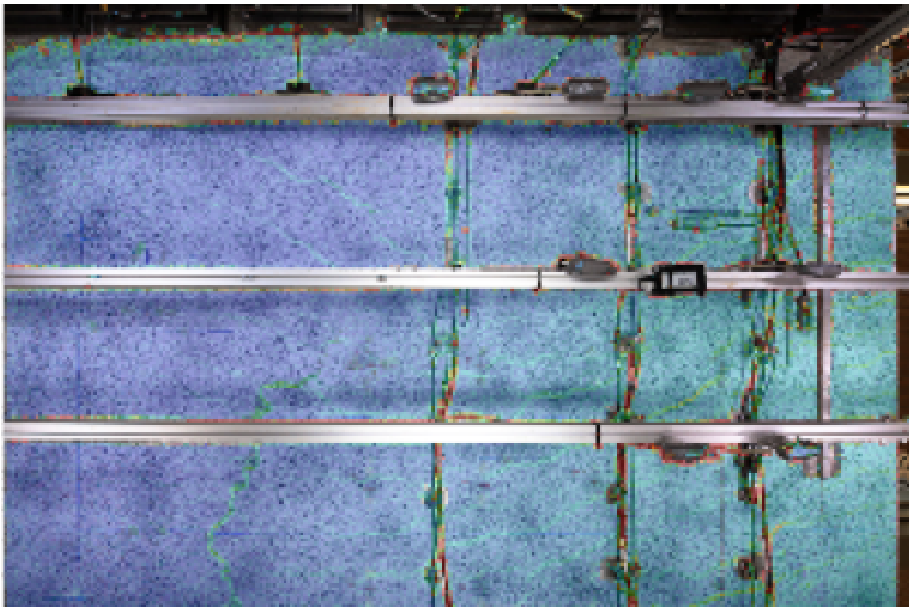

Figure E.30: 300kN [66]

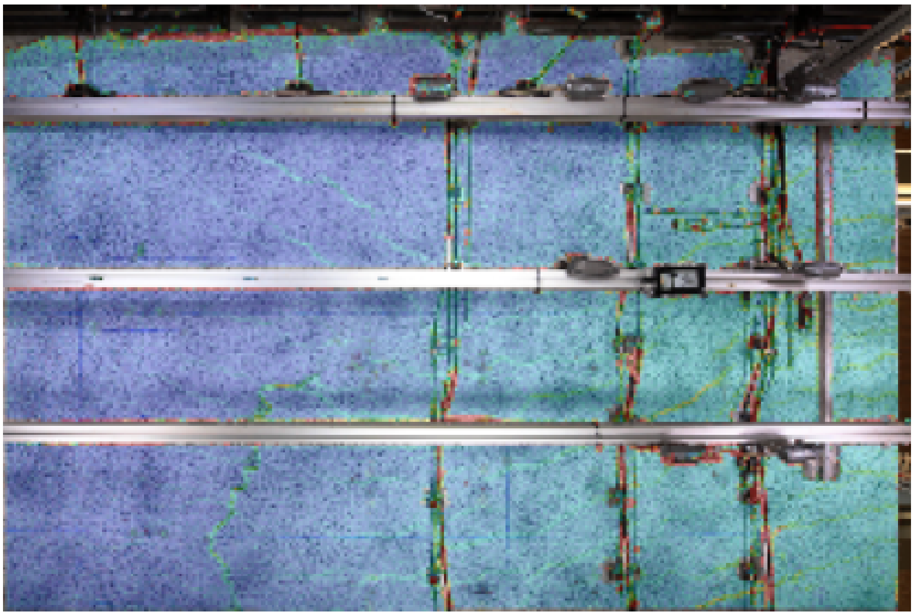

Figure E.31: 350kN [66]

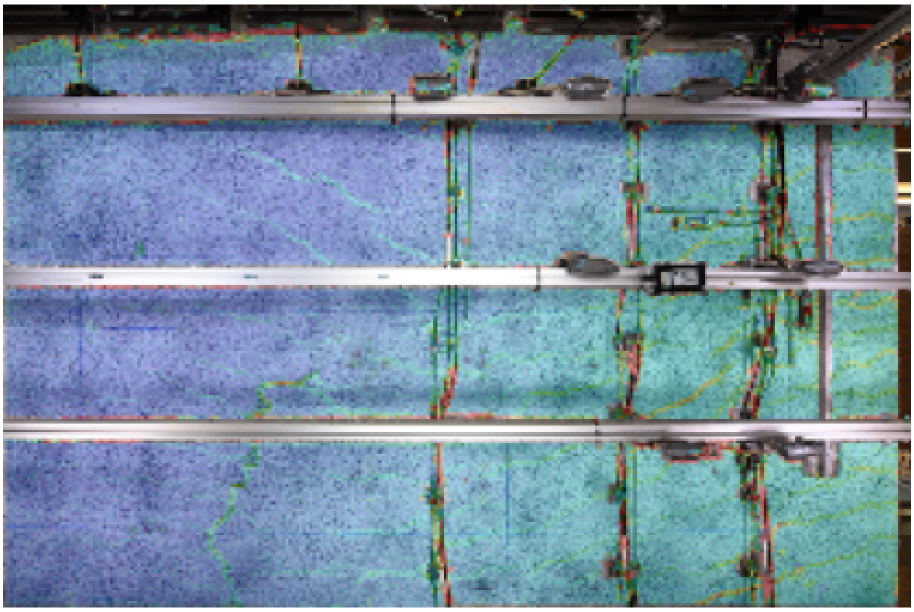

Figure E.32: 400kN [66]

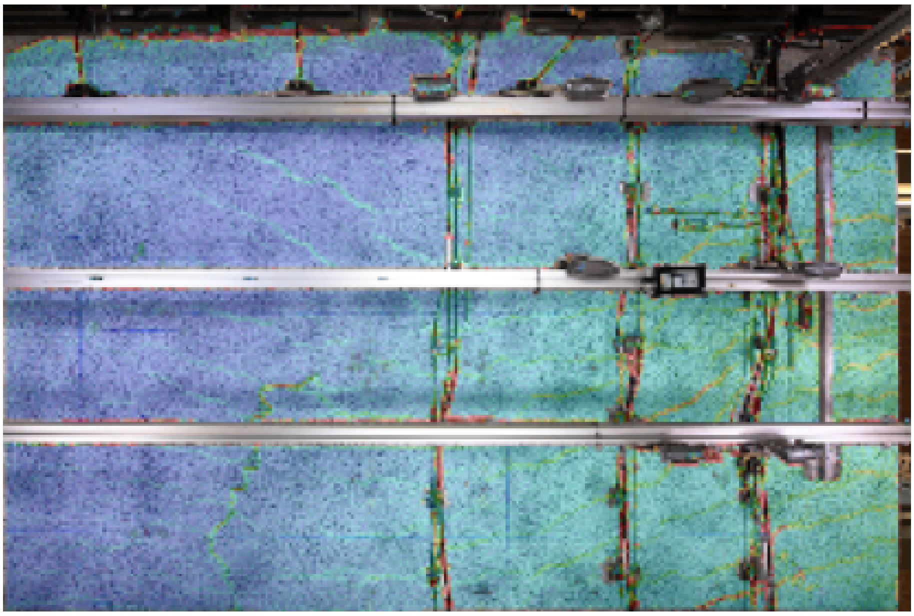

Figure E.33: 450kN [66]

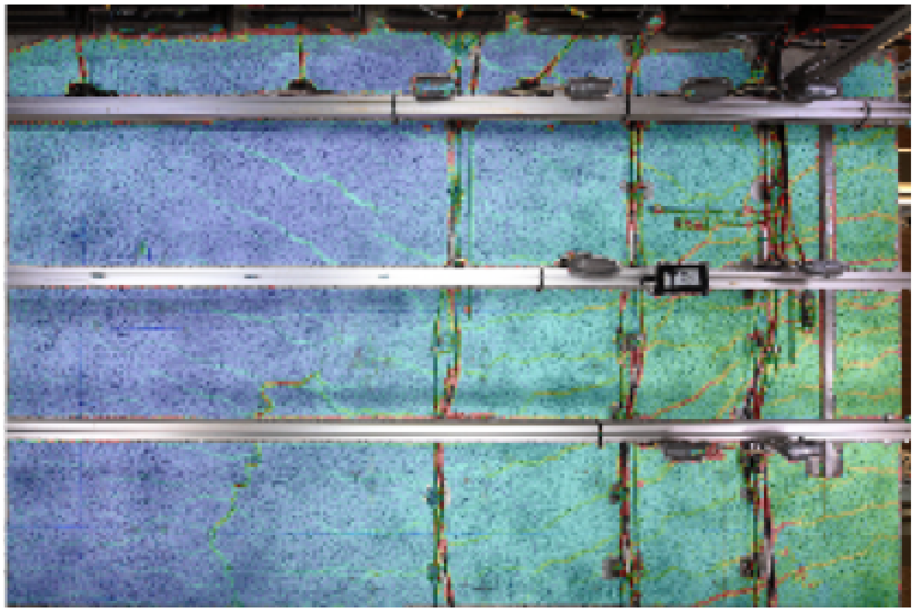

Figure E.34: 500kN [66]

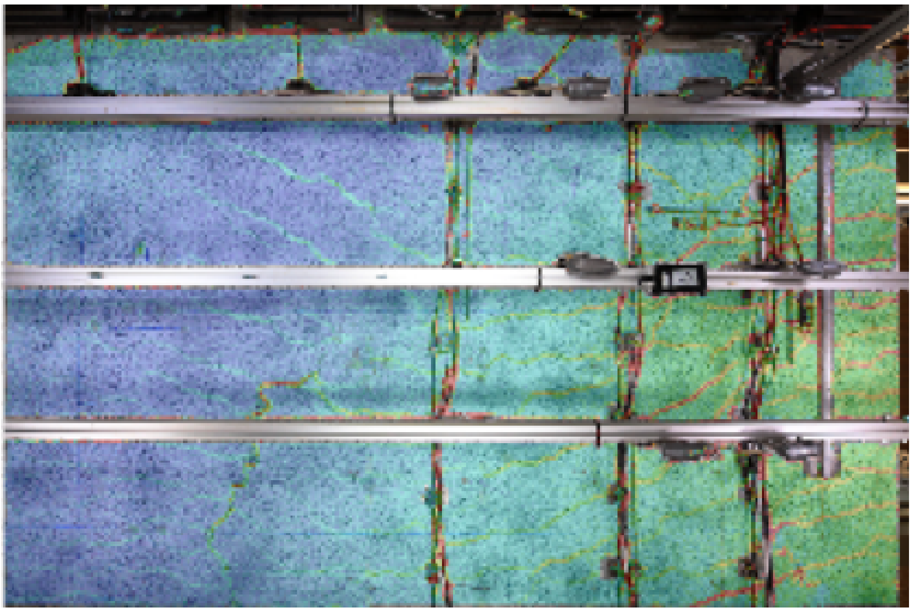
Figure E.35: 550kN [66]

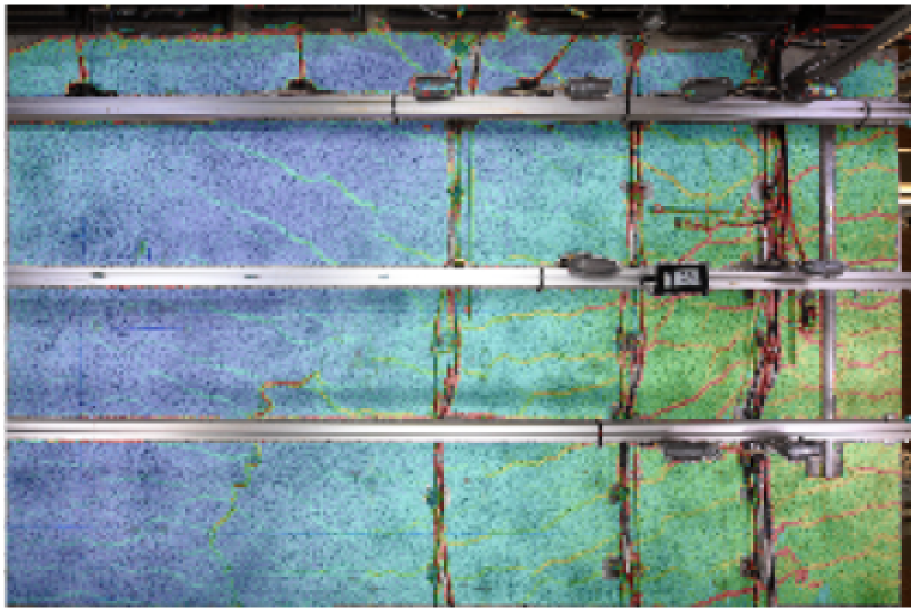
Figure E.36: 600kN [66]

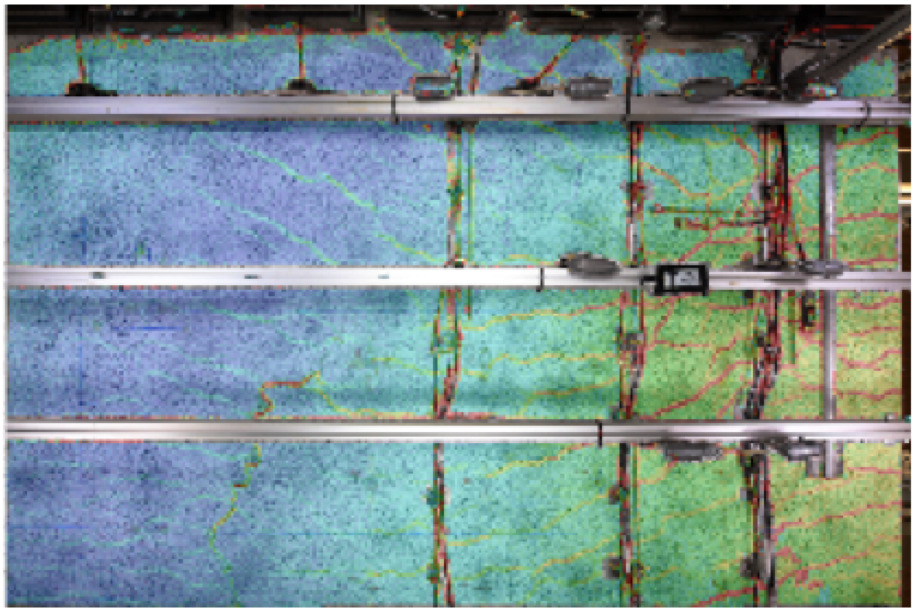

Figure E.37: 650kN [66]

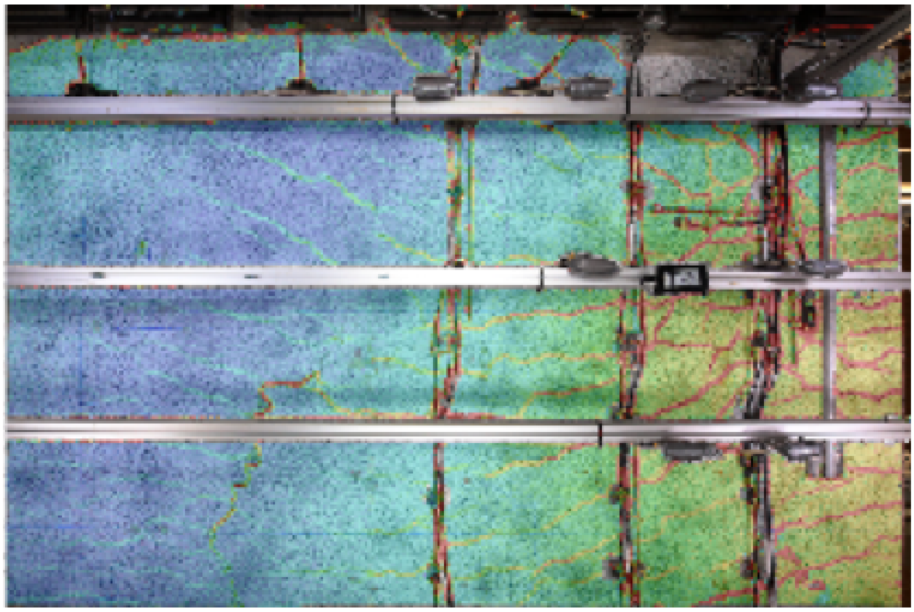

Figure E.38: 700kN [66]

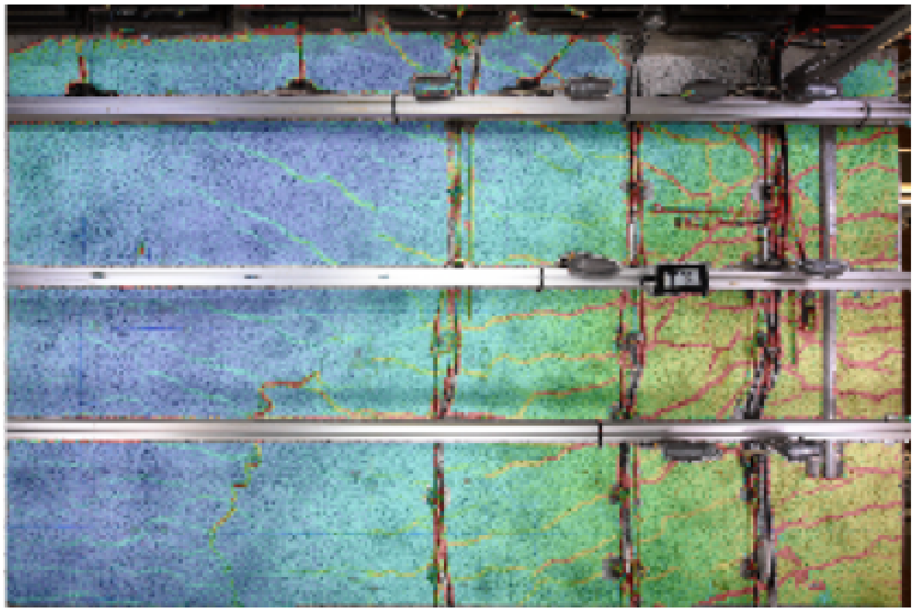

Figure E.39: 715kN [66]

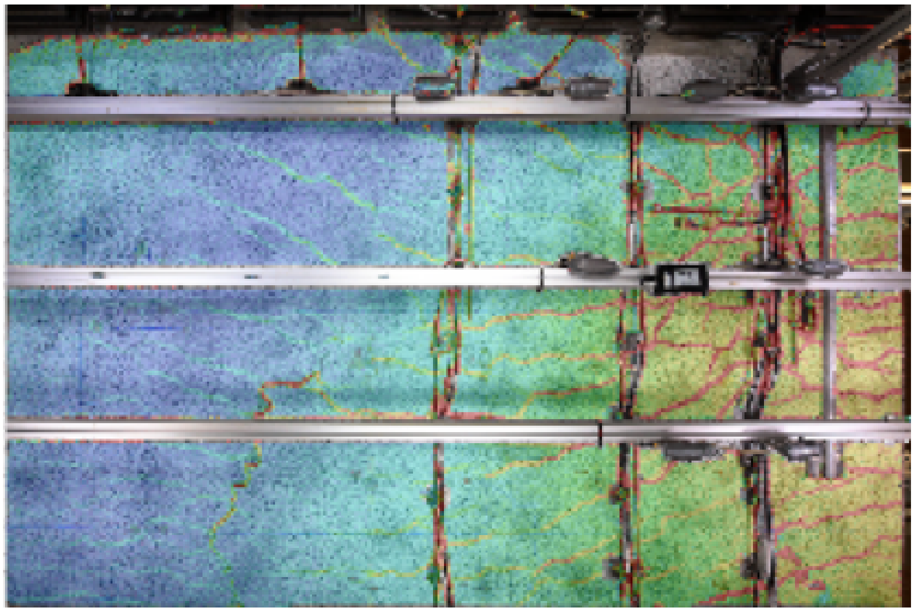

Figure E.40: 727kN [66]

E.0.3 S1E3

In fig. E.41 the range of the DIC measurement on the slab is indicated. Below, the DIC results for S1E3 are shown.

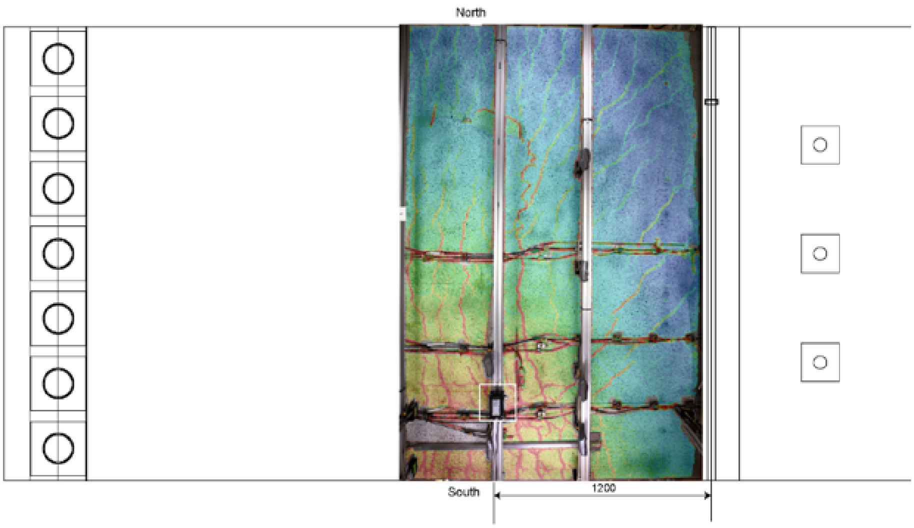

Figure E.41: overview of the DIC range for S1E3 [66]

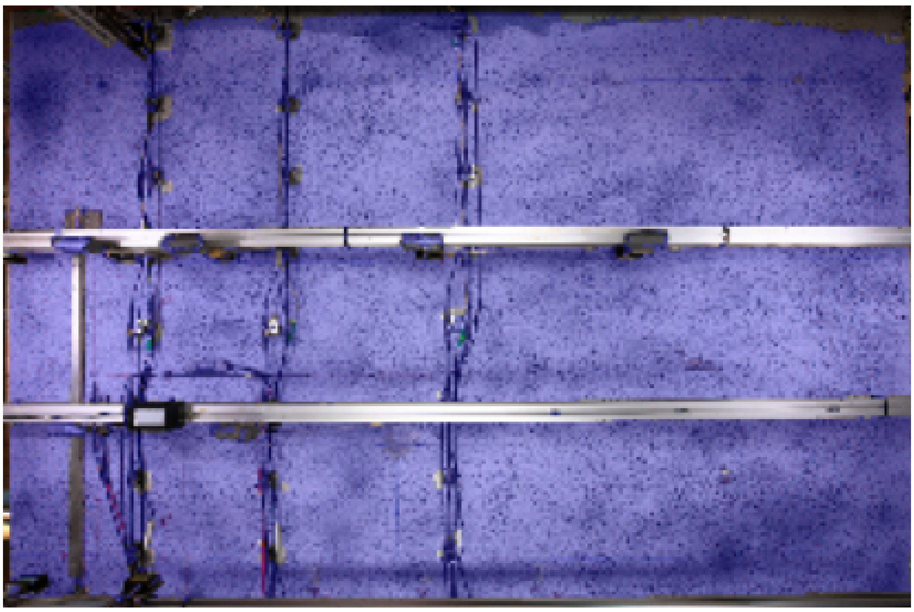

Figure E.42: 0kN [66]

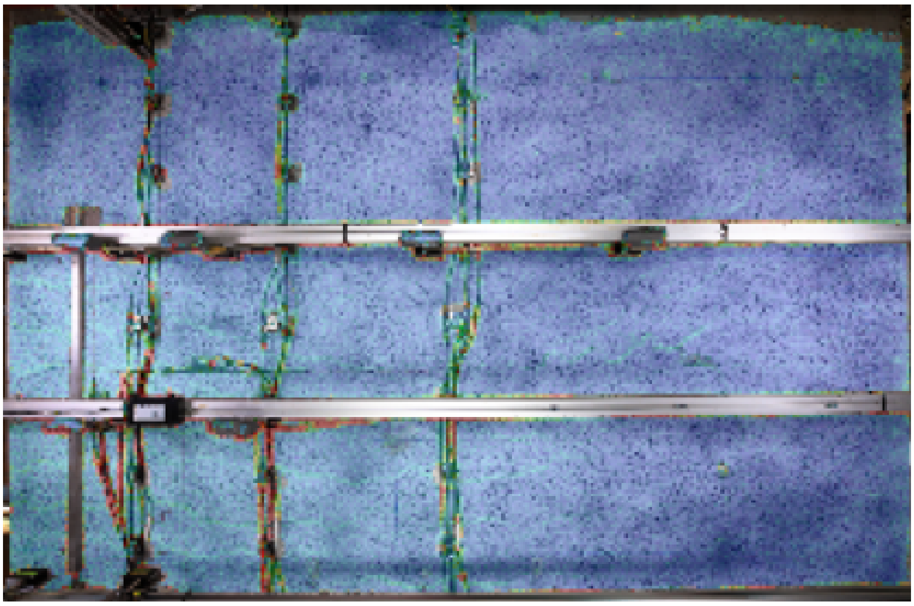

Figure E.43: 50kN [66]

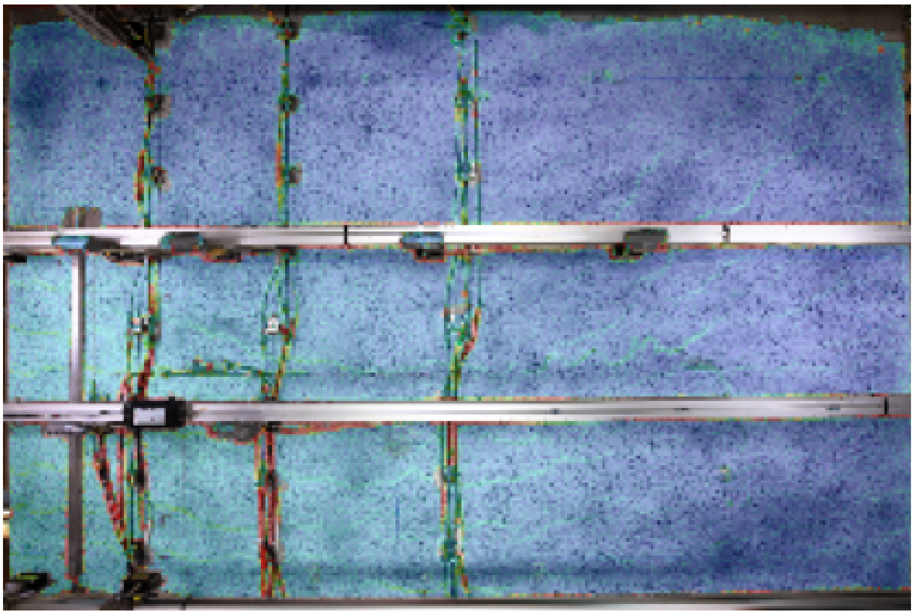

Figure E.44: 100kN [66]

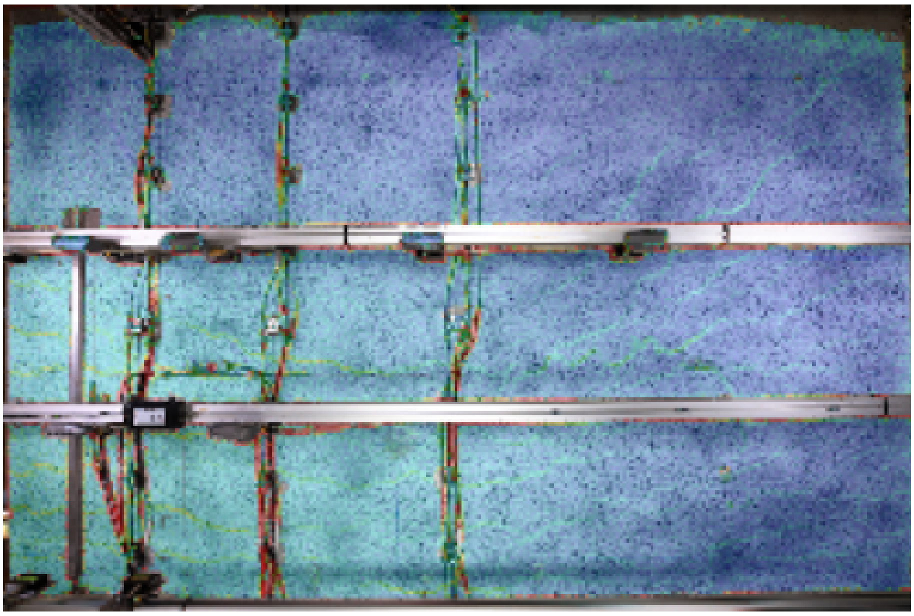

Figure E.45: 150kN [66]

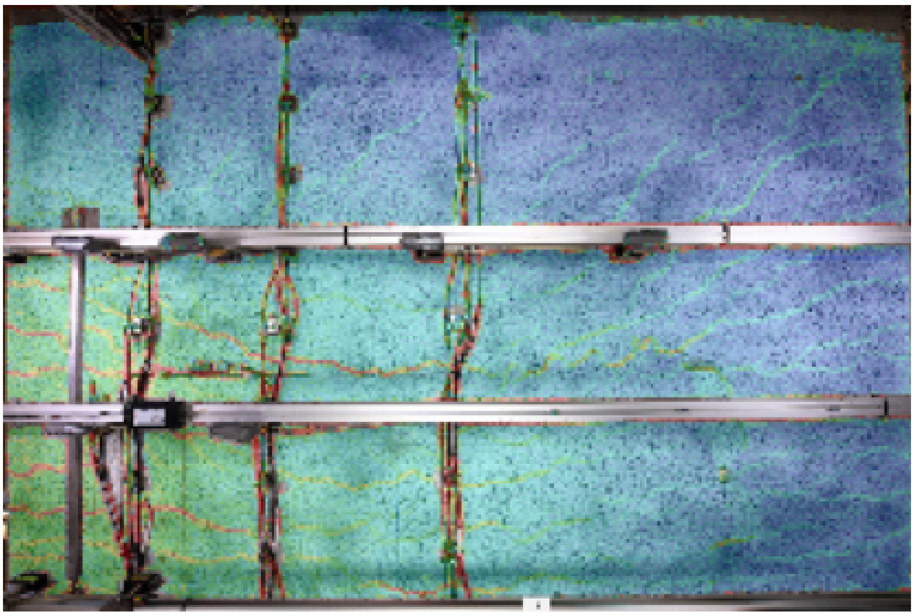

Figure E.46: 200kN [66]

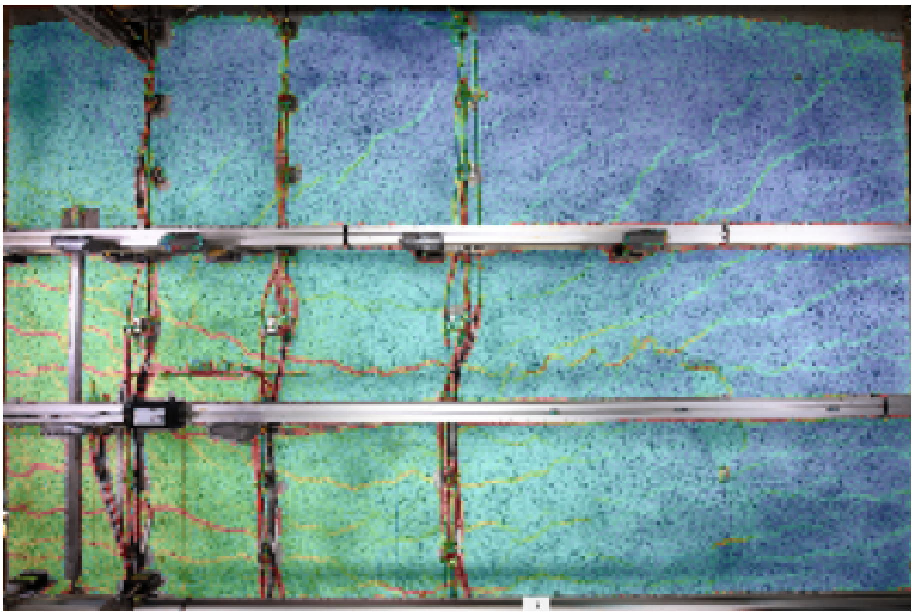

Figure E.47: 250kN [66]

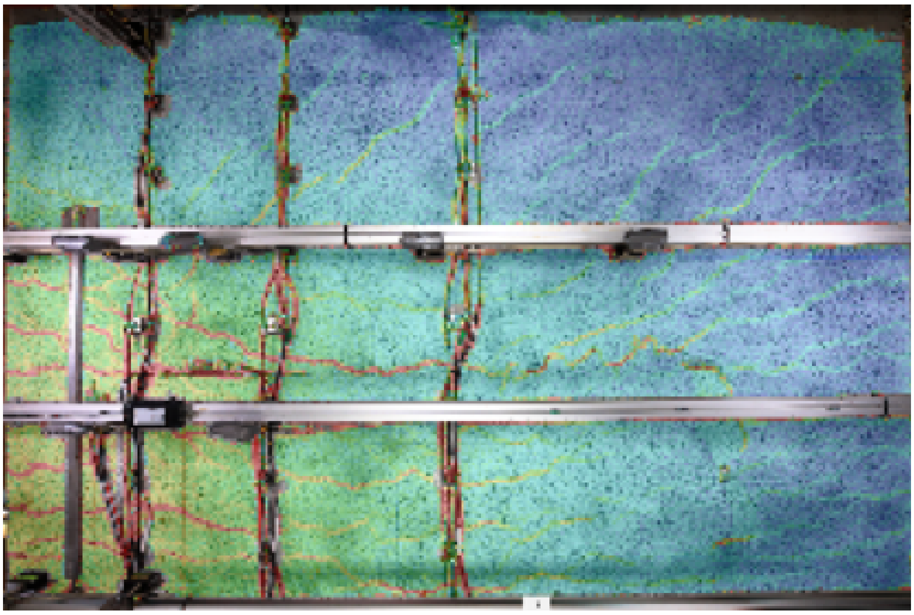

Figure E.48: 300kN [66]

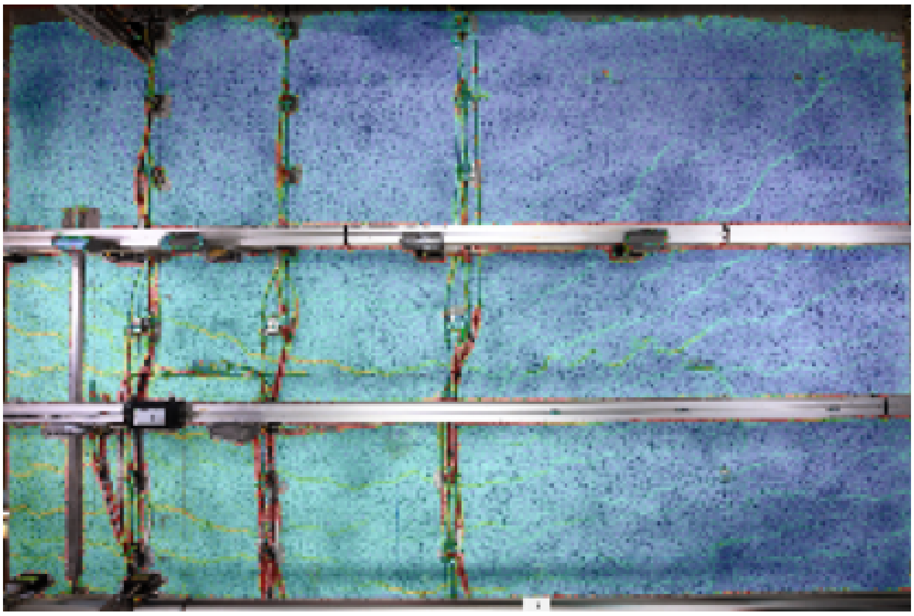

Figure E.49: 350kN [66]

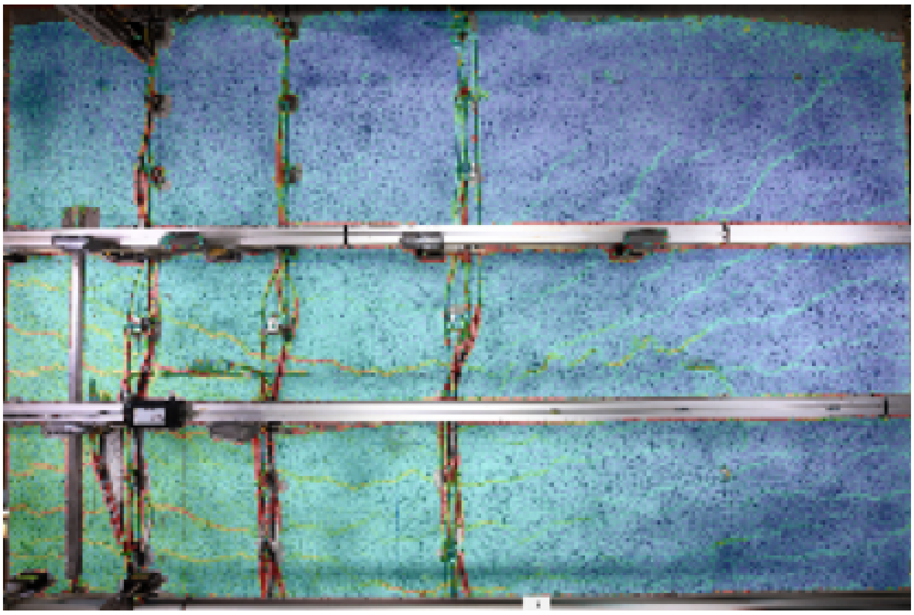

Figure E.50: 400kN [66]

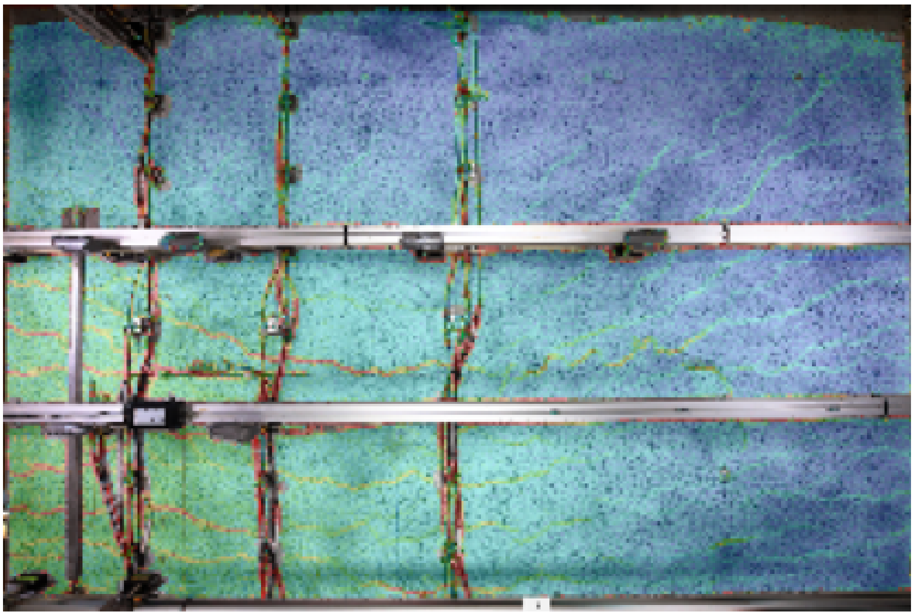
Figure E.51: 450kN [66]

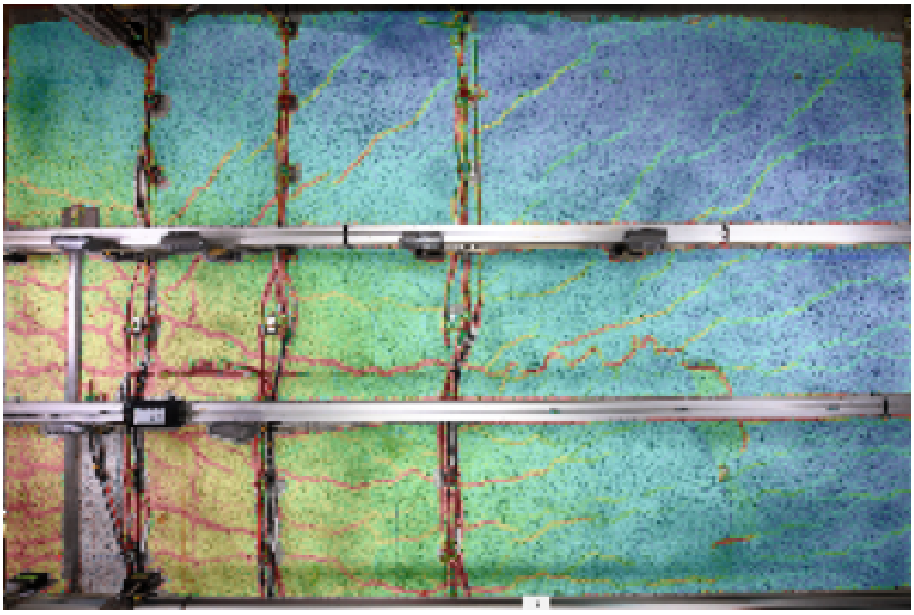
Figure E.52: 500kN [66]

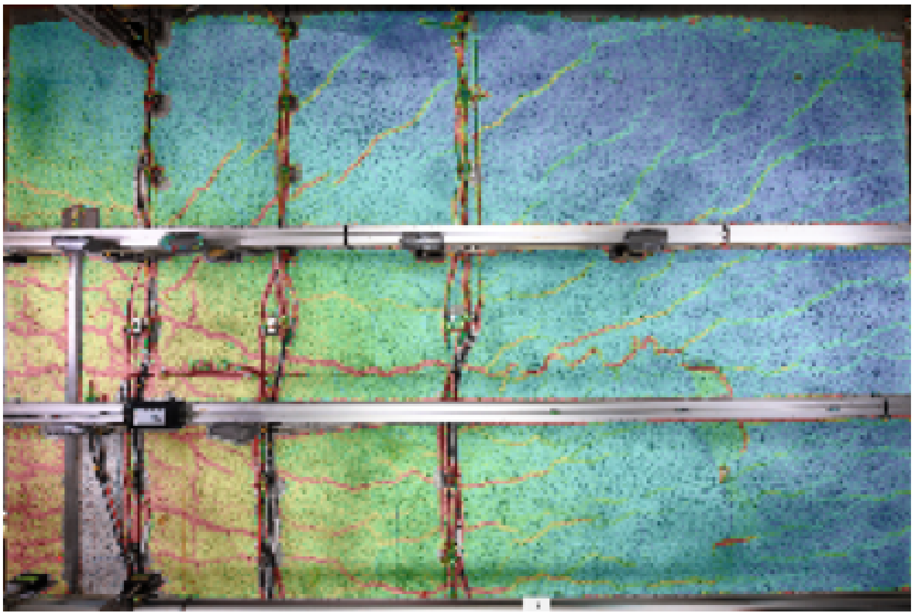
Figure E.53: 550kN [66]

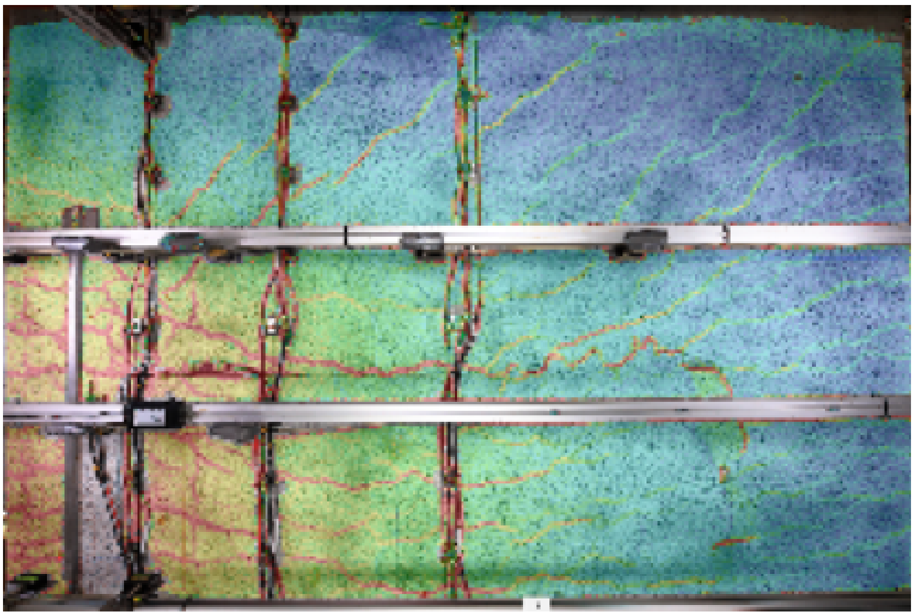
Figure E.54: 600kN [66]

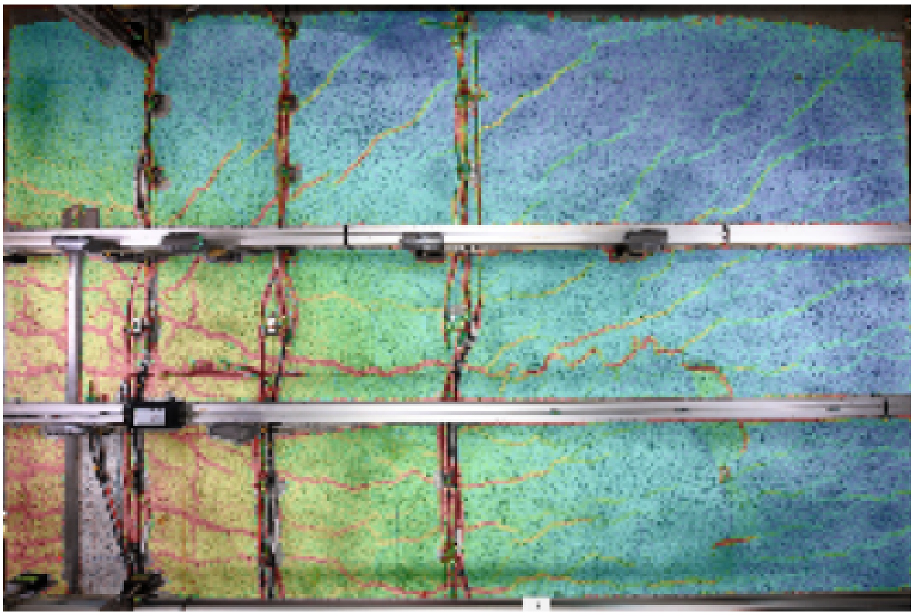

Figure E.55: 624kN [66]

E.0.4 DIC after removal of sensors

As can be observed on previous DIC results, some blind spots are present on the DIC results. Hence, after removal of the sensors, the slab was loaded again to get an overview over all the cracks at the blind spots. below, these results are provided.

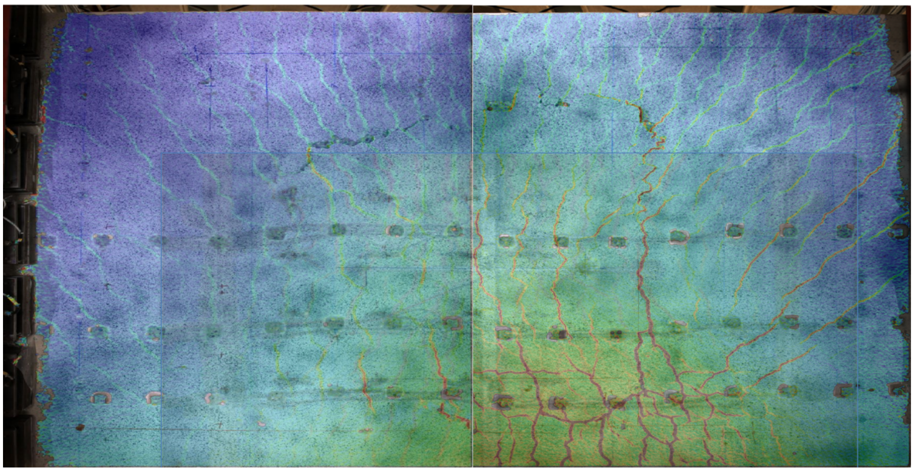

Figure E.56: Combined cracking pattern

Delft
University of
Technology

Delft, Building 23
2628 CN, Stevinweg 1

www.tudelft.nl/en/ceg/about-faculty/departments/engineering-structures/sections-labs/concrete-structures/